Distributed Damage Effect on Progressive Collapse of Structures & Variability Response Functions in Stochastic 2D Elasticity Problems

Evgenia (Jenny) Sideri

Submitted in partial fulfillment of the
requirements for the degree of
Doctor of Philosophy
in the Graduate School of Arts and Sciences

Columbia University
2017

Abstract

Distributed Damage Effect on Progressive Collapse of Structures & Variability Response Functions in 2D Elasticity Stochastic Problems

Evgenia (Jenny) Sideri

This dissertation investigates the distributed damage effect on Progressive Collapse of structures highlighted by applications on the nonlinear static and dynamic behavior of buildings, and contributes to the theoretical development of the Variability Response Function concept and its applicability extension in two-dimensional elasticity stochastic problems.

Part I of this dissertation focuses on the recently emerging research field of Progressive Collapse of structures. The alternate load path method has so far dominated the field of progressive collapse of structures; in order to assess the resilience of structural systems, the concept of the removal of a key element is utilized as a means of damage introduction to the system. Recent studies have indicated that the complete column loss notion is unrealistic and unable to describe a real extreme loading event, e.g. a blast, that will introduce damage to more than one elements in its vicinity. This dissertation presents a new partial distributed damage method (PDDM) for steel moment frames, by utilizing powerful finite element computational tools that are able to capture loss of stability phenomena. Through the application of a damage index δ_j and the investigation of damage propagation, it is shown that the introduction of partial damage in the system can significantly modify the collapse mechanisms and overall affect the response of the structure.

Subsequently, Part I elaborates on the distributed column damage effect on Progressive Collapse vulnerability in steel buildings exposed to an external blast event. Recent terrorist attacks on civil engineering infrastructure around the world have initiated extensive research on progressive collapse analysis of multi-story buildings subjected to blast loading. The widely accepted alternate load path method is a threat-independent method that is able to assess the response of a structure in case of extreme hazard loads, without the consideration of the actual loads occurring. Such simplification offers great advantages but at the same

time fails to incorporate the role of a wider damaged area into the collapse modes of structures. To this end, the investigation of damage distribution on adjacent structural members induced by blast loads is considered critical for the evaluation of structural robustness against abnormal loads that may initiate progressive collapse. This dissertation presents detailed 3D nonlinear finite element dynamic analyses of steel frame buildings in order to examine the spatially distributed response and damage to frame members along the building exterior facing an external blast. A methodology to assess the progressive collapse vulnerability is also proposed, which includes four consecutive steps to simulate the loading event sequence. Three case studies of steel buildings with different structural systems serve as examples for the application of the proposed methodology. A high-rise (20-story) building is firstly subjected to a blast load scenario, while the complex 3D system results in the heavily impacted region are compared with individual column responses (SDOF) obtained from a simplified analytical approach consistent with current design recommendations. Parameters affecting the spatially distributed pressure and response quantities are identified, and the sensitivity of the damage results to the spatial variation of these parameters is established for the case of the 20-story building. Subsequently, two typical mid-rise (10-story) office steel buildings with identical floor plan layout but different lateral load resisting systems are examined; one including perimeter moment resisting frames (MRFs) and one including interior reinforced concrete (RC) rigid core. It is shown that MRFs offer a substantial increase in robustness against blast events, and the role of interior gravity columns identified as the 'weakest links' of the structural framing is discussed.

Part II of this dissertation focuses on the development of Variability Response Functions for apparent material properties in 2D elasticity stochastic problems. The material properties of a wide range of structural mechanics problems are often characterized by random spatial fluctuations. Calculation of apparent properties of such randomly heterogeneous materials is an important procedure, yet no general method besides Monte Carlo simulation exists for evaluating the stochastic variability of these apparent properties for structures smaller

than the representative volume element (RVE). In this direction, the concept of Variability Response Function (VRF) has been proposed as a means to capture the effect of stochastic spectral characteristics of uncertain system parameters modeled by homogeneous stochastic fields on the uncertain response of structural systems, without the need for computationally expensive Monte Carlo simulations. Recent studies have formally proved the existence of VRF for apparent properties for statically determinate linear beams through elastic strain energy equivalence of the heterogeneous and equivalent homogeneous bodies, while a Monte-Carlo based methodology for the generalization of the VRF concept to statically indeterminate beams has been recently developed. In this dissertation, the VRF methodology of apparent properties is extended to two-dimensional elasticity stochastic problems discretized on a finite element domain, in order to analytically formulate a VRF that is independent of the marginal distribution and spectral density function of the underlying random heterogeneous material property field (it depends only on the boundary conditions and deterministic structural configuration). Representative examples that illustrate the approach include two-dimensional plane stress problems and underline the dependence of the VRFs on scale, shape and aspect ratio of the finite elements.

Contents

List of Figures

Acknowledgements

This dissertation summarizes my research work at Columbia university and signals the beginning of a new chapter in my life, outside of academia. Although this is an individual work, I could never have succeeded in graduating without the guidance, support and inspiration of so many people. First and foremost, I am eternally grateful to my advisor, Professor George Deodatis, for always providing technical, professional and personal advice, while showing unlimited zeal in helping me overcome all possible obstacles. Professor Deodatis introduced me to the wonders of research and teaching, as an inspirational teacher himself, treating me always with open doors as a true mentor throughout my whole academic career at Columbia University. I would also like to express my deepest gratitude to my co-advisors, Professor Simos Gerasimidis and Professor Sanjay R. Arwade, for their invaluable encouragement to independently pursue my doctoral research and motivation to explore the depths of so many subjects. I would also like to take this opportunity and thank the rest of my committee members, Professor Maria Feng and Professor Patricia Culligan, for their thoughtful comments and generous insights.

During the past four years, the department of Civil Engineering and Engineering Mechanics has been my home and I am endlessly indebted to all faculty and stuff for supporting me through teaching and research assistantships. Most importantly, I need to thank my fellow Ph.D. students and friends who have patiently kept up with everyday life, shared research and personal concerns, lunch and coffee breaks but most of all fun. To name a few, many thanks to Apostolis Psaros, Maura Torres, Juan Guillermo Londoño, Jinwoo Jang, Ekin

Özer, Miguel Arriaga E Cunha, Luciana Balsamo, Suparno Mukhopadhyay, Dimitris Fafalis, Luc Berger-Vergiat etc. and apologies for inevitably forgetting some names. A very special thank you to Christos Vlachos and Mostafa Mobasher for their friendship and unconditional help to surmount any technical difficultly. I could not have done it without you guys.

Throughout all those years at Columbia University, I could not have wished for a better companion than Athina Spyridaki. Thank you for being my best friend, colleague, collaborating researcher, roommate and basically the sister I never had. To Sertaç, Dimitra and Mai, thank you for always being there when I needed family. Finally, I would like to express my deepest appreciation to my parents and brother for always supporting and motivating me to overcome my fears and take a huge leap in my career by attending Columbia University. Thank you for always believing in me and instilling me the desire for higher education.

To my lovely parents and brother,

για πάντα η δική σας Τζενούλα.

Part I

Distributed Damage Effect on Progressive Collapse of Structures

Chapter 1

Introduction: Part I

1.1 Motivation and Background

Part I of this dissertation expands the knowledge about the influence of distributed damage on progressive collapse vulnerability of structures. Progressive collapse of structures is initiated by a localized triggering event (blast/terrorist attacks, fire, vehicle impact, construction errors etc.) that introduces damage to a structural system, resulting in a disproportionate to the initial event structural response. A characteristic example of progressive but also disproportionate collapse was the Ronan Point Tower disaster of 1968 illustrated in Figure 1.1; a relatively small natural gas explosion at the 18^{th} floor of the building caused failure of load-bearing precast concrete panels at the building corner. Due to the loss of support at the 18^{th} floor, the above floors also collapsed leading to a major debris impact of these collapsing floors and eventually to a chain reaction of collapses all the way to the ground floor. This kind of failure, labeled as sequential or progressive collapse since the initial triggering event was by no means proportionate to the magnitude of final collapse, led to the engineering community and public regulatory agencies to change common building design practice and regulations towards prevention of recurrence of such tragedies.

Due to the recent Alfred P. Murrah Federal Building (1995) and World Trade Center

Figure 1.1: Ronan Point partial collapse (London, 1968) due to local gas explosion on the 18^{th} floor

(2001) blast and impact attacks, the field of progressive collapse initiated by blast and impact loading has attracted the interest of many researchers. In this environment, two documents have dominated the field of regulative progressive collapse published by the Unified Facilities Criteria, Department of Defense (DoD 2009 [1]) and the General Services Administration (GSA 2003 [2]). These two recently published design guidelines suggest the most popular among practitioners and researchers method for progressive collapse analysis, namely the 'threat-independent' Alternate Path Method (APM), which attempts to quantify the robustness of a structural system by focusing on the removal of a key load-bearing element of the system (i.e. column) as a means to introduce damage.

Numerous research studies [3] - [23] have recently emerged in the literature that attempt

to quantify the progressive collapse potential of structures through a variety of different approaches. Most of the research work focuses on developing efficient and reliable progressive collapse analysis methods, in order to assess the capability of structures to withstand localized damage and enhance the structural robustness under extreme loading events. In particular, a very significant publication by Frangopol and Curley 1987 [3] defined in detail important terms such as redundancy and damage and emphasize their correlation and role in structural systems' resistance against collapse, while distinguishing between 'fail-safe' structures (with the ability of redistributing loads and offering multiple load-paths) and 'weakest-link' structures (there are no alternative load paths). Ettouney and DiMaggio 1998 [22] and most importantly Ettouney et al. 2006 [4] demonstrated the critical importance of global stability system considerations and manifested the inability of the alternate path method to account for global response of a structure when performing progressive collapse analysis. The book of Starossek 2009 [5] presented explicit information about the distinction between disproportionate and progressive collapse of structures and described a plethora of different typologies of progressive collapse and the corresponding design methods. Many different aspects of progressive collapse are also discussed in Ellingwood et al. 2007 [6], where the distinction between direct (such as the alternate path method) and indirect methods of analysis is underlined. Marjanishvili and Agnew 2011 [7] compared linear, nonlinear, static and dynamic analyses in 3D building configurations and concluded that material and geometric nonlinearities are essential to account for. Kim and Kim 2009 [9] conducted linear and nonlinear dynamic analysis in 2D frames by taking into account only material nonlinearities, while Khandelwal and El-Tawil 2011 [10] studied the vertical push-down technique through nonlinear dynamic analysis of 2D steel frames as a means to quantify robustness by taking into account not only material but also geometric nonlinearities. Kwasniewski 2010 [12] and Szyniszewski and Krauthammer 2012 [20] performed nonlinear dynamic analysis of 3D frames that incorporated the slab simulation, while the latter identified buckling-induced failure modes by using an energy-based approach. Foley et al. 2007 [15] performed linear

dynamic analysis in 3D frames by replacing the slab with horizontal stiffeners and Alashker et al. 2011 [21] conducted nonlinear dynamic analyses accounting for both material and geometric nonlinearities, while comparing 2D and 3D building models.

Since the response of structures subjected to extreme events is most commonly highly nonlinear, progressive collapse analysis methods that utilize powerful computational tools constitute the only appropriate research approach towards reliable assessment of progressive collapse vulnerability. It is thus crucial that those finite element tools include material and geometric nonlinearities in order to be able to capture nonlinear loss of stability phenomena. Recent papers by Ettouney et al. 2006 [4], Gerasimidis et al. 2014 [8], Gerasimidis 2014 [24] and Spyridaki et al. 2013 [25] have highlighted the significance of stability considerations within a material and geometric nonlinearity analysis framework, as the only approach for correctly predicting collapse mechanisms and the corresponding collapse loads. The most usually observed collapse modes of buildings can be identified as: plastification of beam edges above the location of the column removal (yielding-type beam failure; ductile) as described in Sideri et al. 2013 [26], loss of stability of adjacent to the removal elements (buckling-type column failure; brittle), shear failure of beam to column connections (Khandelwal and El-Tawil 2011 [10]) and less commonly loss of stability failure of the global structural system. The latter mode of collapse is more frequently observed in tall and slender buildings (Yan et al. 2013 [27]). This dissertation focuses on the identification of the first two modes of collapse.

The most widely accepted and used method for progressive collapse is the Alternate Path Method which adopts the notion of a single complete column loss. It is a simplified tool that offers great advantages for engineering practitioners in the sense that is threat-independent, but at the same time fails to incorporate the role of a wider damaged area into the collapse modes of structures. Ellingwood 2002 [28] demonstrated that the single column loss notion is unrealistic, mainly for two reasons. First, even under an extreme local event it is very improbable that an element will fail completely throughout its whole length and

second, if such an extreme event does happen there will be non-negligible damage to other elements (beams or columns) as well. It is therefore very important to take into account distributed damage on adjacent members instead of limiting the aftermath of an extreme loading case, for example a blast scenario, into structural failure and subsequent removal of a single system component. For the specific case of blast events, numerous studies (Sasani et al. 2011 [29], Shi et al. 2010 [30], McConnell and Brown 2011 [31] and Jayasooriya et al. 2011 [32]) have shown that near field explosions may affect a series of columns and beams exposed to blast loading, in which cases the application of the Alternate Path Method would be highly unconservative. Two very important progressive collapse incidents underline the aforementioned non-applicability of the alternate path method. Firstly, the Alfred P. Murrah Building bombing in Oklahoma City, where the extent of blast-induced damage included failure of three main columns within the building's external perimeter as well as failure of some floor slabs in the immediate vicinity of the airblast (Mlakar et al. 1998 [33]). After the loss of support from those columns, a transfer girder also collapsed leading to progressive failure of further columns supported by the girder and subsequent failure of floor areas supported by those columns (Figure 1.2a). Secondly, the World Trade Center collapses in New York City that were initiated due to severe damage caused in multiple structural components by plane impact (Abboud et al. 2003 [34]). The structural failure near the impact zone was significantly aggravated by an extensive fire outbreak until the floors above the impact lost their support, resulting in the collapse of the upper part of the towers and thus to a progression of failures extending all the way to the ground (Figure 1.2b).

The above examples showcase the need for new method for progressive collapse analysis of structures, since the Alternate Path Method of a single column removal scenario, so far proposed by the design guidelines of building control authorities, is unable to correctly model the extent of a serious damaging event and is thus considered not only unrealistic and but most importantly unconservative. In this environment, it is crucial to develop a new method that introduces partial distributed damage to different columns of a structural

(a) Collapse of the 9-story Alfred P. Murrah Federal Building in Oklahoma City (1995)

(b) World Trade Center collapses in New York City (2001)

Figure 1.2: Famous progressive collapse events.

system and investigates the effects of such a distributed damage on the collapse mechanisms of the structural system. This dissertation proposes a new methodology of partial distributed damage scenarios that is compared to the state-of-the art approach of one complete column removal (Gerasimidis and Sideri 2016 [11], Sideri et al. 2015 [78]). The new method is applied to a 2D high-rise steel frame building. After different extent of local damage is parametrically applied to multiple adjacent columns through a damage index δ_j, results of nonlinear structural analyses reveal that partial damage introduction in the system leads not only to more critical collapse loads but also to significant changes in the observed collapse mechanisms.

Following the investigation of the effect of a more widespread damage distribution in the system through the introduction of partial damage scenarios, this dissertation proceeds in developing a methodology for assessing the progressive collapse vulnerability of structures against real hazardous scenarios, i.e. blast events. In contrast to the aforementioned partial damage scenarios that essentially include parametrically applied column damage in an idealized way (by using the damage index δ_j), simulation of explosions is an even more realistic approach for examining real threat extreme load cases that affect many structural components in their vicinity. To this end, the investigation of damage distribution on adjacent structural members induced by blast loads is considered critical for the evaluation of

structural robustness against abnormal loads that may initiate progressive collapse.

In this environment, detailed 3D nonlinear finite element dynamic analyses of steel frame buildings are performed in order to examine the spatially distributed response and damage to frame members along the building exterior facing an external blast (Sideri et al. 2015 [79] and Sideri et al. 2016 [81]). A methodology to assess the progressive collapse vulnerability is also proposed, which includes four consecutive steps to simulate the loading event sequence. Three case studies of steel buildings with different structural systems serve as examples for the application of the proposed methodology. A highrise (20-story) building is firstly subjected to a blast load scenario, while the complex 3D system results in the heavily impacted region are compared with individual column responses (SDOF) obtained from a simplified analytical approach consistent with current design recommendations (Mullen et al. 2015 [80]). Subsequently, two typical mid-rise (10-story) office steel buildings with identical floor plan layout but different lateral load resisting systems are examined; one including perimeter moment resisting frames (MRFs) and one including interior reinforced concrete (RC) rigid core. Comparisons between the performances of the building configurations subjected to the same blast scenario demonstrate the effect of the building layout to the overall structural behavior and progressive collapse. It is shown that MRFs offer a substantial increase in robustness against blast events, and the role of interior gravity columns identified as the "weakest links" of the structural framing that greatly influence the stability behavior and may potentially initiate progressive collapse is finally discussed.

1.2 Part I Outline

Part I of this dissertation is composed of seven chapters. Following this introduction, in Chapter 2, a new method that introduces partial distributed damage to different columns of a structural system and investigates the effects of such a distributed damage on the collapse loads and collapse mechanisms of the structural system is developed. The numerical

application of the aforementioned method on a 15-story steel frame building is presented in Chapter 3. Most of the content of these chapters derives from Sideri et al. 2015 [78] and Gerasimidis and Sideri 2016 [11].

Chapter 4 elaborates on the sensitivity of progressive collapse vulnerability of steel buildings to the distribution of damage within the structural system when facing an external blast. A methodology to assess the progressive collapse vulnerability is also presented, which includes four consecutive steps to simulate the blast loading event sequence. Details of the blast scenario considered and how the blast loads are generated are also provided in this chapter. Subsequently, in Chapters 5 and 6, nonlinear dynamic finite element simulation is performed to investigate the response of a high-rise 20-story and two mid-rise 10-story 3D buildings, assess the damage propagation and explore the possibility of progressive collapse initiation. Most of the content of these chapters derives from Sideri et al. 2015 [79], Mullen et al. 2015 [80] and Sideri et al. 2016 [81].

Finally, Chapter 7 concludes with a summary of the research accomplishments of Part I and provides guidance for potential direction of future research.

Chapter 2

Partial Distributed Damage Method for Progressive Collapse (PDDM)

2.1 Introduction

The vast majority of researchers have accepted the Alternate Path Method as the most useful tool to quantify an abnormal load that may trigger progressive collapse of structures. The core engineering concept of the APM is the removal of a key element as a means of damage introduction to the system in order to assess the resilience of structures. However, recent remarks have questioned the adequacy of the single column loss approach in the sense that it is poorly correlated to real life structural failure events. More specifically, Ellingwood 2002 [28] explained that the single column loss notion is far from being unrealistic, mainly for two reasons. First, even under an extreme local event it is very improbable that an element will fail completely throughout its whole length and second, if such an extreme event does happen there will be non-negligible damage to other elements (beams or columns) as well. Therefore, although practitioners and researchers often make the simplistic assumption that the full column removal notion can easily express a way of incorporating damage in the system, it is not the most accurate, realistic and necessarily conservative means of damage

introduction. Instead, a more widespread partial damage distribution that affects more than one structural elements is a more realistic approach for simulating extreme loading events (for instance blast events).

The concept of partial damage of structural elements has been introduced in the work of Gerasimidis et al. 2014 [35], by examining different cases of single and multiple partial losses of columns, aiming at the investigation of a more distributed damage scenario. However, this study was limited to a short steel frame, for which the stability considerations are generally not critical.

Chapter 2 proposes a new method for progressive collapse analysis by introducing partial distributed damage scenarios and utilizing powerful finite element computational tools that are able to capture loss of stability phenomena. The current state-of-the-art approach of one complete column removal scenario is compared to new partial distributed damage scenarios of multiple adjacent columns. The locality of the damaging event is maintained and the introduction of damage is applied to adjacent columns only. A damage index δ_j is utilized to parametrically attribute different extent of local damage to the columns, where the upper bound is full local damage and the lower bound is intact condition. Subsequently in Chapter 3, the method is applied on a 2D 15-floor steel frame and through the discussion of results, it is shown that the introduction of partial damage to the structural system can significantly modify the collapse mechanisms and overall affect the response of the structure. Through the investigation of damage propagation, it is proven that partial damage not only leads to lower and more critical collapse loads but also changes the observed collapse mechanisms, alternating between yielding-type and stability-type collapse modes.

2.2 Damage index δ_j

Damage introduction in the structural system is performed based on the classical definition of damage by Kachanov 1986 ([36]). Let us consider isotropic damage, in which case cracks and voids are equally distributed in all directions. Damage indexes δ_j which express the damage degree are defined as the following scalar

$$\delta_j = \frac{A - A^{'}}{A}, \quad 0 \leq \delta_j \leq 1 \tag{2.1}$$

where A the overall area of the element j and $A^{'}$ the effective resisting area. The lower bound $\delta_j = 0$ corresponds to the intact state condition (no damage), the upper bound $\delta_j = 1$ corresponds to the fully damaged state, while all the intermediate values of the damage index correspond to the partial damaged state. A structural member is considered removed if the full damage condition $\delta_j = 1$ is valid for all its elements. Essentially

$$if \quad \delta_j = 0 \qquad \Rightarrow \quad No \quad damage \tag{2.2}$$

$$if \quad \delta_j \in (0,1) \qquad \Rightarrow \quad Partial \quad damaged \quad state \tag{2.3}$$

$$if \quad \delta_j = 1 \qquad \Rightarrow \quad Fully \quad damaged \quad state \tag{2.4}$$

The effective stress in case of uniaxial tension is defined as

$$\sigma^{'} = \frac{P}{A'} = \frac{P}{A(1-\delta_j)} = \frac{\sigma}{1-\delta_j} \tag{2.5}$$

where σ is the stress of the pristine element, $\sigma^{'}$ the effective stress of the damaged element and P is the applied tensile force.

Based on the assumption by Lemaitre 1985 [37], the strain response of the body is modified by damage only through the effective stress $\sigma^{'}$. Moreover, let us also assume that the rate of damage growth is determined primarily by the level of the effective stress.

Therefore, the stress-strain behavior of the damaged material can be represented by the constitutive equation of the pristine material (no damage) with the stress in it replaced by the effective stress. In other words, the elastic strain of the damaged material according to Hooke's law is

$$\epsilon = \frac{\sigma^{'}}{E} = \frac{\sigma}{E(1-\delta_j)} \tag{2.6}$$

which indicates that Hooke's law is still valid for the damaged state with the pristine Young's modulus $E^{'}$ being replaced by the effective Young's modulus $E^{'}$. Essentially

$$E^{'} = E(1-\delta_j) \tag{2.7}$$

The damaged state of an element j is thus expressed via the damage index δ_j, which represents the fractured (lost) area deducted from the overall initial section area and subsequently leads to an equivalent reduction of the initial Young's modulus to an effective value $E^{'}$. Hence, simulation of the damaged element is based on two distinct actions:

1. Reduction of the pristine area A to an effective resisting area $A^{'}$
2. Reduction of the pristine Young's modulus E to an effective Young's modulus $E^{'}$

2.3 Partial Distributed Damage scenarios

Following the definition of damage index δ_j and the description of how the damage degree can be simulated for a single structural member, the effect of partial damage distribution on the response of a global structural system is investigated by performing a set of vertical push-down static analyses.

A Damage Scenario vector is defined as follows:

$$DS_f(k): \quad f \in \{1,2,...,n\} \quad and \quad k \in \{1,2,...,11\} \tag{2.8}$$

where f are the different building floors, ranging from 1 to n, where n represents the total number of floors, and k are the different damage scenarios. There are 11 different damage scenarios utilized to introduce damage in key elements of the building, i.e. columns. These damage scenarios include 2 complete column removal scenarios $DS_F(1)$ and $DS_f(11)$ and a set of ten partial distributed damage scenarios $DS_f(2)$ - $DS_f(10)$, for which damage is introduced to two adjacent columns. This configuration represents a realistic damage distribution that affects two adjacent members, for example due to a localized damaging event such a blast event close to two corner columns of a structural frame. Future work of this dissertation would logically include the extension of the above notion into an even more widespread damage distribution that affects more than two structural members, in order to simulate a more severe blast or impact loading.

A typical steel frame such as the one in Figure 2.1 can serve as an example structure to display the aforementioned damage scenarios. The 11 damage scenarios are listed below (the following numbering will be used as reference nomenclature from now on):

$DS_f(1)$. $\delta_j^{A,f} = 1 \quad ; \quad \delta_j^{B,f} = 0$

$DS_f(2)$. $\delta_j^{A,f} = 0.9 \quad ; \quad \delta_j^{B,f} = 0.1$

$DS_f(3)$. $\delta_j^{A,f} = 0.8 \quad ; \quad \delta_j^{B,f} = 0.2$

$DS_f(4)$. $\delta_j^{A,f} = 0.7 \quad ; \quad \delta_j^{B,f} = 0.3$

$DS_f(5)$. $\delta_j^{A,f} = 0.6 \quad ; \quad \delta_j^{B,f} = 0.4$

$DS_f(6)$. $\delta_j^{A,f} = 0.5 \quad ; \quad \delta_j^{B,f} = 0.5$

$DS_f(7)$. $\delta_j^{A,f} = 0.4 \quad ; \quad \delta_j^{B,f} = 0.6$

$DS_f(8)$. $\delta_j^{A,f} = 0.3 \quad ; \quad \delta_j^{B,f} = 0.7$

$DS_f(9)$. $\delta_j^{A,f} = 0.2 \quad ; \quad \delta_j^{B,f} = 0.8$

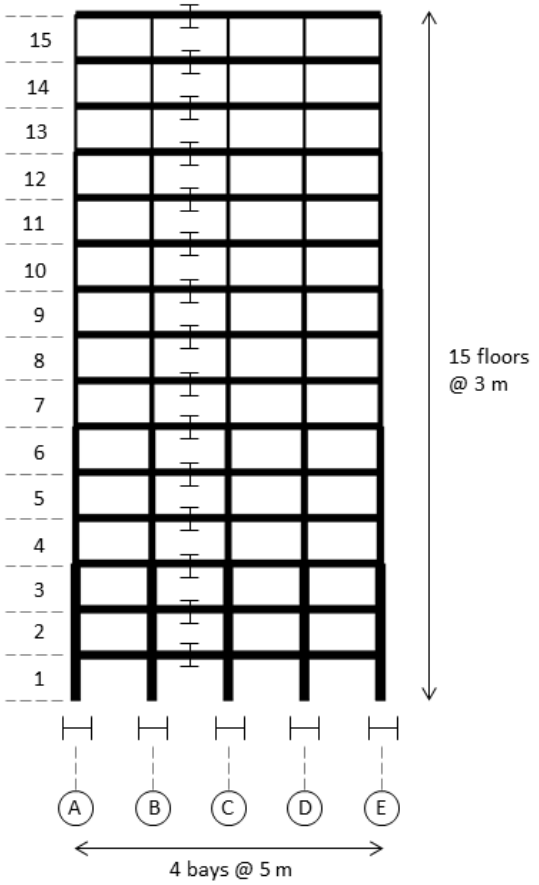

Figure 2.1: Geometric morphology and reference grid of the 15-story moment-resisting steel frame.

$DS_f(10)$. $\delta_j^{A,f} = 0.1 \quad ; \quad \delta_j^{B,f} = 0.9$

$DS_f(11)$. $\delta_j^{A,f} = 0 \quad ; \quad \delta_j^{B,f} = 1$

The first damage scenario $DS_f(1)$ corresponds to the complete loss of corner column A of number f floor. This scenario refers to damage indexes $\delta_j^{A,f} = 1$ (full damage, i.e. column removal) for all the elements of the corner column A of floor f and $\delta_j^{B,f} = 0$ (no damage, i.e. intact column condition) for all the elements of the adjacent column B of floor f. Damage scenarios $DS_f(2) - DS_f(10)$ represent the scenarios for which both columns A and B of floor f are in the state of partial damage. Finally, the last damage scenario $DS_f(11)$ corresponds

to the full column removal of column B of floor f and the intact state condition of column A of floor f.

The selection of the partial damage scenarios is obviously made so that the total level of damage introduced in the structure is equivalent to one full column removal, since in every scenario the following relation is satisfied:

$$\delta_j^{A,f} + \delta_j^{B,f} = 1 \tag{2.9}$$

The reasoning behind this notion is to achieve consistency in comparing the results of the alternate load path method (complete column removal) to the results from the partial distributed damage scenarios.

This set of analyses for all damage scenarios is performed in turn for all floors of the building, $f = (1, 2, ..., n)$. Hence, the total number of progressive collapse scenarios examined is the 11 damage scenarios multiplied by the total number of floors n, i.e. $11 \times n$.

2.4 Propagation of Failure and Progressive Collapse Capacity

Each specific damage scenario includes a certain amount of partial damage introduced to adjacent columns A and B. Following that initial damage introduction to the frame, a first push-down progressive collapse analysis is performed. The results of this analysis have two potential outcomes, referring to two different collapse mechanisms. Either one of the damaged columns will fail through loss of stability, or the beam edges above the damaged region will develop plastic hinges leading to a yielding-type collapse of the frame. Both possible outcomes are described in detail below, along with the definition of the respective collapse loads for each case.

2.4.1 Buckling-type column failure

Analysis I

If the first push-down analysis reveals the buckling failure of a column, the collapse load $CL_{I,f}(k)$ of Analysis I is defined as the load at which the failing column reaches its axial capacity.

Analysis II

The second push-down analysis includes the removal of the previously buckled element from the system. Subsequently, a new push-down progressive collapse analysis is performed by maintaining the same level of damage to the rest of the columns. The collapse load $CL_{II,f}(k)$ of Analysis II is defined in the same way as in Analysis I, i.e. as the vertical load for which the buckling failure of an element occurs through exhaustion of its axial load capacity.

2.4.2 Yielding-type beam failure

Analysis I

In the event that Analysis I leads to a yielding-type failure of beams above the damaged column region, the final collapse load $CL_f(k)$ is defined as the vertical external load for which the beams reach their bending capacity $M_{plastic}$ and thus plastic hinges are formed at the beam edges, leading to an increase of beam displacements and rotations beyond the safety limits. In this case, the damage propagation is ceased by beam yielding and thus there is no need for a second analysis ($CL_f(k) = CL_{I,f}(k)$). Otherwise, if the first analysis leads to the buckling failure of a column, then $CL_{I,f}(k)$ is defined in the same manner as section 2.4.1.

Analysis II

In case a column buckles during Analysis I at the collapse load $CL_{I,f}(k)$, subsequently Analysis II is performed by removing the previously buckled column and maintaining the same damage level for the rest of the columns. The results of Analysis II may now show the yielding-type beam failure collapse mechanism at the load of $CL_{II,f}(k)$.

2.4.3 Progressive Collapse Capacity

The final progressive collapse capacity for every damage scenario is defined as the maximum between the collapse loads of Analyses I and II, i.e. maximum between $CL_{I,f}(k)$ and $CL_{II,f}(k)$:

$$CL_f(k) = max\left\{CL_{I,f}(k), CL_{II,f}(k)\right\} \tag{2.10}$$

The reasoning behind the definition of progressive collapse capacity as final collapse load of the frame, along with description of the propagation of failure, is demonstrated in detail below.

- If Analysis I reveals a column buckling failure at a collapse load $CL_{I,f}(k)$, while Analysis II leads to another column buckling failure at a higher collapse load $CL_{II,f}(k)$, it follows that the set of two analyses correspond to a damage propagation phenomenon that is terminated at the higher load of the second analysis. In other words, the two buckling failures are initiated consecutively or one after the other, meaning that the second one requires an even higher load to occur ($CL_f(k) = CL_{II,f}(k)$).

- If Analysis I identifies a column buckling failure at a collapse load $CL_{I,f}(k)$, while Analysis II leads to a yielding-type beam failure at a higher collapse load $CL_{II,f}(k)$, then the set of two analyses form a damage propagation phenomenon that is finalized at the higher load of the second analysis, meaning that the two failures occur consecutively ($CL_f(k) = CL_{II,f}(k)$).

- If Analysis I reveals a column buckling failure at a collapse load $CL_{I,f}(k)$, while Analysis II leads to another buckling failure at a lower collapse load $CL_{II,f}(k)$, then the second buckling failure is simultaneous to the first one, meaning that the first loading level is high enough to trigger both failures at the same time ($CL_f(k) = CL_{I,f}(k)$).

- If Analysis I identifies a column buckling failure at a collapse load $CL_{I,f}(k)$, while Analysis II leads to a yielding-type beam failure at a lower collapse load $CL_{II,f}(k)$,

then the second yielding-type failure is immediate to the first one, since the first loading level is high enough to cause the second failure simultaneously ($CL_f(k) = CL_{I,f}(k)$).

- If Analysis I identifies a yielding-type beam failure, the progressive collapse phenomenon is arrested by the formation of plastic hinges at the beam edges and the progressive collapse capacity is defined as ($CL_f(k) = CL_{I,f}(k)$).

The aforementioned damage propagation for the assessment of the final progressive collapse capacity is schematically depicted in Figure 2.2.

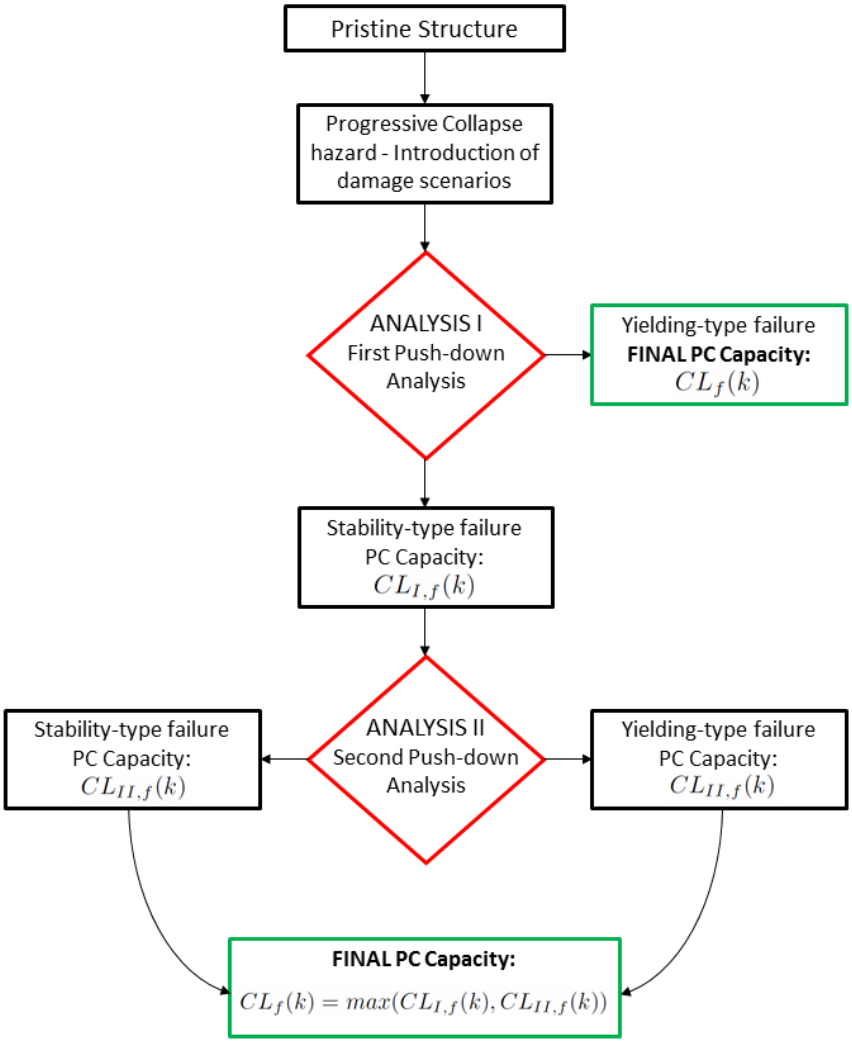

Figure 2.2: Damage propagation procedure for the assessment of the final progressive collapse capacity, according to the new partial distributed damage method (PDDM).

It must be mentioned here that, the research community in the progressive collapse field has generally accepted the notion of subsequent column removals after a member has failed. Alternatively, a more sophisticated approach than the element removal would be to consider the post-buckling behavior of failed components and examine the effect of their presence in the frame's structural behavior. However, it is not within the scope of this thesis to include that kind of phenomena, although it would be an excellent future extension of the current work.

Chapter 3

Partial Distributed Damage Method (PDDM) - Numerical Application

3.1 Introduction

Following Chapter 2 that proposed a new method for progressive collapse analysis including partial distributed damage scenarios, Chapter 3 presents the numerical application of the method on a 2D 15-floor steel frame. The current state-of-the-art Alternate Path Method of a single column loss is compared to partial distributed damage scenarios of two adjacent columns, by utilizing powerful finite element computational tools that are able to capture loss of stability phenomena. Through a damage index δ_j, different extent of local damage is parametrically applied to adjacent columns and then static nonlinear push-down analyses are performed. After discussion and comparison of the analyses results, it is shown that introduction of partial damage in the system greatly affects the overall structural behavior, by leading not only to lower and more critical collapse loads but also to significant modification in the observed collapse mechanisms.

3.2 Description of the Finite Element Model

The 15-floor steel frame used for the analyses is shown in Figure 2.1. It is a typical steel moment resisting frame designed according to the Eurocodes [38] and [39], with floor height equal to $3m$ and bay width equal to $5m$. The tributary load areas are calculated using a selected distance between consecutive frames of $7m$, which is a typical value for steel frames. Indicatively, column sections vary from HEB650 to HEB200, while beam sections range from IPE450 to IPE550. Full section selection, load combinations and design considerations of the frame can be found in the work of Gerasimidis et al. 2012 [40]. The structural steel components follow the non-linear material characteristics of structural steel S235, described by an elastic-plastic material model with bilinear stress-strain behavior. The yield stress of the material is $235MPa$ and and the ultimate stress is $360MPa$ at strain 23%, with isotropic strain hardening.

The frame is simulated using the commercial FEM code ABAQUS Simulia [41], using beam B22 elements to simulate both beams and columns. The mesh representing the finite element model is studied to be sufficiently fine in the areas of interest to accurately capture the structural behavior of the system. Apart from the elements used to model the connections, each column comprises 5 elements while each beam comprises 10 elements, leading to a total number of 1262 elements and 5956 nodes for each model. The rigid body constraint offered in ABAQUS is utilized to model all beam-to-column connections, by constraining the relative motion of regional elements around the connections. All base nodes of first floor columns are considered pinned.

The proposed partial distributed damage method is applied on the 15-story frame for all the aforementioned damage scenarios, leading to a total number of 165 progressive collapse scenarios. Each damage scenario from $DS_f(2)$ to $DS_f(10)$ includes 2 consecutive analyses, except damage scenarios $DS_f(1)$ and $DS_f(11)$ that are described by a single static push-down analysis. All analyses are set to account for both material and geometric nonlinearities

which is shown to be the only appropriate method to detect loss-of-stability phenomena and thus to identify the correct collapse mechanisms (Gerasimidis et al. 2014 [8], Gerasimidis 2014 [24]).

3.3 Analysis Results

3.3.1 Damage Scenarios for the 1^{st} Floor

3.3.1.1 Damage Scenario $DS_1(1)$

The first analysis involves the removal of the corner column of the first floor, $A1$. Figures 3.1a and 3.1b include the horizontal (lateral) displacement at mid-height of column $B1$ and the axial force of column $B1$, with respect to the vertical load applied on the beams of the structure, while Figure 3.1c presents the deformed shape of the structure. All graphs illustrate the buckling failure of column $B1$, while the beams exhibit little plastification and mostly remain within the elastic range. Both the deformed shape and the displacement plot show a rapid increase in the horizontal displacement after the application of the vertical load of $56.4kN/m$, while the axial force increases linearly until the column reaches its axial capacity for the same loading level. After this point it is clear that the member cannot undertake any additional axial force, therefore the collapse load is $CL_1(1) = 56.4kN/m$.

An additional analysis is not required in this case, since the failure of the second column certainly leads to the collapse of the structure. The kind of buckling occurring in this case is nonlinear inelastic buckling, since the axial force cannot exceed the yield capacity of Af_y, where A is the cross sectional area and f_y is the material yield stress. In addition, the Euler buckling capacity of column $B1$ is much higher than its yield capacity, meaning that this column with the prescribed geometry and section properties is prone to nonlinear inelastic buckling rather than linear elastic Euler buckling (which is the case for slender columns). Detailed description of different buckling failure modes can be found in the work

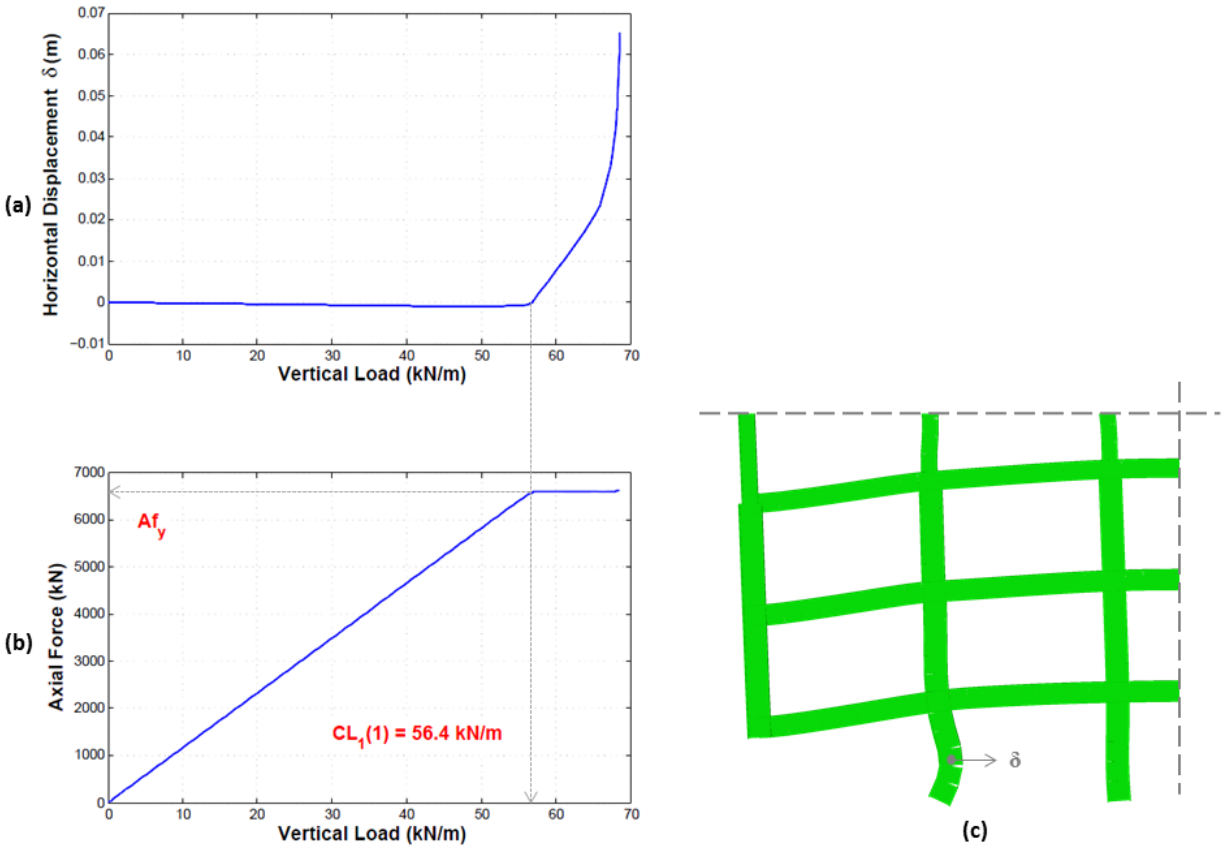

Figure 3.1: Damage scenario $DS_1(1)$: Full column $A1$ removal of the first floor. (a) Horizontal (lateral) displacement δ of the mid-height node of the adjacent-to-the-removal column $B1$, (b) axial force with respect to the the vertical load and (c) deformed shape.

of Gerasimidis 2014 [24]. It must be mentioned at this point that the critical failure mode of all columns examined for this structure is nonlinear inelastic buckling, as opposed to Euler buckling of the weak or strong axis.

3.3.1.2 Damage Scenario $DS_1(2)$

The next analysis performed is the partial damage distribution scenario with $\delta_j^{A,1} = 0.9$ and $\delta_j^{B,1} = 0.1$. This analysis leads to the buckling failure of column $A1$ at the vertical load of $CL_{I,1}(2) = 20.7kN/m$ (illustrated by the dashed line in the plot of the axial force in Figure 3.2a). After the removal of column $A1$, the damage propagation phenomenon

ends with the buckling failure of $B1$ at the collapse load of $CL_{II,1}(2) = 51.0kN/m$ (Figure 3.2b), which defines the progressive collapse capacity for this damage scenario $CL_1(2) = max\{CL_{I,1}(2), CL_{II,1}(2)\} = 51.0kN/m$. This collapse load is lower than the $CL_1(1) = 56.4kN/m$ collapse load of the full column $A1$ removal scenario. A first important finding is the decrease of the capacity when applying a partial distributed damage scenario that includes damage distribution very close to the initial single column removal assumption; only 10% of the damage is 'transferred' from column A1 to B1 and the collapse load is yet decreased also almost by 10%.

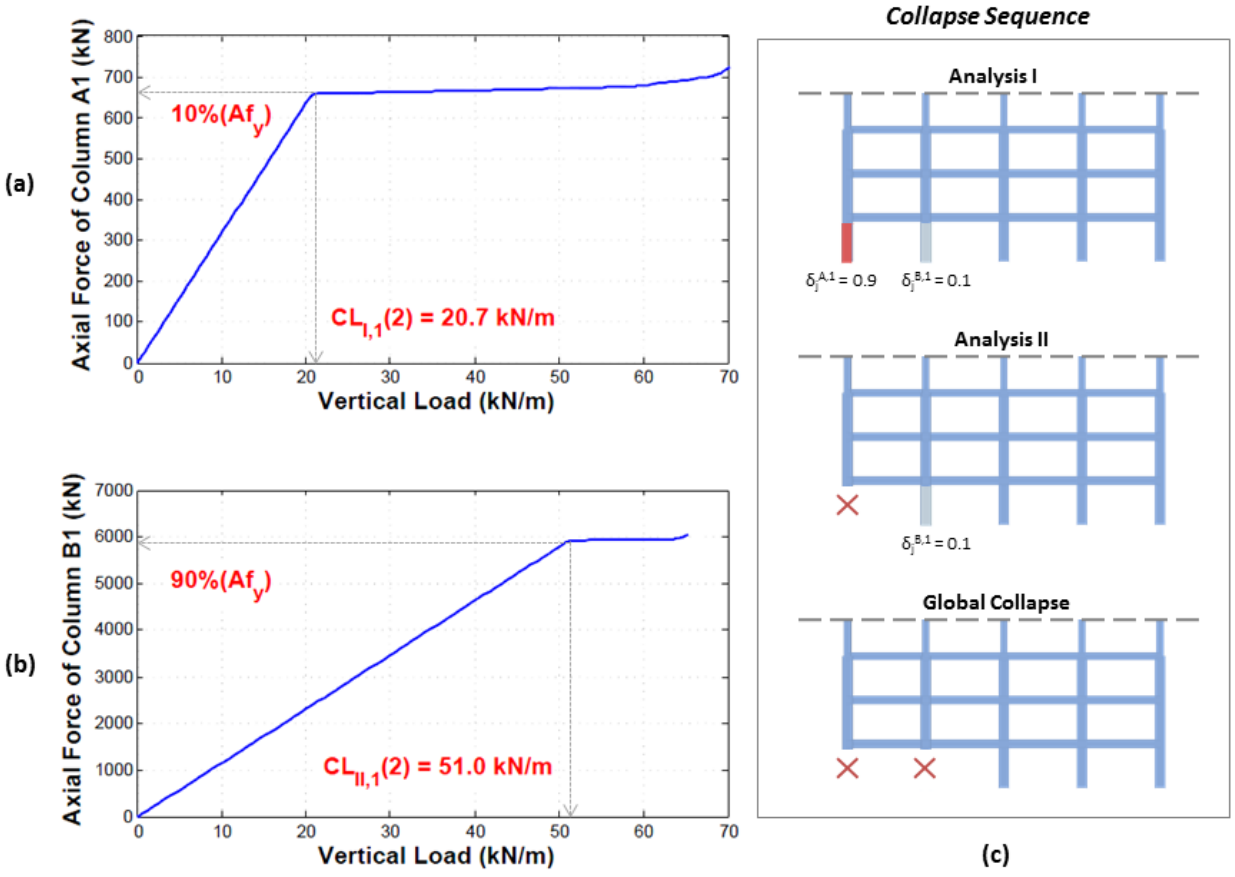

Figure 3.2: Damage scenario $DS_1(2)$: (a) Axial force of column $A1$ for Analysis I, (b) axial force of column $B1$ for Analysis II, with respect to the the vertical load and (c) collapse sequence.

3.3.1.3 Damage Scenarios $DS_1(3)$ - $DS_1(5)$ and $DS_1(11)$

The same trend is observed when the other partial distributed damage scenarios are investigated, reaching the collapse loads of $CL_1(3) = 45.4kN/m$ and $CL_1(4) = 51.5kN/m$ for the cases of $\delta_j^{A,1} = 0.8$; $\delta_j^{B,1} = 0.2$ and $\delta_j^{A,1} = 0.7$; $\delta_j^{B,1} = 0.3$, respectively. Interestingly, the collapse load for both these cases is lower than $CL_1(1) = 56.4kN/m$, which is the collapse load of the complete A1 column removal scenario.

However, for the $DS_1(5)$ ($\delta_j^{A1} = 0.6$ and $\delta_j^{B1} = 0.4$) damage scenario, the collapse mode of the structure is altered. Instead of the buckling failure of $A1$ (which has the highest level of damage), column $B1$ is the one that actually buckles first at $CL_{I,1}(5) = 61.3kN/m$. The collapse load of the second analysis which results in the buckling of $A1$ is now $CL_{II,1}(5) = 36.8kN/m$, which is lower than the initial $61.3kN/m$. Therefore, the loading level of $61.3kN/m$ is large enough to cause the buckling failure of both columns $A1$ and $B1$ and the final collapse load for this case is thus defined as $CL_1(5) = 61.3kN/m$.

At this particular point, it is interesting to examine the complete loss of column $B1$ which is described by $DS_1(11)$. Figure 3.3c depicts the deformed shape of the structure, which shows the buckled shape of column $C1$. When plotting the axial force of that column with respect to the vertical applied load (Figure 3.3b), the axial capacity is reached at $CL_1(11) = 69.0kN/m$, where at the same load the column mid-height horizontal displacement begins to increase rapidly (Figure 3.3a).

The $CL_1(5) = 61.3kN/m$ collapse load is higher than $CL_1(1) = 56.4kN/m$ but lower than $CL_1(11) = 69kN/m$. Moreover, since the first element that buckles in $DS_1(5)$ is $B1$, it is considered more reasonable to compare the $DS_1(5)$ case with the results of $DS_1(11)$ than the results of $DS_1(1)$, even if the damage level initially introduced to $A1$ is higher than $B1$.

Damage scenarios $DS_1(3)$ and $DS_1(4)$ lead to lower collapse loads than the corresponding complete column removal scenarios (either $DS_1(1)$ or $DS_1(11)$).

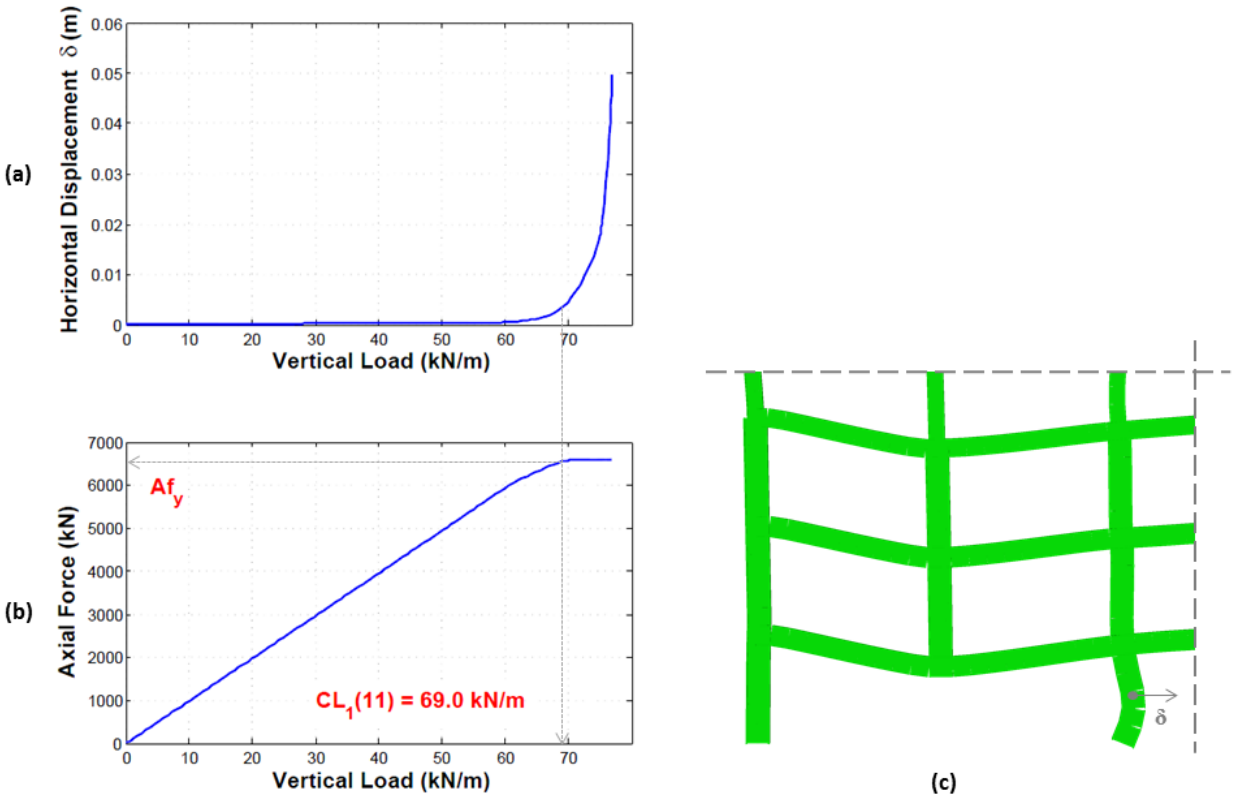

Figure 3.3: Damage scenario $DS_1(11)$: Full column $B1$ removal of the first floor. (a) Horizontal (lateral) displacement δ of the mid-height node of the adjacent-to-the-removal column $C1$, (b) axial force with respect to the the vertical load and (c) deformed shape.

3.3.1.4 Damage Scenarios $DS_1(6)$ - $DS_1(10)$

Similarly to $DS_1(5)$, all partial damage scenarios $DS_1(6)$ - $DS_1(10)$ are compared to the $B1$ full column removal scenario, $DS_1(11)$. The first analysis of $DS_1(6)$ ($\delta_j^{A,1} = 0.5$ and $\delta_j^{B,1} = 0.5$) leads to the buckling failure of column $B1$ at $CL_{I,1}(6) = 52.9kN/m$ and the results of the second analysis show buckling of $A1$ at $CL_{II,1}(6) = 45.2kN/m$. Therefore, the collapse load is the highest of the two, i.e. $CL_1(6) = CL_{I,1}(6) = 52.9kN/m$, which is remarkably lower (23.3%) than $CL_1(11) = 69.0kN/m$.

Furthermore, the scenarios $DS_1(7)$ and $DS_1(8)$ show similar behavior, for which in the first analysis column $B1$ fails and the second analysis reveals the buckling failure of column

$A1$ at $CL_1(7) = CL_{II,1}(7) = 55.0kN/m$ and $CL_1(8) = CL_{II,1}(8) = 62.7kN/m$. Lastly, $DS_1(9)$ and $DS_1(10)$ lead to a final collapse load of $CL_1(9) = 66.9kN/m$ and $CL_1(10) = 67.6kN/m$, respectively, due to the inelastic buckling failure of column $C1$, resembling the collapse mode of the $DS_1(11)$.

The major finding of this analysis is the significant decrease of the collapse load in almost all partial distributed damage scenarios, showing that the notion of complete column removal is a less conservative approach than the proposed partial distributed damage method (PDDM). In addition, there is a noticeable change in the observed collapse mechanisms. The final buckling failure can occur either at columns $A1$, $B1$ or $C1$ interchangeably, depending on the specific partial damage distribution applied in the model.

3.3.2 Partial Damage Distribution at 14^{th} Floor

3.3.2.1 Damage Scenarios $DS_{14}(1)$ and $DS_{14}(11)$

The next discussion of results will present the partial damage distribution study at a higher floor, where the dominant failure is the extensive yielding of beams instead of the buckling collapse mode of a column. The reference point to examine and compare all the partial distributed damage scenarios will be the two column removal analyses of $A14$ and $B14$, corresponding to $DS_{14}(1)$ and $DS_{14}(11)$ respectively.

For the scenario $DS_{14}(1)$, the beam edges at floors 14 and 15 reach the plastic bending moment limit at the vertical load of $CL_{14}(1) = 62.5kN/m$ (Figure 3.4b). At the same load, the vertical displacement of the node above the removal has nearly reached the value of $10cm$, while after this point it continues to grow at a higher rate (Figure 3.4a). Finally, Figure 3.4c displays the deformed shape of the structure which obviously indicates the yielding-type collapse mechanism initiated by the excessive deformation and plastification of the beams above the removal.

The analysis of column $B14$ being removed from the model leads to very similar results.

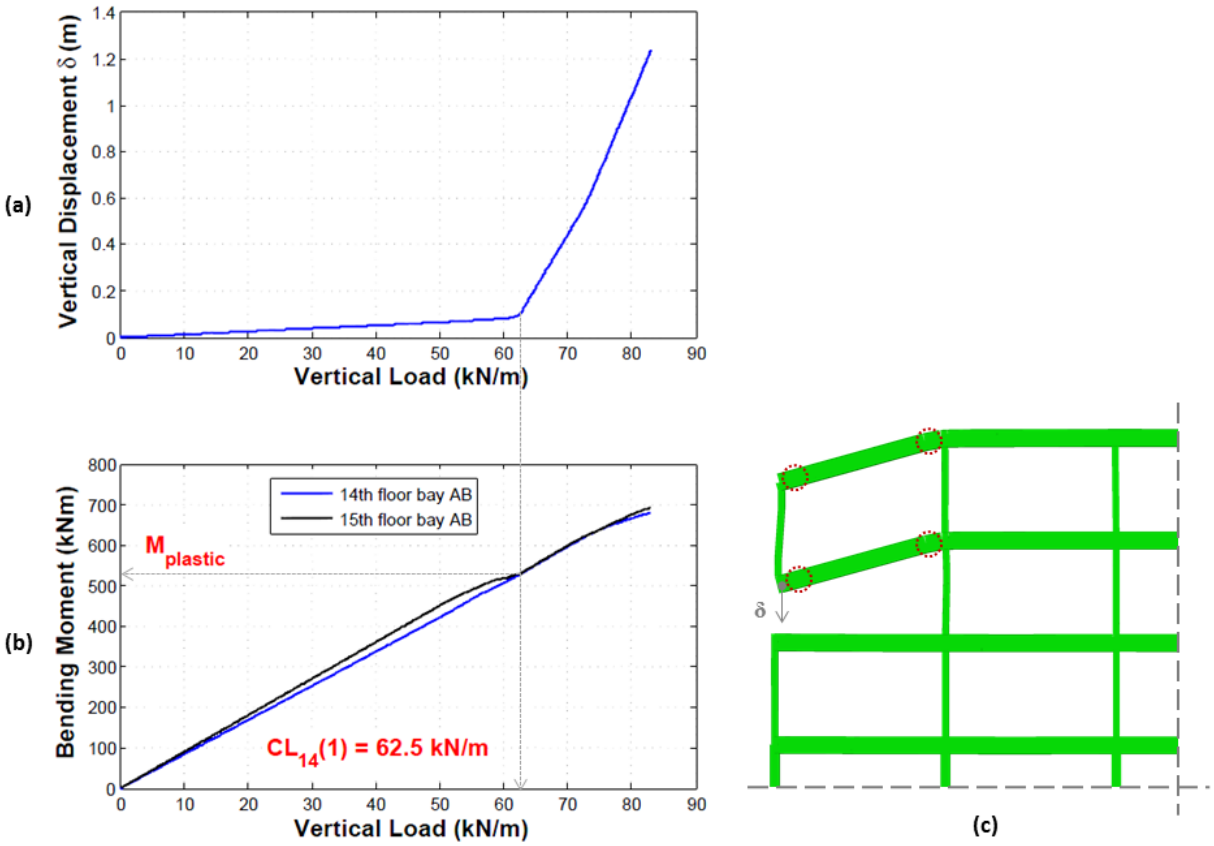

Figure 3.4: Damage scenario $DS_{14}(1)$: Full column $A1$ removal of the 14^{th} floor. (a) Vertical displacement δ of the node above the removal, (b) bending moment at the beam edges of the 14^{th} and 15^{th} floor with respect to the the vertical load and (c) deformed shape.

As depicted in Figure 3.5, plastic hinges are formed at all beams edges of both bays AB and BC, for a collapse load of $CL_{14}(11) = 75.5kN/m$.

3.3.2.2 Damage Scenario $DS_{14}(2)$

Following the same configuration, the next analysis involves the application of 90% damage level for column $A14$, while column $B14$ is damaged only 10%. For this scenario, the inelastic buckling of column $A14$ occurs at a relatively low level of external load. After the removal of this buckled element, the next analysis leads to the yielding-type collapse mechanism of beams at the same vertical load of $CL_{14}(2) = CL_{II,14}(2) = 62kN/m$. The collapse load in

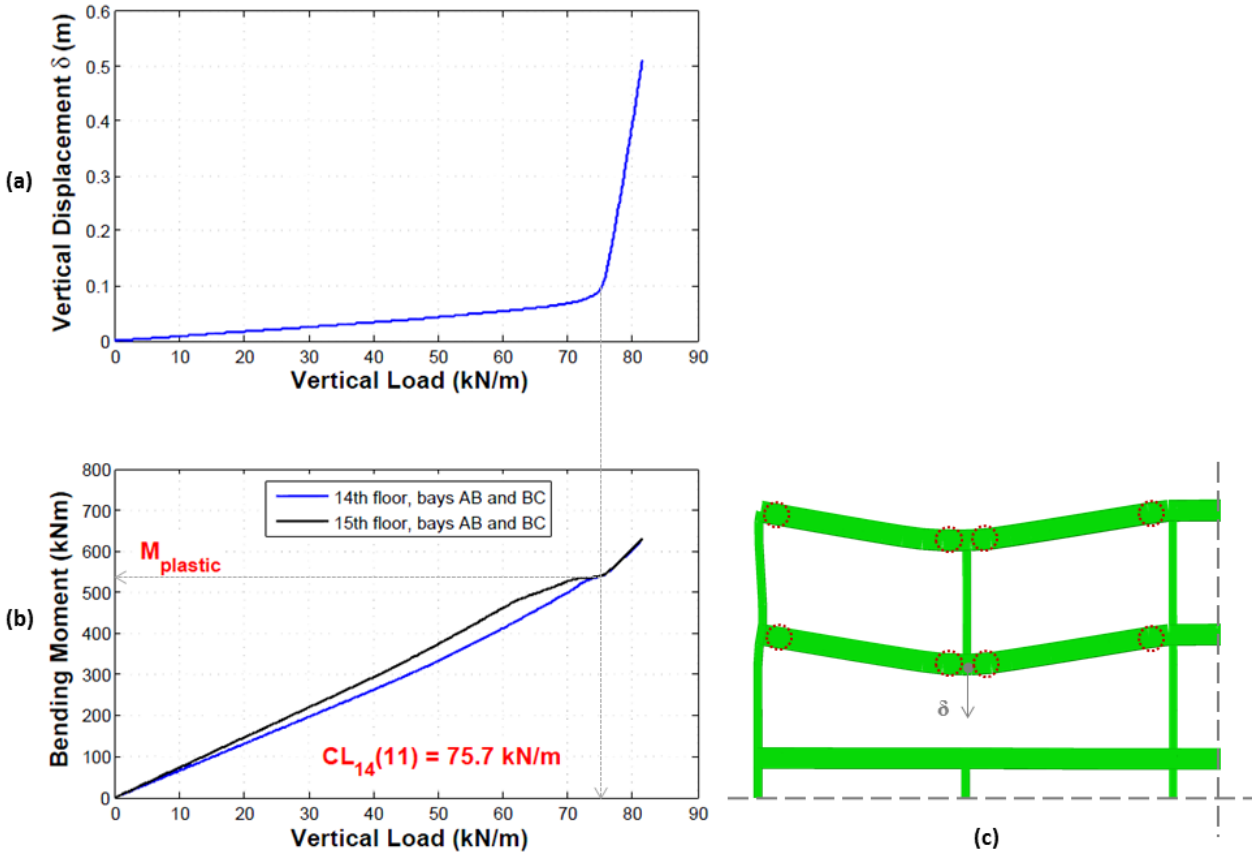

Figure 3.5: Damage scenario $DS_{14}(11)$: Full column $B1$ removal of the 14^{th} floor. (a) Vertical displacement δ of the node above the removal, (b) bending moment at the beam edges of the 14^{th} and 15^{th} floor with respect to the the vertical load and (c) deformed shape.

this case is practically the same as the $DS_{14}(1)$ full $A14$ column removal scenario.

3.3.2.3 Damage Scenario $DS_{14}(3)$

The next analysis involves the application of 80% damage level for column $A14$, while column $B14$ is damaged by 20%. For this scenario, the inelastic buckling of column $A14$ occurs at a higher collapse load than $DS_{14}(2)$ and the second analysis reveals again the yielding-type collapse of the beams above the damaged area, after the removal of the buckled elements. The collapse load in this case is governed by the buckling of column $A14$ and it is higher than the collapse loads of $DS_{14}(1)$ and $DS_{14}(2)$.

3.3.2.4 Damage Scenarios $DS_{14}(4)$ - $DS_{14}(6)$

The next three partial damage scenarios show a significant change in the overall behavior of the structure. Interestingly, when applying $70\%, 60\%$ or 50% damage level for column $A14$ (equivalently $30\%, 40\%$ or 50% damage level for column $B14$) the results of all three analyses show the buckling failure of column $C4$ at the 4^{th} floor for practically the same vertical load of $CL_{I,14}(4) = CL_{I,14}(5) = CL_{I,14}(6) = 89.3kN/m$. Figure 3.6a depicts the plot of the axial forces of both columns $C4$ and $A14$ for Analysis I of damage scenario $DS_{14}(4)$, where it is obvious that column $C4$ reaches its axial capacity before any failure occurs at $A14$. When removing the buckled column $C4$, all three damage scenarios lead to the buckling failure of column $B4$ at a lower loading level of $CL_{II,14}(4) = CL_{II,14}(5) = CL_{II,14}(6) = 64.1kN/m$ (Figure 3.6b for $DS_{14}(4)$). Consequently, the vertical load of $89.3kN/m$ is large enough to cause the buckling failure of both $C4$ and $B4$, therefore $CL_{14}(4) = CL_{14}(5) = CL_{14}(6) = 89.3kN/m$.

Although this load is higher than for the $DS_{14}(1)$ full $A14$ column removal scenario (even higher than the $DS_{14}(11)$ $B14$ removal scenario), the most important finding from this scenario is the tremendous change in the collapse mechanism; instead of the yielding-type collapse mechanism of the beams, the structure fails due to loss of stability of columns at a much lower floor. The assessment of the progressive collapse vulnerability of this structure is highly affected by the specific partial damage distribution scenario applied to the members of the frame. Essentially, the yielding-type of progressive collapse is avoided in the vicinity of the introduction of damage when the damage is distributed almost evenly in two columns. The damaged columns are able to prevent the yielding type of collapse and therefore the collapse is triggered in a completely different area of the frame.

3.3.2.5 Damage Scenarios $DS_{14}(7)$ - $DS_{14}(10)$

Lastly, the damage propagation for $DS_{14}(7)$ - $DS_{14}(10)$ can be described by the buckling failure of $B14$ and then, after the removal of $B14$, by the yielding failure of the beams at

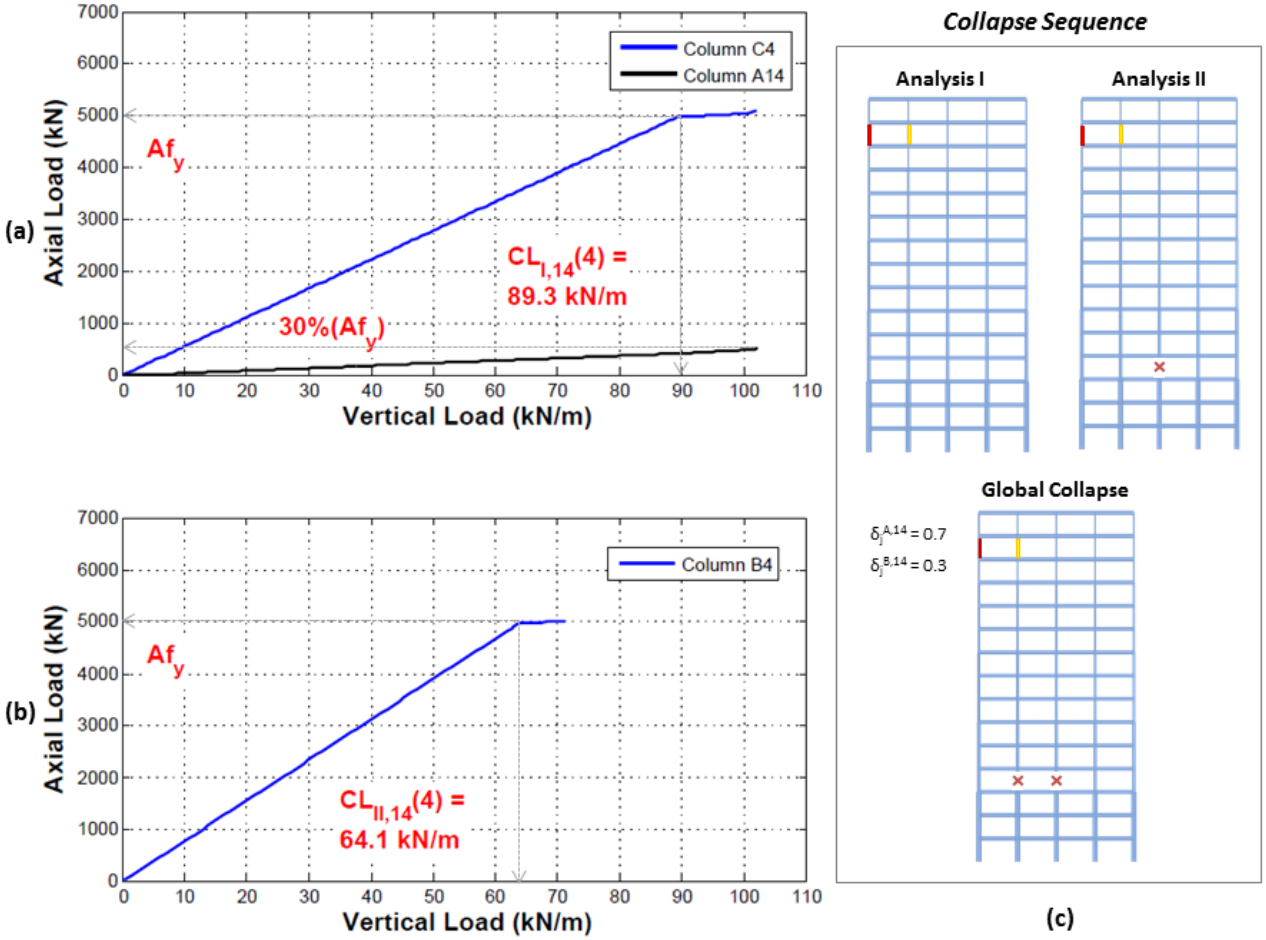

Figure 3.6: Damage scenario $DS_{14}(4)$: (a) Axial force of column $A14$ and $C4$ for Analysis I, (b) axial force of column $B4$ for Analysis II with respect to the the vertical load and (c) collapse sequence.

the 14^{th} and 15^{th} floor. Except $DS_{14}(7)$, the collapse load of which is $CL_{14}(7) = 79.1kN/m$, all the other collapse loads are slightly lower than the $CL_{14}(11) = 75.5kN/m$ collapse load of the full $B14$ column removal scenario.

Overall, the response of the structure is only mildly affected under the event of partial distributed damage at a higher floor, where the dominant collapse mechanism is the beam yielding-type. However, three ($DS_{14}(4)$ - $DS_{14}(6)$) out of nine ($DS_{14}(2)$ - $DS_{14}(10)$) partial distributed damage scenarios reveal that the expected critical collapse mode of beam yielding can be replaced by the inelastic buckling failure of columns located at lower floors, rendering

a parametric partial damage distribution study critical for the correct evaluation of the structural integrity of a system in case of a progressive collapse scenario.

3.3.3 Synopsis of Analysis Results

Figure 3.7 provides the synopsis of all collapse loads for all damage scenarios for the 15 floors of the frame, divided by the collapse load of the single column removal case. The upper part of the graph, Figure 3.7a, illustrates the ratio $CL_f(k)/CL_f(1)$, while the lower part, Figure 3.7b, depicts the ratio $CL_f(k)/CL_f(11)$. The complete column removal at gridlines A or B ($DS_f(1)$ or $DS_f(11)$, denoted by the red line) constitutes the reference alternate load path scenario to which all other scenarios are compared, as it represents the current state-of-the-art progressive collapse approach of the Alternate Path Method (APM). Both graphs show that many damage scenarios included in the proposed Partial Distributed Damage method reach lower collapse loads than $DS_f(1)$ and especially $DS_f(11)$, since they are located below the red line. This trend is less apparent for the upper floors of the structure, where the collapse loads are only mildly affected by the introduction of partial distributed damage, due to the yielding-type nature of collapse mechanisms observed. The reduction of the collapse load for many damage scenarios is remarkable though for the rest of the floors, where buckling failure is dominant, resulting in $CL_f(k)/CL_f(11)$ ratios as low as 0.65 (up to 35% reduction in the collapse load).

Another interesting finding from Figure 3.7 illustrated by the red indicators at the bottom of each graph is that for all floors except at the last two floors, the most critical scenario is $DS_f(3)$ ($\delta_j^{A,f} = 0.8$ and $\delta_j^{B,f} = 0.2$), as it leads to the largest decrease in the collapse load. In contrast, for the 15^{th} floor the most critical scenario in terms of lowest collapse load is the full column $A15$ ($DS_{15}(1)$) removal. This finding, however, depends on the design characteristics of the analyzed frame and cannot generally be extended to other building configurations.

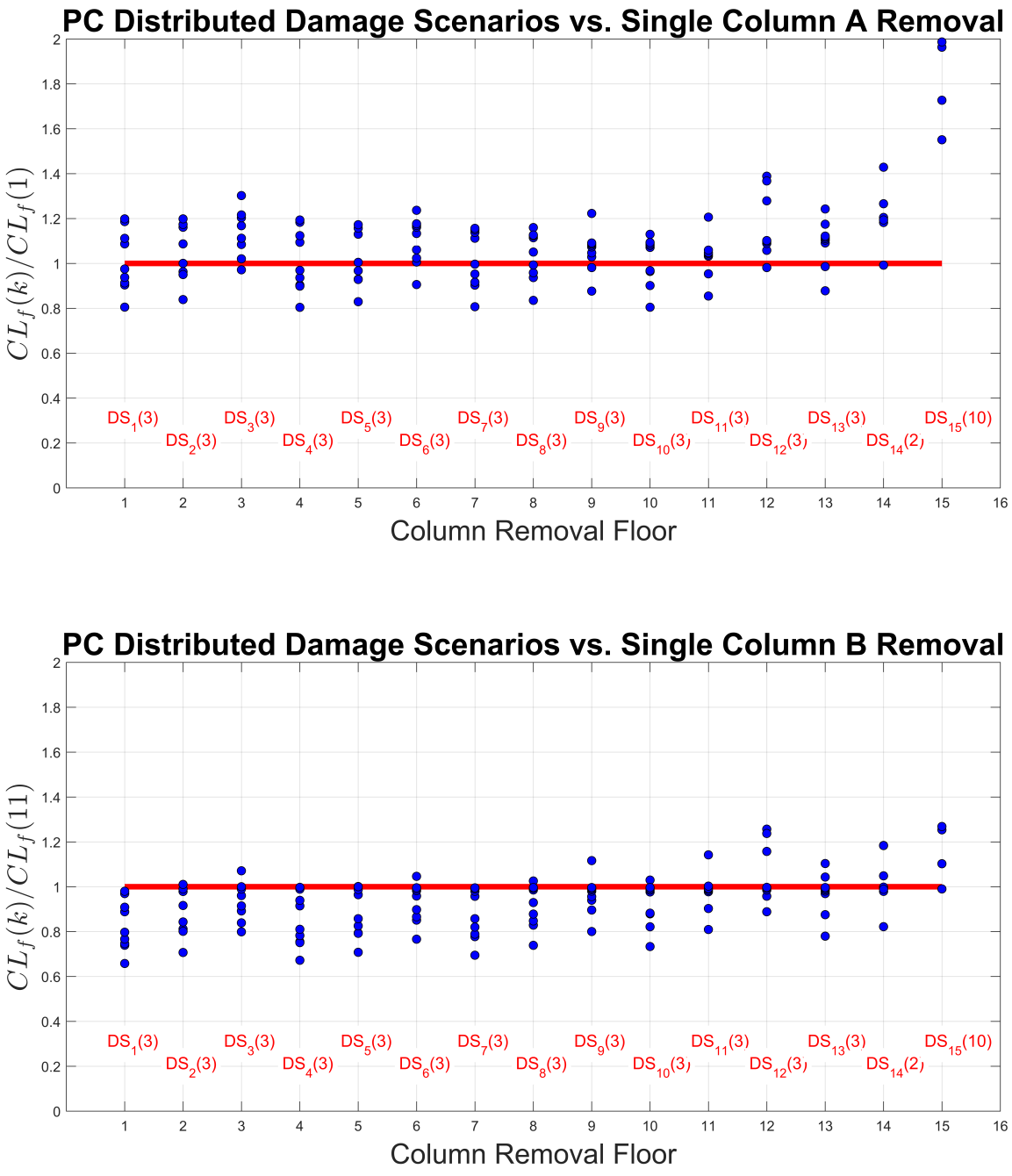

Figure 3.7: Collapse loads of all damage scenarios for the 15 floors of the frame, divided by (a) the collapse load of complete column A removal $CL_f(1)$ and (b) the collapse load of complete column B removal $CL_f(11)$.

3.3.4 Effect of PPDM on Progressive Collapse Capacity

The most important finding of this work is that the capacity of the structure is much lower when the partial distributed damage method is considered in comparison to the simplistic notional column removal approach of the state-of-the-art APM. It is therefore considered highly unconservative for many cases to perform the alternate load path method for progressive collapse analysis of steel frames.

Figure 3.8 highlights the discrepancy of progressive collapse capacity between the new partial distributed damage method and the alternate load path method through an illustrated table. The first row of the table includes the collapse loads corresponding to the complete column A removal for all the different floors $DS_f(1)$, while the last row of the table includes the collapse loads corresponding to the complete column B removal for all the different floors $DS_f(11)$. Essentially, the first and last row of the table represent the collapse loads had the APM been utilized to perform progressive collapse analysis for all the building floors. All these values are in kN/m and refer to vertical downward loading on the beams of the structure. The rest of the rows in the table include a measure of the discrepancy between the state-of-the art and the proposed method which can be defined by the following equation:

$$
\begin{aligned}
d_f(k) &= \frac{CL_f(k) - CL_f(1)}{CL_f(1)} \qquad for \quad k = 2,3,4,5 \\
d_f(k) &= min\left\{\frac{CL_f(k) - CL_f(1)}{CL_f(1)}, \frac{CL_f(k) - CL_f(11)}{CL_f(11)}\right\} \qquad for \quad k = 6 \\
d_f(k) &= \frac{CL_f(k) - CL_f(11)}{CL_f(11)} \qquad for \quad k = 7,8,9,10
\end{aligned}
\tag{3.1}
$$

where $d_f(k)$ is the discrepancy measure between the two methods. Equation 3.1 quantifies the discrepancy measure by comparing damage scenarios for $k = 2,3,4,5$, where there is more damage at column A, to the full column A removal ($k = 1$), while the damage scenarios for $k = 7,8,9,10$, where there is more damage at column B, are compared to the full column B removal ($k = 11$). For the symmetric case where equal amount of damage is applied to both

columns A and B, the minimum of the two comparisons is adopted.

The red colored cells in the table of Figure 3.8 represent the cases for which the collapse load of the new method is lower (and thus more critical) than the collapse load of the alternate load path method. Collectively, there are 92 out of the total 135 analyses with partial distributed damage that reveal more critical collapse loads than the alternate path method. The vast majority of cases where the alternate path method is unconservative showcase the importance of the results.

Furthermore, the decrease in the collapse load in many partial damage scenarios is considered particularly high. For example, for the first floor this decrease reaches $DS_1(6) = -23.3\%$ which is admittedly very high. Other outstanding cases are $DS_4(6) = -21.8\%$, $DS_1(7) = -20.3\%$, $DS_4(4) = -19.6\%$, $DS_1(3) = -19.5\%$, $DS_{10}(3) = -19.5\%$ among many others. This finding is considered the most important one of this work, since it demonstrates that for these cases, the state-of-the-art alternate path method is highly unconservative since it clearly overpredicts the progressive collapse capacity of the structure.

	Floor 1	Floor 2	Floor 3	Floor 4	Floor 5	Floor 6	Floor 7	Floor 8	Floor 9	Floor 10	Floor 11	Floor 12	Floor 13	Floor 14	Floor 15
$DS_f(1)$	56.4	56.4	54.6	53.1	55.9	55.8	53.6	57.7	62.0	59.7	66.5	65.3	61.8	62.5	45.0
$DS_f(2)$	−9.6%	−3.7%	2.0%	−9.7%	−7.0%	0.6%	−9.7%	−6.3%	−1.9%	−9.9%	−4.7%	5.8%	−1.4%	−0.8%	96.3%
$DS_f(3)$	−19.5%	−16.1%	−2.9%	−19.6%	−17.0%	−9.4%	−19.3%	−16.5%	−12.3%	−19.5%	−14.5%	−1.8%	−12.2%	20.5%	98.7%
$DS_f(4)$	−8.7%	−5.0%	8.4%	−10.2%	−7.2%	2.3%	−8.4%	−4.1%	2.9%	−3.6%	4.8%	38.9%	17.4%	42.9%	98.7%
$DS_f(5)$	8.7%	16.1%	30.2%	9.4%	13.0%	23.7%	11.2%	16.0%	22.3%	13.0%	20.6%	36.7%	24.2%	42.8%	98.7%
$DS_f(6)$	−23.3%	−15.7%	−8.5%	−21.8%	−17.4%	−10.2%	−18.0%	−12.2%	−4.4%	−11.8%	−2.3%	15.7%	−3.1%	18.4%	26.8%
$DS_f(7)$	−20.3%	−8.4%	−4.0%	−19.0%	−14.2%	−4.1%	−14.2%	−7.1%	−2.0%	−2.4%	−1.7%	−1.5%	−1.9%	4.9%	26.8%
$DS_f(8)$	−9.1%	1.0%	−1.0%	−6.1%	−1.2%	−1.7%	−2.0%	−1.4%	−1.3%	−1.5%	−1.1%	−1.5%	−1.3%	−2.1%	26.8%
$DS_f(9)$	−3.0%	−1.0%	0.0%	−1.1%	0.1%	−1.1%	−1.0%	−0.7%	−0.8%	−1.0%	−0.7%	−0.7%	−0.8%	−2.1%	10.2%
$DS_f(10)$	−2.0%	1.0%	0.0%	−0.3%	0.0%	−0.5%	−0.5%	−0.4%	−0.4%	−0.3%	0.3%	−0.3%	−0.4%	−1.1%	−1.0%
$DS_f(11)$	69.0	66.9	66.4	63.6	65.5	66.0	62.3	65.2	67.8	65.5	70.2	72.2	69.5	75.5	70.4

Figure 3.8: Detailed discrepancy results for collapse capacity between the alternate path method ($DS_f(1)$, $DS_f(11)$) and partial distributed damage method.

3.3.5 Effect of PPDM on Progressive Collapse Mechanisms

The second important finding of this chapter is the change in the observed collapse mechanisms in case of partial damage distribution. Figure 3.9 demonstrates the damage propagation of all the damage scenarios from 1^{st} to 5^{th} floor performed in this chapter, along with some selected damage scenario deformed shapes for 1^{st} and 3^{rd} floor. Each bar represents the collapse load of one analysis (20 analyses per floor, 300 analyses in total for all 15 floors).The sequence of analyses is shown by consecutive bars, with the red bars illustrating the analyses that yield the higher collapse load and are thus considered the dominant analyses. On top of each bar, the failing element at the end of each analysis is depicted rather than the removed element in the beginning of each analysis, to avoid confusion. The yielding-type collapse mechanisms are denoted by the letter Y (yielding).

The results show the alteration of the failing elements in case of partial distributed damage, as opposed to full column removal scenarios $DS_f(1)$ or $DS_f(11)$. In case of buckling modes of collapse, the element that buckles is not always the adjacent column or the column that the corresponding full removal scenario is indicating. For example, the current state-of-the-art Alternate Load Path Method (damage scenario $DS_1(11)$) predicts the buckling failure of column $C1$ after the complete column $B1$ removal. However, according to the proposed Partial Distributed Damage Method, the deformed shape of Analysis II when considering damage scenario $DS_1(3)$ reveals the buckling failure of column $B1$ (after removing the previously buckled column $A1$ in Analysis I). What is also remarkable is the reduction of the collapse load according to PDDM which in this case is 34%. Similarly, at the 3^{rd} floor, the state-of-the-art APM predicts buckling of column $C4$ (damage scenario $DS_3(1)$), whereas the finally buckling element according to the proposed PDDM (damage scenario $DS_3(3)$) is column $B3$. Therefore, the position of the buckling element highly depends on the damage scenario examined in each case, so an integrated progressive collapse vulnerability analysis must take into account all damage scenarios and thus apply any design or retrofit techniques

on a series of vulnerable elements within the structural system.

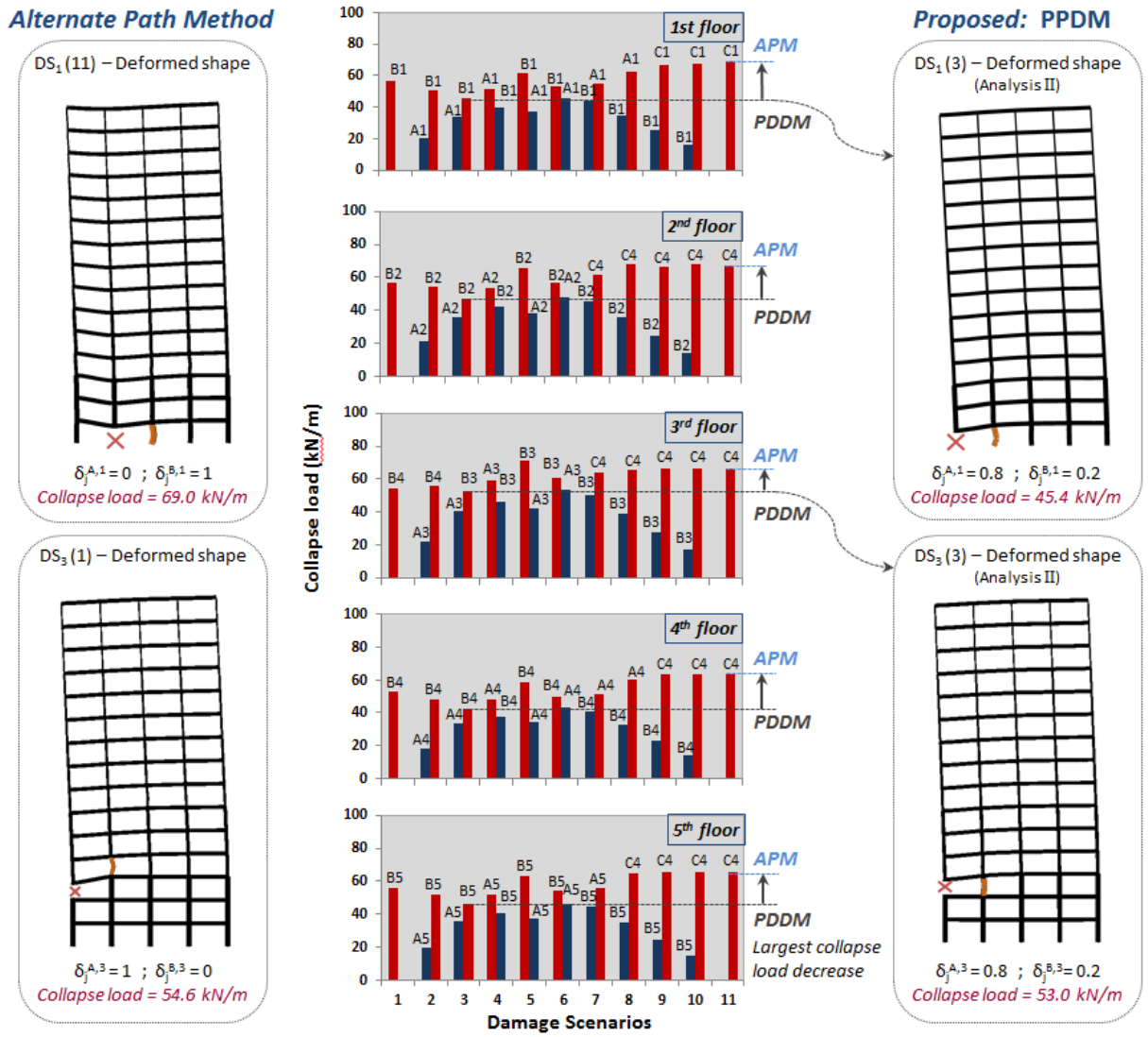

Figure 3.9: Damage propagation and analyses sequence for all damage scenarios at first five floors, with respect to the collapse load, and selected damage scenario deformed shapes for 1^{st} and 3^{rd} floor.

Figure 3.10 depicts the damage propagation of all damage scenarios from 6^{th} to 10^{th} floor, along with some selected damage scenario deformed shapes for 6^{th} and 9^{th} floor. In the same manner as the previous floors, the observed collapse mechanisms highly depend on specific damage scenarios investigated. For instance, at 6^{th} floor, the state-of-the-art APM (damage scenario $DS_6(11)$) predicts buckling failure of column $C7$, while damage

scenario $DS_6(3)$ predicts buckling failure of column $B6$ according to the proposed PPDM. Additionally, when observing the damage scenarios at 9^{th} floor, the proposed PDDM for $DS_6(3)$ results in the buckling failure of column $B9$, in contrast to the state-of-the-art APM that results in the buckling failure of column $B10$.

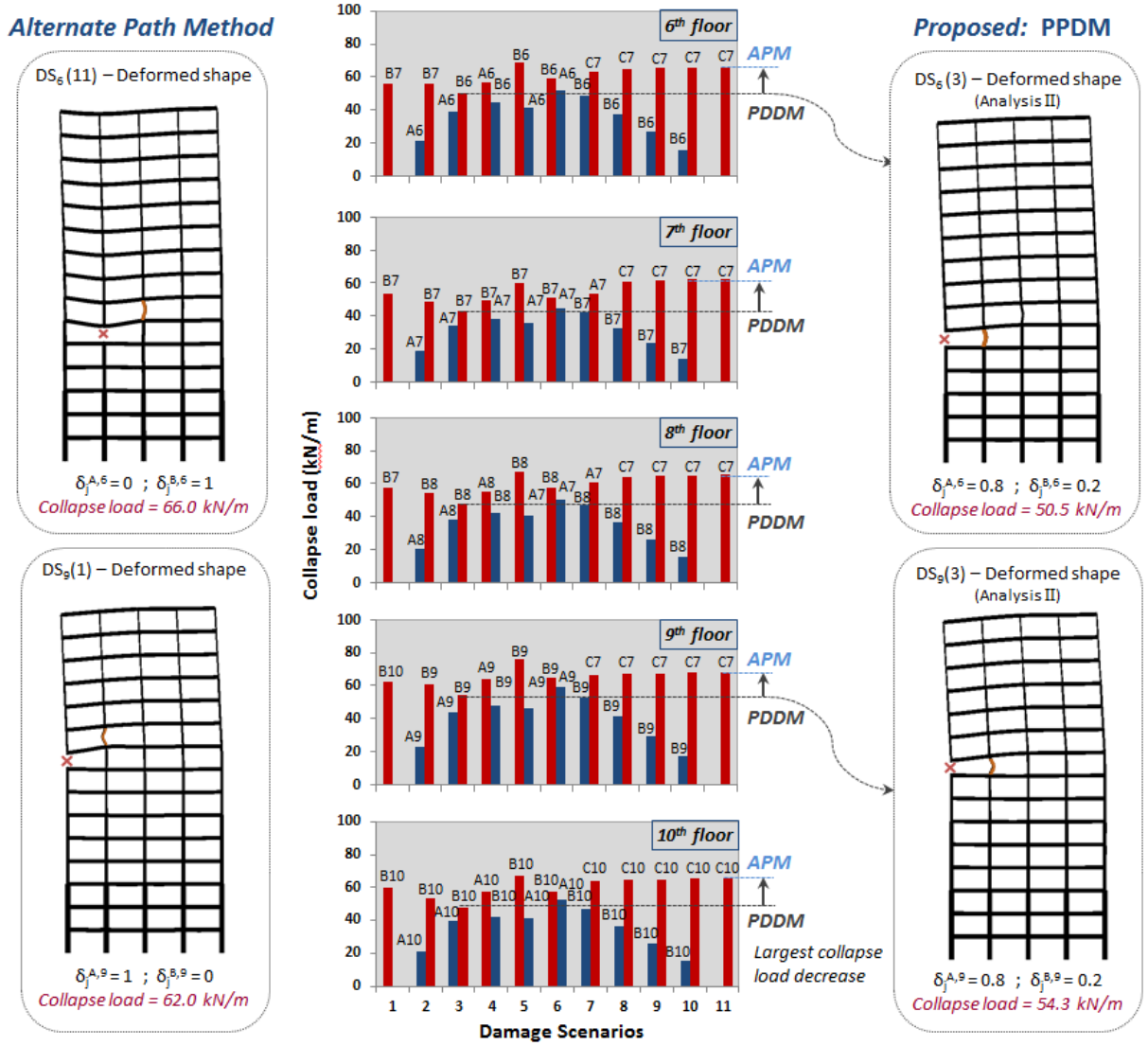

Figure 3.10: Damage propagation and analyses sequence for all damage scenarios from 6^{th} to 10^{th} floor, with respect to the collapse load, and selected damage scenario deformed shapes for 6^{th} and 9^{th} floor.

Finally, Figure 3.11 depicts the damage propagation of all damage scenarios for the last five floors of the building, where the dominant type of failure is beam yielding. The change

in the collapse mechanisms is even more significant for those floors. For example, at the 12^{th} floor, the current state-of-the-art method that includes full column $B12$ removal (damage scenario $DS_{12}(11)$) results in beam yielding failure of the beams spanning above the removal location; a failure type that is by nature ductile and thus allows for safety warning by appearance of significant plastic deformation. Conversely, when applying a more realistic damage distribution scenario such as $DS_{12}(5)$, the collapse mode that the proposed method predicts is tremendously different and includes loss-of-stability of a column at a much lower floor, even outside the damaged area, i.e. column $B4$. In the same environment, similar conclusions can be drawn when comparing the state-of-the-art method to the proposed method at floors 13^{th} - 15^{th}. As illustrated by the deformed shapes of the 14^{th} floor, full column $A14$ removal ($DS_{14}(1)$) leads to yielding-type failure of the above beams, while damage scenario $DS_{14}(5)$ included in the proposed PDDM leads to buckling failure of $C4$ column, as previously discussed in Section 3.3.2.

Hence, it is clear that introducing a more widespread and realistic damage distribution that affects more than one column may not lead to the predicted progressive collapse of the flexural elements above the removal. This happens mainly due to the support that is provided by the partial damaged column; in the APM the removed column is absent and therefore there is a complete loss of support. This work shows that even when a small part of the column remains in the structure, it could prevent the yielding type of collapse. A parametric investigation about how damage is distributed into the system and how it affects the structural response, like the one proposed in the Partial Distributed Damage Method, is therefore crucial in order to detect the most vulnerable elements to loss-of-stability and apply the necessary precautions in their design.

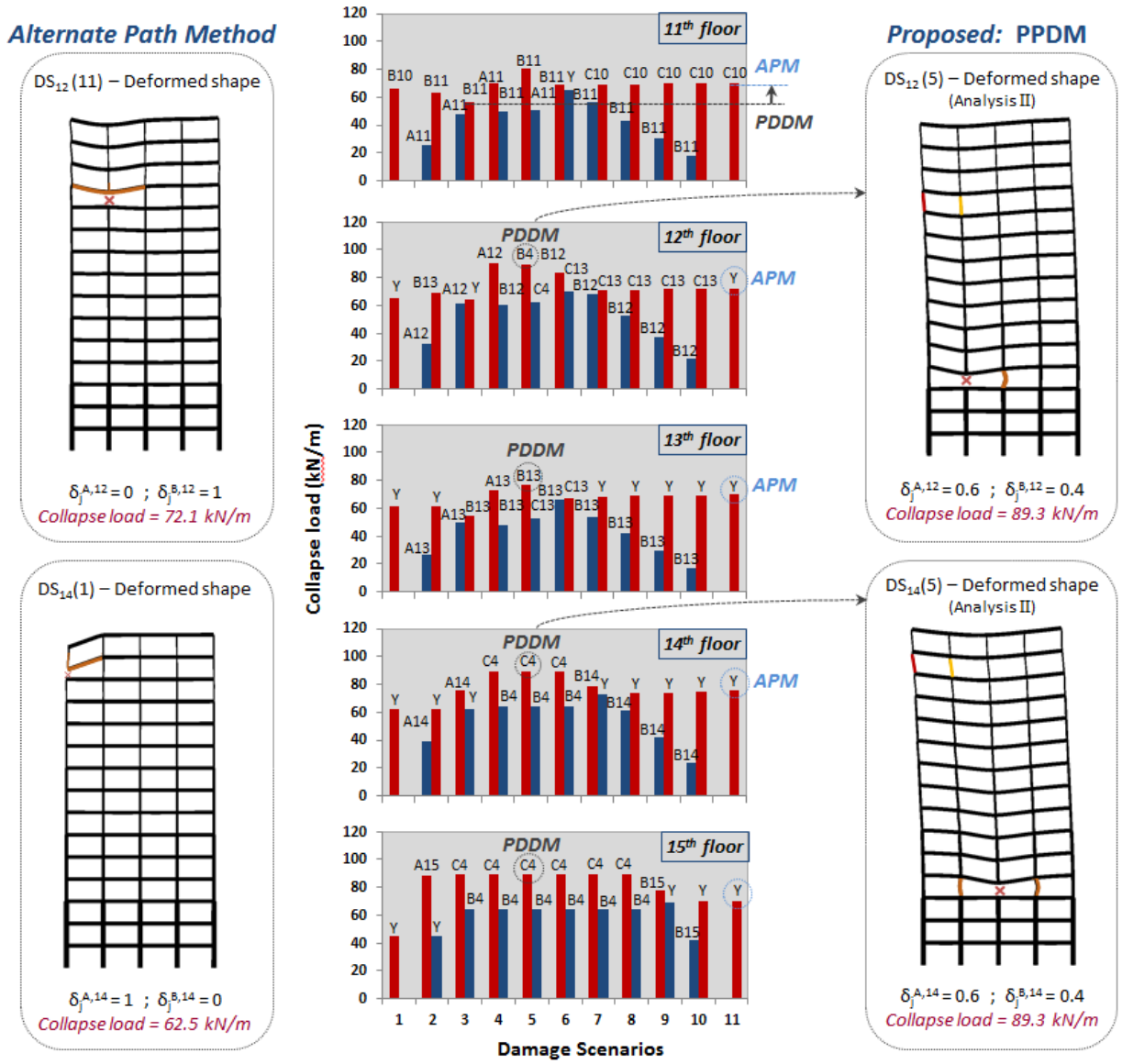

Figure 3.11: Damage propagation and analyses sequence for all damage scenarios from 11^{th} to 15^{th} floor, with respect to the collapse load, and selected damage scenario deformed shapes for 12^{th} and 14^{th} floor.

3.4 Concluding Remarks

Recent studies have questioned the validity of the simplistic current state-of-the-art concept of key element removal for the performance of progressive collapse analysis. Although the alternate path method is simple enough for designers and practitioners to apply, it is far from being realistic. The reasoning behind this questioning is not only because the likelihood of occurrence of an extreme event that is able to cause the complete failure of only one element is extremely small, but also because in the case of an extreme event, the affected damage area will include more than one elements. Chapters 2 and 3 introduce a new method for progressive collapse analysis defining partial distribution damage scenarios. The method is applied on a 15-floor steel frame showing that the column removal concept can be unconservative. The most important findings from the present work are the following:

- For the partial damage scenarios located at the lower floors of the frame (up to the 12^{th} floor), where the dominant collapse mode is the column buckling failure, the collapse loads can be significantly less than the collapse loads of the corresponding full column removal scenarios. As a result, the application of the alternate path method is less conservative, since the structural behavior of the frame is seriously affected by the distribution of damage.

- For the upper floors of the frame (above 12^{th}), where the dominant failure is the yielding-induced collapse mechanism due to beam failure, the partial distributed damage method (PDDM) leads to similar collapse loads with the complete column loss approach. Therefore, partial damage distribution only mildly affects the response of the structure in this case.

- The introduction of distributed damage in the system significantly changes the observed collapse modes of the structure. More specifically, for floors where the dominant failure is buckling, distributed damage can alternate the location of the failing element. For

floors where the alternate path method leads to a yielding-type beam collapse mechanisms near the damaged area, some partial damage scenarios lead to the avoidance of the yielding-type collapse mode and the triggering failure is the buckling failure of elements located outside the damaged area, in much lower floors.

- For all cases examined except for the top two floors of the analyzed building, the partial damage scenario that leads to the lower collapse load is always $DS_f(3)$ ($\delta_j^{A,f} = 0.8$ and $\delta_j^{B,f} = 0.2$).

The conclusions of this work clearly show that the widely used and unrealistic column removal concept of the Alternate Path Method can be less conservative and predict collapse mechanisms and collapse loads which are not the most critical. For this reason, a reliable study to evaluate the progressive collapse capacity of a structure must include a partial damage distribution study as well, through the proposed partial distributed damage method (PDDM).

The next important task in order to extend the findings of this work is the application of the same analysis procedure to a 3D model. However, the collapse mechanisms and thus the main conclusions are expected to remain the same, since the columns examined herein are governed by inelastic nonlinear buckling (able to be captured in a 2D analysis configuration) rather than elastic Euler buckling of the weak axis that can only be detected by a 3D analysis configuration. Finally, another important task is to take into account the post-buckling behavior of the buckled elements and examine the extent to which the collapse loads and mechanisms will be affected.

Chapter 4

Progressive Collapse Vulnerability of 3D High-Rise Steel Buildings under External Blast Loading

4.1 Introduction

As opposed to the Alternate Path method, the notion of direct simulation of blast-loading events to assess the progressive collapse potential of structures is gaining more ground. In this environment, in the United States, FEMA 2003 [42] describes design measures for structural infrastructure to resist blast loads. Marchand and Alfawakhiri 2005 [43] discussed general principles and definitions for explosive loads and progressive collapse, providing recommendations and response predictions for commercial and industrial buildings. Le Blanc et al. 2005 [44] developed an empirical approach for the determination of blast loads. Hamburger and Whittaker 2004 [45] also presented design strategies against blast-induced progressive collapse, while Krauthammer 2005 [46] reviews the blast-related survivability of steel buildings, focusing on steel connections. Sasani et al. 2011 [29] assessed experimentally and analytically the progressive collapse resistance of an actual 11-story RC structure by apply-

ing severe initial damage though explosion and removal of key columns and beams.

Additional studies on progressive collapse-related blast response of structures have emerged in the literature, using up-to-date numerical simulation tools. Luccioni et al. 2004 [47] performed a detailed numerical analysis that accurately reproduced the collapse of a real reinforced concrete building that was hit by a terrorist attack. Krauthammer and Otani 1997 [48] investigated the effect of mesh, gravity and loading on finite element simulation of RC structures under blast loads, providing recommendations and conclusions that may improve the efficiency of the numerical simulations. Yi et al. 2013 [49] presented a new approach for blast load application on highway bridges that is able to simulate both blast reflection and diffraction. Shi et al. 2008 [30] and 2010 [50] proposed a new method for progressive collapse analysis that considers initial damage and non-zero initial conditions to adjacent structural components under blast loading, through the application of a numerical method to generate pressure-impulse diagrams for RC columns. McConnell and Brown 2011 [31] attempted to quantify the blast threat that is representative of the APM analysis framework by computing stand-off distances that correspond to different charge sizes and column properties. They concluded that the single column removal scenario is only representative in case of 'small' charges and relatively large column spacing; otherwise results revealed multiple column failures that render the APM (single column removal) analysis inappropriate. Jayasooriya et al. 2011 [32] studied the non-linear response of key elements of an RC frame building subjected to near field blast events, in order to assess their residual strength capacity and evaluate the overall structural vulnerability to progressive collapse propagation. Fu 2013 [51] investigated the dynamic response of a 3D tall building and focused on shear and ductility demands of columns when subjected to a typical charge at an intermediate floor, while also comparing the results with the equivalent structural behavior based on the alternate path method. Li and Hao 2013 [52] proposed a new method to simulate progressive collapse of reinforced concrete frame buildings that uses the substructure technique, as opposed to the traditional FE simulation. In order to reduce the computational time and computer mem-

ory, the mass and stiffness parts of the structure that exhibit small elastic deformations were condensed to the structural components close to the detonation which were only modeled in detail. Elsanadedy et al. 2014 [53] conducted a two-stage simplified nonlinear dynamic analysis procedure, including a local model stage to assess individual column performance and a global model stage to investigate the overall system performance, in order to study the vulnerability of typical multi-storey steel frame buildings under a near field blast attack. Tadepalli and Mullen 2008 [54] examined the use of single column damage mapping based on simplified pressure estimation considering a limited number of blast loading parameters needed for published semi-empirical equations and the spatial mapping of the columns on the building exterior facing the detonation source. The single-column damage was established using nonlinear FE modeling of the columns using SAP2000 FE software including the fiber model for section response.

The objective of Chapter 4 is to expand the knowledge about the sensitivity of progressive collapse vulnerability of steel buildings to the distribution of damage within the structural system when facing an external blast. In particular, focus will be placed on the investigation of the effect of weakening of adjacent damaged columns on the load redistribution and potential initiation of progressive collapse. A methodology to assess the progressive collapse vulnerability is also presented, which includes four consecutive steps to simulate the blast loading event sequence. Details of the blast scenario considered and how the blast loads are generated are also provided in this chapter.

Subsequently, in the following Chapters 5 and 6 and through using the commercial ABAQUS [41] code, nonlinear dynamic finite element simulation is performed to investigate the response of the system, assess the damage propagation and explore the possibility of progressive collapse initiation. Three case studies of steel buildings are presented covering a range of different steel building structural systems. A high-rise (20-story) steel building from the SAC-FEMA [55] steel project, designed based on practices before the Northridge earthquake for Boston area, will serve as an initial example for the application of a blast

load scenario. Subsequently, two typical mid-rise (10-story) office steel buildings located in Chicago (included in the work of Agarwal and Varma 2014 [56]) with identical floor plan layout but different lateral load resisting systems are used; one including perimeter moment resisting frames and one including interior reinforced concrete (RC) rigid core. Comparisons between the performances of the building configurations subjected to the same blast scenario will demonstrate the effect of the building layout to the overall structural behavior and progressive collapse capacity. Identification of interior gravity columns as the weakest links that greatly influence the stability behavior and may potentially initiate progressive collapse is finally established.

4.2 Simulation of Blast Event - Method of Analysis

The following paragraphs describe the proposed method of analysis for the global progressive collapse vulnerability assessment of buildings under blast loading. As depicted in Figure 4.1 for a typical multi-story 3D building, the proposed method pertains to a 4-step procedure.

Step I

The first step of the analysis includes the static application of the vertical loads onto the structure, which are computed based on the load combination (1.2 Dead Load + 0.5 Live Load) proposed by the DoD 2009 [1] guidelines for progressive collapse analysis. The nature of a static step implies the application of vertical loads as a linear ramp function over a period of $1sec$ in analysis time. Although this step is static, it is combined with the following dynamic steps to form a consecutive step sequence with an overall analysis duration expressed in seconds.

Step II

The second step of the analysis is a dynamic step that lasts $0.5sec$. It basically serves as a transition step between the application of vertical loads and the blast event, to ensure

that the structure is at a stable condition prior to the blast loading. No additional loads are included in this step.

Step III

The third step of the analysis is the actual blast loading step. Within the first few milliseconds of this explicit dynamic step, all members within the substantial influence area of the blast event are loaded by a uniformly distributed pressure load. The response of the structure is subsequently captured by the remaining step duration. A total duration of $3.5sec$ is proposed in this method of analysis, which is considered long enough for vibrations to die out and thus to correctly capture the structural response evolution, but short enough to offer a computationally viable solution. This step can have two possible outcomes; either the structure reaches a steady and stable condition or it collapses. In the latter case, the collapse load of the structure is defined as the vertical load applied in Step I, implying that the blast scenario examined is able to initiate progressive collapse with the existing vertical loads.

Step IV

If the structure manages to survive the blast scenario of Step III, additional vertical load is applied with a linearly increasing ramp function through another dynamic step (vertical push-down analysis). The analysis continues until no additional load can be undertaken and the program shows warning signs of structural failure (the type of failure will depend on the specific structure examined and will be thoroughly addressed in the following section of the numerical application of the proposed method). The final collapse load is computed as the summation of the vertical load applied in Step I ($1.2DL + 0.5LL$) plus the additional vertical load of Step IV that leads to collapse. This final collapse load defines the progressive collapse vulnerability of the building subjected to the blast scenario examined.

For a more detailed explanation of the proposed method, the reader is encouraged to refer to the numerical example demonstrated in Chapters 5 and 6.

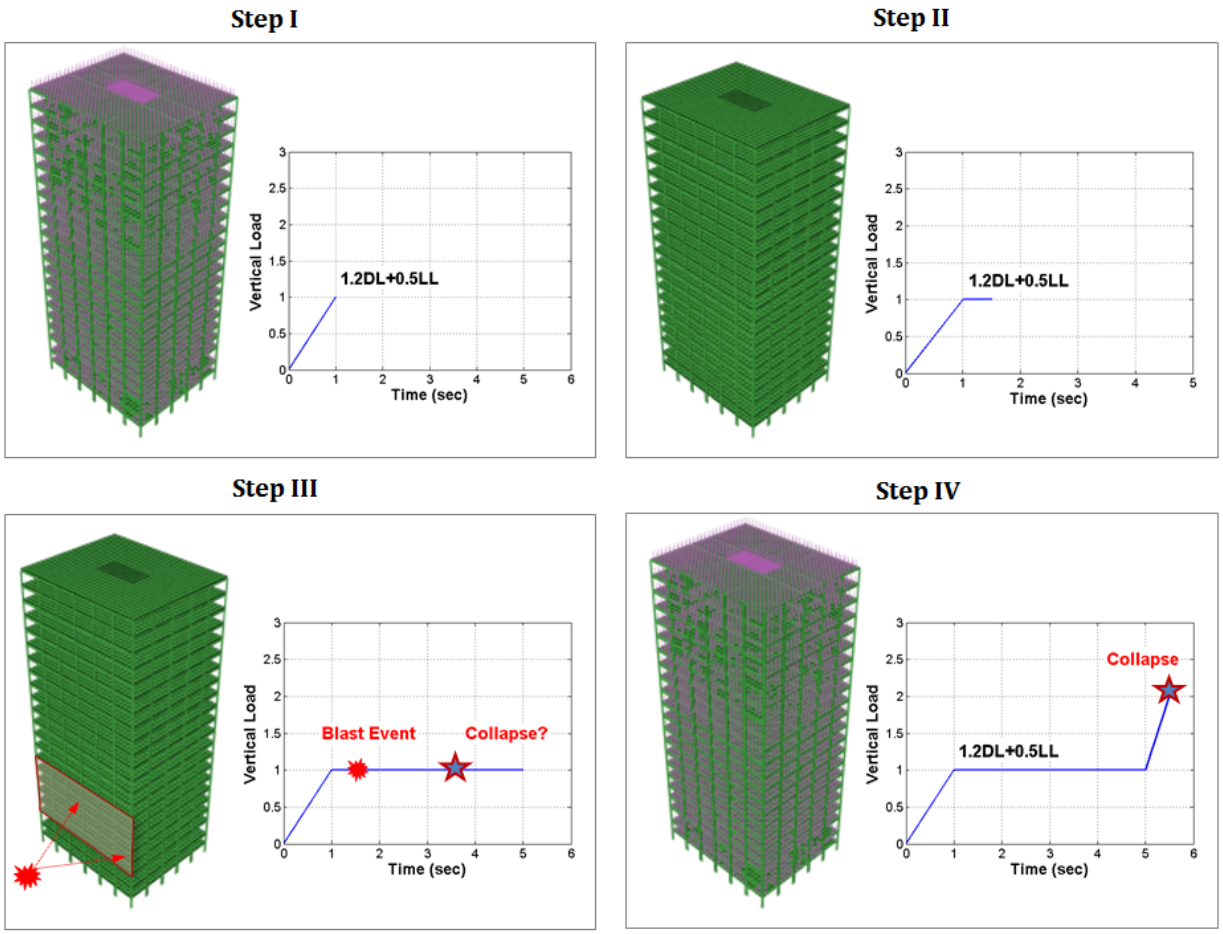

Figure 4.1: The 4 steps of the proposed method of analysis for progressive collapse vulnerability assessment of buildings.

4.3 Blast Scenario and Blast Loads Generation

Various possibilities for a blast scenario were considered including source charge weight and position with respect to the building envelope. A surface blast consistent with a truck or van parked on the street adjacent to the building was selected as a reasonable threat a high-rise building designer might consider. Sensitivity of the pressure distribution and column damage levels to the scenario event definition was first established using the decision-oriented software VAPO [57] which includes a variety of global graphical and local quantitative outputs but is not considered highly accurate. Independent calculations were then made using available

empirical equations by Kingery and Bulmash 1984 [58] and Kinney and Graham 1985 [59] to establish blast parameters that are consistent with available blast resistant design guidance (Unified Facilities Criteria 2008 [60], TM5-1300 1990 [61]) and account only for equivalent TNT charge weight and stand-off distance. Reduction of radial pressures due to angle of incidence at each column face can be estimated through available charts in FEMA 2003 [42]. Blast parameter evaluation can be also performed by a variety of models available in the literature, among which are ConWep [62] and A.T.-Blast [63] that both use empirical formulas from Kingery-Bulmash and TM5-1300. In this particular study, after the above considerations, the commercial software A.T.-Blast designed for GSA was finally chosen as a simplified and efficient method of predicting blast effects of an open hemispheric TNT explosion. The input of the software is weight of charge, standoff distance and angle of incidence, while output blast parameters include shock velocity, time of arrival, overpressure, impulse and load duration.

4.3.1 Overpressure Time Profile and Equivalent Triangular Pulse Simplification

The overpressure time profile of a blast event (above normal atmospheric pressure) is shown in Figure 4.2, according to UFC. It includes a positive phase where the sudden release of energy from the explosive charge causes a sharp rise of pressure, followed by a negative phase. The incidence pressure curve refers to open air pressure when a blast wave travels parallel to a surface, while the reflected pressure curve represents the increase of the blast wave intensity when it impinges on any rigid barrier at any angle not parallel to the direction of wave travel. The related energy release of the explosion, expressed by the so-called blast impulse, is represented by the area under the curve and directly depends on the scaled distance $Z = \frac{R}{W^{1/3}}$ (where R is the standoff distance between the charge and the target and W is the is weight of the charge). Although the actual overpressure time profile of a real blast wave includes an exponential decay during the positive phase, a simplification of the wave

profile is to assume a linear decrease of the overpressure so that the actual impulse per unit area of the blast wave is preserved. This simplification (also known as equivalent triangular pulse) is generally considered accurate enough to correctly evaluate potential blast damage on structures (Baker 1973 [64] and Kinney and Graham 1985 [59]). The equivalent linear load duration (also depicted in Figure 4.2) is directly computed by A.T.-Blast software and is utilized in this study for the application of blast loads on the structural members.

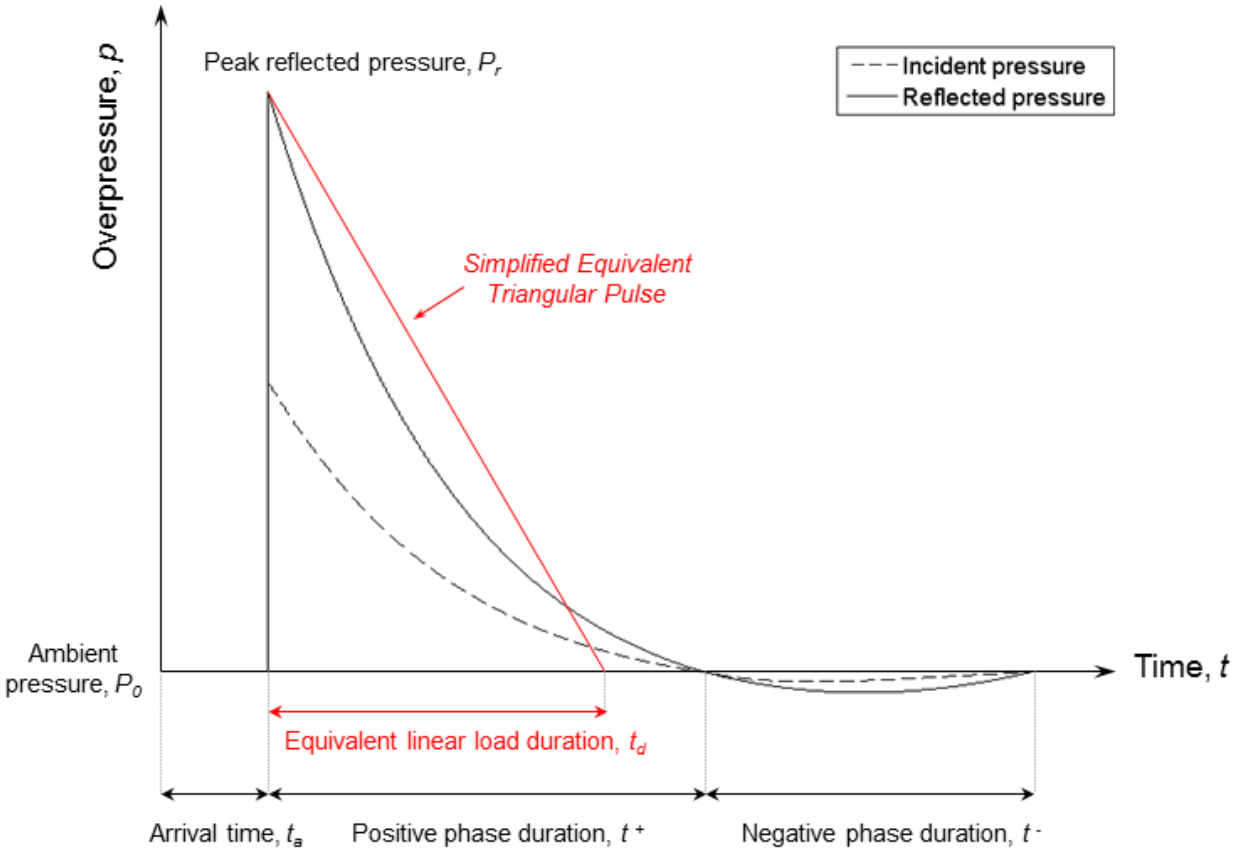

Figure 4.2: Blast wave overpressure time profile and equivalent triangular pulse simplification.

Chapter 5

Progressive Collapse Vulnerability of Steel Buildings under Blast Loading - Numerical Application #1

5.1 Introduction

Chapter 5 presents detailed 3D nonlinear finite element dynamic analyses of steel frame buildings in order to examine the spatially distributed response and damage to frame members along the building exterior facing an external blast, by employing the methodologies developed in Chapter 4. Through using the commercial ABAQUS [41] code, a high-rise (20-story) steel building from the SAC-FEMA-355C [55] steel project, designed based on practices before the Northridge earthquake for Boston area, is simulated to serve as an initial example for the application of a blast load scenario, investigate the response of the system, assess the damage propagation and explore the possibility of progressive collapse initiation. The simulation of the building includes two versions; one where the slab is simulated as a load resisting element and one where the slab is omitted. It is shown that the slab contribution in the load redistribution mechanism after the blast event tremendously affects

the structural behavior and eventually leads to the overall system's stabilization.

Comparison of beam-column subassembly finite element analysis and a simplified analytical approach consistent with current design recommendations are made with the complex system results in the heavily impacted region. Parameters affecting the spatially distributed pressure and response quantities are identified, and the sensitivity of the damage results to the spatial variation of these parameters is established for the case considered.

5.2 Building Description

A 20-story building designed to pre-Northridge requirements [55] around the Boston area is used as a case study as it provides a reasonable problem definition in an urban or suburban setting and, based on recent analyses by Gerasimidis et al. 2014 [8], is tall enough to be vulnerable to progressive collapse. The building consists of perimeter moment resisting frames, interior gravity frames and a two-level basement. The floor plan is depicted in Figure 5.1, along with the location of the blast source and the flexible beam-column connections between the frames to avoid bi-axial bending (every connection is flexible except for the locations denoted by a blue triangle). Only the beams spanning from column to column are included in the 3D model, with the secondary beams being neglected for simplicity. The bay width is $20ft.$ ($6.10m$) and the story height is $18ft.$ ($5.49m$) at the ground level and $13ft.$ ($3.96m$) at the rest of the floors. The nominal design vertical loads are $83psf$ (3.97kPa) for roof and $96psf$ ($4.60kPa$) elsewhere for dead loads, and $20psf$ ($0.96kPa$) for roof and $50psf$ ($2.39kPa$) elsewhere for live loads. The material utilized for all the structural steel components is A572 Gr.50 steel with isotropic strain hardening, yield strength $50ksi$ ($345MPa$) and ultimate strength $65ksi$ ($450MPa$) at strain 18%. The concrete material for the steel-concrete composite slab has a compressive strength of $5.4ksi$ ($37.5MPa$) and a tensile strength of $0.5ksi$ ($3.5MPa$), with Young's modulus $4350ksi$ ($30GPa$). More details about the geometry, member dimensions and section properties can be found in Appendix

B of [55].

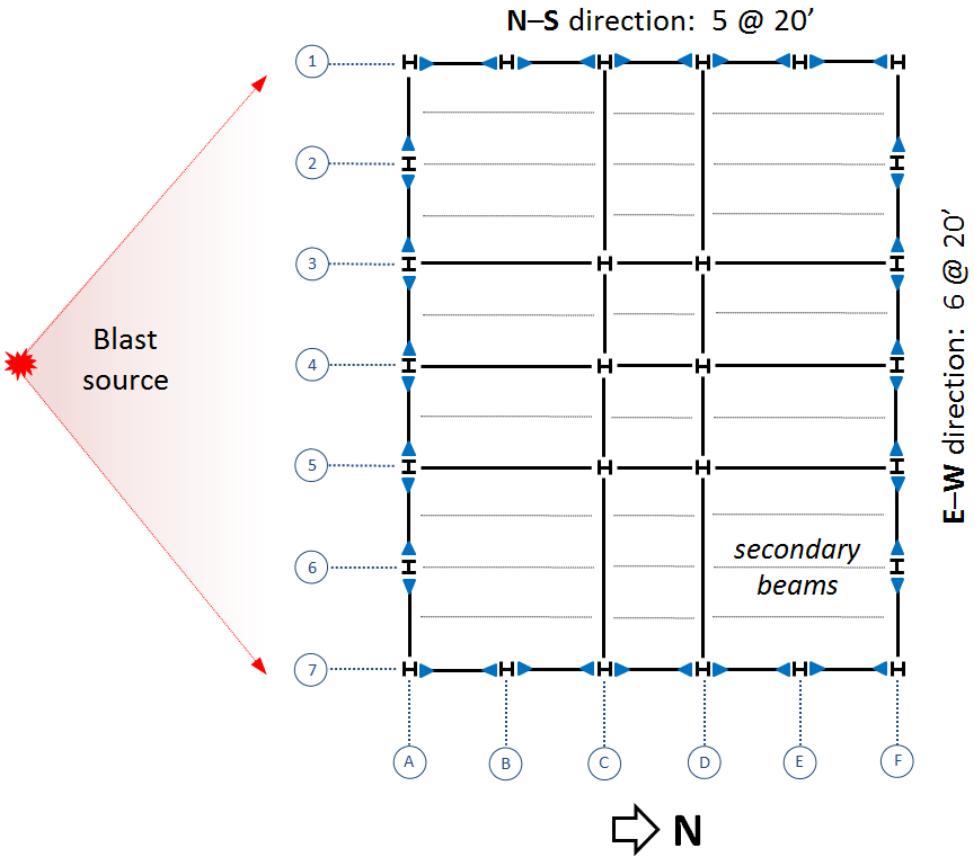

Figure 5.1: Plan view and geometry of 20-story building with perimeter moment resisting frames. Locations of fixed beam-column connections are denoted by blue triangles.

The frame system offers sufficient complexity and variability of member dimensions and section properties to observe variations in the response expected due to loading conditions associated with both gravity generated axial loads and transverse blast pressures. The axial loads vary due to different functions of individual members in the wind and gravity load system response, and the pressures vary due to different distances and incidence angles from the blast source. The primary blast impact region was selected by the authors as the first five floors of the building, since the damage potential of blast pressures applied on higher floors can be considered negligible (see below Section 5.3).

5.3 Single Degree of Freedom Column Analysis

5.3.1 Beam-column Static Analysis

An initial estimate of the damage distribution in the primary blast impact region may be obtained from analysis of individual column responses and subsequent mapping spatially onto the surface of the region, as shown in Tadepalli and Mullen 2008 [54]. Figure 5.2 serves as the basis for this assessment here where the pressure computed for a given column at mid height is applied and the variation over the column height is neglected. The response of the column is considered continuous along the length, and beam-column theory (Timoshenko and Gere 1961 [65], Chen and Liu 1987 [66] is applied. Boundary conditions are assumed to be fix-fix for purposes of comparison with the simulated 3D building system response.

The lateral stiffness of each column is affected by the axial load due to the interaction of axial force and bending moment and to second order effects. Axial loads are determined for each column from the unfactored gravity load (dead plus live) analysis of the 3D building system model. Figure 5.3a shows color contours depicting the variation in the primary blast impact region of gravity generated axial loads, P, for the 20 story building case. The loads have been normalized with respect to the Euler buckling load, $P_e = \frac{\pi^2 EA}{S^2}$, where E=Young's modulus, A=column section area, and S=column slenderness. Note the axial loads vary according to the nature of the designer's choice of a building frame system, and the buckling load varies according to the designer's choice of A and S, within the limitations of governing design criteria from AISC 360-10 [67]. Here, $S = \frac{kL}{r}$, where the effective length factor, $k = 0.5$, for fix-fix end conditions, and the column section radius of gyration, $r = I/A$, again depends on the designer's choice for the second moment of area, I, about the bending axis controlling buckling.

All columns in the blast impact region exhibit normalized axial load ratios, P/P_e, less than 10 percent indicating significant reserve for biaxial bending interaction in light of current

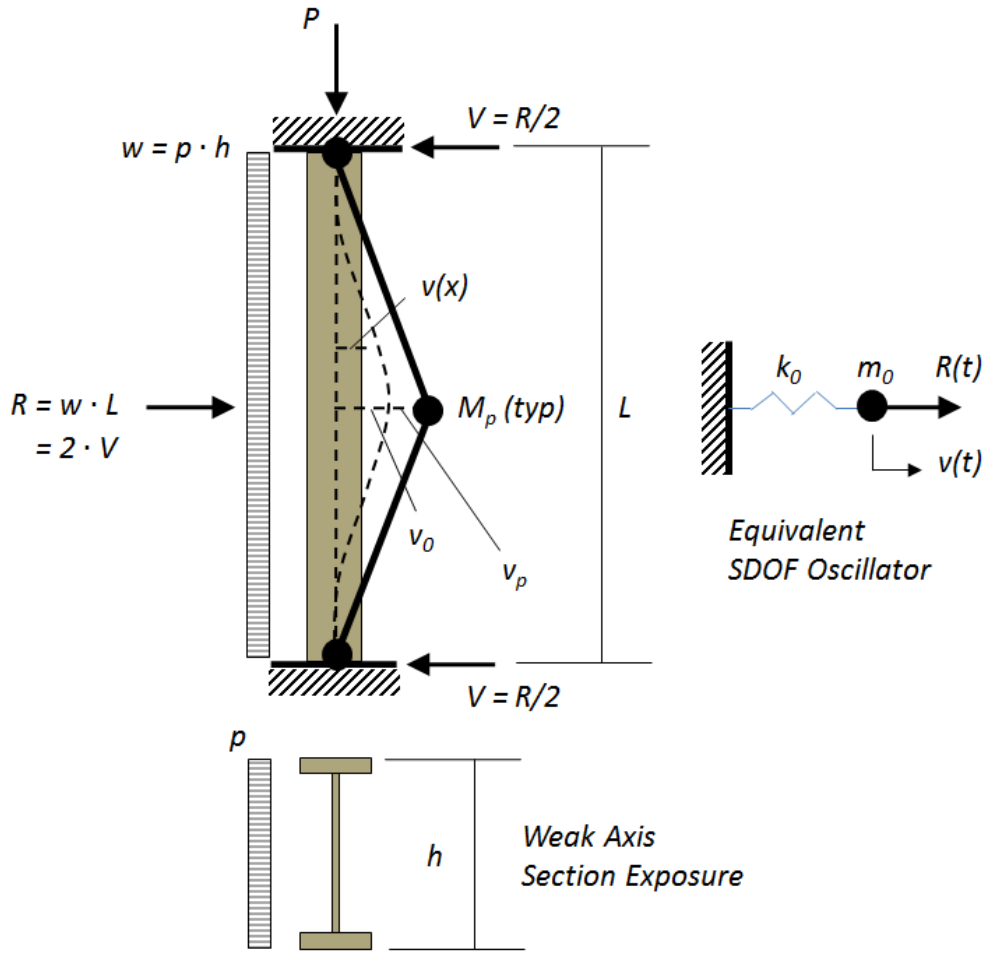

Figure 5.2: Isolated beam-column static analysis parameters, plastic collapse mechanism, and simple dynamic model.

design provisions [67]. If the pin-pin condition is assumed, the ratios become less than 34 percent. Figure 5.3b also shows the weak-axis S for the columns normalized by the limiting value, $S_0 = 4.71\sqrt{\frac{E}{F_y}}$, where F_y=specified minimum yield stress. This value is recognized in design provisions [67] as the one at which buckling switches from inelastic to elastic. All values in Figure 5.3 are significantly less than unity indicating that all columns have been designed to exhibit inelastic buckling. Curiously, the interior columns adjacent to the corners exhibit noticeably higher slenderness. This pattern is also reflected in the higher axial load ratios due to the dependence of P_e on S.

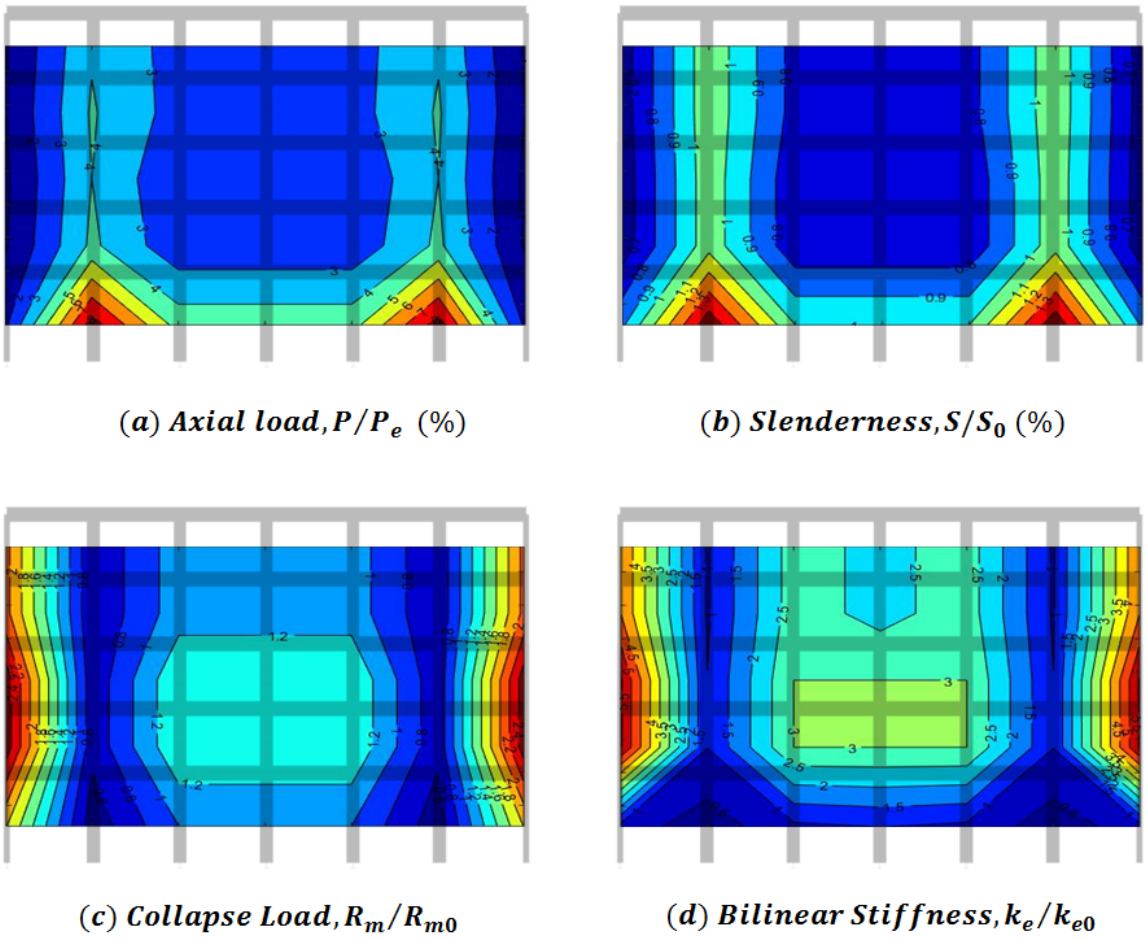

Figure 5.3: Variation of static response parameters for columns in blast impact region.

Static strength of the columns may be characterized by the section fully plastic moment, $M_p = F_y Z$, where Z=plastic section modulus, and by the net lateral load at which a plastic collapse mechanism is formed, $R_m = phL$. For fix-fix end conditions, neglecting elastic contributions in comparison to that at the plastic hinges, the plastic work energy balance at initiation of collapse requires, $R_m = 16\frac{M_p}{L}$. Figure 5.3c shows the variation of the weak axis collapse load, normalized with respect to R_{m0}, the collapse load for the first floor central column. Corner columns are seen to exhibit relatively high plastic section properties. Smaller changes are introduced by the column height difference at the first floor and the slight reduction of section properties beginning at the fourth floor. The columns

next to the corners are seen to be not only more slender but also weaker.

The impulsive nature of the blast event requires characterization of dynamic response as it is quickly found that the peak reflective pressures, p_r, in much of the primary blast impact region are an order of magnitude higher than the static collapse pressures, p_m, for the corresponding columns. Preliminary to the dynamic analysis, it is useful to establish an equivalent lateral spring representation (Biggs 1694 [68]) of the column idealized as a single-degree-of-freedom oscillator. An equivalent spring stiffness, k_0, is used to characterize the mid height lateral displacement, $v(t)$, at any time t throughout the elastic-plastic response history. For fix-fix end conditions, the trilinear static response, developed as hinges form at the ends then at mid height, is captured reasonably well with a reduced effective stiffness, $k_e = 0.80k_0$, for the bilinear elastoplastic static response (Biggs 1694 [68]) and corresponding static collapse displacement at mid-height, $v_p = \dfrac{R_m}{k_e}$.

Beam-column theory indicates that the static deformation and thus stiffness are affected by P,p, and L, all of which have been shown to vary within the blast impact region. A solution of the governing differential equation according to Timoshenko and Gere 1961 [65] for the elastic case and fix-fix end conditions in terms of the above parameters is obtained using the symbolic math software Mathematica [69] which can be shown to agree with a corresponding result found in Chen and Liu 1987 [66]:

$$v(x) = \frac{w}{2EIk^3}\left[k(L-x)x + L\cot\frac{kL}{2} - L\cos\frac{k}{2}(L-2x)\csc\frac{kL}{2}\right] \tag{5.1}$$

$$v_0 = v\left(\frac{L}{2}\right) = \frac{w}{2EIk^3}\left[\frac{L}{2}u + L\cot u - L\csc u\right] \tag{5.2}$$

where $u = \dfrac{kL}{2}$ and $k^2 = \dfrac{P}{EI}$.

A numerical programming MATLAB routine [70] was written to evaluate the expression for v_0 for each column in the impact region allowing for the variation in P, p, and L. A worksheet program was then used to subsequently calculate M_p,R_m, $k_0 = \dfrac{R}{v_0}$, and k_e. Figure 5.3d shows k_e in the blast impact region normalized by k_{e0}, the value at the first floor central

column. Relative stiffness of corner columns over interior ones and relative flexibility of the first story columns over higher stories are again observable in the contour plots. Similarities with the variations in slenderness are observed due to the dependence of both on the column height and section properties.

5.3.2 SDOF Column Damage Analysis

Response of the columns to the blast event must account for both nonlinear material and geometric behavior. Analysis of the columns considered as isolated members assumes the end constraints and axial loading remain constant during the blast event. Time history analysis of the beam-column system shown in Figure 5.2 is performed to estimate $v(t)$ at mid height and establish the permanent offset resulting from any elastoplastic damage. An equivalent elastoplastic single-degree-of-freedom (SDOF) oscillator idealization is adopted for ease of calculation and consistency with recommended design practice AISC 360-10 [67]. The SDOF results will later be compared to those from 3D simulation of the 20 story building system response to provide a measure of the level of approximation implied by this idealization.

Even with such idealization and apparent simplification, there is considerable complexity through the interaction of parameters in the estimation of maximum response and damage for each column. Figure 5.4 attempts to depict and highlight the dependencies of these parameters in the computation sequence which consists of three steps:

1. *nonlinear static analysis* of elastoplastic beam-column deformation to determine parameters R_m, v_0, k_e, and v_p in the presence of distributed pressure, p, and axial load, P

2. *eigenvalue analysis* of elastic beam-column vibration to determine the undamaged natural frequency, f_0, in the presence of axial load, P

3. *time history analysis* of SDOF oscillator, both linear and bilinear elastoplastic, to determine the maximum dynamic response at mid height, v_m, and ductility, $\mu = v_m/v_p$

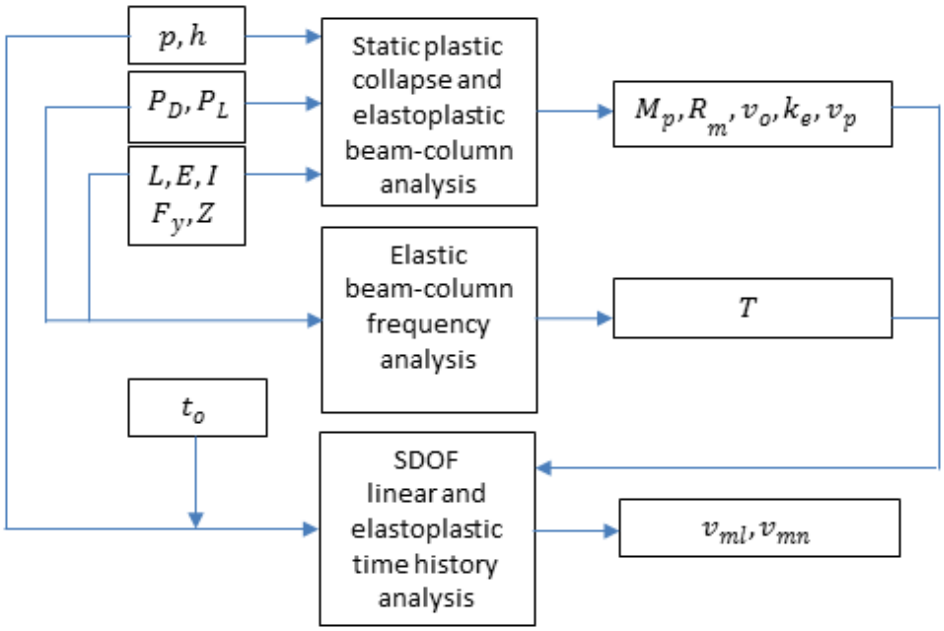

Figure 5.4: Parameter interactions in estimation of maximum response for isolated columns.

The first step has been described in the previous section. Step 2 is formulated using beam-theory by Timoshenko and Gere 1961 [65]. The frequency equation for the fix-fix condition is (Timoshenko and Gere 1961 [65], Chen and Liu 1987 [66]):

$$\Omega - U \sinh M \sin N - \Omega \cosh M \cos N = 0 \tag{5.3}$$

where $M = \sqrt{-U + \sqrt{U^2 + \Omega^2}}$, $N = \sqrt{U + \sqrt{U^2 + \Omega^2}}$, $U = \dfrac{PL^2}{2EI}$, $\Omega = \dfrac{\omega L^2}{\alpha}$ and $\alpha^2 = \dfrac{EI}{m}$. The dependency on P, L, I, and A through $m = \rho \cdot A$ is now apparent through the frequency parameters, M and N.

An approximate solution using the Galef formula (Karnovsky 2001 [71], Bažant and Cedolin 1991 [73]) is used here for simplicity:

$$\Omega = \Omega_0 \sqrt{1 - \frac{P}{P_e}} \tag{5.4}$$

where $\Omega_0 = \Omega(P = 0)$ and $P_e = \dfrac{\pi^2 EA}{S^2}$ = Euler buckling load.

In the absence of axial load, $P = 0$, the column vibrates as a beam whose frequency equation is well known (Karnovsky 2001 [71], Chopra 2011 [74]):

$$\cosh(\beta L)\cos(\beta L) = 1 \tag{5.5}$$

where $\omega^2 = \beta^4\alpha^2$ and $\omega_0 = \left(\frac{3}{2}\right)^2 \cdot \frac{\pi^2}{L^2}\alpha$.

Then,

$$\Omega/\Omega_0 = \omega/\omega_0 = \sqrt{1 - \frac{P}{P_e}} \tag{5.6}$$

where $\omega = 2\pi f = \omega_0\sqrt{1 - \frac{P}{P_e}}$, $f = \frac{3\pi}{4} \cdot \sqrt{\frac{EI}{mL^4}\left(1 - \frac{P}{P_e}\right)}$ and $T = \frac{1}{f}$.

The natural period is now seen to also depend on P, L, I and A (through $m = \rho \cdot A$). Evaluation of the Galef formula for columns in the blast impact region of the 20 story building frame case indicates that, for the fix-fix condition, the effect of the axial load on T is on average about 2 percent and in every case less than 5 percent. For the pin-pin case, the difference may be up to nearly 25 percent. The effect of end conditions on T with or without axial load effects is significant, with the fix-fix case being less than half that for the pin-pin one.

Results for Steps 1 and 2 are independent of any blast scenario. Step 3, however, requires the use of a specific blast time history. For the SDOF analysis, the simplified triangular shape with parameters developed for the 20 story building case are applied to each column in the blast impact region. The variation of the blast peak reflected pressure parameter, p_r, and duration, t_0, for the blast scenario are depicted as contours in Figure 5.5. Each parameter has been normalized to the value at the central column on the first floor. The pressure ratio is seen to decay rapidly to about 10 percent well within the blast impact region, while the duration ratio more than doubles over that distance and is over five times near the edges of the region.

The importance of the duration ratio in terms of the column response lies in the tendency for the impulsive pressure to amplify or de-amplify the response dynamically. Figure 5.6a

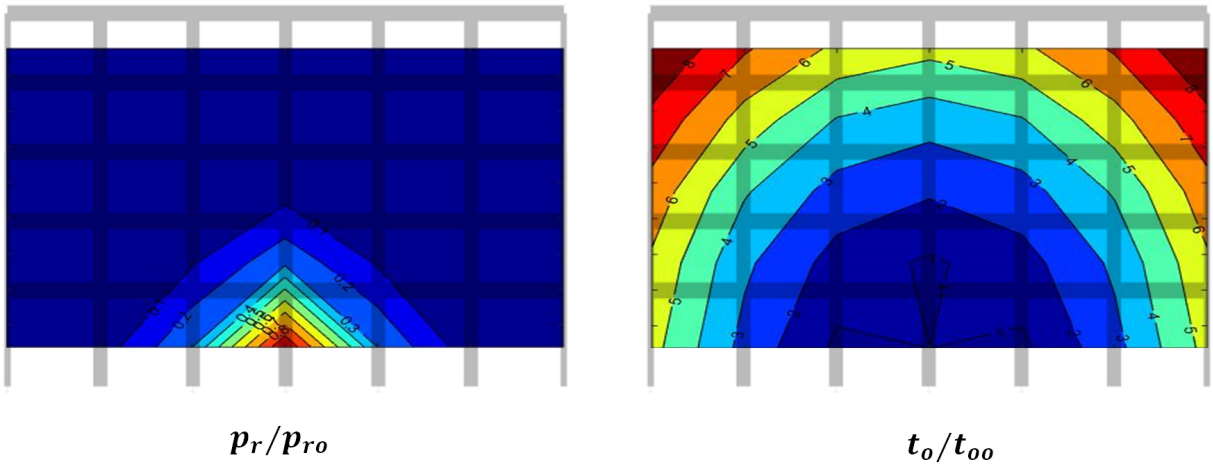

Figure 5.5: Variation of blast pressure time function parameters across impact region.

shows contours of the ratios of the impulse duration to the natural period of the corresponding column in the impact region of the 20 story building case and corresponding blast scenario. The duration ratio ranges from $0.1-0.2$ in the region closest to the blast source to $0.2-0.8$ at points further away. Based on linear SDOF dynamic theory (Biggs 1964 [68], Chopra 2011 [74]), dynamic amplification factors, $DAF = 0.3-1.0$, or de-amplification would occur in the peak dynamic responses in the nearer region and amplification factors , $DAF = 1.0-1.5$, or amplification would be predicted at the edges of the region.

Both linear and nonlinear SDOF time histories have been computed for each column to assess the peak response and damage potential as measured by the ductility, $\mu = v_m/v_p$. Peak ductility ratios are shown in Figure 5.6b and c as estimated from pseudostatic response, $v_0 = R/k_e$, and linear dynamic time history analysis,$v_{ml} = max\,[v_l(t)] \cong (v_0 \cdot DAF)$, respectively. An exact result was derived using the Duhamel integral (Chopra 2011 [74]) for the case of a triangular pulse with variable rise time, and a numerical programming MATLAB routine [70] was written to evaluate the theoretical result, and compute a response time history analysis from which v_{ml} was determined.

The pseudostatic and linear dynamic peak ductility ratios plotted in Figure 5.6 indicate a significant amount of plasticity and damage potential. A more accurate assessment is provided by a nonlinear time history analysis which is performed using a numerical programming

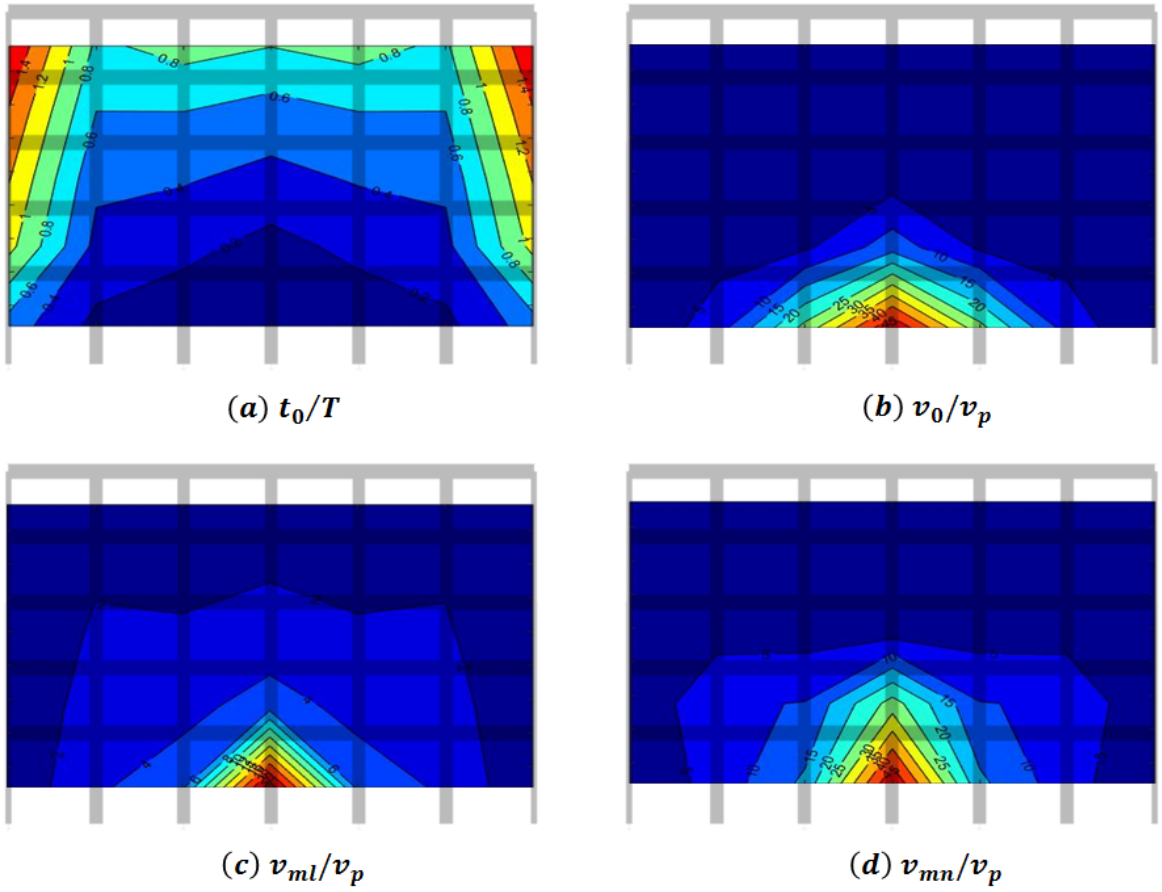

Figure 5.6: Variation of column response characteristics within blast impact region.

MATLAB routine [70] that implements the Newmark method with average acceleration and modified Newton-Raphson iterations (Chopra 2011 [74]).

As Figure 5.4 indicates, the nonlinear spring properties, k_e, are derived from Step 1 and T is derived from Step 2. For a given blast scenario and column location p_r and t_0 are generated and the nonlinear SDOF time history response analysis is performed in Step 3. The resulting dynamic peak ductility ratios are plotted as contours over the impact region in Figure 5.6d. The rapid decay of the ratios is comparable to that of the linear dynamic case, but the ratios themselves are more reflective of the pseudostatic case. At the central first floor column, the ratio exceeds 150 with the surrounding columns experiencing ratios of about 15. The largest value is unattainable and reflects complete loss of load carrying capacity. The surrounding

column values are achievable only with special connection detailing and reflect near loss of capacity and significant redistribution of load transfer in the frame system. In reality, these values overpredict the actual response because of three-dimensional effects that account for the relaxation of the fix-fix conditions due to rotation and translation of the column ends. The latter varies throughout the impact region as the frame system deforms in a complex three-dimensional manner which will be discussed in subsequent sections.

5.4 Results of 3D Finite Element Analysis

Following the initial damage distribution estimate in the primary blast impact region of individual columns, the global progressive collapse vulnerability assessment against the blast scenario will be performed by the 3D finite element analysis of the building.

5.4.1 FE Model Setup

The ability of the general purpose finite element (FE) software, ABAQUS, to capture complex member and system damage modes in high-rise steel moment frame buildings has been demonstrated in recent studies (Gerasimidis et al. 2014 [8], Gerasimidis and Sideri 2016 [11], Gerasimidis 2014 [24], Spyridaki et al. 2013 [25]). A representation of the high-rise building case developed to previously study progressive collapse under gravity loads only is shown in Figure 5.7. Two versions of the same building are examined in this study; Figure 5.7a demonstrates the model which does not include floor slabs as load resisting elements. Rather, the slab influence is restricted to the dead load effect they transfer as uniform loads onto the beams. In addition, Figure 5.7b depicts the full model after the simulation of floor slabs, which now receive the dead and live loads in the form of uniform applied pressure. Only the beams spanning from column to column were simulated, while the secondary beams were neglected.

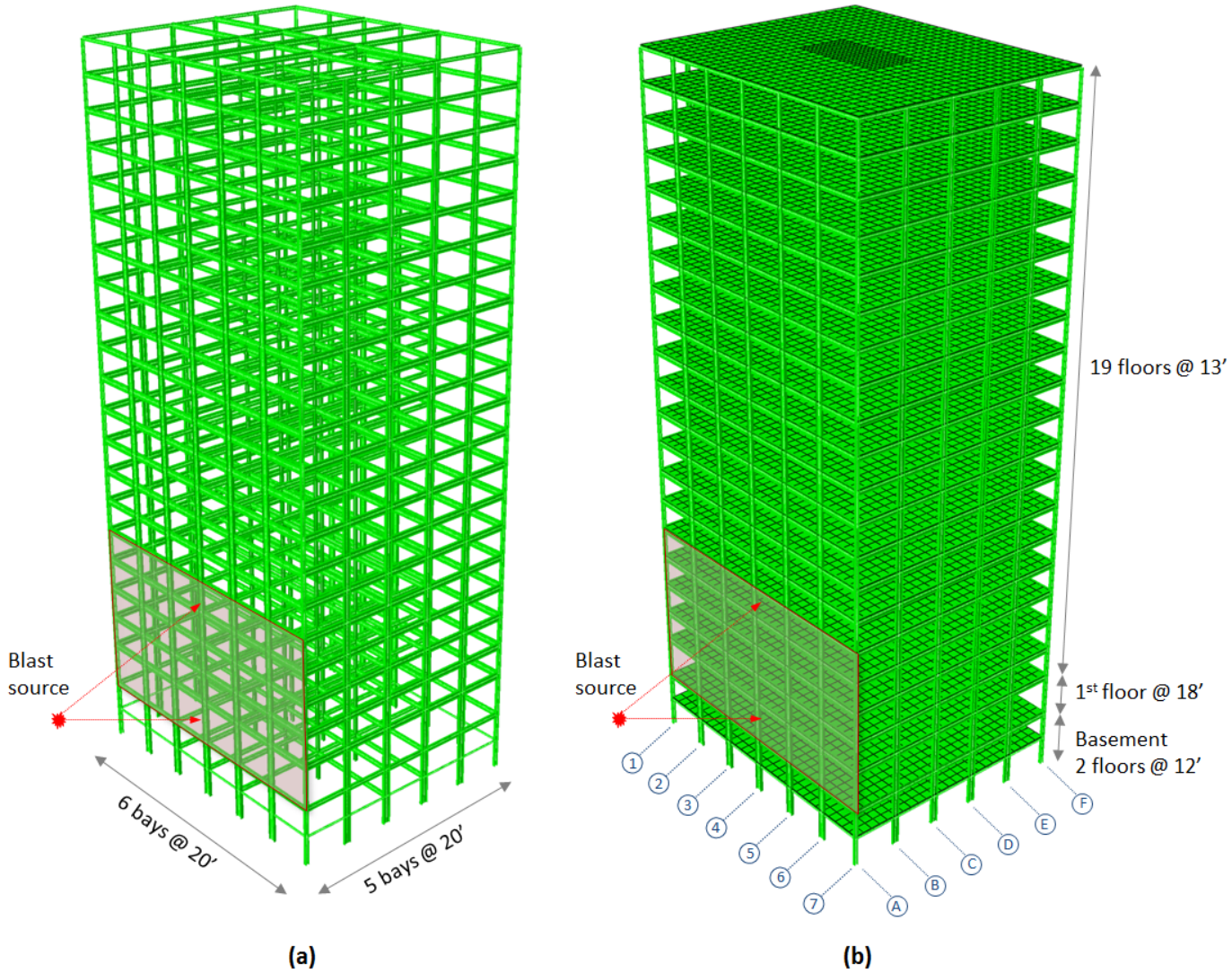

Figure 5.7: Geometry and reference grid of the finite element model of the high-rise 20-story building: (a) no slab simulation model and (b) with slab simulation model. The shaded area indicates the region that will be heavily impacted from the blast source.

The steel-concrete composite slab consisting of $3in$ metal deck and $2.5in$ concrete fill was simulated, for the sake of simplicity, by an equivalent $4.5in$ uniform and homogeneous concrete slab. The elements used for the slab simulation are 4-node shell elements S4R. The contribution of the steel ribbed deck was included by using equivalent steel reinforcement bars embedded in the concrete shell elements, as proposed by the simplified slab modeling approach of Alashker et al. 2011 [21]. This equivalent reinforcement as well as additional steel reinforcement in the slab were modeled as smeared reinforcement layers with a constant

thickness equal to the area of each rebar divided by the reinforcing bar spacing. All beams and columns were simulated with the beam element B32OS offered in ABAQUS library, which can account for the warping rigidity of open-section members under torsional loading. All base nodes and perimeter nodes of the two-level basement are considered pinned. The flexible beam-column connections were simulated by the moment release command of ABAQUS input file usage at the appropriate locations between the moment resisting frames and the gravity frames. The analysis is set to account for both material and geometric nonlinearities which is proven as the only appropriate method to identify the correct collapse mechanisms accounting for loss-of-stability phenomena (Gerasimidis et al. 2014 [8], Gerasimidis 2014 [24], Spyridaki et al. 2013 [25]).

5.4.2 Materials

An elastic-plastic material model in ABAQUS was utilized to describe the nonlinear material characteristics of the A572 Gr. 50 steel of the structural steel components. As mentioned in the building description section, the steel material has yield strength $50ksi$ ($F_y = 345MPa$) and ultimate strength $65ksi$ ($F_u = 450MPa$) at strain $\epsilon_u = 18\%$, with isotropic strain hardening. The material of concrete was modeled by using the CDP (Concrete Damaged Plasticity) model in ABAQUS proposed by Lubliner at al. 1989 [75] and Lee and Fenves 1998 [76] which can effectively describe the plastic behavior of uni-axial compression test. According to this model, the inelastic behavior of concrete is represented by utilizing concepts of isotropic damaged elasticity in combination with isotropic tensile and compressive plasticity. The concrete compressive and tensile strength was assumed $5.4ksi$ ($f_{cu}37.5MPa$) and $0.5ksi$ ($f_{ct} = -3.5MPa$), respectively, with Young's modulus $4350ksi$ ($30GPa$). Parameters of the concrete damaged plasticity model were obtained by Kmiecik and Kaminski 2011 [77]. The stress-strain relation was defined for both the compressive and tensile behavior using the Desay and Krishnan formula and the modified Wang and Hsu formula, respectively, as given in Kmiecik and Kaminski 2011 [77]. After reaching the point of tensile cracking, the

tensile stress-strain relationship softens as the load is transferred to the reinforcement. The stress-strain relationship for both the steel and the concrete material utilized is illustrated in Figure 5.8a and 5.8b, respectively.

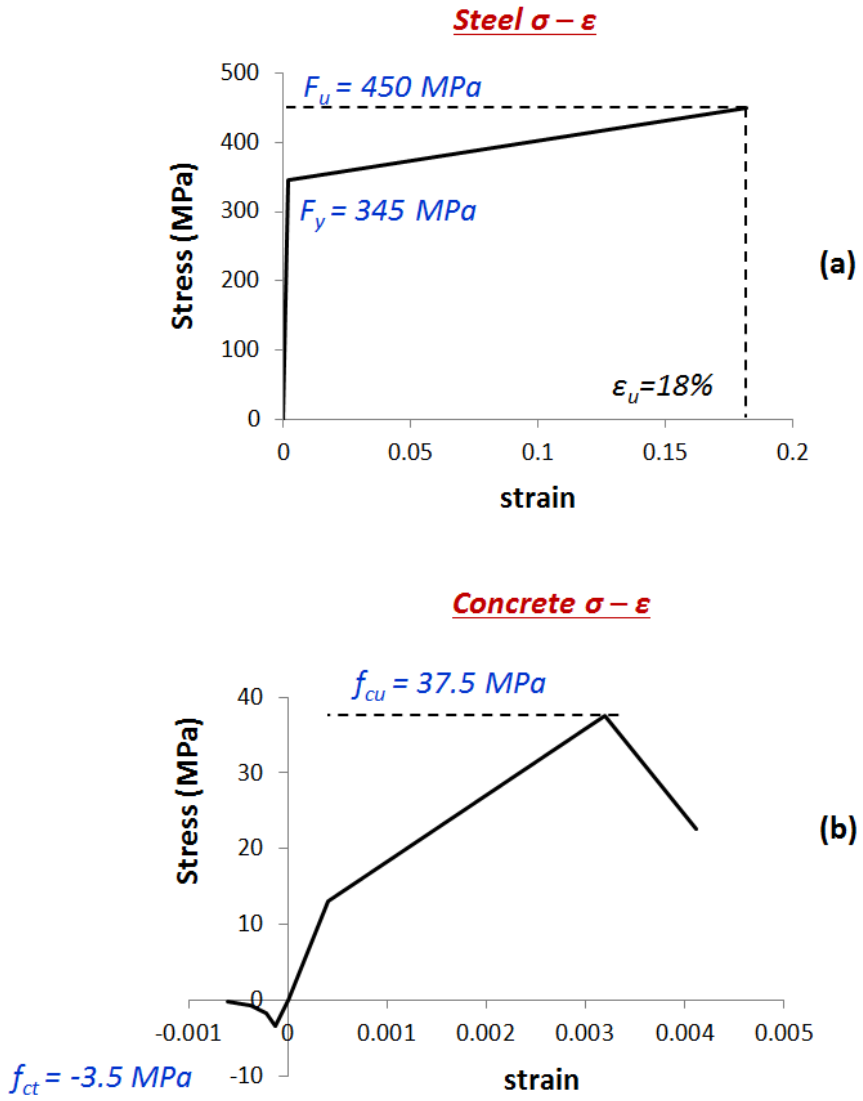

Figure 5.8: Stress-strain relationship for a) steel and b) concrete material utilized.

5.4.3 Blast Loads Application

In the present study, dead and live load cases have been combined with a dynamic blast pressure load case consisting of variable input time functions for reflected pressure at each of the columns significantly impacted by the blast scenario load case. For the building and scenario considered, pressures with potential for causing damage were generated over a region covering the five stories above ground level as indicated by the shaded area in Figure 5.7. The blast pressures applied on floors above the first five were neglected, since their damage potential is considered insignificant (according to Figures 5.5 and 5.6).

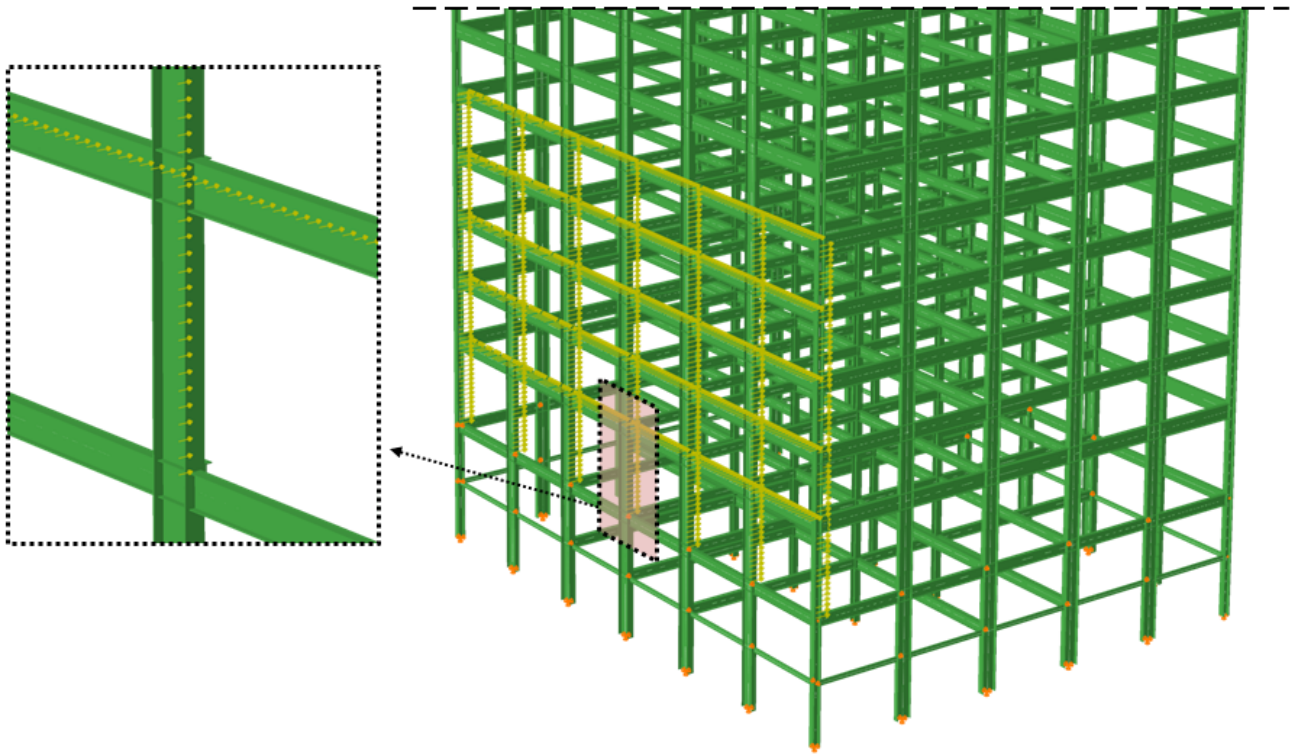

Figure 5.9: Blast load exposure of all columns and beams of first five floors in the weak axis orientation.

For simplicity, the time functions were assumed to be triangular with peak pressure and duration parameters generated using the A.T.-Blast software (Figure 4.2), applied to the mid-column height position and reduced to account for the angle of incidence. The pressure

was assumed to be uniformly distributed over the column face, both width and height. The blast scenario considered exposes the blast pressure to all exterior columns and beams in the weak axis orientation as shown in Figure 5.9. For simplicity, façades and in-fill wall elements are assumed to be destroyed and transfer no load to the frame system. No attempt is made to track damage to interior elements due to the debris flow and vertical and horizontal travel of the blast wave inside the system.

5.4.4 No Slab Simulation

Dead and design live gravity loads were statically applied as uniform line loads on beam members at all floors, equivalent to $4.92kPa$ that corresponds to $1.2DL+0.5LL$. A dynamic response was then computed with the spatially distributed blast load time functions. The blast wave time of arrival was seen to have negligible contributions to the column and overall system responses and thus was not included in the final model. Figure 5.10a depicts the axial force time histories of first floor exterior columns, while Figure 5.10b provides displacement time histories at the nodes of first floor columns where the largest transverse deformations were observed. Zoomed versions of the same plots are also provided in order to illustrate the system's response in more detail during the main blast event (between $1.5-2.5sec$). For reference, horizontal lines show the range of yield displacements of effective nonlinear single-degree-of-freedom (SDOF) systems (Biggs 1964 [68]) corresponding to the first floor columns idealized as beam-columns with ends fixed against both translation and rotation. The important parameters controlling these estimates were described in the section about single degree of freedom column analysis of this paper.

The histories in Figure 5.10 indicate that the floor column responses consist of three phases, roughly delineated by the times: $1.5-1.53sec$, $1.53-1.8sec$, and $1.8-2.5sec$. Phase I occurs during the impulse event during which all the exterior columns of the first floor undergo plastic deformation and their axial forces reach temporary tensile values. In Phase II the highly nonlinear response of the exterior columns becomes apparent (significant loss of

axial load capacity), when finally Phase III shows a clear initiation of a collapse mechanism since all exterior columns deform excessively beyond the safety limits. However, as Figure 5.5 indicates the pressure decays significantly at the corners, in part due to a high angle of incidence, the corner columns are able to respond elastically during all phases.

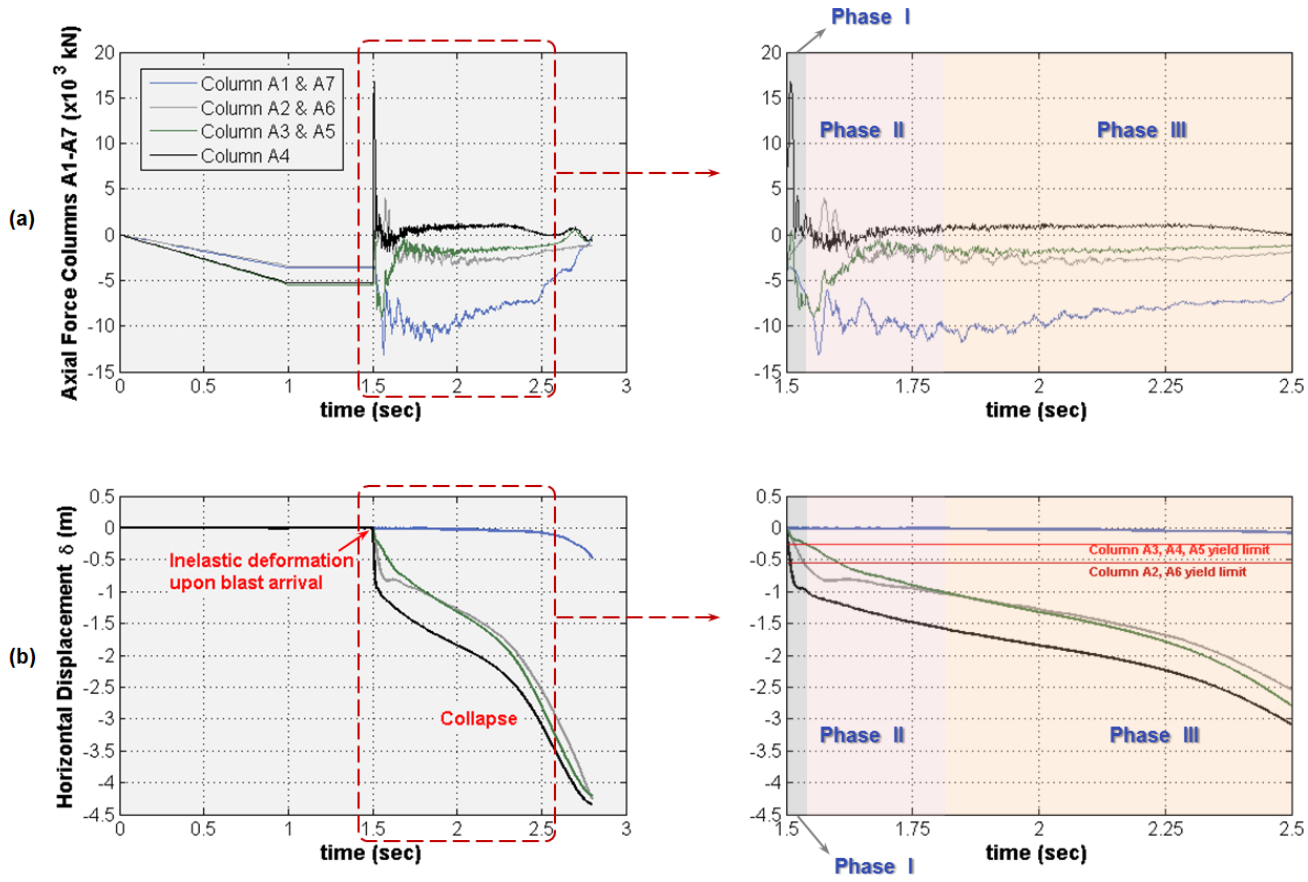

Figure 5.10: High-rise 20-story building, no slab simulation: a) Axial force time history and b) horizontal displacement δ time history of exterior columns A1-A7 (blast arrival is at $t = 1.5sec$)

The system behavior in the latter two phases develops after the direct influence of the blast event on the columns and is captured in snapshots of the frame deformed shapes shown in Figure 5.11. The top figures show the deformed shape through front views, while the bottom figures illustrate the system's behavior through side views. The $t = 1.53sec$ case corresponds roughly to the end of the impulse loading. Most of the deformation is concentrated at the face closest to the blast source. At $t = 1.80sec$, after the impulse loading,

the 3D system deformation begins to become noticeable in interior frames and apparently is leading to amplified bending of the columns in the lower floors. Moreover, since at $t = 1.80sec$ a large portion of the lower floors appears to be exhibiting large deformation, the beginning of a collapse mechanism at the first floor level is apparent. Finally, at $t = 2.50sec$, the lateral deformation begins to be accompanied by vertical collapse of all floors above the first floor. It is therefore evident that the structure cannot survive the dead and live vertical load combination along with the blast threat considered, dictating a progressive collapse vulnerability in terms of final vertical collapse load of $4.92kPa$ ($1.2DL + 0.5LL$ load combination).

The above case corresponds to the response of the frame system without consideration of the floor slab stiffness which is most noticeable in the large relative deformation that is permitted between the corner and adjacent columns, where no beam is present in the N-S direction of the blast (secondary beams of gridlines 2 and 6 in floor plan layout of Figure 5.1 are not included in the 3D model). In addition the mass of the floor slabs is accounted for only in the vertical dead load and thus axial forces in the columns. In the dynamic solution the mass generates inertial forces contributing to the force balance calculation and thus inter-story displacement and associated bending in the columns. It is thus considered critical to perform the same analysis of the system including the slab in order to compare the different building responses.

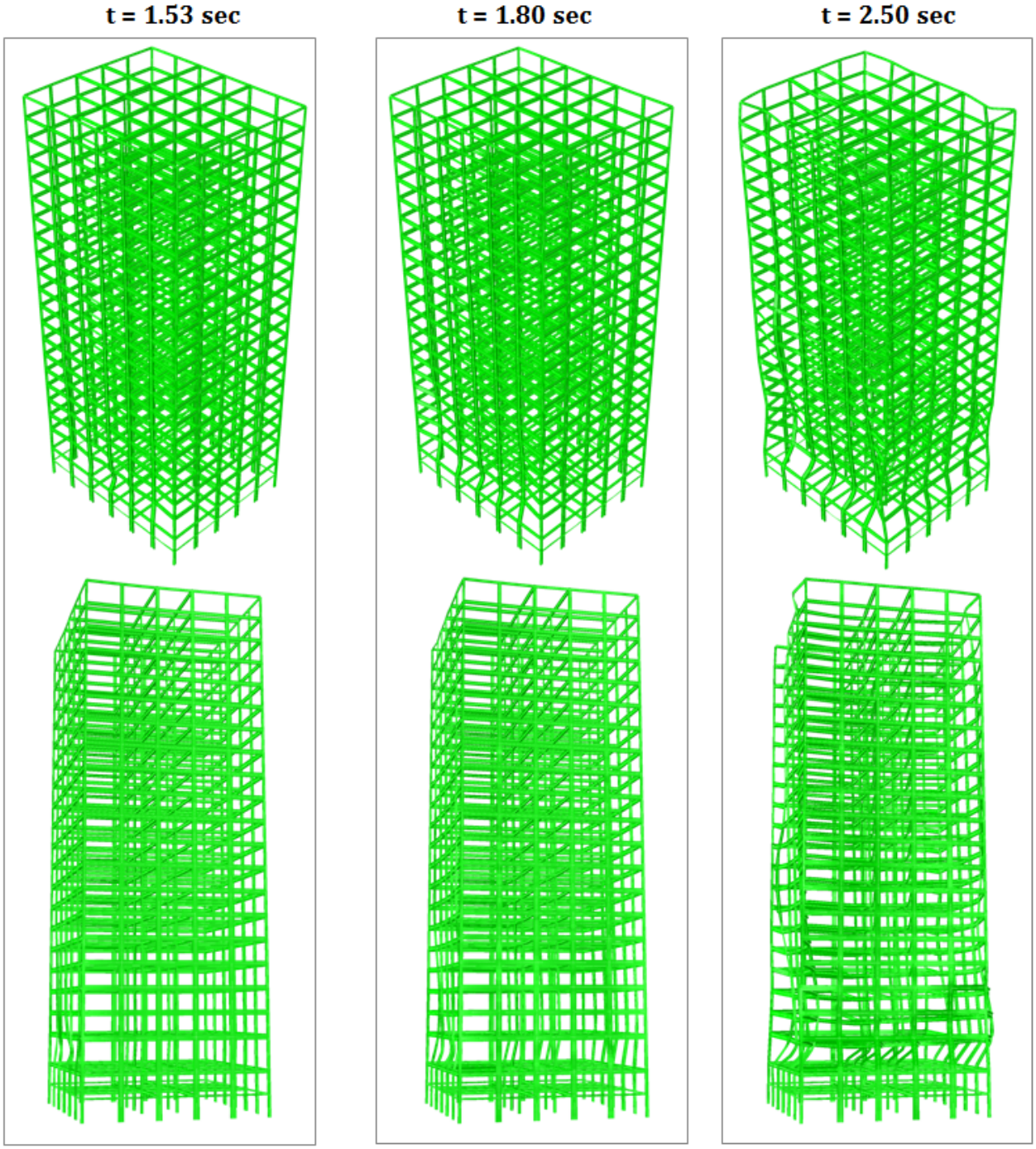

Figure 5.11: High-rise 20-story building, no slab simulation: Deformed shape at $t = 1.53sec$, $t = 1.80sec$ and $t = 2.5sec$, both front and side views (blast arrival is at $t = 1.5sec$).

5.4.5 With Slab Simulation

The same high-rise 20-story building was further examined to study the effect of the slab in the response. After the static application of the dead and live gravity loads combination (Steps I and II), the building is subjected to the blast-induced damage distribution scenario (Step III). Figure 5.12a illustrates the deformed shape of the structure right after the blast detonation ($t = 1.55sec$) where excessive deformation of columns directly affected by the blast is evident. The deformation contours are maximized around the lower floors of the building where the blast loads are clearly larger due to the shorter stand-off distance and the reduced angle of incidence. Horizontal displacements at column midspan along with the respective axial forces of first floor columns A2-A6 are plotted in Figure 5.12b and Figure 5.12c. All axial forces are linearly increased during Step I and maintain a constant value during Step II, while horizontal displacements are zero. During the first milliseconds of the blast event of Step III, a major disturbance is terms of axial force is clearly observed that drives the columns into a short-term tensile state. As the analysis progresses, the behavior of the first floor column A4 evidently indicates structural failure since the axial force drops to negligible values accompanied by excessive horizontal displacements of more than $1m$ (this column failure can be considered equivalent to a column removal scenario of typical progressive collapse analysis suggested in DoD 2009 [1] and GSA 2003 [2]). However, the initiation of a global progressive collapse mechanism is avoided; the available load redistribution mechanism within the structural system is able to arrest the blast disturbance. More specifically, the slab action is able to safely redistribute loads to the interior gravity columns after the extensive damage of exterior first floor columns, without further propagation of failure. Therefore the system eventually survives the threat until the end of dynamic Step III.

Subsequently, additional load is applied statically in order to determine the final collapse load of the building. During static Step IV, the building collapses due to the inelastic buckling

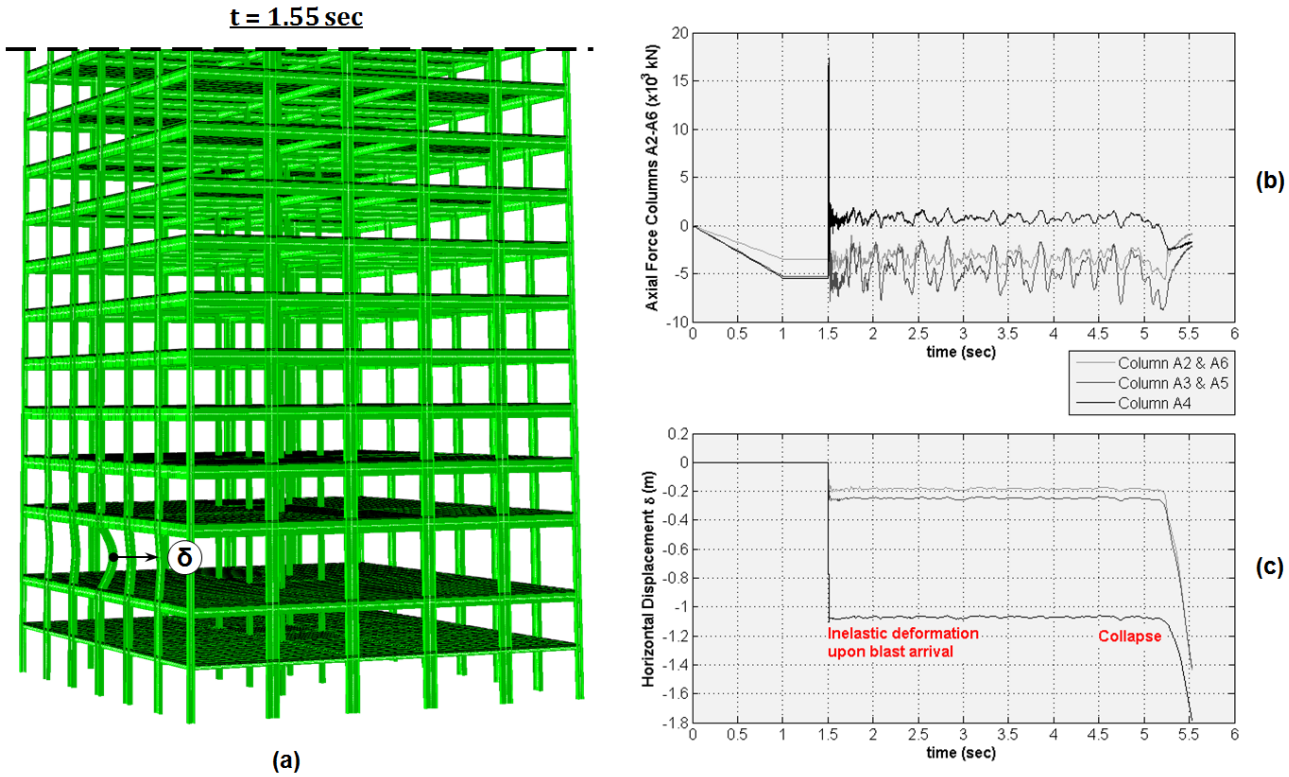

Figure 5.12: High-rise 20-story building, with slab simulation: a) Deformed shape at $t = 1.55sec$, b) axial forces time history and c) horizontal displacements δ time history at midspan of exterior columns along gridline A (blast arrival is at $t = 1.5sec$ and vertical push-down starts at $t = 5sec$).

failure of all basement level interior gravity columns along gridline C (Figure 5.13a). The axial force and displacement time history of interior gravity column C3 is indicatively plotted in Figure 5.13b and Figure 5.13c, respectively, where the inelastic column yield capacity Af_y (A is the cross sectional area and f_y is the material yield stress) is reached at $t = 5.18sec$ and at the same time there is a rapid increase of lateral displacement (snap-through). After this point the analysis is diverging with error messages of negative eigenvalues of the stiffness matrix, another characteristic signature of loss-of-stability failure mechanism along with the exhaustion of the axial load capacity. The additional load until collapse of Step IV is calculated at $t = 5.18sec$ as $6.03kPa$. The final collapse load is the summation of the initial load of $6.72kPa$ ($1.2DL + 0.5LL$ load combination) plus the additional load of $6.03kPa$, meaning $12.75kPa$ in total or $1.9(1.2DL+0.5LL)$. In other words, the vertical load capacity

of the building is $1.9(1.2DL + 0.5LL)$ which constitutes its progressive collapse vulnerability when exposed to the specific blast scenario investigated in this study. It is also noteworthy to comment on the role of interior gravity columns in the progressive collapse mechanism of the structure, since their inelastic buckling capacity define the final collapse load and collapse mode of the entire system. Further discussion on the importance of interior gravity columns will be presented in the following Chapter 6.

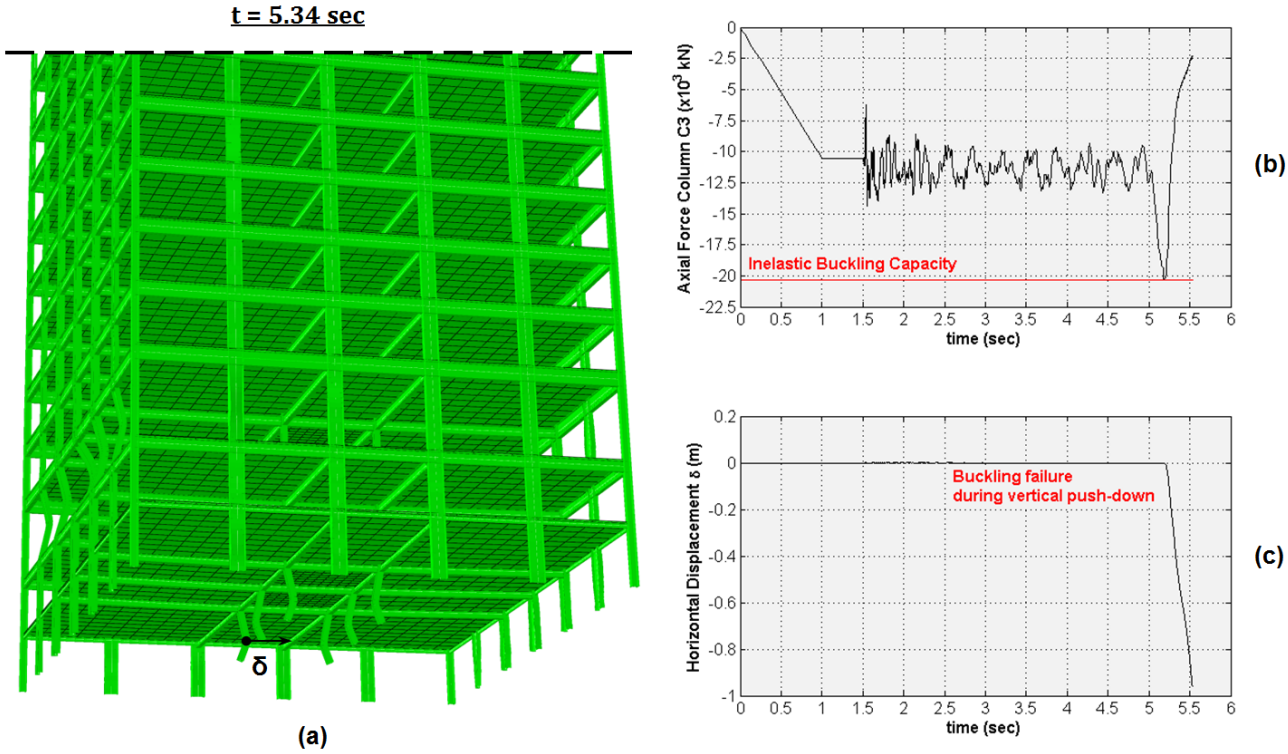

Figure 5.13: High-rise 20-story building, with slab simulation: a) Deformed shape at $t = 5.34sec$, b) axial forces time history and c) horizontal displacements δ time history at midspan of interior columns along gridline C3 (blast arrival is at $t = 1.5sec$ and vertical push-down starts at $t = 5sec$).

5.5 Comparison of 3D Response with SDOF Nonlinear Analytical Results

Figure 5.14 illustrates the displacement time histories of the first floor columns after the initiation of the blast event, as computed by both the dynamic nonlinear 3D simulation including the slab and the dynamic nonlinear individual SDOF column analyses. The comparison indicates similarities mostly regarding to columns mildly affected by the blast event (column A1), while for the columns that were most severely damaged the discrepancies between the 3D and SDOF curves are more significant. This can be attributed to the fact that the 3D system responds globally and thus the column response is more realistic; the columns are not restricted to deform only individually but also as an integrated part of the global system. Conversely, the SDOF curves have been obtained by having idealized boundary conditions on both ends of the columns. The largest discrepancy between the 3D and SDOF curves is observed for column A4 which has experienced the largest lateral load due to the blast event, surprisingly leading to SDOF deformations about six times larger than those of the 3D curve. The aforementioned comparisons highlight the level of approximation introduced by the SDOF idealizations and provide insights on the structural behavior dependencies of individual elements within the global structural system. Although an initial estimate of the blast-induced damage distribution on individual elements is useful, the final structural response is dictated by the 3D model's behavior.

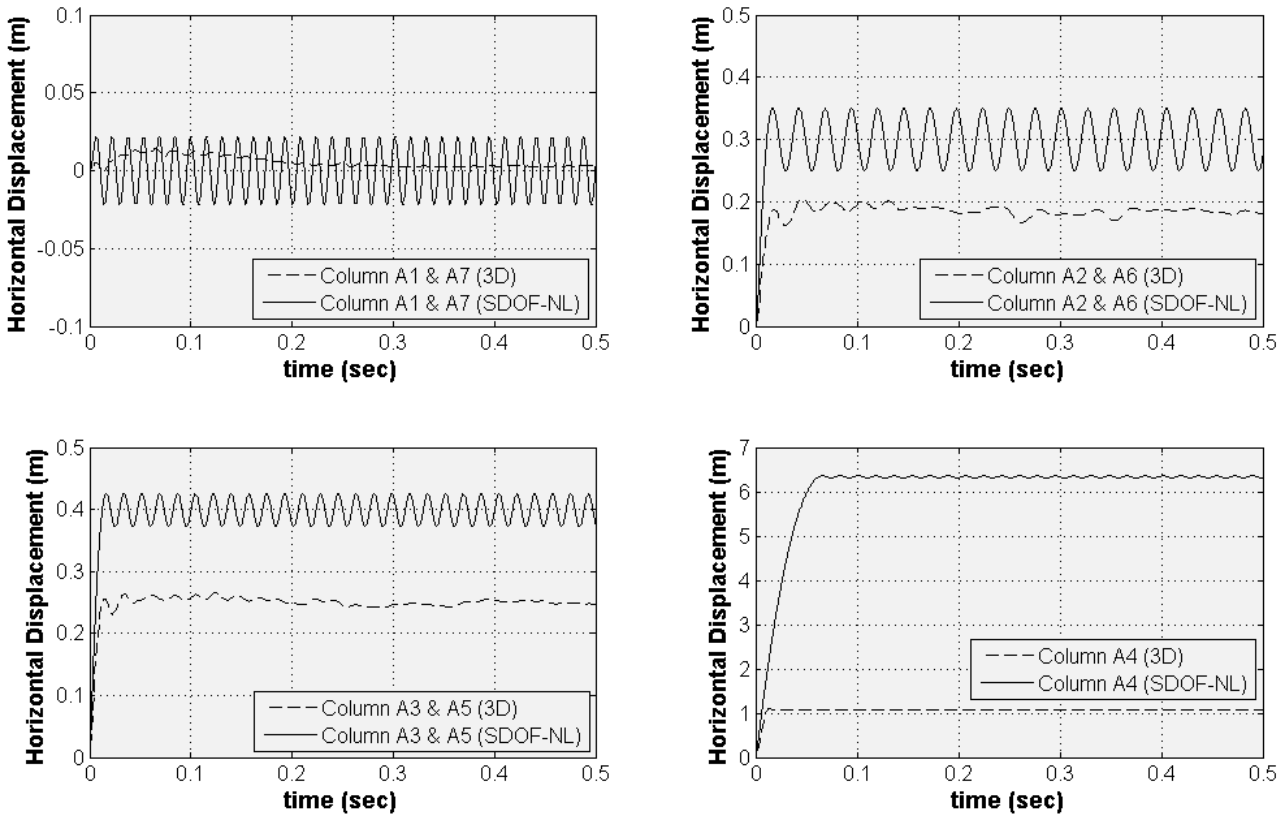

Figure 5.14: Displacement time histories of the first floor columns after the initiation of the blast event; comparison between the individual SDOF column responses and the 3D 20-story building model including the slab simulation.

5.6 Concluding Remarks

This chapter investigates the effect of damage distribution to the progressive collapse potential of a high-rise 20-story steel building when subjected to an external blast detonation scenario. Results from the numerical simulations and insights from damage propagation indicate the following conclusions.

- Identification of the parameters that affect the spatially distributed pressure and response quantities, as well as their interdependencies, is established. Comparisons between the nonlinear SDOF damage results and the 3D 20-story building model including the slab simulation indicate that the individual column responses can be most

accurately predicted for the columns only mildly affected by the blast event. However, the columns in the heavily impacted blast region experience a much more severe level of damage when simulated in a 3D global system configuration; the discrepancies between the SDOF and 3D damage results are mainly attributed to the idealized end condition assumption of the individual column analyses.

- The 3D nonlinear dynamic analysis of the high-rise 20-story building subjected to external blast *without* slab modeling shows the initiation of a progressive collapse mechanism due to the highly nonlinear response and excessive deformation of exterior columns. However, the same building model *including* the slab simulation has a radically different behavior; the slab contribution in the load redistribution mechanism leads to the overall system's stabilization and thus progressive collapse is avoided. Therefore, simulation of the slab is of utmost importance for the correct evaluation of progressive collapse vulnerability.

- The progressive collapse mechanisms of the building establish the role of interior gravity columns in the assessment of resistance against progressive collapse. Identification of these members as the weakest links of the structural system is made, since their loss-of-stability failure defines the collapse mechanism and collapse load of the building. As discussed in the analysis results section, after flexural failure of exterior columns due to lateral blast loading, load redistribution causes increase in axial forces of interior gravity columns until they reach their inelastic buckling capacity. This loss-of-stability collapse mechanism can only be detected in 3D nonlinear dynamic analysis configurations that take into account both material and geometric nonlinearities, performed by powerful finite element computational tools.

Chapter 6

Progressive Collapse Vulnerability of Steel Buildings under Blast Loading - Numerical Application #2

6.1 Introduction

Chapter 6 presents a second numerical application of the methodology developed in Chapter 4, which includes detailed 3D nonlinear finite element dynamic analyses of mid-rise steel frame buildings in order to examine the spatially distributed response and damage to frame members along the building exterior facing an external blast, by employing the methodologies developed in Chapter 4. Two typical mid-rise (10-story) office steel buildings with identical floor plan layout but different lateral load resisting systems are examined; one including perimeter moment resisting frames (MRFs) and one including interior reinforced concrete (RC) rigid core. It is shown that MRFs offer a substantial increase in robustness against blast events, and the role of interior gravity columns identified as the 'weakest links' of the structural framing is discussed.

6.2 Building Description/Finite element model

Additional progressive collapse vulnerability analysis was performed for the case of two 10-story office buildings designed according to U.S. building codes for combinations of dead, live, earthquake and wind loads in Chicago, USA. The design of the buildings was conducted by Agarwal and Varma 2014 [56] for two identical plan layouts but different lateral load resisting systems. Figure 6.1a depicts the plan views of the first building that uses perimeter MRFs to resist lateral loads and pin-connected gravity frames to resist vertical loads, while Figure 6.1b shows the second building which uses an interior RC rigid core for lateral loads and gravity frames for vertical loads. Geometry, gridlines, column orientations, location of the pinned and fixed beam-to-column connections as well as the location of the RC rigid wall for the second building are also illustrated in the same figure. The bay width is $25ft.$ $(7.62m)$ and the story height is $12ft.$ $(3.66m)$. The nominal design vertical loads are $65psf$ (3.1kPa) for dead loads and $50psf$ $(2.4kPa)$ for live loads. The material for all structural steel components is A992 steel with yield strength $50ksi$ $(345MPa)$ and ultimate strength $65ksi$ $(450MPa)$ with isotropic strain hardening. Detailed member design and section assignment for both buildings can be found in Agarwal and Varma 2014 [56].

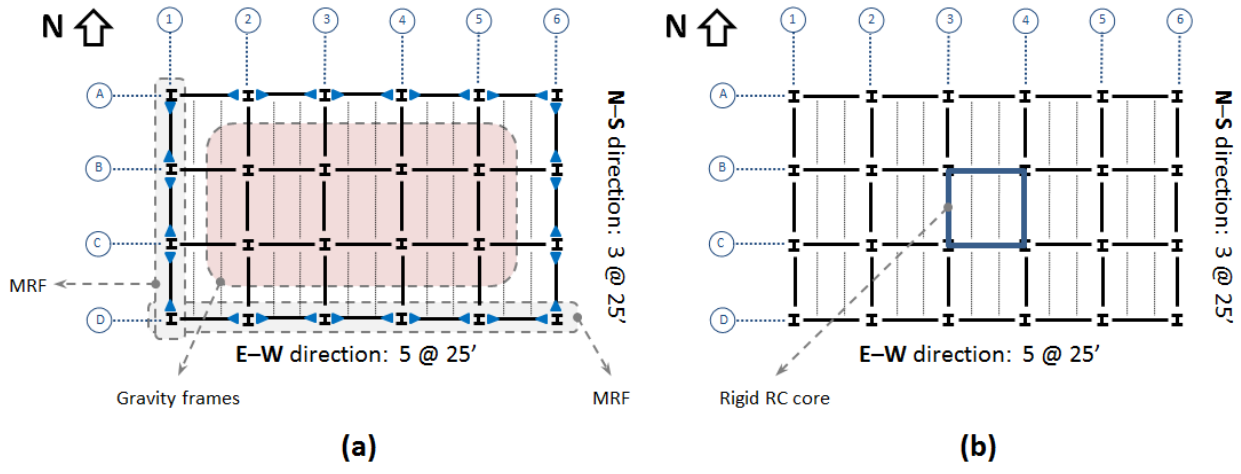

Figure 6.1: Plan view of 10-story office building with (a) perimeter moment resisting frames and (b) interior RC rigid core. Locations of fixed beam-column connections are denoted by blue triangles.

The composite slab consists of $2.5in$ $(0.065m)$ thick light weight concrete on $3in$ $(0.075m)$ deep ribbed deck that spans between two secondary beams. According to the design, no additional reinforcement was required to carry the design loads. The modeling of the slab was simplified to an equivalent uniform and homogeneous concrete slab, where the contribution of the steel ribbed deck was simulated by equivalent steel reinforcement bars. Cracking and crushing of concrete was accounted for by using the same Concrete Damaged Plasticity model as described for the case of the 20-story building. Compressive strength was assumed $5.4ksi$ $(37.5MPa)$ with Young's modulus $4350ksi$ $(30GPa)$, while tensile strength was assumed $0.5ksi$ $(3.5MPa)$. The stress-strain relationship for both the steel and the concrete material utilized is illustrated in Figure 5.8a and 5.8b, respectively, as was the case for the 20-story building described in Chapter5. The elements used for the ABAQUS finite element model were B32OS beam elements for beams and columns and S4R shell elements for the slab. The interior RC rigid core was modeled simplistically by restraining the two horizontal directions of the neighboring nodes to simulate the rigidity and the very high lateral stiffness of the rigid core, as described in Agarwal and Varma 2014 [56]. Moment releases were utilized at appropriate locations between the moment resisting frames and the gravity frames. Column design dictates that all base nodes are pinned.

The method of blast load application is similar to the 20-story building case. The same blast scenario of a surface blast consistent with a truck or van parked on the street adjacent to the building was analyzed as a reasonable threat. The blast source exposes the highlighted region (Figure 6.2) of the first five floors to uniformly distributed pressures along the beam length and column height in the weak axis orientation. Blast loads were computed in a similar manner as the 20-story building case by utilizing the ATBLAST software to account for variable stand-off distances and angles of incidence for each member.

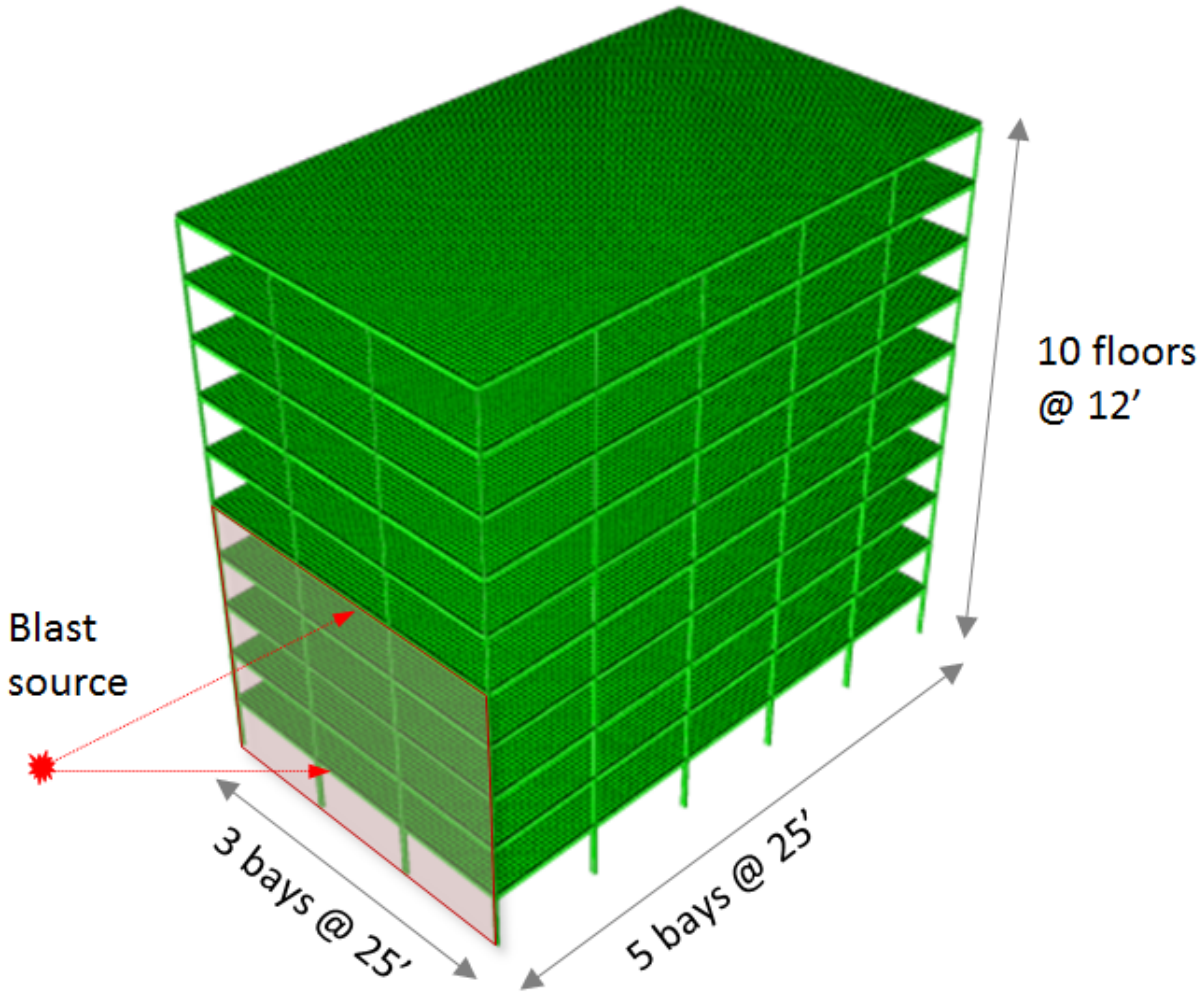

Figure 6.2: Geometry of the finite element model of the mid-rise 10-story building. The shaded area indicates the region that will be heavily impacted from the blast source.

6.3 Results of 3D Finite Element Analysis

6.3.1 10-story Building with Perimeter Moment Resisting Frames

Progressive collapse analysis under blast loading was firstly performed for the 10-story building with perimeter MRFs in order to evaluate its progressive collapse vulnerability. The same dead and live load combination $1.2DL + 0.5LL$ is applied as uniform pressure load on the slabs of each floor during Steps I and II. Figure 6.3a illustrates the deformed shape of the structure shortly after it experiences the blast-induced damage of Step III. Similarly with

the behavior of the 20-story building with perimeter MRFs including the slab simulation, larger deformation is observed at the first floor exterior columns especially along the gridlines B1 and C1. The axial load time histories of the same columns (Figure 6.3b) demonstrate a short-term tensile state but shortly after the impact event they stabilize to fairly the same values. The horizontal displacement time histories shown in Figure 6.3c indicate a large inelastic horizontal deformation (approximately $12cm$) that becomes residual until the end of Step III. However, despite the damage of columns B1 and C1 the system avoids the initiation of progressive collapse due to the same reasons as the 20-story building; firstly, exterior columns are strong enough to resist failure from blast loads and secondly, the available load redistribution mechanism via the slab action is capable of stabilizing the entire structure.

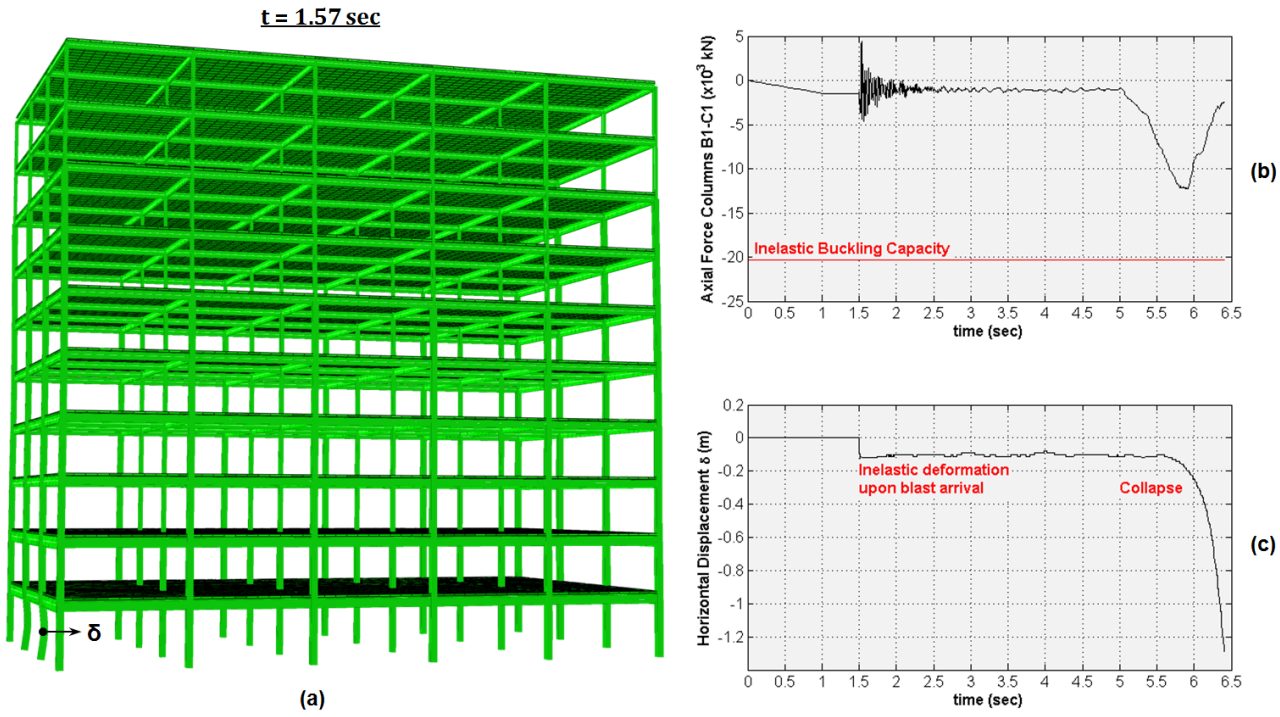

Figure 6.3: Mid-rise 10-story building with perimeter moment resisting frames: a) Deformed shape at $t = 1.57sec$, b) axial forces time history and c) horizontal displacements δ time history at midspan of exterior columns B1 and C1 (blast arrival is at $t = 1.5sec$ and vertical push-down starts at $t = 5sec$).

Additional vertical load during Step IV is needed for the evaluation of progressive collapse vulnerability (vertical push-down analysis). As previously observed, the final collapse mechanism is initiated due to inelastic buckling of interior gravity columns shown by the exhaustion of inelastic column yield capacity Af_y (Figure 6.4b) that causes sudden increase in horizontal displacement at $t = 5.29sec$ (Figure 6.4c), beyond which the analysis is showing warning signs of instability. Propagation of damage to the rest of the interior gravity columns that experience inelastic buckling consecutively is portrayed in Figure 6.4a. The final collapse load is the summation of the design vertical load of $4.92kPa$ ($1.2DL + 0.5LL$ load combination) plus the additional load of $7.13kPa$, meaning $12.05kPa$ in total or $2.45(1.2DL+0.5LL)$, which expresses the progressive collapse vulnerability of the building when exposed to the blast threat examined herein.

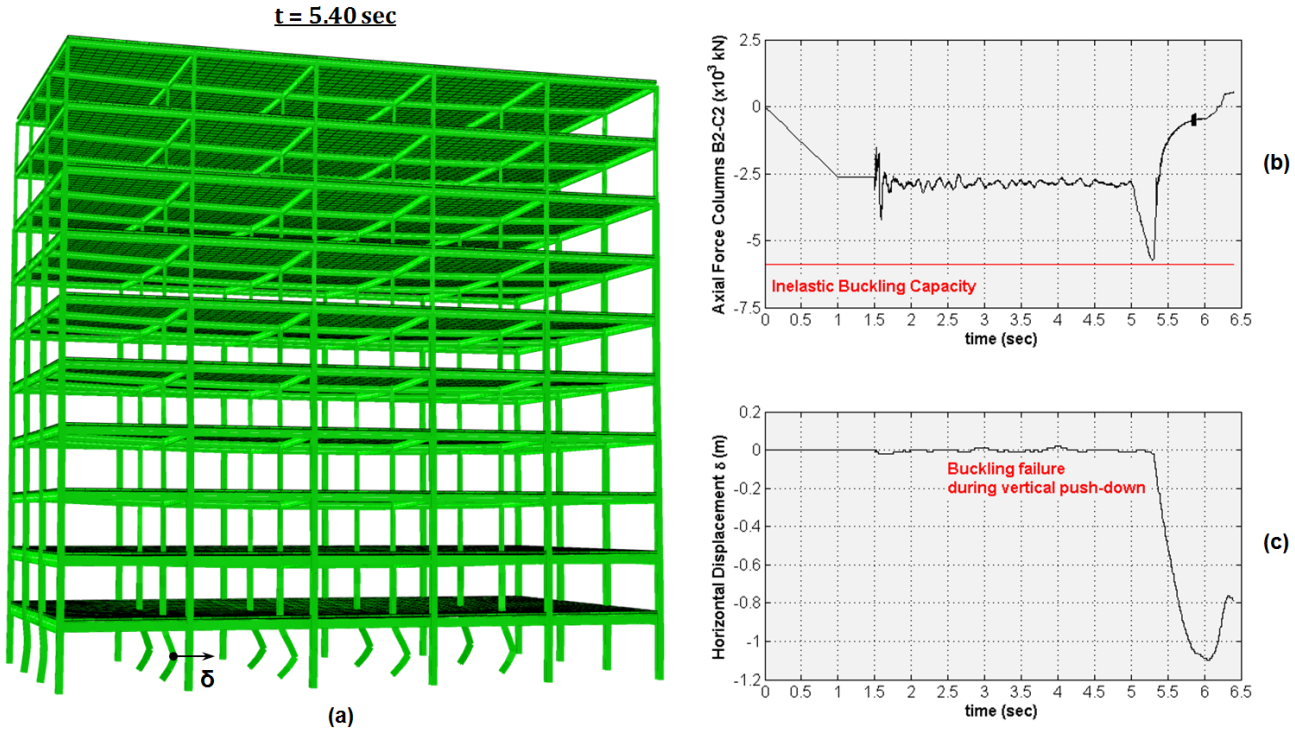

Figure 6.4: Mid-rise 10-story building with perimeter moment resisting frames: a) Deformed shape at $t = 5.40sec$, b) axial forces time history and c) horizontal displacements δ time history at midspan of interior gravity columns B2 and C2 (blast arrival is at $t = 1.5sec$ and vertical push-down starts at $t = 5sec$).

The results from both analyses of buildings with perimeter moment resisting frames (high-rise 20-story and mid-rise 10-story building) establish the role of the interior gravity columns in the progressive collapse mechanism; the overall stability of the structural system is directly dependent on the inelastic buckling capacity of interior gravity columns even if an external blast scenario causes extensive damage and failure to exterior columns. Therefore, a noteworthy conclusion derived from the aforementioned analyses is that the design of exterior columns to provide lateral stiffness against earthquake and wind loads not only renders the building robust enough to survive a major blast threat but also reveals that the interior gravity columns are the weakest link of the structural system; these columns are susceptible to inelastic buckling and are next in line to fail, defining the loss-of-stability collapse mode of the global system.

6.3.2 10-story Building with Interior Core of RC Shear Walls

The same blast scenario and progressive collapse analysis was performed for the 10-story building case with interior core of RC shear walls. The behavior of the building is radically different than the one with perimeter MRFs, due to the different exterior beam and column section design. Since the interior RC core is designed to provide lateral stiffness, all exterior beams and columns are designed to carry only gravity loads and are therefore assigned smaller sections. Nevertheless, the same steel sections for interior gravity columns and beams are used in both 10-story building configurations.

The deformed shape of the building with interior core of RC shear walls is displayed in Figure 6.5 at four different stages in respective times of dynamic Step III (at $t = 1.53sec$, $t = 1.80sec$, $t = 2.5sec$, $t = 3.0sec$). Upon blast arrival at $t = 1.5sec$ all first floor exterior columns fail completely and a global collapse initiation is eminent. Large exterior column deformation is exhibited at early stages of the blast event and due to the loss of those columns, large vertical displacement of the slabs is also unavoidable. Gravity load redistribution to the interior gravity columns (gridline 2) through the floor slab leads to excessive axial loading

of those columns as well, until they reach their inelastic column yield capacity Af_y and fail due to inelastic buckling at $t = 1.75sec$. Propagation of failure to the rest of the interior gravity columns (gridline 3) is depicted at the later stages of the analysis.

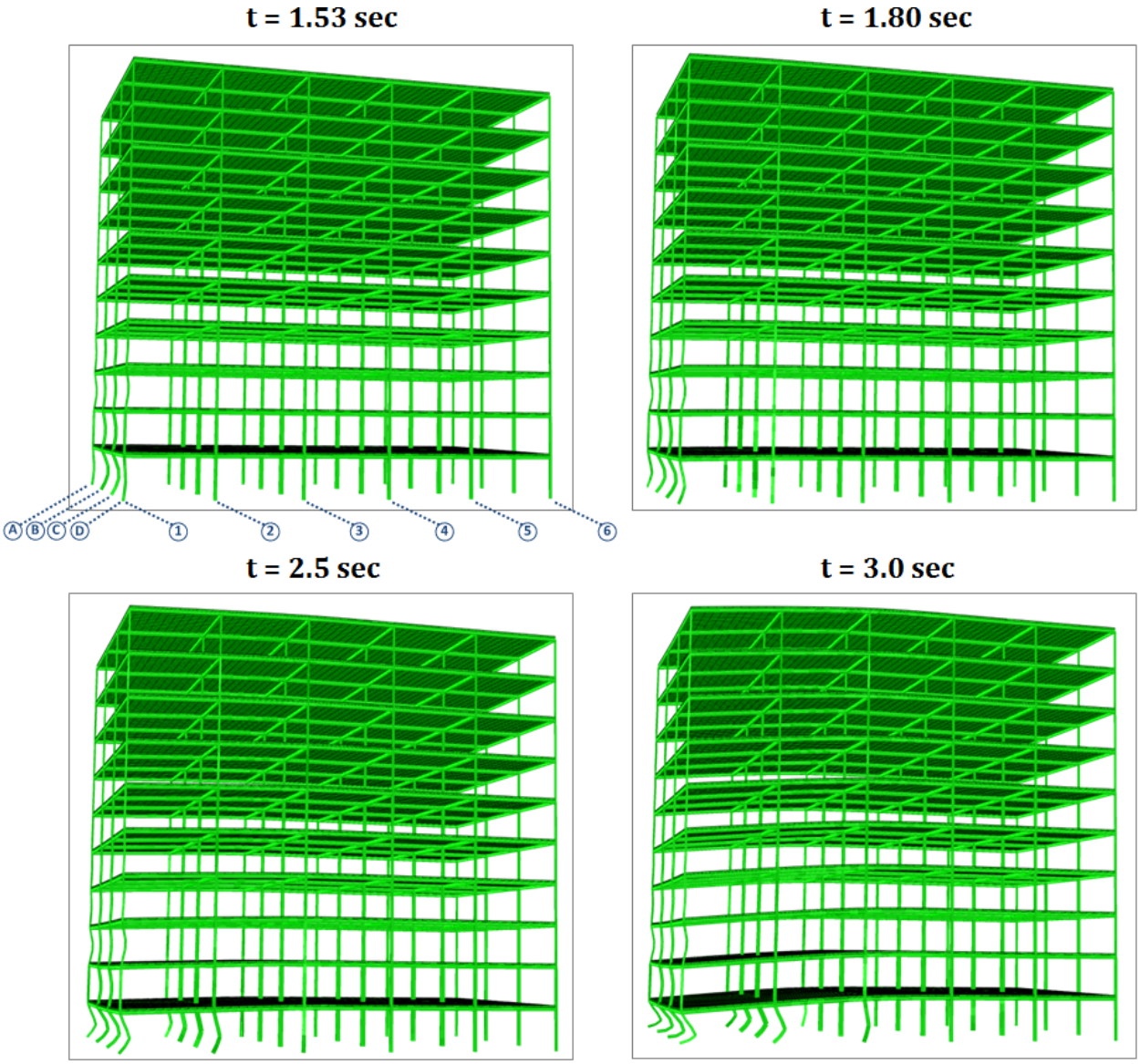

Figure 6.5: Mid-rise building with interior RC rigid core: Damage propagation and progressive collapse initiation at four stages of dynamic Step III ($t = 1.5sec$ denotes blast arrival).

Figures 6.6 and 6.7 illustrate the axial force and horizontal displacement time histories at midspan of all first floor exterior columns and interior gravity columns of gridline 2, respectively. While it is obvious that exterior columns immediately lose their capacity to

bear axial loads at $t = 1.5sec$, the buckling failure of interior gravity columns occurs after the analysis progresses some milliseconds more (at $t = 1.75sec$ for columns B2-C2, while at $t = 2.2sec$ for columns A2-D2) and thereafter their axial capacity drops dramatically as well, with the simultaneous large increase in horizontal displacement (snapping behavior - characteristic indicator of loss of stability). Therefore, unlike the building with perimeter MRFs, even under service level gravity loads ($1.2DL + 0.5LL$) this structure cannot survive the damage induced by the blast scenario considered herein (there is no need to perform Step IV).

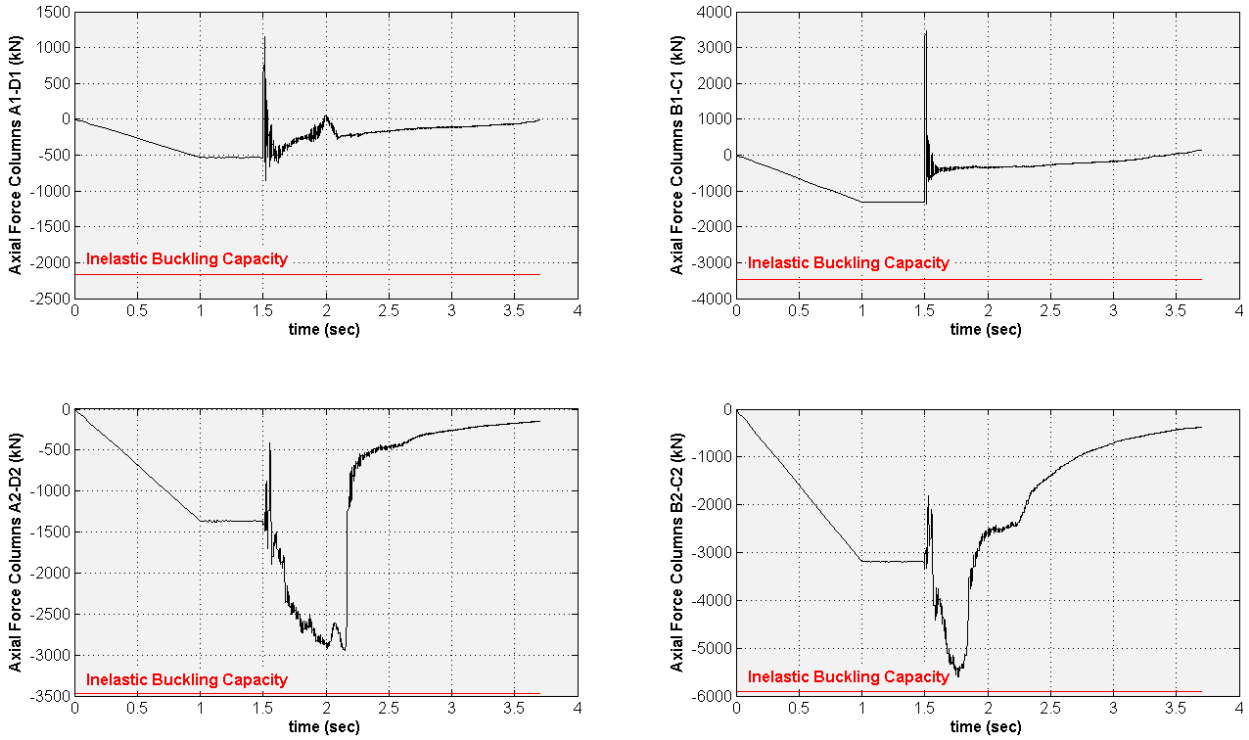

Figure 6.6: Mid-rise 10-story building with interior RC rigid core: Axial forces and respective inelastic buckling capacities (Af_y) of exterior columns (gridline 1) and interior gravity columns (gridline 2), with respect to time (blast arrival is at $t = 1:5sec$).

In conclusion, the absence of perimeter MRFs increases the vulnerability of the 10-story building to progressive collapse, since smaller perimeter columns and beams are unable to stabilize the overall structural behavior and prevent collapse. Although current results are limited to the specific building examples analyzed, similar behavior of both buildings

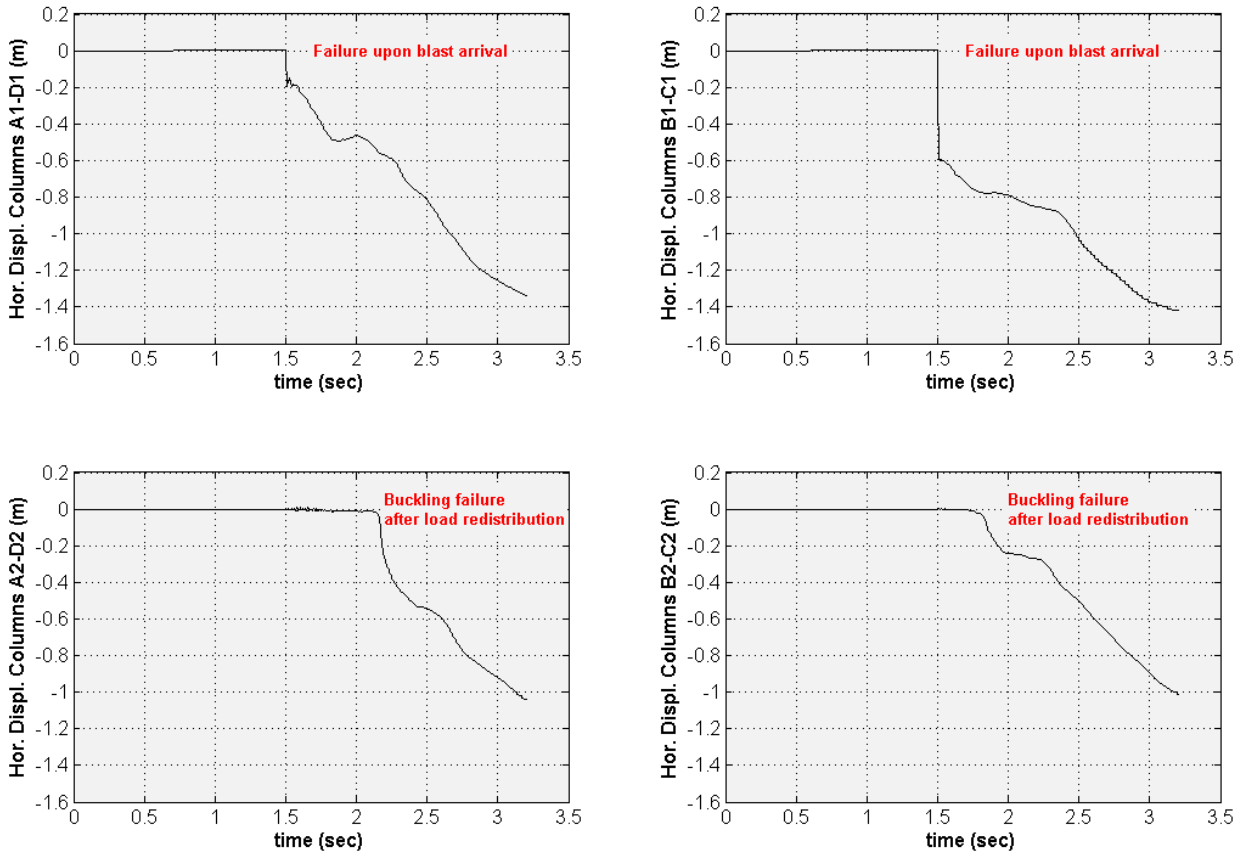

Figure 6.7: Mid-rise 10-story building with interior RC rigid core: Horizontal displacements at midspan of exterior columns (gridline 1) and interior gravity columns (gridline 2), with respect to time (blast arrival is at $t = 1.5sec$).

with perimeter MRFs (high-rise 20-story and mid-rise 10-story building) that survive the blast threat examined in comparison to progressive collapse initiation of the building with an interior rigid core are a strong indicator of the importance of structural design against lateral loads in the robustness of structures subjected to blast attacks.

Moreover, it is noteworthy to conclude that interior gravity columns play again a key role in the assessment of resistance against progressive collapse, since they are found prone to inelastic buckling failure in all cases considered. Identifying a loss-of-stability-collapse mechanism of interior gravity columns in 3D building configurations has not yet attracted enough attention from the research community. Although most researchers in the field of progressive collapse have focused on yielding-type failures triggered by the plastification of beams in the vicinity of an abnormal event (above a column removal, i.e. Alternate

Path Method), it is within the authors' belief that such brittle collapse modes are more critical and should be carefully addressed for the correct assessment of progressive collapse vulnerability of structures (Gerasimidis et al. 2014 [8], Gerasimidis 2014 [24] and Spyridaki et al. 2013 [25]).

6.4 Concluding Remarks

This chapter investigates the effect of damage distribution to the progressive collapse potential of two mid-rise 10-story steel buildings when subjected to an external blast detonation scenario. Results from the numerical simulations and insights from damage propagation indicate the following conclusions.

- Comparison between the analyses results of the two 10-story mid-rise buildings (one with perimeter MRFs and and one with interior RC rigid core as a lateral load resisting system) identifies the major role of structural design against lateral loads in the robustness of structures subjected to blast attacks. For the case of the building with interior RC rigid core, the exterior columns (which belong to the gravity system) cannot stabilize the overall system's response and total collapse is unavoidable. Conversely, the larger column sections of the building with perimeter moment resisting frames act as a safety valve to ensure the system's structural integrity after the end of the blast attack (lower progressive collapse potential).

- The progressive collapse mechanisms of the all the buildings presented in Chapters 5 and 6 establish the role of interior gravity columns in the assessment of resistance against progressive collapse. Identification of these members as the weakest links of the structural system is made, since their loss-of-stability failure defines the collapse mechanism and collapse load of the buildings. As discussed in the analysis results section, after flexural failure of exterior columns due to lateral blast loading, load redistribution causes increase in axial forces of interior gravity columns until they reach

their inelastic buckling capacity. This loss-of-stability collapse mechanism can only be detected in 3D nonlinear dynamic analysis configurations that take into account both material and geometric nonlinearities, performed by powerful finite element computational tools. Although such brittle-type failures are difficult to capture, they should receive more attention by the research community in the progressive collapse field.

Chapter 7

Conclusions: Part I

7.1 Research Contributions

Part I of this dissertation examines the distributed damage effect on progressive collapse of structures. Chapters 2 and 3 develop a new method that introduces partial distributed damage to different columns of a structural system and investigates the effects of such a distributed damage on the collapse loads and collapse mechanisms of the structural system. Subsequently, Chapters 4, 5 and 6 develop a methodology for examining the spatially distributed response and damage to frame members along the building exterior facing an external blast and assessing the progressive collapse vulnerability. The main conclusions and most important findings of Part I of this dissertation are the following:

1. The capacity of the 15-story steel frame is much lower when considering the partial distributed damage method in comparison to the simplistic notional column removal approach of the state-of-the-art APM. It is therefore considered highly unconservative for many cases to perform the alternate load path method for progressive collapse analysis of steel frames, since it may clearly overpredict the progressive collapse capacity of the structure.

2. The introduction of distributed damage in the system significantly changes the ob-

served collapse modes of the structure. There is a clear discrepancy between the collapse modes predicted by the state-of-the-art APM and the proposed Partial Distributed Damage method; distributed damage can alternate the location of a failing buckling element or (most importantly) lead to the avoidance of the yielding-type ductile collapse mode and trigger a brittle buckling failure of elements located even outside the damaged area. A parametric investigation about how damage is distributed into the system and how it affects the structural response, like the one proposed in the Partial Distributed Damage Method, is therefore crucial in order to detect the most vulnerable elements to loss-of-stability and apply the necessary precautions in their design.

3. The widely used and unrealistic column removal concept of the Alternate Path Method can be less conservative and predict collapse mechanisms and collapse loads which are not the most critical. For this reason, a reliable study to evaluate the progressive collapse capacity of a structure must include a partial damage distribution study as well, through the proposed partial distributed damage method (PDDM).

4. The simulation of the slab when conducting 3D nonlinear dynamic analysis of steel buildings subjected to external blast is of utmost importance for the correct evaluation of progressive collapse vulnerability. It is shown that, for the case of the high-rise 20-story building, the slab simulation radically affects the structural behavior; the slab contribution in the load redistribution mechanism leads to the overall system's stabilization and thus progressive collapse is avoided.

5. Nonlinear dynamic SDOF damage analyses can most accurately predict individual column responses that are only mildly affected by an intense blast scenario. Conversely, these SDOF analyses fail to describe the behavior of columns in the heavily impacted blast region, which experience a much more severe level of damage when simulated in a 3D global system configuration. The discrepancies between the SDOF and 3D

damage results are mainly attributed to the idealized end condition assumption of the individual column analyses. It is therefore considered critical to simulate a building exposed to a severe blast event in a 3D finite element model configuration, as it is highly unconservative to simplistically rely on single degree of freedom column analyses that ignore the global system's response.

6. Comparison between the response of the 10-story mid-rise building with perimeter MRFs and the 10-story building with interior rigid concrete core establishes the major role of structural design against lateral loads in the robustness of structures subjected to blast attacks. It is shown that nonlinear dynamic analyses of the 10-story building (as well as the 20-story building) with perimeter MRFs reveal increased robustness against progressive collapse; the larger perimeter column sections act as a safety valve to ensure the system's structural integrity after the end of the blast attack. Conversely, for the case of the 10-story building with interior rigid core, the exterior columns (which belong to the gravity system) cannot stabilize the overall system's response and total collapse is unavoidable (higher progressive collapse potential).

7. The progressive collapse mechanisms of all models presented in this study establish the role of interior gravity columns in the assessment of resistance against progressive collapse. Identification of these members as the weakest links of the structural system is made, since their loss-of-stability failure governs the collapse mechanism and defines the collapse load of the buildings. This loss-of-stability collapse mechanism can only be detected in 3D nonlinear dynamic analysis configurations that take into account both material and geometric nonlinearities, performed by powerful finite element computational tools. Although such brittle-type failures are difficult to capture, they should receive more attention by the research community in the progressive collapse field during evaluation, rehabilitation of existing buildings and design of future buildings.

7.2 Future Work

An important task in order to extend the findings of this work is the application of the Partial Distributed Damage Method to more than two adjacent columns, for example a region that includes three or four columns. In this case, a more widespread and severe damage scenario that affects more than two adjacent columns could be simulated by parametrically applying different extent of local damage to the columns located in the heavily impacted region. However, direct comparison with the APM single column removal notion may not be applicable anymore, since the locality of the damaging event is no longer maintained if more than two columns are partially damaged.

Another extension of the Partial Distributed Damage Method is the application of the same analysis procedure to a 3D model. However, the collapse mechanisms and thus the main conclusions are expected to remain the same, since the columns examined herein are governed by inelastic nonlinear buckling (able to be captured in a 2D analysis configuration) rather than elastic Euler buckling of the weak axis that can only be detected by a 3D analysis configuration. Finally, another important task is to take into account the post-buckling behavior of the buckled elements and examine the extent to which the collapse loads and mechanisms will be affected.

For the extension of the work pertaining to the investigation of progressive collapse vulnerability of structures when exposed to an external blast event, more blast scenarios and different building configurations should be considered. Additional tasks would be to include the simulation of connections in the 3D finite element models, in order to be able to capture more possible collapse mechanisms such as shear failure of beam to column connections. Ultimately, a simplified approach to predict the main progressive collapse mechanisms of buildings for predefined levels of blast-induced damage should be developed. Additional numerical and experimental research is recommended to further investigate and corroborate the findings of this thesis.

Part II

Variability Response Functions in 2D Elasticity Stochastic Problems

Chapter 8

Introduction: Part II

8.1 General Background

Part II of this dissertation proceeds with the study of structural behavior but from a probabilistic rather than deterministic point of view, by extending the well-known concept of Variability Response Function as a means to efficiently evaluate the response variability of stochastic structural systems with very limited information about the stochastic characteristics of uncertain system parameters.

The general research field of Probabilistic Engineering Mechanics attempts to quantify the uncertainties existing in many structural systems and analyze their effect on the systems' performance. Those uncertainties associated with the system parameters may refer to the geometry of the structure, boundary conditions, magnitude and distribution of the applied loading, material properties etc. The performance and most importantly failure of a structural system is profoundly dependent on the assumed threshold quantities of those uncertain parameters. The use of deterministic models that include average or extreme (maximum/minimum) values for the uncertain parameters may result in significant errors in the process of structural response prediction that sometimes can be unconservative. For example, materials are often characterized by random heterogeneity (such as concrete or composites)

and loads are often governed by randomly time-fluctuating values (such as earthquake or wind loads), while failing to incorporate their inherent uncertainty may lead to overestimation or underestimation of the respective response quantities.

To this end, the field of Probabilistic Engineering Mechanics aims at the uncertainty quantification of stochastic structural systems in order to correctly identify the response variability and associated failure modes. Uncertainty quantification is performed within the framework of probability theory and theory of random processes and fields, which describes the stochasticity of time and space-dependent uncertainties of system parameters, respectively. However, such uncertainty quantification, essential in order to correctly simulate random processes or fields, is often challenging due to lack of data, noisy measurements, model error etc.

In this context, this thesis aims at establishing a methodology for describing uncertainties embedded in material properties of structural systems, while focusing on two-dimensional linear elasticity problems characterized by spatially heterogeneous material properties. The stochastic finite element method (SFEM) will also be employed, which generally incorporates probabilistic analysis into Computational Mechanics.

In many problems of structural and continuum mechanics, material properties that exhibit random spatial fluctuations or heterogeneity are often replaced by a set of homogenized, effective or apparent material properties, obtained by establishing some kind of equivalence between the heterogeneous and homogeneous versions of the problem (e.g. strain energy equivalence). The calculation of apparent material properties is particularly significant for the application of the finite element method into such problems in order to minimize the need for highly refined meshes around local areas of randomly varying material properties. The work of Sab 1992 [82] demonstrates that when the size of a problem domain exceeds a characteristic volume defined as the representative volume element (RVE), the apparent properties can be considered deterministic in the sense that the variance of those apparent properties approaches negligible or practically zero values. In other words, as the volume

of a problem domain increases, then the variance of apparent properties decreases until the point when the volume approaches the RVE and consequently the variance reaches negligible values. Conversely, when the apparent properties are computed over a problem domain smaller than the RVE, the original stochastic problem that contains randomly fluctuating material properties can be replaced by an equivalent homogeneous problem with apparent material properties that are still stochastic but spatially invariant (constant). This apparent material property randomness defines the uncertainty of the response of the equivalent homogeneous problem. It must be mentioned at this point that the characteristic volume of the RVE is not by any means a predetermined quantity but rather an engineering choice above which the response variability still exists but practically becomes negligible for engineering applications.

8.1.1 Variability Response Function Concept

The estimation of the variance of apparent properties can be performed by the widely-used brute force Monte Carlo (MC) simulation. Monte Carlo simulation is the most universal method for describing uncertain system parameters, simulating random processes or fields and acquiring probabilistic information of response quantities. However, this method can be overly computationally expensive and thus it is crucial to develop new approaches that circumvent the need for MC simulations such as the variability response function (VRF) concept first introduced by Shinozuka 1987 [83]. The main advantage of such an approach is that the variability response function is able to connect the spectral density of randomly varying material properties to the variance of apparent material properties, while being independent of the spectral density function (SDF) and probability distribution function (PDF) of the underlying random heterogeneous property field for the case of statically determinate structures (it is only dependent on the deterministic boundary conditions and deterministic structural configuration of the problem). This VRF independence on the probabilistic characteristics of uncertain system parameters is particularly important, since there are general

difficulties in establishing detailed probabilistic information (such as the SDF and PDF) of those uncertain parameters due to lack of data, model error, noisy measurements etc. For statically indeterminate structures, the generalized variability response function (GVRF) methodology (Miranda and Deodatis 2012 [95] and Teferra and Deodatis 2012 [96]) has shown to produce approximate GVRFs that are only mildly dependent on the SDF and PDF of the uncertain system parameters.

A variability response function is essentially a Green's function that relates the variance of a system response quantity (i.e. displacement or in this case apparent material property) to the SDF of uncertain system parameters (usually the underlying random material properties) by a simple straightforward integration of the product of the aforementioned SDF and the analytical deterministic VRF expression. The resulting variance is not only obtained significantly more rapidly compared to MC simulations but is also exact, since no approximation of any kind is involved for the case of statically determined structures. Moreover, the VRF concept offers the possibility to assess the influence of the spectral content of the underlying material property field on the sensitivity of the response variability. For example, the VRF for the response displacement of a stochastic structural system can be expressed as

$$Var\left[u(x)\right] = \int_{-\infty}^{\infty} VRF\left(x,\kappa\right) S_{ff}\left(\kappa\right)\, d\kappa \tag{8.1}$$

where $S_{ff}(\kappa)$ is the spectral density function (SDF) of the homogeneous random field f(x) modeling the system stochasticity.

The VRF is also conceptually analogous to the Frequency Response Function, encountered in Structural Dynamics, which is essentially a transfer function that expresses the structural response in terms of displacement, velocity or acceleration due to an applied dynamic force (Chopra 2011 [74]). Finally, the VRF can also provide spectral distribution-free upper and lower bounds on the variance of the response. On the one hand, an SDF with a given variance defined by the Dirac delta function at the peak of the VRF can provide the

supremum (upper bound) of the response variance while, on the other hand, an SDF with a given variance defined by the Dirac delta function at wavenumbers of the smallest VRF value can provide the lower bound of the response variance. Alternatively, an SDF with a given variance defined by a finite power white noise can provide the lower bound of the response variance, which approaches zero as the upper cut-off wavenumber κ_u approaches infinity (Shinozuka 1987 [83]).

8.1.2 Brief Literature Review

The VRF concept was first introduced by Shinozuka 1987 [83] and later developed by Deodatis and Shinozuka 1989 [84]. The VRF has a closed-form exact analytical expression only for statically determinate structures, however in the work of Deodatis 1990 [85], a first-order Taylor expansion of the stiffness matrix was utilized to calculate an approximate VRF within a finite element framework. The Weighted Integral Method was later developed in order to calculate the stochastic part of the stiffness matrix with respect to a stochastic random field (Shinozuka and Deodatis 1988 [86], Deodatis 1991 [87] and Deodatis and Shinozuka 1991 [88]). A series of approximate VRFs were further presented in the papers of Wall and Deodatis 1994 [89], Graham and Deodatis 1998 [90], Deodatis et al. 2003 [91], Deodatis et al. 2003 [92] and Graham and Deodatis 2001 [93], where the first-order expansion renders the results approximate and only sufficiently accurate for small values of the variance of stochastic system properties.

Uncertainty quantification via the VRF concept has been already explored for computing the variance of displacement response of statically determinate linear structural systems (Wall and Deodatis 1994 [89], Graham and Deodatis 1998 [90] and Papadopoulos et al. 2005 [94]), while a generalized variability response function (GVRF) methodology has been proposed for the investigation of displacement response variability of statically indeterminate linear (Miranda and Deodatis 2012 [95]) and nonlinear (Teferra and Deodatis 2012 [96]) structural systems. The GVRF methodology has shown to produce GVRFs for statically

indeterminate beams that are only mildly dependent on the SDF and PDF of the uncertain system parameters. The VRF approach has also been developed to establish analytically-derived exact variability response functions for apparent properties of linear statically determinate beams (Arwade and Deodatis 2011 [97]) as well as generalized variability response functions for apparent properties of linear statically indeterminate beam systems (Teferra et al. 2012 [98]). Teferra et al. 2014 [99] extended the GVRF methodology to applications of two-dimensional plane stress linear problems characterized by statically homogeneous random fields in order to evaluate the variability of displacement response and effective compliance. Furthermore, the existence of VRF for apparent material properties in a stochastic finite element context is formally proven for the heat conduction problem by Arwade et al. 2015 [100], where the computation of apparent material properties is performed using linear and nonlinear shape functions in one and two dimensions, and sensitivity of the proposed VRF regarding the shape and scale of the finite element is discussed. An excellent review of the literature can be also found in the PhD theses of Manuel Miranda 2009 [101] and Kirubel Teferra 2012 [102].

8.1.3 Objectives

The objectives of Part II of this dissertation include an extension of the VRF concept for apparent material properties to two-dimensional elasticity problems within a stochastic finite element framework, by utilizing strain energy equivalence between the heterogeneous and equivalent homogeneous versions of the problem. Analytical formulation of VRFs for apparent material properties is presented with applications in 4-node quadrilateral plane stress finite elements. Finally, characteristic features of the VRFs are examined and discussed, while a series of examples are illustrated in order to underline the VRF dependence on the scale, shape and aspect ratio of the example finite elements.

8.2 Problem statement

Let $\Omega \subset \mathbb{R}^2$ define a solid body defined by coordinates $\mathbf{x} \in \mathbb{R}^2$, which is locally point-wise isotropic and occupied by a material with properties characterized by the spatially varying and random (heterogeneous) constitutive matrix $C(\mathbf{x}), \mathbf{x} \in \mathbb{R}^2$, subject to Neumann and Dirichlet boundary conditions. The strong form of the boundary value problem can be written as follows

$$\begin{aligned}
&\sigma_{ij,j} + b_i = 0 \\
&\sigma_{ij,j} = C_{ijkl}(\mathbf{x})\epsilon_{kl} \\
&\epsilon_{ij} = \frac{1}{2}(u_{i,j} + u_{j,i}) \\
&\sigma_{ij} n_j = \bar{t}_i \ \in \Gamma_t \\
&u_i = \bar{u}_i \ \in \Gamma_u \\
&\Gamma_t \cup \Gamma_u = \partial\Omega \ \text{ and } \ \Gamma_t \cap \Gamma_u = \emptyset
\end{aligned} \tag{8.2}$$

where σ and ϵ are stress and strain tensors, respectively, and u and b are displacement and body force vectors, respectively. The spaces Γ_t and Γ_u are defined as the spaces of prescribed traction $\bar{t}$ and prescribed displacement $\bar{u}$, respectively. The boundary $\partial\Omega$ defined by the outward unit normal vector n is the union of spaces Γ_t and Γ_u. The heterogeneous constitutive matrix $C(\mathbf{x})$ is a function of position x due to random fluctuations of the elastic modulus or Poisson's ratio of the heterogeneous material occupying Ω.

Consider now a body, subject to the same boundary conditions, occupied by a material with properties defined by the stochastic spatially invariant (homogeneous) matrix $\bar{C}(\mathbf{x}), \mathbf{x} \in IR^2$. The homogeneous matrix $\bar{C}$ is itself stochastic, but not spatially varying, when the material volume V_Ω is smaller than the representative volume element (RVE). $\bar{C}$ is constant within Ω but is a function of the displacement boundary conditions, traction, and an integral expression of $C(\mathbf{x})$.

It is now desirable to replace the heterogeneous material with a homogeneous material

that is, in some sense, equivalent. In elasticity problems, the definition of apparent properties may depend on a function that has some physical meaning so that the energetics of the homogeneous and the heterogeneous problems are equivalent, for example a key displacement or strain energy. The primary objective of this paper is the uncertainty quantification of $\bar{C}$ when the definition of apparent properties lies in the equivalence of strain energy. In this direction, it is considered that the elastic strain energy of the apparent properties is equivalent to that in the heterogeneous version of the problem under the same set of loading. The equivalence of strain energy can be expressed as

Strain energy of homogeneous problem = Strain energy of heterogeneous problem

or

$$\begin{aligned} \frac{1}{2}\int_{\Omega} \epsilon_0(\mathbf{x}) \cdot \bar{C} \cdot \epsilon_0(\mathbf{x})\, dV &= \frac{1}{2}\int_{\Omega} \epsilon(\mathbf{x}) \cdot C \cdot \epsilon(\mathbf{x})\, dV \\ &= \int_{\Gamma_t} u(\mathbf{x})\bar{t}(\mathbf{x})\, d\Gamma_t \end{aligned} \tag{8.3}$$

where $\epsilon_0(\mathbf{x})$ is the strain of the homogeneous body and '$\cdot$' denotes the tensor inner product. Consider now the case where the Poisson's ratio ν is a deterministic constant and only the heterogeneous elastic modulus $E(\mathbf{x})$ is randomly varying (the shear modulus $G(\mathbf{x}) = \dfrac{E(\mathbf{x})}{2(1+\nu)}$ must also be heterogeneous and perfectly correlated to the elastic modulus to preserve isotropy). Then the apparent elastic modulus $\bar{E}$ can be factored out from the effective constitutive tensor $\bar{C} = \bar{E}\bar{C}'$ and thus it can be expressed as

$$\bar{E} = \frac{\displaystyle\int_{\Gamma_t} u(\mathbf{x})\bar{t}(\mathbf{x})\, d\Gamma_t}{\dfrac{1}{2}\displaystyle\int_{\Omega} \epsilon_0(\mathbf{x}) \cdot \bar{C}' \cdot \epsilon_0(\mathbf{x})\, dV} = \frac{\displaystyle\int_{\Omega} \epsilon(\mathbf{x}) \cdot C \cdot \epsilon(\mathbf{x})\, dV}{\displaystyle\int_{\Omega} \epsilon_0(\mathbf{x}) \cdot \bar{C}' \cdot \epsilon_0(\mathbf{x})\, dV} \tag{8.4}$$

The effective elastic modulus is bounded by the Reuss and Voigt bounds, respectively, as

follows

$$\begin{aligned} \bar{E}_r &\leq \bar{E} \leq \bar{E}_v \\ \bar{E}_r &= \frac{1}{V_\Omega}\left[\int_\Omega E(\mathbf{x})^{-1}\, dV\right]^{-1} \\ \bar{E}_v &= \frac{1}{V_\Omega}\int_\Omega E(\mathbf{x})\, dV \end{aligned} \tag{8.5}$$

Equation (8.4) gives the variance of the apparent elastic modulus:

$$Var[\bar{E}] = \frac{1}{C^*} Var\left[\int_{\Gamma_t} u(\mathbf{x})\bar{t}(\mathbf{x})\, d\Gamma_t\right] \tag{8.6}$$

where $C^* = \dfrac{1}{2}\displaystyle\int_\Omega \epsilon_0(\mathbf{x}) \cdot \bar{C}' \cdot \epsilon_0(\mathbf{x})\, dV$.

The purpose of this study is to propose a stochastic scheme for the computation of apparent properties in two-dimensional elasticity problems, either plane stress or plane strain, when the problem domain occupies a finite volume smaller than the RVE. The randomness in the problem is introduced by the randomly varying elastic modulus defined as $E(x,y) = E_0\,(1 + f(x,y))$, where E_0 is the deterministic nominal elastic modulus and $f(x,y)$ is a zero mean homogeneous random field with spectral density function $S_{ff}(\kappa_1, \kappa_2)$ that is a function of the wavenumbers $\kappa_1, \kappa_2 \in \mathbb{R}^n$. The ultimate goal is to analytically provide a Variability Response Function for the variance of the apparent elastic modulus $\bar{E}$ such that

$$Var\left[\bar{E}\right] = \int_{-\infty}^{\infty}\int_{-\infty}^{\infty} VRF_{\bar{E}}\left(\kappa_1, \kappa_2\right) S_{ff}\left(\kappa_1, \kappa_2\right)\, d\kappa_1\, d\kappa_2 \tag{8.7}$$

where $VRF_{\bar{E}}\left(\kappa_1, \kappa_2\right)$ is a VRF of the apparent material properties that is independent of the spectral characteristics of $f(x,y)$, while only dependent on the deterministic boundary conditions and deterministic structural configuration of the problem. Ultimately, using $VRF_{\bar{E}}$ as a means to compute $Var\left[\bar{E}\right]$, the uncertainty of $\bar{E}$ can be efficiently evaluated.

8.3 Simulation of 1D and 2D Homogeneous Gaussian Random Fields via Spectral Representation

Monte-Carlo simulation is a robust method for efficient and accurate simulation of engineering problems in a fully stochastic framework that would be otherwise only considered deterministically. The Spectral Representation Method (SRM) introduced by Shinozuka 1972 [103] is a widely-used technique for the simulation of sample realizations of random fields and will be used in this dissertation as well. The basis of SRM is the use of the Spectral Density Function (SDF) in the frequency domain which is easy to physically interpret. SRM is also mathematically simple compared to other simulation techniques such as the Karhunen-Loève decomposition [104] - [107], since the sample realizations are generated by just a finite summation of cosine functions.

8.3.1 Simulation of 1D Homogeneous Gaussian Random Fields

Let us first define some important quantities. Consider a homogeneous random field $F(x)$. The autocorrelation function (ACF) $R_f(x, \xi)$ describes how different space instances are correlated to each other and is defined as

$$R_f(x, \xi) = E[F(x) \cdot F(x + \xi)] \tag{8.8}$$

where x is the space instance, ξ is the separation distance or space lag and $E[\cdot]$ denotes the expected value. For homogeneous fields, the ACF is only a function of the space lag, i.e. $R_f(x, \xi) = R_f(\xi)$. In addition, the Spectral Density Function (SDF) $S_f(\kappa)$ measures the distribution of power of the field in the wavenumber domain (equivalent to frequency domain for random processes), where κ is the wavenumber. As mentioned before, SDF serves as the basis of SRM. The ACF and SDF are related via a Fourier pair known as the

Wiener-Khintchine theorem or transform [108] - [111], as following

$$\begin{aligned} R_f(\xi) &= \int_{-\infty}^{\infty} S_f(\kappa) e^{i\kappa\xi}\, d\kappa \\ S_f(\kappa) &= \frac{1}{2\pi} \int_{-\infty}^{\infty} R_f(\xi) e^{-i\kappa\xi}\, d\xi \end{aligned} \tag{8.9}$$

where $i = \sqrt{-1}$ is the imaginary unit. Therefore, a Fast Fourier Transform (FFT) is only needed in order to transfer form SDF to ACF and vice versa, in an extremely fast and efficient manner. This implies that whether the ACF or SDF is known, assumed or estimated, simulation of sample realizations through the SRM technique is straightforward through this simple transformation.

The next quantity to define is the Gaussian random field. Gaussian random fields are established as the most widely-used random fields due to the existence of closed form expressions for complete characterization, the consequences of central limit theorem , and the efficiency of their simulation. A homogeneous random field $G(x)$ is a Gaussian random field if and only if every finite set of N samples $(G(x_1) = g_1, G(x_2) = g_2, ..., G(x_N) = g_N)$ is a set of N Gaussian random variables with the following N^{th} order joint probability distribution function

$$\phi_N(\mathbf{g}) = \frac{1}{sqrt(2\pi)^N \det\rho_{gg}} exp\left(-\frac{1}{2}(\mathbf{g}-\mu_g)^T \rho_{gg}^{-1}(\mathbf{g}-\mu_G)\right) \tag{8.10}$$

where is the ρ_{gg} covariance matrix and μ_g is the vector of means of the N samples. The autocorrelation function of the Gaussian random field depends only on the distance between two instances, x_1 and x_2, and is defined as

$$R_g(\xi) = E[G(x_1)G(x_2)] = \int_{-\infty}^{\infty}\int_{-\infty}^{\infty} g_1 g_2 \phi_2(\mathbf{g})\, dg_1\, dg_2 \tag{8.11}$$

The SRM technique relies on equation (8.12) for the generation of a sample realization

$g(x)$ of a homogeneous Gaussian random field $G(x)$:

$$g(x) = \sqrt{2} \sum_{j=0}^{N-1} \sqrt{2S_g(\kappa_j)\Delta\kappa} \cdot cos(\kappa_j x + \phi_j) \tag{8.12}$$

where ϕ_j are independent uniformly distributed random phase angles between 0 and 2π. This equation, which is a relatively simple mathematical expression as it comprises a summation of cosines, is analogous for the simulation of stationary Gaussian random processes, where wavenumber κ is replaced by frequency ω and space instance x is replaced by time t. The wavenumber domain is discretized as

$$\begin{aligned} \Delta\kappa &= \frac{\kappa_u}{N} \\ \kappa_j &= j\Delta\kappa \end{aligned} \tag{8.13}$$

The upper cutoff wavenumber κ_u is chosen such that $S_g(\kappa > \kappa_u)$ can be assumed negligible. Thus, κ_u is a fixed value and hence $\Delta\kappa \to 0$ as $N \to \infty$ so that $N\Delta\kappa = \kappa_u$. The following criterion is usually satisfied to estimate the value of κ_u:

$$2\int_0^{\kappa_u} S_g(\kappa)\, d\kappa = (1-\epsilon)\int_{-\infty}^{\infty} S_g(\kappa)\, d\kappa = (1-\epsilon)\mathrm{Var}(g) \tag{8.14}$$

for $\epsilon <<< 1$, for example $\epsilon = 0.01, 0.001$. Equation (8.14) expresses the SDF property that its integral over the whole wavenumber domain $\kappa \in (-\infty, \infty)$ is the variance of $g(x)$. In order to avoid aliasing, the space increments Δx are restricted by the Nyquist wavenumber (analogous to the Nyquist frequency) (Shinozuka and Deodatis 1991 [112]):

$$\Delta x \leq \frac{2\pi}{2\kappa_u} \tag{8.15}$$

The following properties of the generated samples should be also mentioned (Shinozuka and Deodatis 1991 [112]):

1. The generated samples are periodic with wavelength $\lambda = \dfrac{2\pi}{\Delta\kappa}$

2. Over multiples of the wavelength or as space approaches infinity, samples are ergodic in the mean and autocorrelation, which is established if $S(\kappa = 0) = 0$.

3. As $N \to \infty$, the generated samples are asymptotically Gaussian through the Central Limit Theorem. However, in Shinozuka and Deodatis 1991 [112] it was shown that N does not need to be very large before the samples tend to Gaussianity.

The FFT technique (e.g. Bringham 1988 [113]) is utilized in order to drastically reduce the computational time of sample generation through SRM. In this environment, equation (8.12) becomes

$$g(x) = \mathrm{Re}\left\{ \sqrt{2} \sum_{j=0}^{N-1} \sqrt{2S_g(\kappa_j)\Delta\kappa} \cdot e^{i\phi_j} e^{i\kappa_j x} \right\} \tag{8.16}$$

The sample function $g_k = g(x_k)$ is now restricted to be discrete. As an example of the SRM application through FFT technique, a series of sample functions were generated through a selected SDF expressed as

$$S_g(\kappa) = 0.02\kappa^2 e^{-2|\kappa|} \tag{8.17}$$

with variance $\sigma_g^2 = 0.01$ of a zero mean homogeneous stochastic field $G(x)$ which represents the spatial variability of the elastic modulus of a beam structure with length equal to $L = 10m$. Figure 8.1 depicts one characteristic generated sample function. The value of N, which expresses the discretization in the wavenumber domain, is sufficiently high to achieve Gaussianity. Figure 8.2 illustrates the comparison between the histogram of all simulated points along the beam (each beam has a total of 38 elements) of all sample realizations and the well-known Gaussian pdf with same mean and variance. The histogram agrees well with the Gaussian pdf as it is shown that the pdf curve intersects the centroid of the histogram bars. The large number of simulated points, equal to $700,000 \times 38 = 26,600,000$, is sufficient to generate extreme values close to the impressive value of $\pm 6 \cdot \sigma$, as observed by the left

and right tails of Figure 8.3.

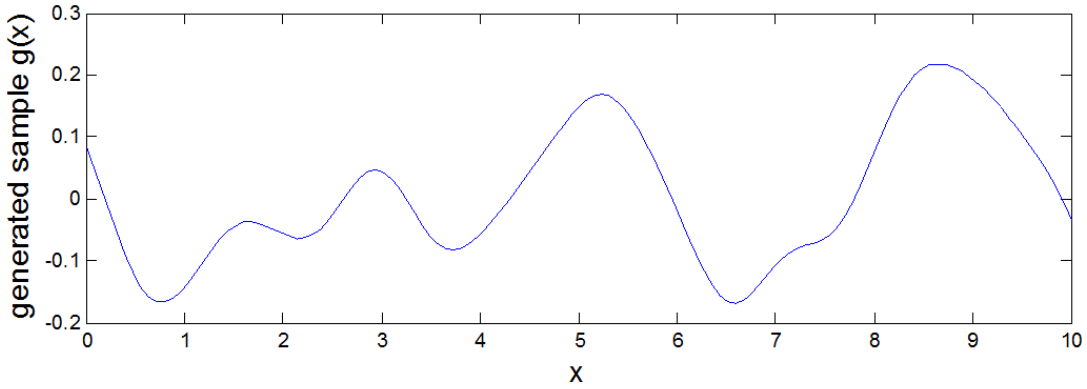

Figure 8.1: Generated sample function g(x) of zero mean homogeneous random field that represents the spatial variability of the elastic modulus of a beam structure with length equal to $L = 10m$.

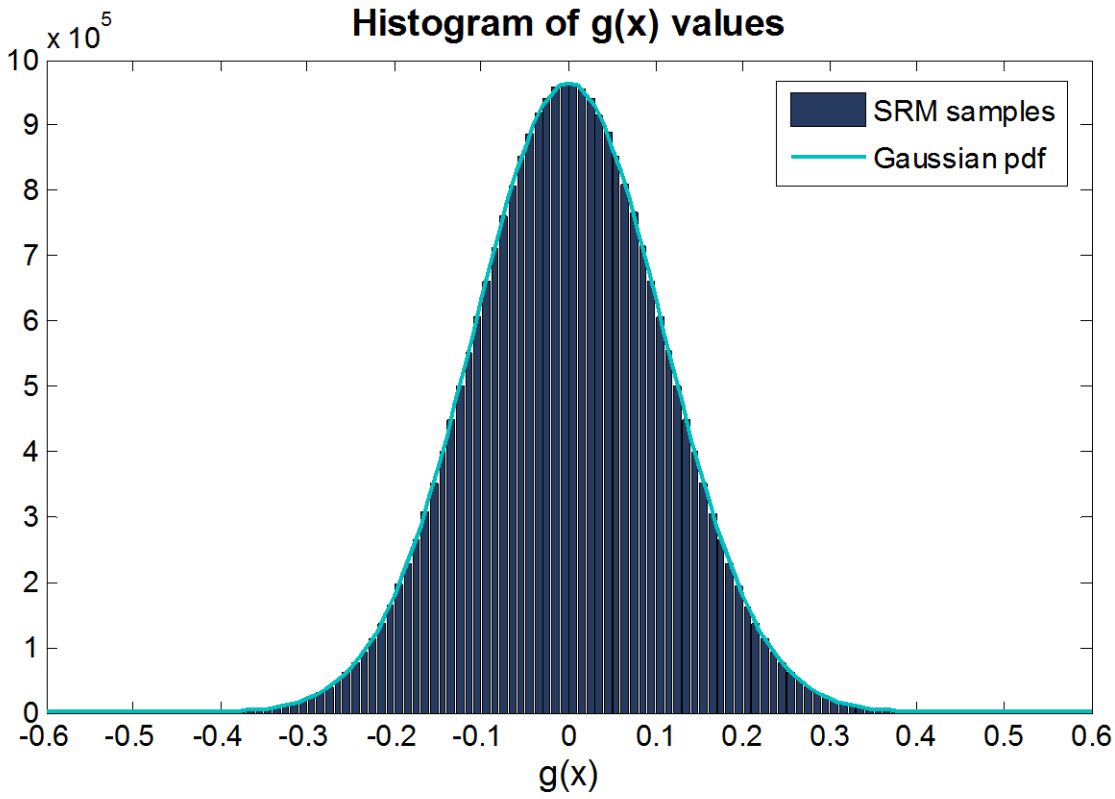

Figure 8.2: Histogram of generated samples and Gaussian pdf.

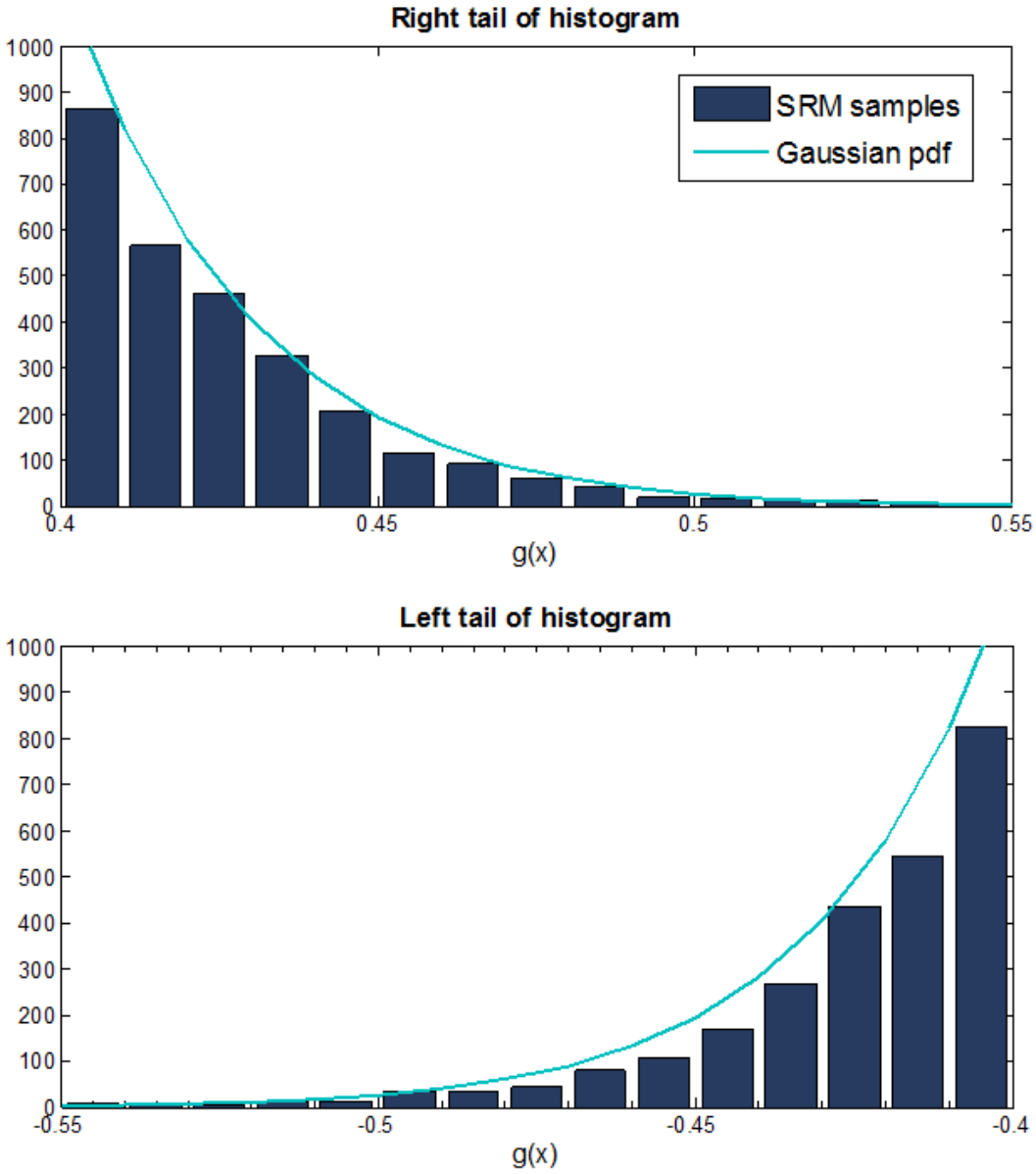

Figure 8.3: Right and left tail of histogram of generated samples and Gaussian pdf.

8.3.2 Simulation of 2D Homogeneous Gaussian Random Fields

The simulation of multi-dimensional Gaussian random fields via Spectral Representation is a straightforward extension of the simulation of one dimensional Gaussian random fields described in Section 8.3.1 and is thoroughly presented in Shinozuka and Deodatis 1996 [114]. A brief review of the simulation method will be given below. Let $f_0(x_1, x_2)$ be a two-dimensional univariate homogeneous zero mean Gaussian field with Spectral Density Function $S_{f_0f_0}(\kappa_1, \kappa_2)$ and Autocorrelation Function $R_{f_0f_0}(\xi_1, \xi_2)$ such that:

$$\begin{aligned} R_{f_0f_0}(\xi_1, \xi_2) &= E[f_0(x_1 + \xi_1, x_2 + \xi_2) \cdot f_0(x_1, x_2)] \\ R_{f_0f_0}(\xi_1, \xi_2) &= \int_{-\infty}^{\infty} \int_{-\infty}^{\infty} S_{f_0f_0}(\kappa_1, \kappa_2) e^{i(\kappa_1\xi_1 + \kappa_2\xi_2)} \, d\kappa_1 \, d\kappa_2 \end{aligned} \tag{8.18}$$

where $E[\cdot]$ denotes the mathematical expectation, ξ_1 and ξ_2 are the separation distances along the x_1 and x_2 directions, respectively, and κ_1 and κ_2 are the corresponding wavenumbers. A 2D sample function can be generated through the following equation

$$\begin{aligned} f_0(x_1, x_2) = &\sqrt{2} \sum_{n_1=0}^{\infty} \sum_{n_2=0}^{\infty} \left\{ \sqrt{2S_{f_0f_0}(\kappa_{1n_1}, \kappa_{2n_2})\Delta\kappa_1\Delta\kappa_2} \cdot cos(\kappa_{1n_1}x_1 + \kappa_{2n_2}x_2 + \Phi^{(1)}_{n_1n_2}) + \right. \\ &\left. \sqrt{2S_{f_0f_0}(-\kappa_{1n_1}, \kappa_{2n_2})\Delta\kappa_1\Delta\kappa_2} \cdot cos(-\kappa_{1n_1}x_1 + \kappa_{2n_2}x_2 + \Phi^{(2)}_{n_1n_2}) \right\} \end{aligned} \tag{8.19}$$

where $\Phi^{(1)}_{n_1n_2}$ and $\Phi^{(2)}_{n_1n_2}$ are two different sets of independent identically distributed uniform random phase angles between $[0, 2\pi]$. $\Phi^{(1)}_{n_1n_2}$ and $\Phi^{(2)}_{n_1n_2}$ are also two-dimensional arrays of length $N_1 \times N_2$, and the discretized wavenumber domain is given by

$$\begin{aligned} \Delta\kappa_1 = \frac{\kappa_{1u}}{N_1} \quad &\Rightarrow \quad \kappa_{1n_1} = n_1\Delta\kappa_1 \\ \Delta\kappa_2 = \frac{\kappa_{2u}}{N_2} \quad &\Rightarrow \quad \kappa_{2n_2} = n_2\Delta\kappa_2 \end{aligned} \tag{8.20}$$

Equation (8.19) can be rewritten by taking advantage of the relationship between cosine

and the exponential function, into the following form, known as the FFT technique formula used to drastically reduce the computational time of generating sample realizations:

$$f(p_1\Delta x_1, p_2\Delta x_2) = \mathrm{Re}\Bigg\{ 2 \sum_{n_1=0}^{M_1-1} \sum_{n_2=0}^{M_2-1} \sqrt{S_{f_0 f_0}(\kappa_{1n_1}, \kappa_{2n_2})\Delta\kappa_1\Delta\kappa_2} \cdot \exp[i\phi^{(1)}_{n_1 n_2}] \\ \cdot \exp\left(i\frac{2\pi n_1 p_1}{M_1} + i\frac{2\pi n_2 p_2}{M_2} \right) + \\ \sqrt{S_{f_0 f_0}(\kappa_{1n_1}, -\kappa_{2n_2})\Delta\kappa_1\Delta\kappa_2} \cdot \exp[i\phi^{(2)}_{n_1 n_2}] \cdot \exp\left(i\frac{2\pi n_1 p_1}{M_1} - i\frac{2\pi n_2 p_2}{M_2} \right) \Bigg\} \tag{8.21}$$

where $p_1 = 0, 1, ..., M_1 - 1$ and $p_2 = 0, 1, ..., M_2 - 1$. Δx_1, Δx_2 and $\Delta\kappa_1$, $\Delta\kappa_2$ are related in the following way:

$$\Delta x_1 \Delta\kappa_1 = \frac{2\pi}{M_1} \quad \text{and} \quad \Delta x_2 \Delta\kappa_2 = \frac{2\pi}{M_2} \tag{8.22}$$

In order to avoid aliasing, the space increments have to obey the following conditions:

$$\Delta x_1 \leq \frac{2\pi}{2\kappa_{1u}} \quad \text{and} \quad \Delta x_2 \leq \frac{2\pi}{2\kappa_{2u}} \tag{8.23}$$

which is equivalent to

$$M_1 \geq 2N_1 \quad \text{and} \quad M_2 \geq 2N_2 \tag{8.24}$$

It can be shown that as $M_1, M_2 \to \infty$, each sample function is ergodic in the mean and autocorrelation. Equation (8.21) is used to generate sample function of the zero mean homogeneous two-dimensional random field of Section 9.3.2; the utilized SDF and one sample function are illustrated in Figures 9.7 and 9.8, respectively.

8.4 Part II Outline

Part II of this dissertation consists of four chapters and is organized as follows. Following this introductory chapter, Chapter 9 presents the formulation of finite element based Variability Response Functions for apparent material properties in 2D linear elasticity stochastic problems. The analytical calculation of VRFs is formulated for different geometries of finite elements, including a square isoparametric finite element in natural coordinate system, a generic rectangular element in physical Cartesian coordinate system and finally an arbitrary quadrilateral element that is mapped from physical to natural coordinate system.

Chapter 10 presents the analytical calculation of a series of VRFs for finite elements with varying geometry; rectangles with different values of $L_x^{(e)}$ and $L_y^{(e)}$, as well as quadrilateral elements with different nodal coordinates. The VRF dependencies on scale, shape and aspect ratio of the example elements is illustrated and discussed.

Part II concludes with a discussion on the accomplishments and limitations of the VRF concept for apparent material properties in Chapter 11, while potential direction of future research is also contemplated. Most of the content of Part II derives from Sideri et al. 2016 [115].

Chapter 9

Finite Element based VRFs for Apparent Material Properties

9.1 Introduction

This chapter will elaborate on the formulation of finite element based Variability Response Functions for apparent material properties of 2D linear elasticity stochastic problems. The VRF formulation will be presented for the following finite element geometries that summarize all possibilities for the simulation of any two-dimensional finite element model geometry:

1. Square isoparametric finite element in natural coordinate system
2. Generic rectangular element in physical Cartesian coordinate system
3. Arbitrary quadrilateral element that is mapped from physical to natural coordinate system

The first VRF formulation for a square isoparametric 2×2 finite element in natural coordinate system constitutes the simplest case for finite element meshing. The second VRF formulation for a generic rectangular element extends the applicability of the previous formulation in the Cartesian coordinate system. The final VRF formulation for an arbitrary

quadrilateral element constitutes the most complicated version of the problem, where the concept of mapping from physical to natural coordinate system is employed in order to develop a VRF for any element of arbitrary geometry; the calculations, which would otherwise be impossible due to the very complex algebraic expressions of the Cartesian shape functions, are facilitated by using the Jacobian matrix that normalizes the coordinates, i.e. maps the physical to natural coordinates. For demonstration and simplicity purposes, the VRF formulation for an arbitrary quadrilateral element will be calculated for an example trapezoid element. However, this VRF formulation is not limited to this specific example; it and can be extended by using the exact same procedure for any shape of quadrilateral element.

9.2 Finite Element Analysis of Linear Elastic Plane Stress Problem

In this section, plane stress finite elements will be developed in the framework of classical 2D linear elasticity. The necessary governing equations (strong form) are presented below

$$\begin{aligned} &\text{Equilibrium equation: } \nabla_S^T \sigma + b = 0 \\ &\text{Kinematics equation (strain-displacement relation): } \epsilon = \nabla_S u \\ &\text{Constitutive equation (stress-strain relation): } \sigma = D\epsilon \end{aligned} \tag{9.1}$$

where σ is the stress tensor, ϵ is the strain tensor, D is the constitutive tensor, u is the displacement vector and ∇_S is the symmetric gradient matrix operator defined as

$$\nabla_S = \begin{bmatrix} \dfrac{\partial}{\partial x} & 0 \\ 0 & \dfrac{\partial}{\partial y} \\ \dfrac{\partial}{\partial x} & \dfrac{\partial}{\partial y} \end{bmatrix} \tag{9.2}$$

There are two types of boundary conditions; the portion of the boundary where the traction is prescribed is denoted by Γ_t, while the portion of the boundary where the dis-

placement is prescribed is denoted by Γ_u. The traction boundary condition can be expressed as $\sigma\, n = t \in \Gamma_t$, where n is the outward unit normal vector, while the displacement boundary condition is written as $u = \bar{u} \in \Gamma_u$. The displacement boundary condition is an essential boundary condition, meaning that it must be satisfied by the displacement field, while the traction boundary condition is a natural boundary condition. The displacement and traction cannot be both prescribed on any portion of the boundary, therefore $\Gamma_t \cap \Gamma_u = \emptyset$. However, either the displacement or traction must be prescribed on any portion of the boundary, i.e. $\Gamma_t \cup \Gamma_u = \partial\Omega$.

If Ω is subject to plane stress conditions, the following approximations hold

$$\sigma_{zz} = \sigma_{yz} = \sigma_{xz} = 0 \tag{9.3}$$

leading to the following vectors for stress, strain and displacement

$$\begin{aligned} \sigma^T &= \begin{bmatrix} \sigma_{xx} & \sigma_{yy} & \sigma_{xy} \end{bmatrix} \\ \epsilon^T &= \begin{bmatrix} \epsilon_{xx} & \epsilon_{yy} & 2\gamma_{xy} \end{bmatrix} \\ u^T &= \begin{bmatrix} u_x(x,y) & u_y(x,y) \end{bmatrix} \end{aligned} \tag{9.4}$$

The constitutive tensor or material property matrix is defined as

$$D^{(e)}(x,y) \;=\; \frac{E^{(e)}(x,y)}{1-\nu^2} \begin{bmatrix} 1 & \nu & 0 \\ \nu & 1 & 0 \\ 0 & 0 & \dfrac{1-\nu}{2} \end{bmatrix} \tag{9.5}$$

where $E(x,y)$ is the heterogeneous elastic modulus and ν is deterministic Poisson's ratio.

The strains in the z direction are given by

$$\begin{aligned} \epsilon_{zz} &= -\frac{\nu}{E}(\sigma_{xx} + \sigma_{yy}) \\ \epsilon_{yz} &= \epsilon_{xz} = 0 \end{aligned} \tag{9.6}$$

To obtain the weak form of the equilibrium equation of equation (9.1), we multiply the equilibrium equation by a kinematically admissible virtual displacement field v, i.e. $\mathrm{v} = 0 \in \Gamma_u$), integrate over the domain and employ the divergence theorem. Under the assumption that the body force is zero, the weak form can be expressed as

$$\begin{aligned} &\int_\Omega \nabla_S \ \sigma \ \mathrm{v} \ d\Omega = \sigma \ n \ \mathrm{v}\Big|_{\Gamma_t} - \int_\Omega \sigma \ \nabla_S \ \mathrm{v} \ d\Omega \quad \Rightarrow \\ &\int_\Omega \sigma \ \nabla_S \ \mathrm{v} \ d\Omega - t \ \mathrm{v} = 0 \end{aligned} \tag{9.7}$$

9.3 Formulation of VRFs of a Square Isoparametric Plane Stress Element in Natural Coordinate System

This section describes the derivation of the variability response function for apparent material properties, in order to analyze stochastic plane stress problems by using the bilinear isoparametric 2×2 square element shown in Figure 9.1. The derivation will be conducted in the natural (ξ, η) coordinate system, which essentially corresponds to the case where a rectangular element in physical Cartesian (x, y) coordinate system is already mapped into a square element in the natural (ξ, η) coordinate system (Figure 9.1).

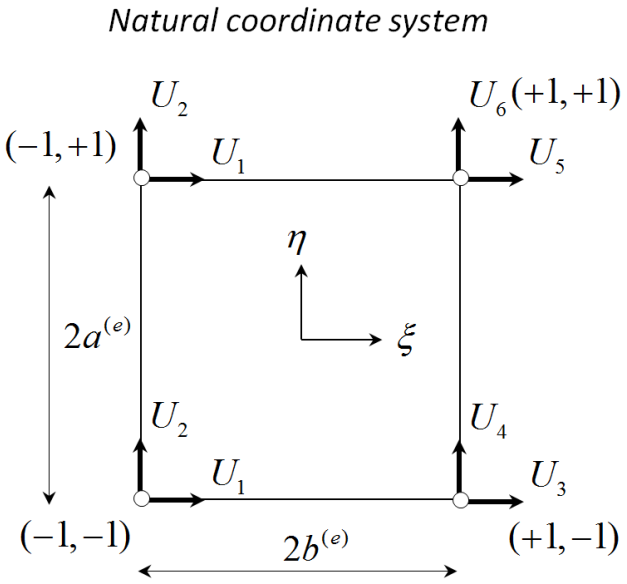

Figure 9.1: 4-node square plane stress element in natural coordinate system.

The element has eight degrees of freedom (two per node) and isoparametric shape functions given by Hughes 1987 [116] as shown in Figure 9.2

$$\begin{aligned} N_1 &= \frac{1}{4}(1-\xi)(1-\eta) \;;\; N_2 = \frac{1}{4}(1+\xi)(1-\eta) \\ N_3 &= \frac{1}{4}(1+\xi)(1+\eta) \;;\; N_4 = \frac{1}{4}(1-\xi)(1+\eta) \end{aligned} \tag{9.8}$$

where ξ and η are the natural coordinates defined in Figure 9.1. The strain-displacement

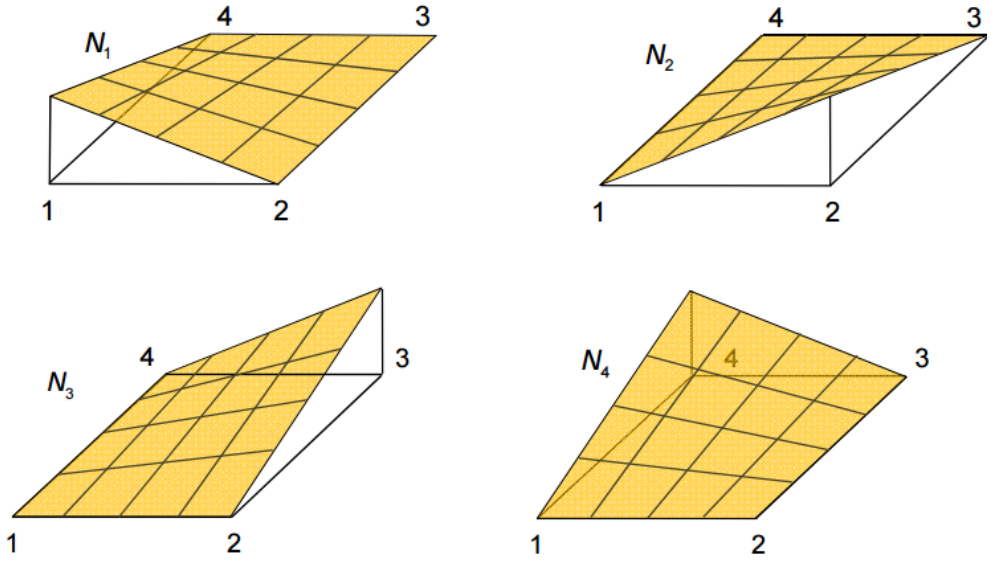

Figure 9.2: Graphical illustration of bilinear 4-node element shape functions.

matrix is 3×8 given by

$$B^{(e)}(\xi,\eta) = \frac{1}{4}\begin{bmatrix} \eta-1 & 0 & 1-\eta & 0 & \eta+1 & 0 & -1-\eta & 0 \\ 0 & \xi-1 & 0 & -\xi-1 & 0 & \xi+1 & 0 & 1-\xi \\ \xi-1 & \eta-1 & -\xi-1 & 1-\eta & \xi+1 & \eta+1 & 1-\xi & -1-\eta \end{bmatrix} \tag{9.9}$$

The nodal values of the ξ and η coordinates are

$$\begin{aligned} &\xi_1 = -1 \ ; \ \xi_2 = +1 \ ; \ \xi_3 = +1 \ ; \ \xi_4 = -1 \\ &\eta_1 = -1 \ ; \ \eta_2 = -1 \ ; \ \eta_3 = +1 \ ; \ \eta_4 = +1 \end{aligned} \tag{9.10}$$

The material property matrix is defined for plane-stress problems as

$$D^{(e)}(\xi,\eta) \ = \ \frac{E^{(e)}(\xi,\eta)}{1-\nu^2}\begin{bmatrix} 1 & \nu & 0 \\ \nu & 1 & 0 \\ 0 & 0 & \dfrac{1-\nu}{2} \end{bmatrix} \tag{9.11}$$

In the above equation, ν denotes Poisson's ratio as a deterministic constant and $E^{(e)}(\xi,\eta)$ is the heterogeneous randomly varying elastic modulus defined by the equation

$$E^{(e)}(\xi,\eta) = E_0\left(1 + f(\xi,\eta)\right) \tag{9.12}$$

where E_0 is the nominal elastic modulus and $f(\xi,\eta)$ is a zero mean homogeneous random field with spectral density function $S_{ff}(\kappa_1,\kappa_2)$ that is a function of the wavenumbers $\kappa_1,\kappa_2 \in \mathbb{R}^n$. It must be reminded at this point that the shear modulus $G^{(e)}(\xi,\eta)$ must also be heterogeneous and perfectly correlated to the elastic modulus $E^{(e)}(\xi,\eta)$ (since the Poisson's ratio is a deterministic constant), in order to preserve isotropy.

The strain energy stored within each element of the heterogeneous body can be expressed by

$$W_{het}^{(e)} = \frac{1}{2}\iint\limits_{\Omega} U^{(e)T}\Big([B]^T[D][B]\Big)U^{(e)}\,d\Omega \tag{9.13}$$

where $U^{(e)}$ is the displacement vector of each element. Considering now an imposed unit displacement along the 1^{st} degree of freedom, the expression for the strain energy leads to

$$W_{het}^{(e)} = \frac{1}{2}\iint\limits_{\Omega} \begin{bmatrix} 1 & 0 & 0 & 0 & 0 & 0 & 0 & 0 \end{bmatrix} \Big([B]^T[D][B]\Big) \begin{bmatrix} 1 \\ 0 \\ 0 \\ 0 \\ 0 \\ 0 \\ 0 \\ 0 \end{bmatrix} d\Omega \tag{9.14}$$

which reduces to

$$W_{het}^{(e)} = \frac{1}{2}\iint\limits_{\Omega}\Big([B]^T[D][B]\Big)_{11}\,d\Omega = \frac{1}{2}\int\limits_{-1}^{1}\int\limits_{-1}^{1}\left(\frac{E_0\,(1+f(\xi,\eta))}{16(1-\nu^2)}\cdot\left[\,(\eta-1)^2+\left(\frac{1-\nu}{2}\right)(\xi-1)^2\,\right]\right)d\xi\,d\eta \tag{9.15}$$

The respective element strain energy of the homogeneous body with apparent properties is

$$W_{hom}^{(e)} = \frac{1}{2}\int\limits_{-1}^{1}\int\limits_{-1}^{1}\left(\frac{\bar{E}_1}{16(1-\nu^2)}\cdot\left[\,(\eta-1)^2+\left(\frac{1-\nu}{2}\right)(\xi-1)^2\,\right]\right)d\xi\,d\eta \tag{9.16}$$

where $\bar{E}_1$ is the equivalent apparent elastic modulus for the 1^{st} degree of freedom. By equating the two expressions for strain energy, the apparent elastic modulus $\bar{E}_1$ reduces to the expression

$$\bar{E}_1 = E_0\ \cdot\ \frac{\displaystyle\int\limits_{-1}^{1}\int\limits_{-1}^{1}(1+f(\xi,\eta))\cdot\left[(\eta-1)^2+\left(\frac{1-\nu}{2}\right)(\xi-1)^2\right]d\xi\,d\eta}{\displaystyle\int\limits_{-1}^{1}\int\limits_{-1}^{1}\left[(\eta-1)^2+\left(\frac{1-\nu}{2}\right)(\xi-1)^2\right]d\xi\,d\eta} \tag{9.17}$$

Let us define the denominator in the expression of $\bar{E}_1$, which is only a deterministic constant, as

$$M_1 = \int\limits_{-1}^{1}\int\limits_{-1}^{1}\left[(\eta-1)^2+\left(\frac{1-\nu}{2}\right)(\xi-1)^2\right]d\xi\,d\eta \tag{9.18}$$

The variance of $\bar{E}_1$ is calculated by taking the expectation and the mean square of the above equation. The expectation is given by

$$E\left[\bar{E}_1\right] = E_0 \tag{9.19}$$

The square of the expectation is given by

$$\begin{aligned}\left[\bar{E}_1\right]^2 =& \frac{E_0^2}{M_1^2} \cdot \int_{-1}^{1}\int_{-1}^{1}\int_{-1}^{1}\int_{-1}^{1}\left[(\eta-1)^2+\left(\frac{1-\nu}{2}\right)(\xi-1)^2\right]\times \\ & \left[(w-1)^2+\left(\frac{1-\nu}{2}\right)(u-1)^2\right](1+f(\xi,\eta))\,(1+f(u,w))\;d\xi\,d\eta\,du\,dw\end{aligned} \tag{9.20}$$

The mean square of $\bar{E}_1$ is given by the equation

$$\begin{aligned}E\left[\bar{E}_1^2\right] = & \frac{E_0^2}{M_1^2}\cdot \int_{-1}^{1}\int_{-1}^{1}\int_{-1}^{1}\int_{-1}^{1}\left[(\eta-1)^2+\left(\frac{1-\nu}{2}\right)(\xi-1)^2\right]\times \\ & \left[(w-1)^2+\left(\frac{1-\nu}{2}\right)(u-1)^2\right]\Big[1+R_{ff}(s_1,s_2)\Big]\,d\xi\,d\eta\,du\,dw\end{aligned} \tag{9.21}$$

where $R_{ff}(s_1,s_2) = E\Big[f(\xi,\eta)f(u,w)\Big]$ is the spatial correlation function of $f(\xi,\eta)$ and $s_1, s_2 \in \mathbb{R}$ are vectors of distances with $s_1 = \xi - u$ and $s_2 = \eta - w$.

The variance of the apparent material property $\bar{E}_1$ can be therefore expressed as

$$\begin{aligned}Var\left[\bar{E}_1\right] =& E\left[\bar{E}_1^2\right] - E\left[\bar{E}_1\right]^2 = \\ & \frac{E_0^2}{M_1^2}\cdot \int_{-1}^{1}\int_{-1}^{1}\int_{-1}^{1}\int_{-1}^{1}\left[(\eta-1)^2+\left(\frac{1-\nu}{2}\right)(\xi-1)^2\right]\times \\ & \left[(w-1)^2+\left(\frac{1-\nu}{2}\right)(u-1)^2\right]\;\cdot\; R_{ff}(s_1,s_2)\,d\xi\,d\eta\,du\,dw\end{aligned} \tag{9.22}$$

If the spectral density $S_{ff}(\kappa_1,\kappa_2)$ is substituted for $R_{ff}(s_1,s_2)$ through the Wiener-Khintchine transform, and if we change the order of integration, then

$$Var\left[\bar{E}_1\right] = \int_{-\infty}^{\infty}\int_{-\infty}^{\infty} VRF_{\bar{E}_1}(\kappa_1,\kappa_2)\,S_{ff}(\kappa_1,\kappa_2)\;d\kappa_1\,d\kappa_2 \tag{9.23}$$

where $VRF_{\bar{E}_1}$ is defined as

$$\begin{aligned} VRF_{\bar{E}_1}(\kappa_1,\kappa_2) \;=\; & \frac{E_0^2}{M_1^2}\cdot\int_{-1}^{1}\int_{-1}^{1}\int_{-1}^{1}\int_{-1}^{1}\left[(\eta-1)^2+\left(\frac{1-\nu}{2}\right)(\xi-1)^2\right]\times \\ & \left[(w-1)^2+\left(\frac{1-\nu}{2}\right)(u-1)^2\right]\cdot e^{-i(\kappa_1 s_1+\kappa_2 s_2)}\,d\xi\,d\eta\,du\,dw \end{aligned} \tag{9.24}$$

After some algebra

$$\begin{aligned} VRF_{\bar{E}_1}(\kappa_1,\kappa_2) \;=\; & \frac{4E_0^2}{\kappa_1^6\kappa_2^6\left(\frac{8\nu}{3}-8\right)^2}\Big[4\kappa_1^3\kappa_2^3(-1+\nu)-4\kappa_1^2\kappa_2^2(-1+\kappa_2^2)(-1+\nu)-\kappa_2^4(-1+\nu)^2-2 \\ & \kappa_1^4(2+2\kappa_2^2(-1+\nu)+\kappa_2^4(7+(-4+\nu)\nu))+cos(2\kappa_1)(-4\kappa_1^4(-1+\kappa_2^4(-3+\nu)-\kappa_2^2(-1+\nu))-4\kappa_1^3\kappa_2^3 \\ & (-1+\nu)-2\kappa_1^2\kappa_2^2(2+\kappa_2^2(-3+\nu))(-1+\nu)+\kappa_2^4(-1+\nu)^2+(4\kappa_1^4(-1-\kappa_2^2(-3+\nu)+\kappa_2^4(-1+\nu))+4\kappa_1^3 \\ & \kappa_2^3(-1+\nu)+2\kappa_1^2\kappa_2^2(2+\kappa_2^2(-3+\nu))(-1+\nu)-\kappa_2^4(-1+\nu)^2)cos(2\kappa_2))+cos(2\kappa_2)(2\kappa_1^4(2+\kappa_2^2 \\ & (2+\kappa_2^2(-1+\nu))(-3+\nu))-4\kappa_1^3\kappa_2^3(-1+\nu)+4\kappa_1^2\kappa_2^2(-1+\kappa_2^2)(-1+\nu)+\kappa_2^4(-1+\nu)^2+2\kappa_1\kappa_2^2 \\ & (2\kappa_1^3\kappa_2-2\kappa_1^2(-1+\kappa_2^2)-\kappa_2^2(-1+\nu))(-1+\nu)sin(2\kappa_1))+2\kappa_1\kappa_2(\kappa_2(-2\kappa_1^3\kappa_2+2\kappa_1^2(-1+ \\ & \kappa_2^2)+\kappa_2^2(-1+\nu))(-1+\nu)sin(2\kappa_1)+4\kappa_1 sin(\kappa_1)(\kappa_1\kappa_2^2(1+\kappa_1\kappa_2)(-1+\nu)cos(\kappa_1)+(\kappa_1^2(2 \\ & +\kappa_2^2(-1+\nu))-\kappa_2^2(-1+\nu)-\kappa_1\kappa_2^3(-1+\nu))sin(\kappa_1))sin(2\kappa_2))\Big] \end{aligned} \tag{9.25}$$

Equations 9.23 and 9.25 are key expressions for the exact computation of the variance of apparent properties within the finite element, without the need for computationally expensive Monte-Carlo simulations or any other kind of approximations. Additionally, the final expression for the VRF is only dependent on deterministic quantities like the isoparametric element's dimensions a and b, Poisson's ratio ν and nominal elastic modulus E_0, while it is independent of the spectral density function S_{ff} and probability distribution function PDF of the zero mean homogeneous random field $f(\xi,\eta)$.

Figure 9.3 depicts the plot of $VRF_{\bar{E}_1}$ for the 1^{st} degree of freedom in one quadrant along positive values of κ_1 and κ_2, with the various parameters assigned as following: $E_0 = 125\cdot 10^6$ and $\nu = 0.3$. As a typical characteristic of VRFs, the spectral contribution to variance has a peak for $\kappa_1 = \kappa_2 = 0$ and displays a decaying sequence of peaks with increasing wavenumber.

The maximum value of the VRF for $\kappa_1 = \kappa_2 = 0$ is equal to E_0^2. In addition, the VRF is not isotropic in the κ space, since the decay rate is faster along the $\kappa_1 = \kappa_2$ diagonal than along the κ_1 and κ_2 axes. The decay rate is also faster along κ_1 axis, while it is slower along κ_2 axis. Another usual characteristic of the VRF is the asymptotic values of $\lim_{\kappa_1,\kappa_2\to\infty} VRF_{\bar{E}}(\kappa_1,\kappa_2) = 0$. Detailed discussion of the symmetry properties of the VRF is found in the following section.

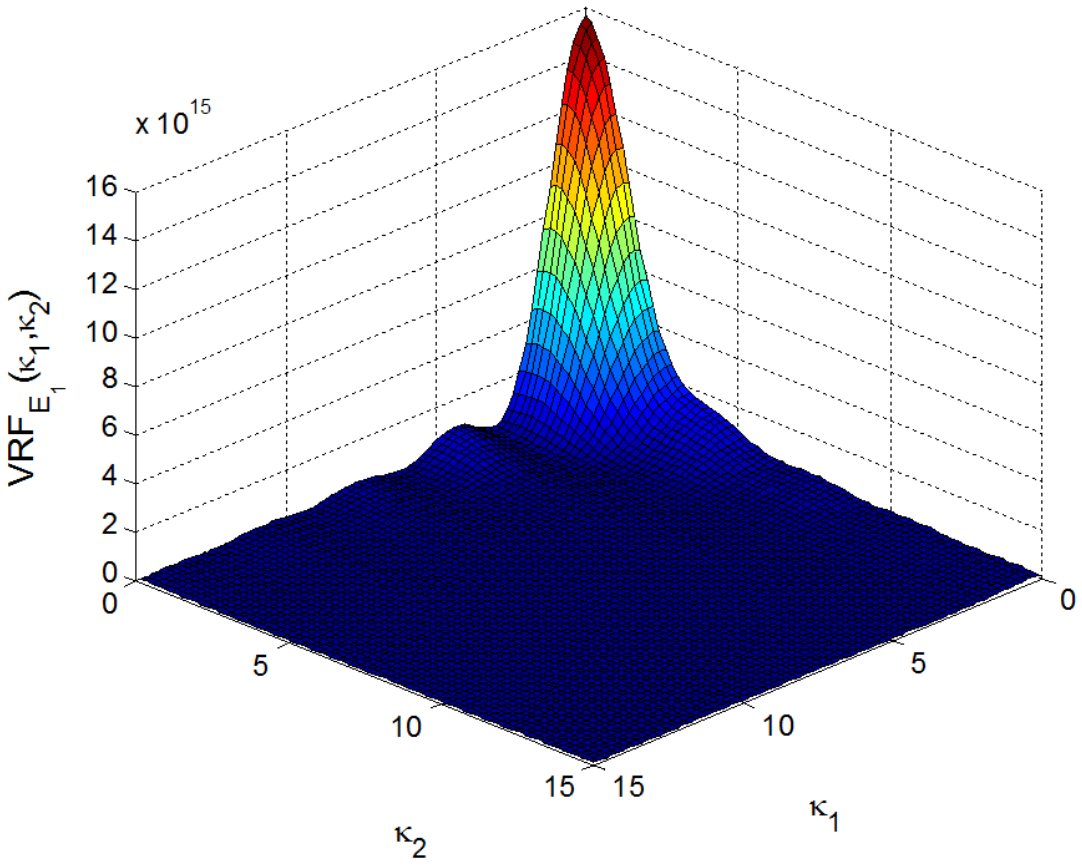

Figure 9.3: $VRF_{\bar{E}_1}(\kappa_1,\kappa_2)$ of 1^{st} degree of freedom of 4-node 2×2 square element in natural coordinate system.

Similarly, the rest of the VRFs are derived for the remaining 7 degrees of freedom, by imposing unit displacements in the respective d.o.f. according to Figure 9.1 and performing the same calculations. The expressions for the rest of the VRFs are as following:

$$VRF_{\bar{E}_2}(\kappa_1,\kappa_2) = \frac{E_0^2}{M_2^2}\cdot\int_{-1}^{1}\int_{-1}^{1}\int_{-1}^{1}\int_{-1}^{1}\left[(\xi-1)^2+\left(\frac{1-\nu}{2}\right)(\eta-1)^2\right]\times \left[(u-1)^2+\left(\frac{1-\nu}{2}\right)(w-1)^2\right]\cdot e^{-i(\kappa_1 s_1+\kappa_2 s_2)}\,d\xi\,d\eta\,du\,dw \tag{9.26}$$

$$VRF_{\bar{E}_3}(\kappa_1,\kappa_2) = \frac{E_0^2}{M_3^2}\cdot\int_{-1}^{1}\int_{-1}^{1}\int_{-1}^{1}\int_{-1}^{1}\left[(\eta-1)^2+\left(\frac{1-\nu}{2}\right)(\xi+1)^2\right]\times \left[(w-1)^2+\left(\frac{1-\nu}{2}\right)(u+1)^2\right]\cdot e^{-i(\kappa_1 s_1+\kappa_2 s_2)}\,d\xi\,d\eta\,du\,dw \tag{9.27}$$

$$VRF_{\bar{E}_4}(\kappa_1,\kappa_2) = \frac{E_0^2}{M_4^2}\cdot\int_{-1}^{1}\int_{-1}^{1}\int_{-1}^{1}\int_{-1}^{1}\left[(\xi+1)^2+\left(\frac{1-\nu}{2}\right)(\eta-1)^2\right]\times \left[(u+1)^2+\left(\frac{1-\nu}{2}\right)(w-1)^2\right]\cdot e^{-i(\kappa_1 s_1+\kappa_2 s_2)}\,d\xi\,d\eta\,du\,dw \tag{9.28}$$

$$VRF_{\bar{E}_5}(\kappa_1,\kappa_2) = \frac{E_0^2}{M_5^2}\cdot\int_{-1}^{1}\int_{-1}^{1}\int_{-1}^{1}\int_{-1}^{1}\left[(\eta+1)^2+\left(\frac{1-\nu}{2}\right)(\xi+1)^2\right]\times \left[(w+1)^2+\left(\frac{1-\nu}{2}\right)(u+1)^2\right]\cdot e^{-i(\kappa_1 s_1+\kappa_2 s_2)}\,d\xi\,d\eta\,du\,dw \tag{9.29}$$

$$VRF_{\bar{E}_6}(\kappa_1,\kappa_2) = \frac{E_0^2}{M_6^2}\cdot\int_{-1}^{1}\int_{-1}^{1}\int_{-1}^{1}\int_{-1}^{1}\left[(\xi+1)^2+\left(\frac{1-\nu}{2}\right)(\eta+1)^2\right]\times \left[(u+1)^2+\left(\frac{1-\nu}{2}\right)(w+1)^2\right]\cdot e^{-i(\kappa_1 s_1+\kappa_2 s_2)}\,d\xi\,d\eta\,du\,dw \tag{9.30}$$

$$VRF_{\bar{E}_7}(\kappa_1,\kappa_2) = \frac{E_0^2}{M_7^2}\cdot\int_{-1}^{1}\int_{-1}^{1}\int_{-1}^{1}\int_{-1}^{1}\left[(\eta+1)^2+\left(\frac{1-\nu}{2}\right)(\xi-1)^2\right]\times \left[(w+1)^2+\left(\frac{1-\nu}{2}\right)(u-1)^2\right]\cdot e^{-i(\kappa_1 s_1+\kappa_2 s_2)}\,d\xi\,d\eta\,du\,dw \tag{9.31}$$

$$VRF_{\bar{E}_8}(\kappa_1,\kappa_2) = \frac{E_0^2}{M_8^2}\cdot\int_{-1}^{1}\int_{-1}^{1}\int_{-1}^{1}\int_{-1}^{1}\left[(\xi-1)^2+\left(\frac{1-\nu}{2}\right)(\eta+1)^2\right]\times \left[(u-1)^2+\left(\frac{1-\nu}{2}\right)(w+1)^2\right]\cdot e^{-i(\kappa_1 s_1+\kappa_2 s_2)}\,d\xi\,d\eta\,du\,dw \tag{9.32}$$

where the deterministic quantities of $M_2 - M_8$ are defined as

$$M_2 = \int_{-1}^{1}\int_{-1}^{1}\left[(\xi-1)^2+\left(\frac{1-\nu}{2}\right)(\eta-1)^2\right]d\xi\,d\eta \tag{9.33}$$

$$M_3 = \int_{-1}^{1}\int_{-1}^{1}\left[(\eta-1)^2+\left(\frac{1-\nu}{2}\right)(\xi+1)^2\right]d\xi\,d\eta \tag{9.34}$$

$$M_4 = \int_{-1}^{1}\int_{-1}^{1}\left[(\xi+1)^2+\left(\frac{1-\nu}{2}\right)(\eta-1)^2\right]d\xi\,d\eta \tag{9.35}$$

$$M_5 = \int_{-1}^{1}\int_{-1}^{1}\left[(\eta+1)^2+\left(\frac{1-\nu}{2}\right)(\xi+1)^2\right]d\xi\,d\eta \tag{9.36}$$

$$M_6 = \int_{-1}^{1}\int_{-1}^{1}\left[(\xi+1)^2+\left(\frac{1-\nu}{2}\right)(\eta+1)^2\right]d\xi\,d\eta \tag{9.37}$$

$$M_7 = \int_{-1}^{1}\int_{-1}^{1}\left[(\eta+1)^2+\left(\frac{1-\nu}{2}\right)(\xi-1)^2\right]d\xi\,d\eta \tag{9.38}$$

$$M_8 = \int_{-1}^{1}\int_{-1}^{1}\left[(\xi-1)^2 + \left(\frac{1-\nu}{2}\right)(\eta+1)^2\right] d\xi\, d\eta \tag{9.39}$$

Figure 9.4 illustrates the plot of $VRF_{\bar{E}_1} - VRF_{\bar{E}_8}$ for all the degrees of freedom of the 2×2 square element in one quadrant along positive values of κ_1 and κ_2, with the same values for the parameters: $E_0 = 125 \cdot 10^6$ and $\nu = 0.3$. Pairs of VRFs for the degrees of freedom $\bar{E}_1$ & $\bar{E}_5$, $\bar{E}_2$ & $\bar{E}_6$, $\bar{E}_3$ & $\bar{E}_7$ and $\bar{E}_4$ & $\bar{E}_8$ are identical.

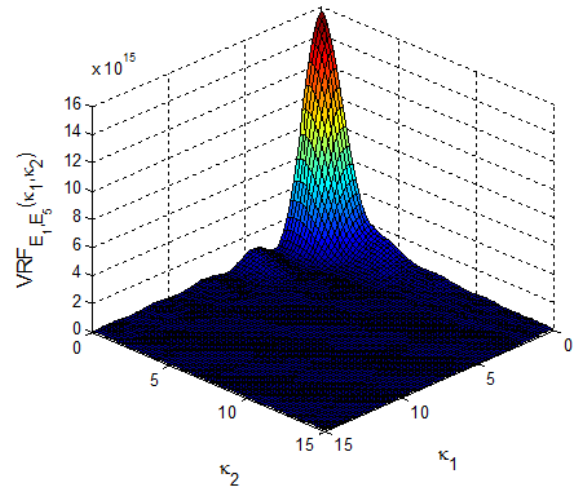

(a) $VRF_{\bar{E}_1}(\kappa_1, \kappa_2)$ & $VRF_{\bar{E}_5}(\kappa_1, \kappa_2)$

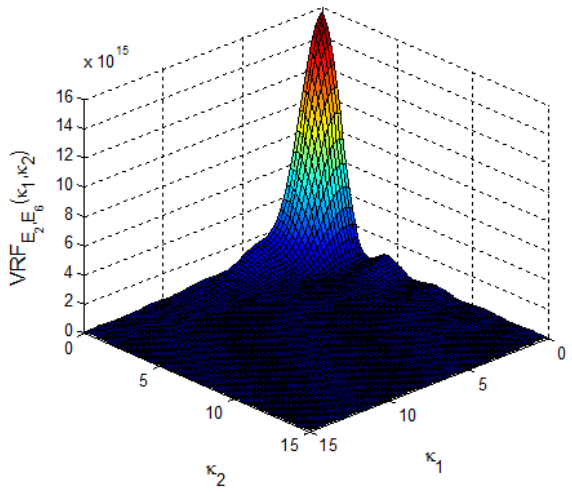

(b) $VRF_{\bar{E}_2}(\kappa_1, \kappa_2)$ & $VRF_{\bar{E}_6}(\kappa_1, \kappa_2)$

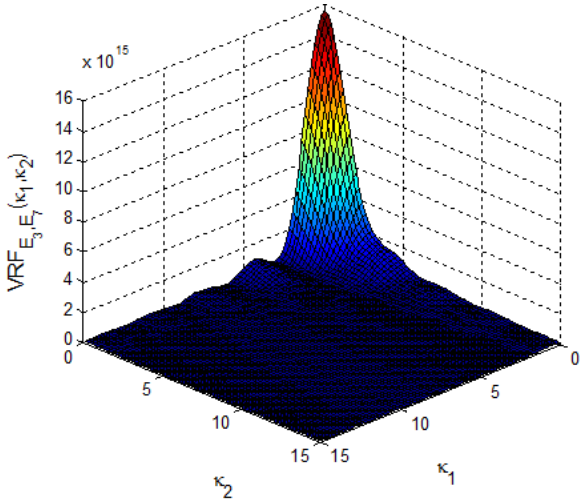

(c) $VRF_{\bar{E}_3}(\kappa_1, \kappa_2)$ & $VRF_{\bar{E}_7}(\kappa_1, \kappa_2)$

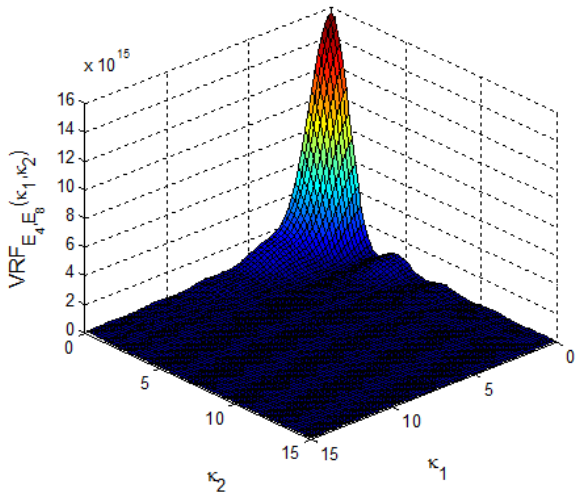

(d) $VRF_{\bar{E}_4}(\kappa_1, \kappa_6)$ & $VRF_{\bar{E}_8}(\kappa_1, \kappa_2)$

Figure 9.4: $VRF_{\bar{E}_1-\bar{E}_8}(\kappa_1, \kappa_2)$ of all degrees of freedom of 4-node 2×2 square element in natural coordinate system.

9.3.1 Symmetry Properties of VRFs

The VRFs of all degrees of freedom $VRF_{\bar{E}_1} - VRF_{\bar{E}_8}$ exhibit a series of symmetries that stem from the symmetric geometry of the 4-node square element itself.

1. Symmetry around κ_1 axis ($\kappa_2 = 0$) and κ_2 axis ($\kappa_1 = 0$). This property allows for plotting the VRFs in only one quadrant ($\kappa_1, \kappa_2 > 0$), as depicted in Figure 9.3 for $VRF_{\bar{E}_1}$.

2. Non-symmetry when $\kappa_1, \kappa_2 \neq 0$, for example around $\kappa_1 = \kappa_2$ axis, as illustrated also in Figure 9.3. This property dictates that the variance computed from equation 8.7, if a non-symmetric power spectrum S_{ff} is also chosen, will have a different value in each quadrant. Therefore, the computed variance must be the summation of the variances in each quadrant (for more details, refer to examples in the following section).

3. Pairs of VRFs of apparent properties $\bar{E}_1$ & $\bar{E}_5$, $\bar{E}_2$ & $\bar{E}_6$, $\bar{E}_3$ & $\bar{E}_7$ and $\bar{E}_4$ & $\bar{E}_8$ are identical, that is $VRF_{\bar{E}_1} = VRF_{\bar{E}_5}$, $VRF_{\bar{E}_2} = VRF_{\bar{E}_6}$, $VRF_{\bar{E}_3} = VRF_{\bar{E}_7}$ and $VRF_{\bar{E}_4} = VRF_{\bar{E}_8}$. Those pairs of degrees of freedom refer to diagonal matches in horizontal and vertical directions.

4. VRFs of horizontal degrees of freedom $\bar{E}_1$ & $\bar{E}_5$ are identical to vertical $\bar{E}_4$ & $\bar{E}_8$ when rotated by 90°.

5. VRFs of vertical degrees of freedom $\bar{E}_2$ & $\bar{E}_6$ are identical to horizontal $\bar{E}_3$ & $\bar{E}_7$ when rotated by 90°.

6. VRFs of horizontal degrees of freedom $\bar{E}_1$ & $\bar{E}_5$ are identical to horizontal $\bar{E}_3$ & $\bar{E}_7$ when κ_1 and κ_2 are switched in the respective analytical expressions (meaning that they are mirrored around κ_1 and κ_2 axis).

7. VRFs of vertical degrees of freedom $\bar{E}_2$ & $\bar{E}_6$ are identical to vertical $\bar{E}_4$ & $\bar{E}_8$ when κ_1 and κ_2 are switched in the respective analytical expressions (meaning that they are

mirrored around κ_1 and κ_2 axis).

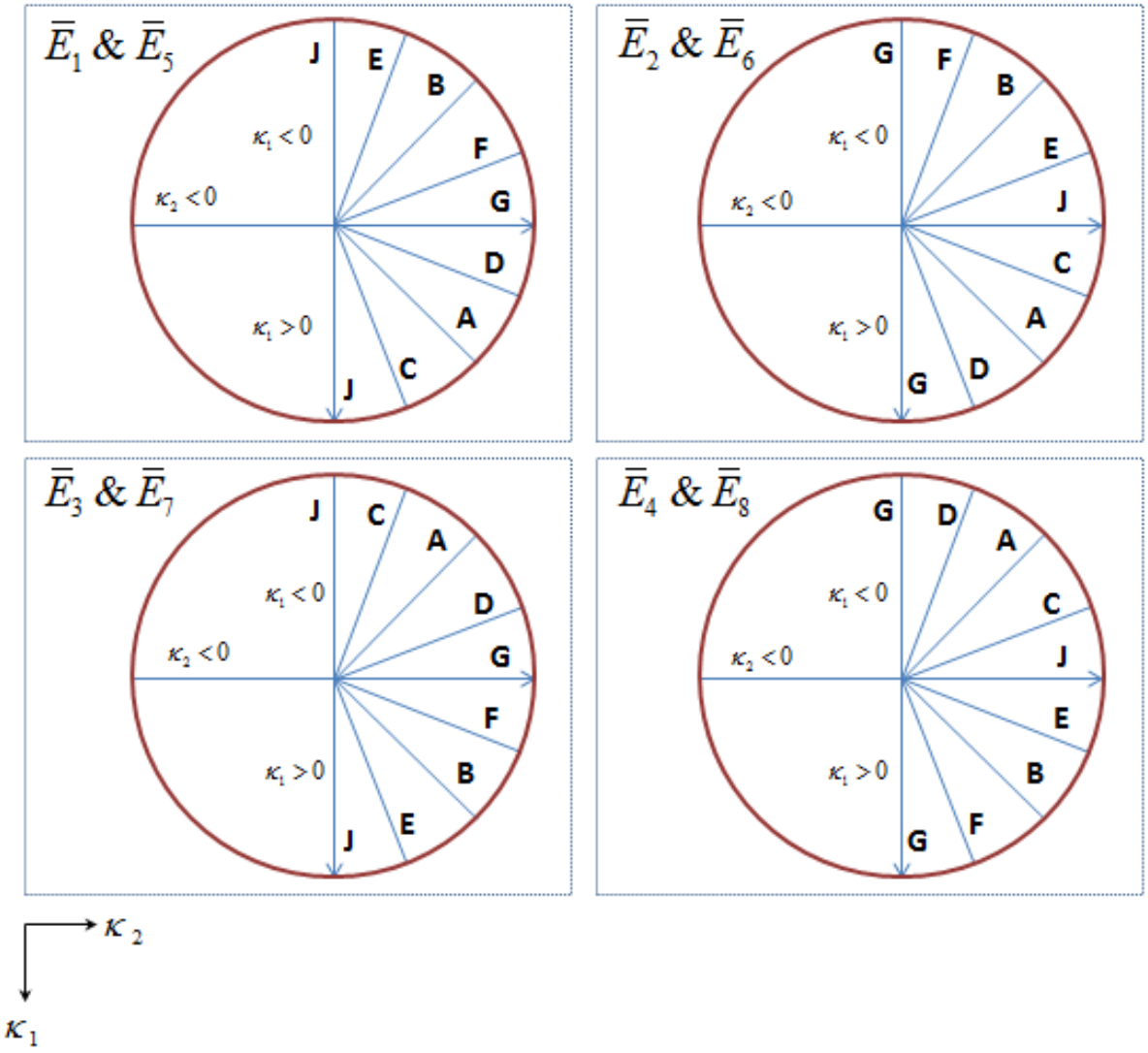

Figure 9.5: Virtual plot of VRFs of all degrees of freedom in two quadrants (the other two are symmetric). Letter notation denotes which radii are identified as identical 'slice' plots.

As an illustration of the above symmetries, Figure 9.5 shows a virtual plot of the VRFs of all the degrees of freedom at 2 quadrants (the other two quadrants are directly symmetric). The letter notation denotes which radii are identified as identical 'slices' of the VRF plots. For example, symmetry property 4 is obvious when comparing the circle of $\bar{E}_1$ & $\bar{E}_5$ to the circle of $\bar{E}_4$ & $\bar{E}_8$. Similarly, symmetry property 5 is confirmed when observing the pattern of radii for the circles of $\bar{E}_2$ & $\bar{E}_6$ and $\bar{E}_3$ & $\bar{E}_7$. Lastly, symmetry properties 6 and 7 are

also clarified in Figure 9.5, as they refer to the way the VRFs are mirrored around κ_2 axis (same holds for κ_1 axis for the symmetric quadrants not shown in the figure for simplicity).

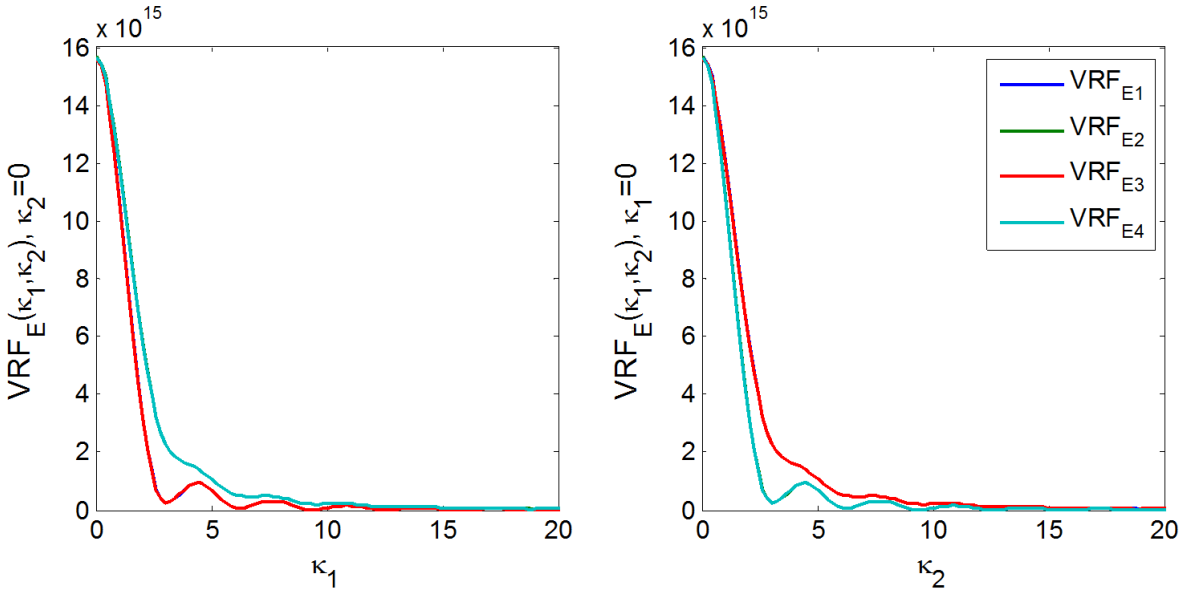

(a) Edge sections with $\kappa_1 = 0$ and $\kappa_2 = 0$.

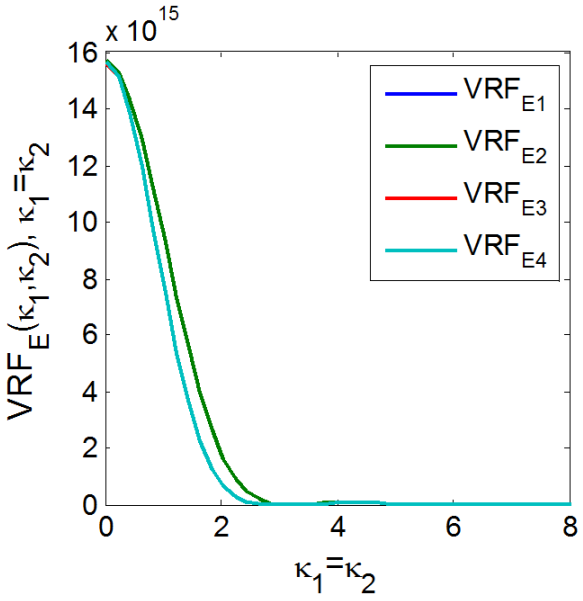

(b) Diagonal sections with $\kappa_1 = \kappa_2$.

Figure 9.6: VRFs of degrees of freedom $\bar{E}_1 - \bar{E}_4$ of 4-node square element in natural coordinate system.

Figure 9.6a and b depicts the VRFs of degrees of freedom $\bar{E}_1 - \bar{E}_4$ in edge sections obtained by setting $\kappa_1 = 0$ and $\kappa_2 = 0$ and in diagonal sections with $\kappa_1 = \kappa_2$, respectively

(VRFs of degrees of freedom $\bar{E}_5 - \bar{E}_8$ are identical to the first four curves, as indicated in symmetry property 3). The radii denoted with the letter 'J' are essentially depicted in the edge sections ($\kappa_1 = 0$ and $\kappa_2 = 0$) where VRFs of degrees of freedom $\bar{E}_1$ & $\bar{E}_3$ and $\bar{E}_2$ & $\bar{E}_4$ coincide. Moreover, the radii denoted with the letters 'A' and 'B' are depicted in the diagonal sections ($\kappa_1 = \kappa_2$) where VRFs of degrees of freedom $\bar{E}_1$ & $\bar{E}_2$ and $\bar{E}_3$ & $\bar{E}_4$ coincide, respectively. These 'slice' plots confirm symmetry properties 6 and 7 because when $\kappa_1 = \kappa_2$ then the wavenumbers κ_1 and κ_2 can be considered switched to each other.

It is therefore obvious that the VRFs for the 8 degrees of freedom are all related to each other. The aforementioned symmetry properties indicate that there is only one truly independent VRF expression which can be utilized to generate the VRF expressions of all the rest of the degrees of freedom. The following numerical validation demonstrates results for the target variance of apparent material properties $Var\left[\bar{E}\right]$ between different degrees of freedom.

9.3.2 Numerical Validation of VRFs

The numerical validation of all VRFs for the 8 degrees of freedom will be performed by analytically calculating the variance of apparent material properties according to equation (9.23) and comparing the results to direct Monte Carlo simulations with a sufficient number of sample functions for convergence. Consider now the spectral density function shown in Figure 9.7:

$$S_{ff,1} = \frac{0.0002}{\pi} \cdot e^{-0.024 \cdot \kappa_1^2 - 0.015 \cdot \kappa_2^2} \quad , \quad \kappa_1, \kappa_2 \in \mathbb{R}^n \tag{9.40}$$

with variance $\sigma_{ff}^2 = 0.01$ of the zero mean homogeneous random field $f(\xi, \eta)$. This example spectrum is non-symmetric since the decay rate is faster along κ_1 axis, while it is slower along κ_2 axis. Figure 9.8 displays a sample function in the natural (ξ, η) coordinate system generated from the above spectrum by employing the Spectral Representation Method in two dimensions following the procedures in Shinozuka and Deodatis 1996 [114], as described

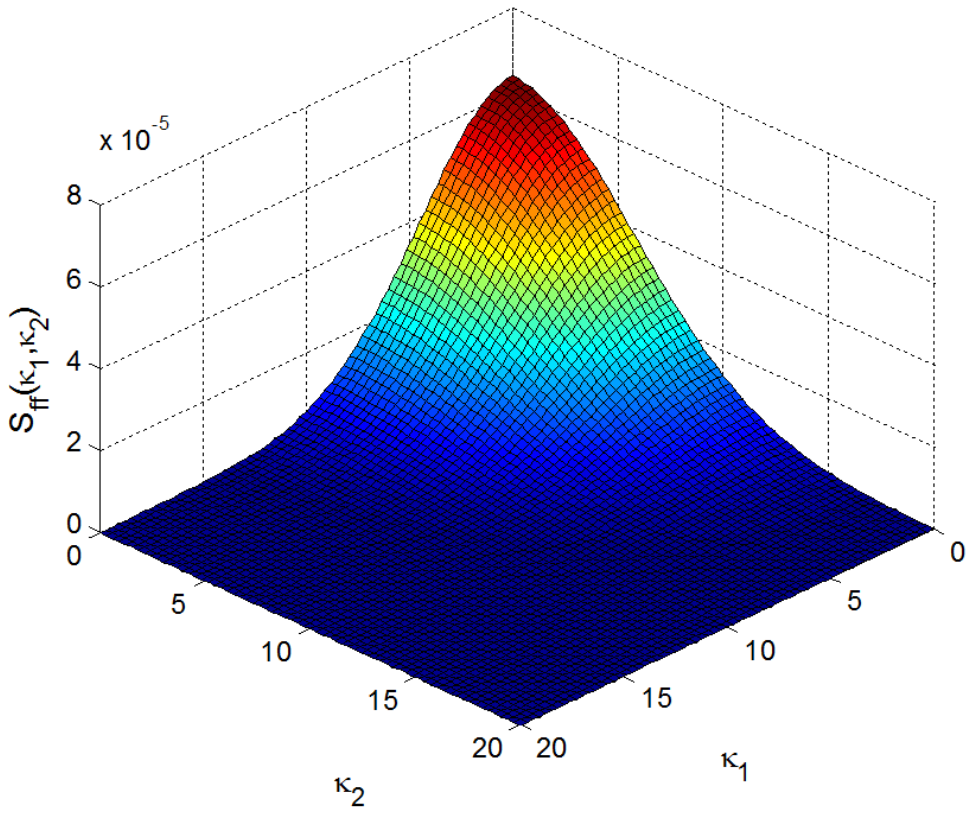

Figure 9.7: Non-symmetric spectral density function $S_{ff,1}(\kappa_1, \kappa_2)$ of zero mean homogeneous random field $f(x, y)$.

in Section 8.3.2 of this thesis. The computational cost of generating sample functions was drastically reduced by using the Fast Fourier Transform technique (e.g. Brigham 1988 [113]).

The analytically calculated variances of apparent properties for the 8 degrees of freedom through the respective variability response functions $VRF_{\bar{E}_1} - VRF_{\bar{E}_8}$ and equation (9.23) are:

$$\begin{aligned} Var\left[\bar{E}_1\right] = Var\left[\bar{E}_3\right] = Var\left[\bar{E}_5\right] = Var\left[\bar{E}_7\right] = 1.108 \cdot 10^{13} \\ Var\left[\bar{E}_2\right] = Var\left[\bar{E}_4\right] = Var\left[\bar{E}_6\right] = Var\left[\bar{E}_8\right] = 1.091 \cdot 10^{13} \end{aligned} \tag{9.41}$$

by using the same parameters $E_0 = 125 \cdot 10^6$ and $\nu = 0.3$. These values agree well with results obtained from direct MC simulations with one million generated sample functions for $f(\xi, \eta)$ through using equation (9.17), which yield for example $Var\left[\bar{E}_1\right] = 1.112 \cdot 10^{13}$ and $Var\left[\bar{E}_2\right] = 1.097 \cdot 10^{13}$. Note that the very large number of sample functions that need to be generated in order to achieve convergence is attributed to the two-dimensionality of

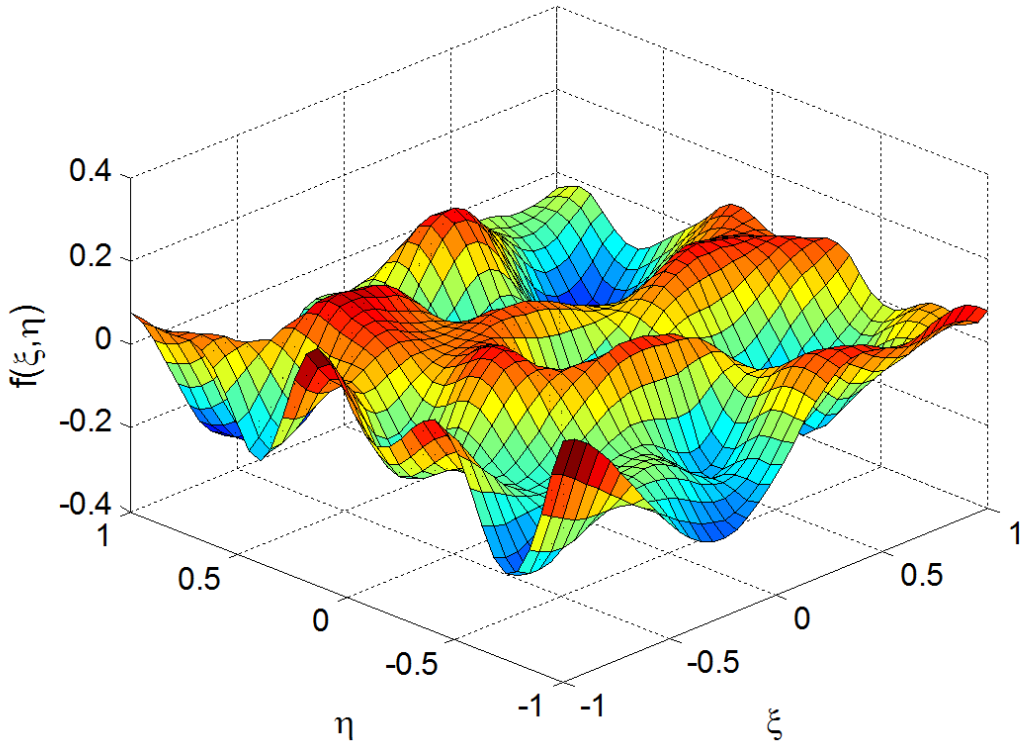

Figure 9.8: Generated sample function of the zero mean homogeneous stochastic field $f(\xi, \eta)$ using the non-symmetric spectral density function $S_{ff,1}(\kappa_1, \kappa_2)$ with variance $\sigma^2_{ff} = 0.01$.

the problem examined in this study. The small discrepancy between the analytical VRF approach and MC simulations stems from various potential sources of numerical error, such as error associated with the finite number of sample functions used in the MC simulations (even if there is convergence) and most importantly error associated with the numerical integration of the product of the VRFs and the spectral density function for predicting the variance in equation (9.23) (sensitivity of the value of the numerical integral on discretization of variables etc.)

Overall, the variability response functions introduced in this study provide very similar results for the predicted variance of apparent properties for the 8 degrees of freedom of the isoparametric square element. Although there is not a unique value for the variance but rather two values, it is considered by the authors that the VRF expressions effectively predict almost identical values for the variance of apparent material properties (1.5% error between the two predicted values). Nevertheless, it is proven that there is only one truly

independent VRF expression; this single expression can be utilized to generate the rest of the VRF expressions that can in turn predict two distinct but very similar values for the variance of apparent material properties.

However, when the spectral density function of the zero mean homogeneous random field $f(\xi, \eta)$ that characterizes the spatially varying elastic modulus $E(\xi, \eta)$ is in fact symmetric, then the VRFs of all the degrees of freedom predict the exact same value for the variance of apparent material properties. Let us consider for example the following symmetric SDF:

$$S_{ff,2} = \frac{0.0002}{\pi} \cdot e^{-0.02 \cdot \kappa_1^2 - 0.02 \cdot \kappa_2^2} \quad , \quad \kappa_1, \kappa_2 \in \mathbb{R}^n \tag{9.42}$$

The analytically calculated variances of apparent properties for the 8 degrees of freedom are in this case an identical number; $Var\left[\bar{E}_1\right] = Var\left[\bar{E}_2\right] = Var\left[\bar{E}_3\right] = Var\left[\bar{E}_4\right] = Var\left[\bar{E}_5\right] = Var\left[\bar{E}_6\right] = Var\left[\bar{E}_7\right] = Var\left[\bar{E}_8\right] = 1.093 \cdot 10^{13}$.

It should be noted at this point that the one truly independent VRF expression (reduced from the initial 8 degrees of freedom of the square 2×2 element) that predicts one or two values for the variance of apparent properties in case of a symmetric or non-symmetric spectrum, respectively, constitutes a minimum number of independent VRF expressions, i.e. an idealized case for a square finite element directly defined in the natural coordinate system. The number of independent VRF expressions may be more than one, when considering arbitrary shapes of finite elements. In the next sections of this chapter, it will be shown that for rectangular elements there are two independent VRF expressions, however for arbitrary shaped elements there are four independent VRF expressions.

9.4 Formulation of VRFs of a Rectangular Plane Stress Element in Physical Cartesian Coordinate System

Consider now a rectangular element in the physical Cartesian (x, y) coordinate system, without being mapped into the natural (ξ, η) coordinate system. In this case, the derivation of the VRFs for each degree of freedom will depend on the specific dimensions $L_x^{(e)}$ and $L_y^{(e)}$ of the element. This allows for analytical formulation of a series of VRFs which are dependent on the scale, shape and aspect ratio of example rectangular elements. The aforementioned dependence discussion and relevant conclusions are the main focus of Chapter 10: Examples that follows.

The derivation of $VRF_{\bar{E}_1} - VRF_{\bar{E}_8}$ in the physical Cartesian (x, y) coordinate system will follow the same procedure as the VRFs derivation in the natural (ξ, η) coordinate system. The shape functions for the 8 degrees of freedom are given by Segerlind 1984 [117]

$$\begin{aligned} N_1(x,y) &= \left[1 - \frac{x}{L_x^{(e)}}\right]\left[1 - \frac{y}{L_y^{(e)}}\right] \;;\; N_2(x,y) = \frac{x}{L_x^{(e)}}\left[1 - \frac{y}{L_y^{(e)}}\right] \\ N_3(x,y) &= \frac{xy}{L_x^{(e)} L_y^{(e)}} \;;\; N_4(x,y) = \frac{y}{L_y^{(e)}}\left[1 - \frac{x}{L_x^{(e)}}\right] \end{aligned} \tag{9.43}$$

where x and y are the physical coordinates defined in Figure 9.1. The strain-displacement matrix is 3×8 given by

$$B^{(e)}(x,y) = \begin{bmatrix} \frac{-L_y^{(e)} + y}{L_x^{(e)} L_y^{(e)}} & 0 & \frac{L_y^{(e)} - y}{L_x^{(e)} L_y^{(e)}} & 0 & \frac{y}{L_x^{(e)} L_y^{(e)}} & 0 & \frac{-y}{L_x^{(e)} L_y^{(e)}} & 0 \\ 0 & \frac{-L_x^{(e)} + x}{L_x^{(e)} L_y^{(e)}} & 0 & \frac{-x}{L_x^{(e)} L_y^{(e)}} & 0 & \frac{x}{L_x^{(e)} L_y^{(e)}} & 0 & \frac{L_x^{(e)} - x}{L_x^{(e)} L_y^{(e)}} \\ \frac{-L_x^{(e)} + x}{L_x^{(e)} L_y^{(e)}} & \frac{-L_y^{(e)} + y}{L_x^{(e)} L_y^{(e)}} & \frac{-x}{L_x^{(e)} L_y^{(e)}} & \frac{L_y^{(e)} - y}{L_x^{(e)} L_y^{(e)}} & \frac{x}{L_x^{(e)} L_y^{(e)}} & \frac{y}{L_x^{(e)} L_y^{(e)}} & \frac{L_x^{(e)} - x}{L_x^{(e)} L_y^{(e)}} & \frac{-y}{L_x^{(e)} L_y^{(e)}} \end{bmatrix} \tag{9.44}$$

where $L_x^{(e)}$ and $L_y^{(e)}$ are the dimensions of element (e) along the x and y axes, respectively

(see Figure 9.1).

The material property matrix and the random varying elastic modulus, as well as the expressions for the strain energy of the homogeneous and heterogeneous bodies are formulated as in Section 9.3. After imposing a unit displacement along the 1^{st} degree of freedom, the strain energy of the heterogeneous body is defined by the equation

$$W_{het}^{(e)} = \frac{1}{2} \iint_{\Omega} \begin{bmatrix} 1 & 0 & 0 & 0 & 0 & 0 & 0 & 0 \end{bmatrix} \Big([B]^T [D][B] \Big) \begin{bmatrix} 1 \\ 0 \\ 0 \\ 0 \\ 0 \\ 0 \\ 0 \\ 0 \end{bmatrix} d\Omega \tag{9.45}$$

which reduces to

$$\begin{aligned} W_{het}^{(e)} &= \frac{1}{2} \iint_{\Omega} \Big([B]^T [D][B] \Big)_{11} d\Omega = \\ &\frac{1}{2} \int_0^{L_y^{(e)}} \int_0^{L_x^{(e)}} \left(\frac{E_0 \left(1 + f(x,y)\right)}{1-\nu^2} \cdot \left[\left(\frac{y - L_y^{(e)}}{L_x^{(e)} L_y^{(e)}} \right)^2 + \left(\frac{1-\nu}{2} \right) \left(\frac{x - L_x^{(e)}}{L_x^{(e)} L_y^{(e)}} \right)^2 \right] \right) dx\, dy \end{aligned} \tag{9.46}$$

where E_0 is the nominal elastic modulus and $f(x, y)$ is a zero mean homogeneous random field with spectral density function $S_{ff}(\kappa_1, \kappa_2)$ that is a function of the wavenumbers $\kappa_1, \kappa_2 \in \mathbb{R}^n$. The respective element strain energy of the homogeneous body is

$$W_{hom}^{(e)} = \frac{1}{2} \int_0^{L_y^{(e)}} \int_0^{L_x^{(e)}} \left(\frac{\bar{E}_1}{1-\nu^2} \cdot \left[\left(\frac{y - L_y^{(e)}}{L_x^{(e)} L_y^{(e)}} \right)^2 + \left(\frac{1-\nu}{2} \right) \left(\frac{x - L_x^{(e)}}{L_x^{(e)} L_y^{(e)}} \right)^2 \right] \right) dx\, dy \tag{9.47}$$

where $\bar{E}_1$ is the equivalent apparent elastic modulus for the 1^{st} degree of freedom. By equating the two expressions for the strain energy, the apparent elastic modulus $\bar{E}_1$ in the (x, y) Cartesian coordinate system reduces to the expression

$$\bar{E}_1 = E_0 \cdot \frac{\int_0^{L_y^{(e)}} \int_0^{L_x^{(e)}} (1 + f(x,y)) \cdot \left[\left(\frac{y - L_y^{(e)}}{L_x^{(e)} L_y^{(e)}} \right)^2 + \left(\frac{1-\nu}{2} \right) \left(\frac{x - L_x^{(e)}}{L_x^{(e)} L_y^{(e)}} \right)^2 \right] dx\, dy}{\int_0^{L_y^{(e)}} \int_0^{L_x^{(e)}} \left[\left(\frac{y - L_y^{(e)}}{L_x^{(e)} L_y^{(e)}} \right)^2 + \left(\frac{1-\nu}{2} \right) \left(\frac{x - L_x^{(e)}}{L_x^{(e)} L_y^{(e)}} \right)^2 \right] dx\, dy} \tag{9.48}$$

Let us define the deterministic denominator in the expression of $\bar{E}_1$ as

$$M_1 = \int_0^{L_y^{(e)}} \int_0^{L_x^{(e)}} \left[\left(\frac{y - L_y^{(e)}}{L_x^{(e)} L_y^{(e)}} \right)^2 + \left(\frac{1-\nu}{2} \right) \left(\frac{x - L_x^{(e)}}{L_x^{(e)} L_y^{(e)}} \right)^2 \right] dx\, dy \tag{9.49}$$

The target variance of $\bar{E}_1$ is calculated by computing the expectation and the mean square of the above equation. After some algebra

$$\begin{aligned} Var\left[\bar{E}_1\right] =& E\left[\bar{E}_1^2\right] - E\left[\bar{E}_1\right]^2 = \\ & \frac{E_0^2}{M_1^2} \cdot \int_0^{L_y^{(e)}} \int_0^{L_x^{(e)}} \int_0^{L_y^{(e)}} \int_0^{L_x^{(e)}} \left[\left(\frac{y - L_y^{(e)}}{L_x^{(e)} L_y^{(e)}} \right)^2 + \left(\frac{1-\nu}{2} \right) \left(\frac{x - L_x^{(e)}}{L_x^{(e)} L_y^{(e)}} \right)^2 \right] \times \\ & \left[\left(\frac{w - L_y^{(e)}}{L_x^{(e)} L_y^{(e)}} \right)^2 + \left(\frac{1-\nu}{2} \right) \left(\frac{u - L_x^{(e)}}{L_x^{(e)} L_y^{(e)}} \right)^2 \right] \cdot R_{ff}(s_1, s_2)\, dx\, dy\, du\, dw \end{aligned} \tag{9.50}$$

where $R_{ff}(s_1, s_2) = E\Big[f(x,y) f(u,w)\Big]$ is the spatial correlation function of $f(x, y)$ and $s_1, s_2 \in \mathbb{R}$ are vectors of separation distances with $s_1 = x - u$ and $s_2 = y - w$.

If the spectral density $S_{ff}(\kappa_1, \kappa_2)$ is substituted for $R_{ff}(s_1, s_2)$ through the Wiener-

Khintchine transform, and if we change the order of integration, then

$$Var\left[\bar{E}_1\right] = \int_{-\infty}^{\infty}\int_{-\infty}^{\infty} VRF_{\bar{E}_1}\left(\kappa_1,\kappa_2\right) S_{ff}\left(\kappa_1,\kappa_2\right)\, d\kappa_1\, d\kappa_2 \tag{9.51}$$

where $VRF_{\bar{E}_1}$ is defined as

$$\begin{aligned} VRF_{\bar{E}_1}(\kappa_1,\kappa_2) \;=\; & \frac{E_0^2}{M_1^2}\cdot \int_0^{L_y^{(e)}}\int_0^{L_x^{(e)}}\int_0^{L_y^{(e)}}\int_0^{L_x^{(e)}} \left[\left(\frac{y-L_y^{(e)}}{L_x^{(e)}L_y^{(e)}}\right)^2 + \left(\frac{1-\nu}{2}\right)\left(\frac{x-L_x^{(e)}}{L_x^{(e)}L_y^{(e)}}\right)^2\right]\times \\ & \left[\left(\frac{w-L_y^{(e)}}{L_x^{(e)}L_y^{(e)}}\right)^2 + \left(\frac{1-\nu}{2}\right)\left(\frac{u-L_x^{(e)}}{L_x^{(e)}L_y^{(e)}}\right)^2\right]\cdot e^{-i(\kappa_1 s_1+\kappa_2 s_2)}\, dx\, dy\, du\, dw \end{aligned} \tag{9.52}$$

After some algebra

$$\begin{aligned} VRF_{\bar{E}_1}(\kappa_1,\kappa_2) \;=\; & \frac{E_0^2}{2\kappa_1^6\kappa_2^6 L_x^4 L_y^4\left(\frac{L_x}{6L_y}+\frac{L_y}{3L_x}-\frac{L_x\nu}{6L_y}\right)^2}\Big[\kappa_1^4(32+\kappa_2^4(4L_y^4-2L_x^2L_y^2(-1+\nu)+ \\ & L_x^4(-1+\nu)^2)+8\kappa_2^2L_x^2(-1+\nu))-8\kappa_1^3\kappa_2^3L_xL_y(-1+\nu)+8\kappa_1^2\kappa_2^2(-4+\kappa_2^2L_y^2)(-1+\nu)+8\kappa_2^4(-1+\nu)^2- \\ & (\kappa_1^4(32+\kappa_2^2(-2L_y^2+L_x^2(-1+\nu))(8+\kappa_2^2L_x^2(-1+\nu)))-8\kappa_1^3\kappa_2^3L_xL_y(-1+\nu)+8\kappa_1^2\kappa_2^2(-4+ \\ & \kappa_2^2L_y^2)(-1+\nu)+8\kappa_2^4(-1+\nu)^2)cos(\kappa_2L_y)-2cos(\kappa_1L_x)(\kappa_1^4(16+\kappa_2^2(2\kappa_2^2L_y^4-L_x^2(-4+\kappa_2^2L_y^2) \\ & (-1+\nu)))-4\kappa_1^3\kappa_2^3L_xL_y(-1+\nu)-2\kappa_1^2\kappa_2^2(8+\kappa_2^2(-2L_y^2+L_x^2(-1+\nu)))(-1+\nu)+4\kappa_2^4(-1+\nu)^2+ \\ & (\kappa_1^4(-16+\kappa_2^2(8L_y^2+L_x^2(-4+\kappa_2^2L_y^2)(-1+\nu)))+4\kappa_1^3\kappa_2^3L_xL_y(-1+\nu)+2\kappa_1^2\kappa_2^2(8+\kappa_2^2 \\ & (-2L_y^2+L_x^2(-1+\nu)))(-1+\nu)-4\kappa_2^4(-1+\nu)^2)cos(\kappa_2L_y))-4\kappa_1\kappa_2(-\kappa_1L_y(\kappa_1^2(8+\kappa_2^2L_x^2(-1+\nu))- \\ & 4\kappa_2^2(-1+\nu)-\kappa_1\kappa_2^3L_xL_y(-1+\nu))(-1+cos(\kappa_1L_x))sin(\kappa_2L_y)+1/2\kappa_2L_x(-1+\nu)sin(\kappa_1L_x)(2(2\kappa_2^2+ \\ & \kappa_1^2(4+\kappa_2L_y(\kappa_1L_x-k2L_y))-2\kappa_2^2\nu)(-1+cos(\kappa_2L_y))+\kappa_1^2\kappa_2L_y(4+\kappa_1\kappa_2L_xL_y)sin(\kappa_2L_y)))\Big] \end{aligned} \tag{9.53}$$

Naturally, the above VRF expression is only dependent on the following deterministic quantities: element's specific dimensions $L_x^{(e)}$ and $L_y^{(e)}$, Poisson's ratio ν and nominal elastic modulus E_0, while it is independent of the spectral density function S_{ff} and probability distribution function of the zero mean homogeneous random field $f(x,y)$.

The rest of the VRFs for the remaining 7 degrees of freedom are derived similarly, by

imposing unit displacements in the respective d.o.f. and performing the same calculations. The expressions for the rest of the VRFs in the physical Cartesian coordinate system are as following

$$VRF_{\bar{E}_2}(\kappa_1,\kappa_2) = \frac{E_0^2}{M_2^2}\cdot\int_0^{L_y^{(e)}}\int_0^{L_x^{(e)}}\int_0^{L_y^{(e)}}\int_0^{L_x^{(e)}}\left[\left(\frac{x-L_x^{(e)}}{L_x^{(e)}L_y^{(e)}}\right)^2+\left(\frac{1-\nu}{2}\right)\left(\frac{y-L_y^{(e)}}{L_x^{(e)}L_y^{(e)}}\right)^2\right]\times \left[\left(\frac{u-L_x^{(e)}}{L_x^{(e)}L_y^{(e)}}\right)^2+\left(\frac{1-\nu}{2}\right)\left(\frac{w-L_y^{(e)}}{L_x^{(e)}L_y^{(e)}}\right)^2\right]\cdot e^{-i(\kappa_1 s_1+\kappa_2 s_2)}\,dx\,dy\,du\,dw \tag{9.54}$$

$$VRF_{\bar{E}_3}(\kappa_1,\kappa_2) = \frac{E_0^2}{M_3^2}\cdot\int_0^{L_y^{(e)}}\int_0^{L_x^{(e)}}\int_0^{L_y^{(e)}}\int_0^{L_x^{(e)}}\left[\left(\frac{L_y^{(e)}-y}{L_x^{(e)}L_y^{(e)}}\right)^2+\left(\frac{1-\nu}{2}\right)\left(\frac{x}{L_x^{(e)}L_y^{(e)}}\right)^2\right]\times \left[\left(\frac{L_y^{(e)}-w}{L_x^{(e)}L_y^{(e)}}\right)^2+\left(\frac{1-\nu}{2}\right)\left(\frac{u}{L_x^{(e)}L_y^{(e)}}\right)^2\right]\cdot e^{-i(\kappa_1 s_1+\kappa_2 s_2)}\,dx\,dy\,du\,dw \tag{9.55}$$

$$VRF_{\bar{E}_4}(\kappa_1,\kappa_2) = \frac{E_0^2}{M_4^2}\cdot\int_0^{L_y^{(e)}}\int_0^{L_x^{(e)}}\int_0^{L_y^{(e)}}\int_0^{L_x^{(e)}}\left[\left(\frac{x}{L_x^{(e)}L_y^{(e)}}\right)^2+\left(\frac{1-\nu}{2}\right)\left(\frac{L_y^{(e)}-y}{L_x^{(e)}L_y^{(e)}}\right)^2\right]\times \left[\left(\frac{u}{L_x^{(e)}L_y^{(e)}}\right)^2+\left(\frac{1-\nu}{2}\right)\left(\frac{L_y^{(e)}-w}{L_x^{(e)}L_y^{(e)}}\right)^2\right]\cdot e^{-i(\kappa_1 s_1+\kappa_2 s_2)}\,dx\,dy\,du\,dw \tag{9.56}$$

$$VRF_{\bar{E}_5}(\kappa_1,\kappa_2) = \frac{E_0^2}{M_5^2}\cdot\int_0^{L_y^{(e)}}\int_0^{L_x^{(e)}}\int_0^{L_y^{(e)}}\int_0^{L_x^{(e)}}\left[\left(\frac{y}{L_x^{(e)}L_y^{(e)}}\right)^2+\left(\frac{1-\nu}{2}\right)\left(\frac{x}{L_x^{(e)}L_y^{(e)}}\right)^2\right]\times \left[\left(\frac{w}{L_x^{(e)}L_y^{(e)}}\right)^2+\left(\frac{1-\nu}{2}\right)\left(\frac{u}{L_x^{(e)}L_y^{(e)}}\right)^2\right]\cdot e^{-i(\kappa_1 s_1+\kappa_2 s_2)}\,dx\,dy\,du\,dw \tag{9.57}$$

$$VRF_{\bar{E}_6}(\kappa_1,\kappa_2) = \frac{E_0^2}{M_6^2}\cdot\int_0^{L_y^{(e)}}\int_0^{L_x^{(e)}}\int_0^{L_y^{(e)}}\int_0^{L_x^{(e)}}\left[\left(\frac{x}{L_x^{(e)}L_y^{(e)}}\right)^2+\left(\frac{1-\nu}{2}\right)\left(\frac{y}{L_x^{(e)}L_y^{(e)}}\right)^2\right]\times \left[\left(\frac{u}{L_x^{(e)}L_y^{(e)}}\right)^2+\left(\frac{1-\nu}{2}\right)\left(\frac{w}{L_x^{(e)}L_y^{(e)}}\right)^2\right]\cdot e^{-i(\kappa_1 s_1+\kappa_2 s_2)}\,dx\,dy\,du\,dw \tag{9.58}$$

$$VRF_{\bar{E}_7}(\kappa_1,\kappa_2) = \frac{E_0^2}{M_7^2}\cdot\int_0^{L_y^{(e)}}\int_0^{L_x^{(e)}}\int_0^{L_y^{(e)}}\int_0^{L_x^{(e)}}\left[\left(\frac{y}{L_x^{(e)}L_y^{(e)}}\right)^2+\left(\frac{1-\nu}{2}\right)\left(\frac{L_x^{(e)}-x}{L_x^{(e)}L_y^{(e)}}\right)^2\right]\times \left[\left(\frac{w}{L_x^{(e)}L_y^{(e)}}\right)^2+\left(\frac{1-\nu}{2}\right)\left(\frac{L_x^{(e)}-u}{L_x^{(e)}L_y^{(e)}}\right)^2\right]\cdot e^{-i(\kappa_1 s_1+\kappa_2 s_2)}\,dx\,dy\,du\,dw \tag{9.59}$$

$$VRF_{\bar{E}_8}(\kappa_1,\kappa_2) = \frac{E_0^2}{M_8^2}\cdot\int_0^{L_y^{(e)}}\int_0^{L_x^{(e)}}\int_0^{L_y^{(e)}}\int_0^{L_x^{(e)}}\left[\left(\frac{L_x^{(e)}-x}{L_x^{(e)}L_y^{(e)}}\right)^2+\left(\frac{1-\nu}{2}\right)\left(\frac{y}{L_x^{(e)}L_y^{(e)}}\right)^2\right]\times \left[\left(\frac{L_x^{(e)}-u}{L_x^{(e)}L_y^{(e)}}\right)^2+\left(\frac{1-\nu}{2}\right)\left(\frac{w}{L_x^{(e)}L_y^{(e)}}\right)^2\right]\cdot e^{-i(\kappa_1 s_1+\kappa_2 s_2)}\,dx\,dy\,du\,dw \tag{9.60}$$

where the deterministic quantities of $M_2 - M_8$ are defined as

$$M_2 = \int_0^{L_y^{(e)}}\int_0^{L_x^{(e)}}\left[\left(\frac{y-L_y^{(e)}}{L_x^{(e)}L_y^{(e)}}\right)^2+\left(\frac{1-\nu}{2}\right)\left(\frac{x-L_x^{(e)}}{L_x^{(e)}L_y^{(e)}}\right)^2\right]dx\,dy \tag{9.61}$$

$$M_3 = \int_0^{L_y^{(e)}}\int_0^{L_x^{(e)}}\left[\left(\frac{L_y^{(e)}-y}{L_x^{(e)}L_y^{(e)}}\right)^2+\left(\frac{1-\nu}{2}\right)\left(\frac{x}{L_x^{(e)}L_y^{(e)}}\right)^2\right]dx\,dy \tag{9.62}$$

$$M_4 = \int_0^{L_y^{(e)}}\int_0^{L_x^{(e)}}\left[\left(\frac{x}{L_x^{(e)}L_y^{(e)}}\right)^2+\left(\frac{1-\nu}{2}\right)\left(\frac{L_y^{(e)}-y}{L_x^{(e)}L_y^{(e)}}\right)^2\right]dx\,dy \tag{9.63}$$

$$M_5 = \int_0^{L_y^{(e)}} \int_0^{L_x^{(e)}} \left[\left(\frac{y}{L_x^{(e)} L_y^{(e)}} \right)^2 + \left(\frac{1-\nu}{2} \right) \left(\frac{x}{L_x^{(e)} L_y^{(e)}} \right)^2 \right] dx\, dy \tag{9.64}$$

$$M_6 = \int_0^{L_y^{(e)}} \int_0^{L_x^{(e)}} \left[\left(\frac{x}{L_x^{(e)} L_y^{(e)}} \right)^2 + \left(\frac{1-\nu}{2} \right) \left(\frac{y}{L_x^{(e)} L_y^{(e)}} \right)^2 \right] dx\, dy \tag{9.65}$$

$$M_7 = \int_0^{L_y^{(e)}} \int_0^{L_x^{(e)}} \left[\left(\frac{y}{L_x^{(e)} L_y^{(e)}} \right)^2 + \left(\frac{1-\nu}{2} \right) \left(\frac{L_x^{(e)} - x}{L_x^{(e)} L_y^{(e)}} \right)^2 \right] dx\, dy \tag{9.66}$$

$$M_8 = \int_0^{L_y^{(e)}} \int_0^{L_x^{(e)}} \left[\left(\frac{L_x^{(e)} - x}{L_x^{(e)} L_y^{(e)}} \right)^2 + \left(\frac{1-\nu}{2} \right) \left(\frac{y}{L_x^{(e)} L_y^{(e)}} \right)^2 \right] dx\, dy \tag{9.67}$$

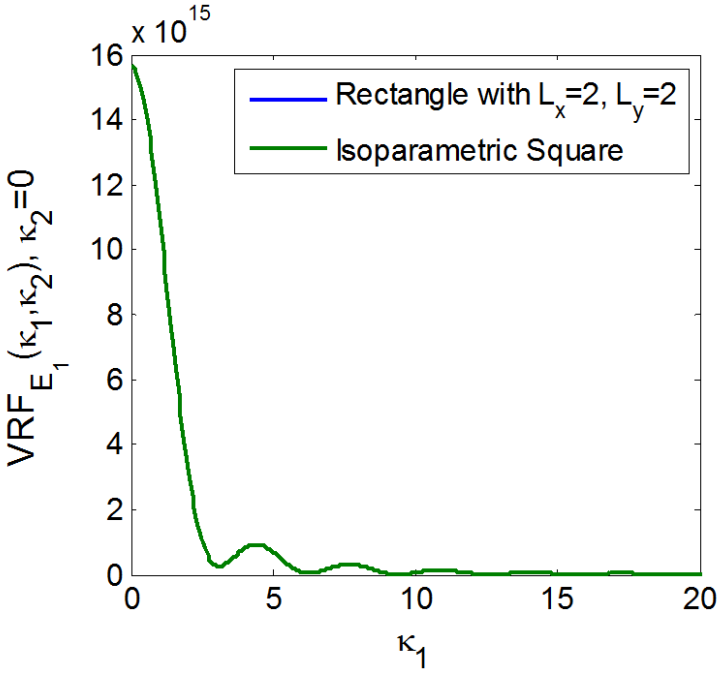

Figure 9.9: Comparison of $VRF_{\bar{E}_1}$ curves of rectangle element with $L_x^{(e)} = 2$ and $L_y^{(e)} = 2$ and isoparametric square element of Section 9.3.

9.4.1 Example 1 - Analytical Verification

Let us firstly consider an example rectangle element with $L_x^{(e)} = 2$ and $L_y^{(e)} = 2$. The VRFs of all degrees of freedom in this case are reduced, as expected, to those computed for the isoparametric 2×2 square element of Section 9.3 shown in Figure 9.6. In other words, equation (9.25) of $VRF_{\bar{E}_1}$ for the isoparametric 2×2 square plane stress element in natural coordinate system provides an identical VRF curve as equation (9.53) of the rectangular plane stress element in physical Cartesian coordinate system with $L_x^{(e)} = 2$ and $L_y^{(e)} = 2$ (Figure 9.9). Moreover, the two curves provide identical values for the analytically calculated variances for the 8 degrees of freedom through equation (9.23) and by utilizing the non-symmetric spectrum of equation (9.40); indicatively for the first degree of freedom $Var\left[\bar{E}_1\right] = 1.108 \cdot 10^{13}$ (see equation 9.41).

9.4.2 Example 2

The VRFs of degrees of freedom $\bar{E}_1 - \bar{E}_4$ for a second example rectangle element with $L_x^{(e)} = 0.5$ and $L_y^{(e)} = 2$ are plotted in Figure 9.10 in edge sections obtained by setting $\kappa_1 = 0$ and $\kappa_2 = 0$ and in diagonal sections with $\kappa_1 = \kappa_2$, by using the parameters $E_0 = 125 \cdot 10^6$ and $\nu = 0.3$. All VRFs display their maximum value of E_0^2 for zero wavenumber. The same symmetry properties 1-3 are observed as was the case for the isoparametric square element; the VRFs are symmetric around κ_1 and κ_2 axis and they are non-symmetric for $\kappa_1, \kappa_2 \neq 0$. Furthermore, the expressions for the pairs $\bar{E}_1$ & $\bar{E}_5$, $\bar{E}_2$ & $\bar{E}_6$, $\bar{E}_3$ & $\bar{E}_7$ and $\bar{E}_4$ & $\bar{E}_8$ are still identical. However, the rest of the symmetries 4-7 seem to have been quite diminished but not entirely; the curves seem to appear in close but not identical pairs according to the edge and diagonal sections shown in Figure 9.10. Nevertheless, it can be shown that there are only two independent expressions for the VRFs of different degrees of freedom that can predict two values of variance of apparent material properties. Let us again consider the non-symmetric spectral density function of equation (9.40). The analytically calculated variances

of apparent properties for the 8 degrees of freedom through the respective variability response functions $VRF_{\bar{E}_1} - VRF_{\bar{E}_8}$ and equation (9.51) are:

$$\begin{aligned} Var\left[\bar{E}_1\right] = Var\left[\bar{E}_3\right] = Var\left[\bar{E}_5\right] = Var\left[\bar{E}_7\right] = 3.752 \cdot 10^{13} \\ Var\left[\bar{E}_2\right] = Var\left[\bar{E}_4\right] = Var\left[\bar{E}_6\right] = Var\left[\bar{E}_8\right] = 3.392 \cdot 10^{13} \end{aligned} \tag{9.68}$$

Overall, the variability response functions for a generic rectangular element provide very similar results for the predicted variance of apparent properties for the 8 degrees of freedom. Although there is not a unique VRF but rather two independent expressions, those VRFs essentially predict very comparable values for the variance of apparent material properties (6.5% error between the two predicted values). Moreover, if the spectrum utilized were to be symmetric as is the case with the spectral density function of equation (9.42), there are still two different values for the variance of apparent material properties:

$$\begin{aligned} Var\left[\bar{E}_1\right] = Var\left[\bar{E}_3\right] = Var\left[\bar{E}_5\right] = Var\left[\bar{E}_7\right] = 3.812 \cdot 10^{13} \\ Var\left[\bar{E}_2\right] = Var\left[\bar{E}_4\right] = Var\left[\bar{E}_6\right] = Var\left[\bar{E}_8\right] = 3.454 \cdot 10^{13} \end{aligned} \tag{9.69}$$

in contrast to the isoparametric square element of Section 9.3 where there is a single value for the variance in case of a symmetric SDF.

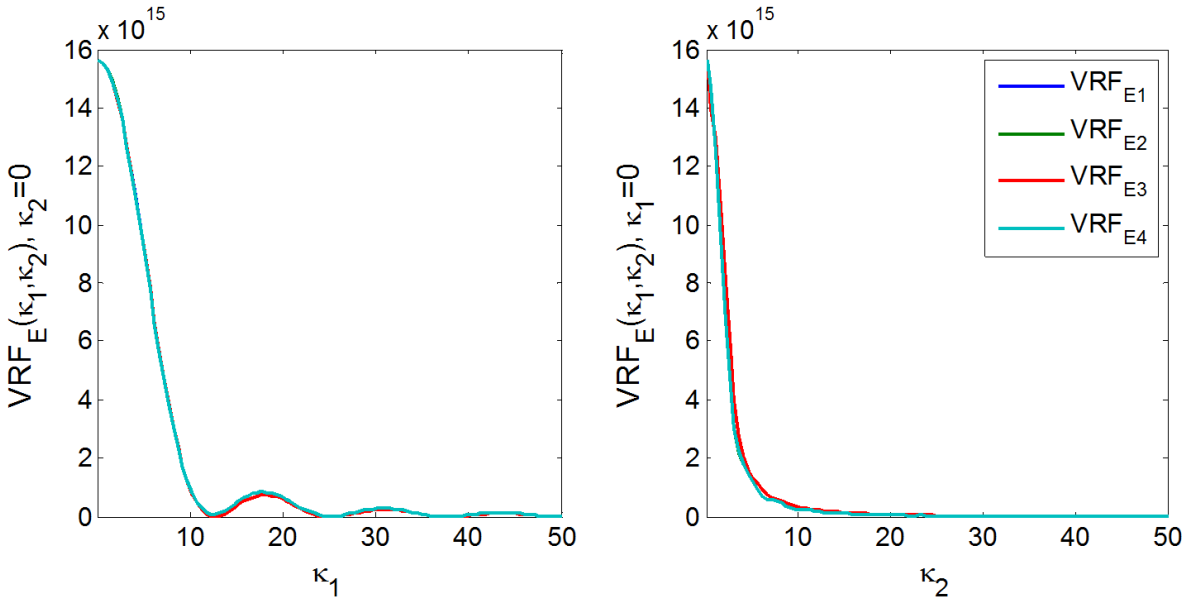

(a) Edge sections with $\kappa_1 = 0$ and $\kappa_2 = 0$.

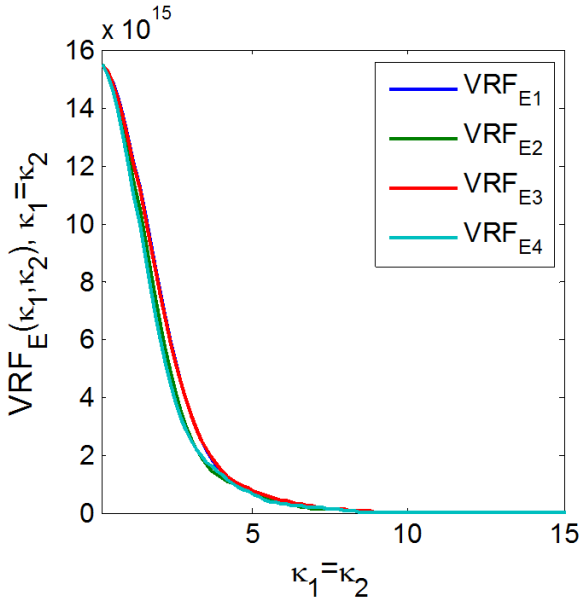

(b) Diagonal sections with $\kappa_1 = \kappa_2$.

Figure 9.10: VRFs of degrees of freedom $\bar{E}_1 - \bar{E}_4$ of 4-node example rectangular element with $L_x^{(e)} = 0.5$ and $L_y^{(e)} = 2$ in physical coordinate system.

9.5 Formulation of VRFs of a Quadrilateral Isoparametric Plane Stress Element in Natural Coordinate System

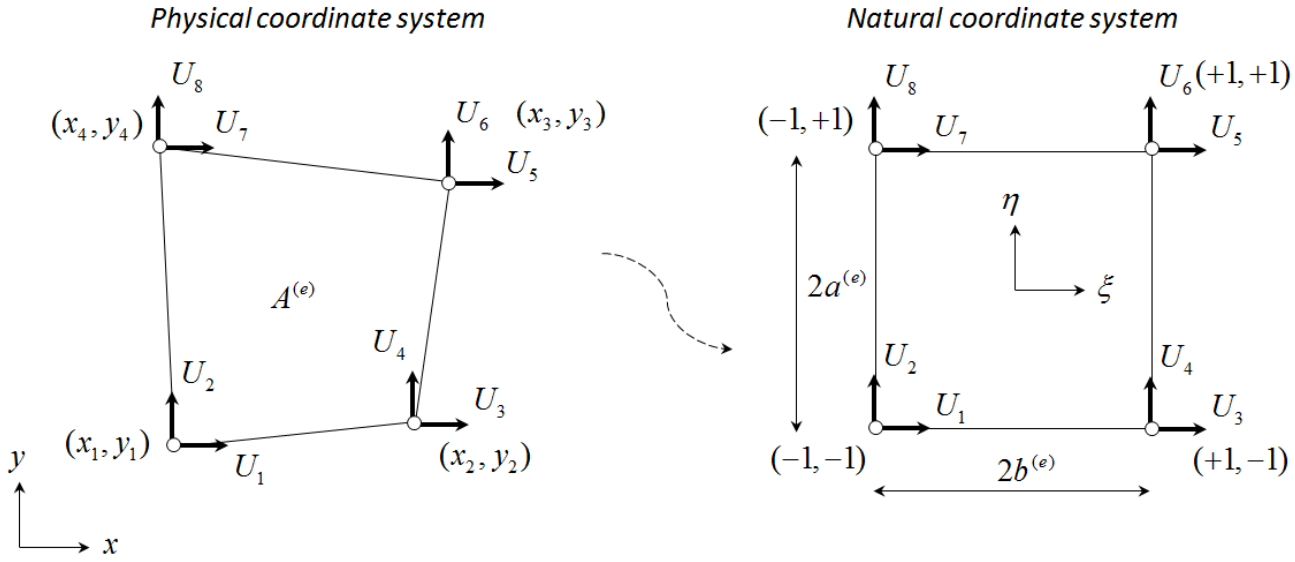

Figure 9.11: Quadrilateral 4-node plane stress element and mapping from physical to natural coordinate system.

After the formulation of VRFs of apparent material properties for rectangular elements in both the natural and physical coordinate system, the most general case is to develop a VRF in the natural coordinate system for any 4-node quadrilateral element, including arbitrary shapes such as trapezoids, that can accommodate simulation of complex geometry systems. Figure 9.11 depicts such a general isoparametric formulation where a quadrilateral element in the physical (x, y) coordinate system is mapped into an equivalent isoparametric square element in the natural (ξ, η) coordinate system. The VRF formulation will follow the same procedure as the previous sections, while for demonstration and simplicity purposes, the VRF will be calculated for an example trapezoid element (Figure 9.12). However, this VRF formulation is not limited to this specific example; it and can be performed for any shape of quadrilateral element.

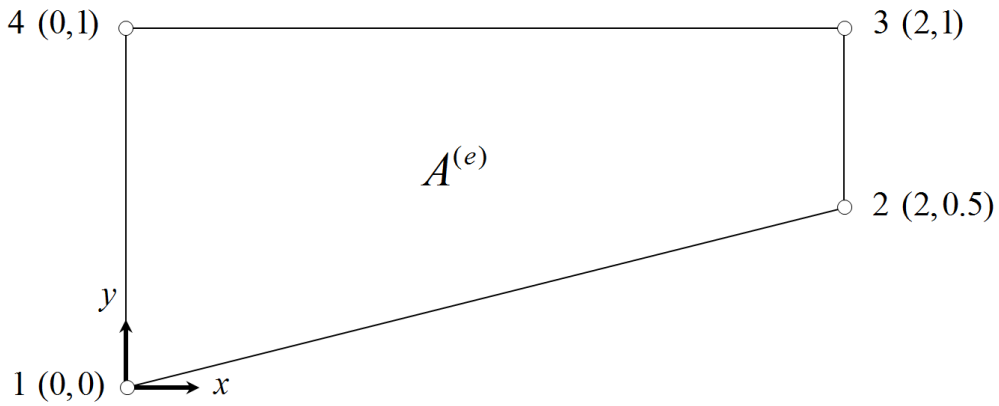

Figure 9.12: Trapezoid example finite element with nodal coordinates.

The isoparametric shape functions of the parent element are given by equation (9.8). The nodal coordinate matrix and Jacobian matrix for the example trapezoid element is

$$[x^{(e)}\ y^{(e)}] = \begin{bmatrix} x_1^{(e)} & y_1^{(e)} \\ x_2^{(e)} & y_2^{(e)} \\ x_3^{(e)} & y_3^{(e)} \\ x_4^{(e)} & y_4^{(e)} \end{bmatrix} = \begin{bmatrix} 0 & 0 \\ 2 & 0.5 \\ 2 & 1 \\ 0 & 1 \end{bmatrix} \tag{9.70}$$

$$J^{(e)} = [GN] \cdot [x^{(e)}\ y^{(e)}] = \begin{bmatrix} \frac{\partial N_1}{\partial \xi} & \frac{\partial N_2}{\partial \xi} & \frac{\partial N_3}{\partial \xi} & \frac{\partial N_4}{\partial \xi} \\ \frac{\partial N_1}{\partial \eta} & \frac{\partial N_2}{\partial \eta} & \frac{\partial N_3}{\partial \eta} & \frac{\partial N_4}{\partial \eta} \end{bmatrix} \begin{bmatrix} x_1^{(e)} & y_1^{(e)} \\ x_2^{(e)} & y_2^{(e)} \\ x_3^{(e)} & y_3^{(e)} \\ x_4^{(e)} & y_4^{(e)} \end{bmatrix} \tag{9.71}$$

After substituting

$$J^{(e)} = \frac{1}{4}\begin{bmatrix} \eta-1 & 1-\eta & 1-\eta & 1+\eta & -1-\eta \\ \xi-1 & -\xi-1 & 1+\xi & 1+\xi & 1-\xi \end{bmatrix}\begin{bmatrix} 0 & 0 \\ 2 & 0.5 \\ 2 & 1 \\ 0 & 1 \end{bmatrix} \tag{9.72}$$

and thus

$$J^{(e)} = \begin{bmatrix} 1 & 0.125-0.125\eta \\ 0 & 0.375-0.125\xi \end{bmatrix} \tag{9.73}$$

where G is the gradient operator in the natural (ξ, η) coordinate system and thus $[GN]$ is the partial derivative matrix of the isoparametric shape functions. The determinant and inverse of the Jacobian are

$$|J^{(e)}| = 0.375-0.125\xi \ , \ (J^{(e)})^{-1} = \begin{bmatrix} 1 & \dfrac{\eta-1}{3-\xi} \\ 0 & \dfrac{8}{3-\xi} \end{bmatrix} \tag{9.74}$$

For the 3×8 strain-displacement matrix $B^{(e)}(\xi,\eta)$, we perform the following calculations

$$(J^{(e)})^{-1}\cdot[GN] = \frac{1}{4}\begin{bmatrix} \dfrac{\eta-1}{3-\xi}(\xi-1)+\eta-1 & \dfrac{\eta-1}{3-\xi}(-1-\xi)+1-\eta & \dfrac{\eta-1}{3-\xi}(\xi+1)+\eta+1 & \dfrac{\eta-1}{3-\xi}(1-\xi)-1-\eta \\ \dfrac{8}{3-\xi}(\xi-1) & \dfrac{8}{3-\xi}(-1-\xi) & \dfrac{8}{3-\xi}(\xi+1) & \dfrac{8}{3-\xi}(1-\xi) \end{bmatrix} \tag{9.75}$$

and thus $B^{(e)}(\xi,\eta) = \frac{1}{4}\times$

$$\begin{bmatrix} \frac{\eta-1}{3-\xi}(\xi-1)+\eta-1 & 0 & \frac{\eta-1}{3-\xi}(-1-\xi)+1-\eta & 0 & \frac{\eta-1}{3-\xi}(\xi+1)+\eta+1 & 0 & \frac{\eta-1}{3-\xi}(1-\xi)-1-\eta & 0 \\ 0 & \frac{8}{3-\xi}(\xi-1) & 0 & \frac{8}{3-\xi}(-1-\xi) & 0 & \frac{8}{3-\xi}(\xi+1) & 0 & \frac{8}{3-\xi}(1-\xi) \\ \frac{8}{3-\xi}(\xi-1) & \frac{\eta-1}{3-\xi}(\xi-1)+\eta-1 & \frac{8}{3-\xi}(-1-\xi) & \frac{\eta-1}{3-\xi}(-1-\xi)+1-\eta & \frac{8}{3-\xi}(\xi+1) & \frac{\eta-1}{3-\xi}(\xi+1)+\eta+1 & \frac{8}{3-\xi}(1-\xi) & \frac{\eta-1}{3-\xi}(1-\xi)-1-\eta \end{bmatrix} \tag{9.76}$$

The material property matrix is defined for plane-stress problems as

$$D^{(e)}(x,y) \;=\; \frac{E^{(e)}(x,y)}{1-\nu^2}\begin{bmatrix} 1 & \nu & 0 \\ \nu & 1 & 0 \\ 0 & 0 & \dfrac{1-\nu}{2} \end{bmatrix} \tag{9.77}$$

In the above equation, ν denotes Poisson's ratio and $E^{(e)}(x,y)$ is the randomly varying elastic modulus defined by the equation

$$E^{(e)}(x,y) = E_0\,(1+f(x,y)) \tag{9.78}$$

where E_0 is the nominal elastic modulus and $f(x,y)$ is a zero mean homogeneous random field with spectral density function $S_{ff}(\kappa_1,\kappa_2)$ that is a function of the wavenumbers $\kappa_1,\kappa_2 \in \mathbb{R}^n$. Note that $f(x,y)$ is expressed in the physical Cartesian coordinate system and thus it must be mapped to the natural (ξ,η) coordinate system. Let us recall the mapping of the physical element from the parent element through the four-node shape functions

$$x(\xi,\eta) = \mathbf{N}(\xi,\eta)\mathbf{x}^{(e)} \quad , \quad y(\xi,\eta) = \mathbf{N}(\xi,\eta)\mathbf{x}^{(e)} \tag{9.79}$$

where $\mathbf{N}(\xi,\eta)$ are the four-node element shape functions in the parent coordinate system and $\mathbf{x}^{(e)}$, $\mathbf{y}^{(e)}$ are column matrices denoting x and y coordinates of element nodes. For the example trapezoid element considered:

$$x(\xi,\eta) = \frac{1}{4}\begin{bmatrix}(1-\xi)(1-\eta) & (1+\xi)(1-\eta) & (1+\xi)(1+\eta) & (1-\xi)(1+\eta)\end{bmatrix}\begin{bmatrix}0\\2\\2\\0\end{bmatrix} \tag{9.80}$$

$$= 1+\xi$$

$$y(\xi,\eta) = \frac{1}{4}\begin{bmatrix}(1-\xi)(1-\eta) & (1+\xi)(1-\eta) & (1+\xi)(1+\eta) & (1-\xi)(1+\eta)\end{bmatrix}\begin{bmatrix}0\\0.5\\1\\1\end{bmatrix} \tag{9.81}$$

$$= 0.125\xi + 0.375\eta - 0.125\xi\cdot\eta + 0.625$$

Therefore, the randomly varying elastic modulus $E^{(e)}\left[x(\xi,\eta), y(\xi,\eta)\right]$, present in the material property matrix $D^{(e)}\left[x(\xi,\eta), y(\xi,\eta)\right]$, is transformed to the natural coordinate system as

$$\begin{aligned} E^{(e)}\left[x(\xi,\eta), y(\xi,\eta)\right] &= E_0\left(1 + f\left[x(\xi,\eta), y(\xi,\eta)\right]\right) \\ &= E_0\left(1 + f(1+\xi, 0.125\xi + 0.375\eta - 0.125\xi\cdot\eta + 0.625)\right) \end{aligned} \tag{9.82}$$

After imposing a unit displacement along the 1^{st} degree of freedom, the strain energy of

the heterogeneous body is defined by the equation

$$W_{het}^{(e)} = \frac{1}{2}\iint_{\Omega} \begin{bmatrix} 1 & 0 & 0 & 0 & 0 & 0 & 0 & 0 \end{bmatrix} \Big([B]^T[D][B]\Big) \begin{bmatrix} 1 \\ 0 \\ 0 \\ 0 \\ 0 \\ 0 \\ 0 \\ 0 \end{bmatrix} d\Omega \tag{9.83}$$

which reduces to

$$\begin{aligned} W_{het}^{(e)} \;=\; & \frac{1}{2}\iint_{\Omega} \Big([B]^T[D][B]\Big)_{11}\, d\Omega = \frac{1}{2}\int_{-1}^{1}\int_{-1}^{1} \Big([B]^T[D][B]\Big)_{11} |J^{(e)}|\, d\xi\, d\eta = \\ & \frac{1}{2}\int_{-1}^{1}\int_{-1}^{1} \frac{E^{(e)}\left[x(\xi,\eta), y(\xi,\eta)\right])}{16(1-\nu^2)} \left(\left[\frac{\eta-1}{3-\xi}(\xi-1)+\eta-1\right]^2 + \left(\frac{1-\nu}{2}\right)\left[\frac{8}{3-\xi}(\xi-1)\right]^2 \right) \cdot \\ & (0.375 - 0.125\xi)\, d\xi\, d\eta \end{aligned} \tag{9.84}$$

The respective element strain energy of the homogeneous body with apparent properties $W_{hom}^{(e)}$ is derived similarly by substituting the randomly varying elastic modulus $E^{(e)}\left[x(\xi,\eta), y(\xi,\eta)\right]$ with the equivalent apparent elastic modulus for the 1^{st} degree of freedom $\bar{E}_1$

$$\begin{aligned} W_{hom}^{(e)} \;=\; & \frac{1}{2}\int_{-1}^{1}\int_{-1}^{1} \frac{\bar{E}_1}{16(1-\nu^2)} \left(\left[\frac{\eta-1}{3-\xi}(\xi-1)+\eta-1\right]^2 + \left(\frac{1-\nu}{2}\right)\left[\frac{8}{3-\xi}(\xi-1)\right]^2 \right) \cdot \\ & (0.375 - 0.125\xi)\, d\xi\, d\eta \end{aligned} \tag{9.85}$$

By equating the two expressions for strain energy, the apparent elastic modulus $\bar{E}_1$ re-

duces to the expression

$$\bar{E}_1 = E_0 \cdot \frac{\int_{-1}^{1}\int_{-1}^{1}(1+f\left[x(\xi,\eta),y(\xi,\eta)\right])\left(\left[\frac{\eta-1}{3-\xi}(\xi-1)+\eta-1\right]^2+\left(\frac{1-\nu}{2}\right)\left[\frac{8}{3-\xi}(\xi-1)\right]^2\right)(0.375-0.125\xi)\,d\xi\,d\eta}{\int_{-1}^{1}\int_{-1}^{1}\left(\left[\frac{\eta-1}{3-\xi}(\xi-1)+\eta-1\right]^2+\left(\frac{1-\nu}{2}\right)\left[\frac{8}{3-\xi}(\xi-1)\right]^2\right)(0.375-0.125\xi)\,d\xi\,d\eta} \tag{9.86}$$

where M_1 is defined as the deterministic denominator of the above equation

$$M_1 = \int_{-1}^{1}\int_{-1}^{1}\left(\left[\frac{\eta-1}{3-\xi}(\xi-1)+\eta-1\right]^2+\left(\frac{1-\nu}{2}\right)\left[\frac{8}{3-\xi}(\xi-1)\right]^2\right)(0.375-0.125\xi)\,d\xi\,d\eta \tag{9.87}$$

The target variance of $\bar{E}_1$ is calculated by computing the expectation and the mean square of the above equation. After performing the same algebraic manipulations as in the previous sections

$$\begin{aligned} Var\left[\bar{E}_1\right] &= E\left[\bar{E}_1^2\right] - E\left[\bar{E}_1\right]^2 = \\ &\frac{E_0^2}{M_1^2}\cdot\int_{-1}^{1}\int_{-1}^{1}\int_{-1}^{1}\int_{-1}^{1}\left(\left[\frac{\eta-1}{3-\xi}(\xi-1)+\eta-1\right]^2+\left(\frac{1-\nu}{2}\right)\left[\frac{8}{3-\xi}(\xi-1)\right]^2\right)\times \\ &\left(\left[\frac{w-1}{3-u}(u-1)+w-1\right]^2+\left(\frac{1-\nu}{2}\right)\left[\frac{8}{3-u}(u-1)\right]^2\right)\times \\ &(0.375-0.125\xi)\cdot(0.375-0.125u)\cdot e^{-i(\kappa_1\cdot s_1+\kappa_2\cdot s_2)}\cdot R_{ff}(s_1,s_2)\,d\xi\,d\eta\,du\,dw \end{aligned} \tag{9.88}$$

where $R_{ff}(s_1,s_2)$ is the spatial correlation function of $f\left[x(\xi,\eta),y(\xi,\eta)\right]$ and $s_1,s_2\in\mathbb{R}$ are vectors of separation distances with

$$\begin{aligned} s_1 &= 1+\xi-(1+u) = \xi-u \\ s_2 &= 0.125\xi+0.375\eta-0.125\xi\cdot\eta+0.625-(0.125u+0.375w-0.125u\cdot w+0.625) \\ &= 0.125(\xi-u)+0.375(\eta-w)-0.125(\xi\cdot\eta-u\cdot w) \end{aligned} \tag{9.89}$$

If the spectral density $S_{ff}(\kappa_1,\kappa_2)$ is substituted for $R_{ff}(s_1,s_2)$ through the Wiener-

Khintchine transform, and if we change the order of integration, then

$$Var\left[\bar{E}_1\right] = \int_{-\infty}^{\infty}\int_{-\infty}^{\infty} VRF_{\bar{E}_1}\left(\kappa_1,\kappa_2\right) S_{ff}\left(\kappa_1,\kappa_2\right)\, d\kappa_1\, d\kappa_2 \tag{9.90}$$

where $VRF_{\bar{E}_1}$ is defined as

$$\begin{aligned} VRF_{\bar{E}_1}(\kappa_1,\kappa_2) \;=\; & \frac{E_0^2}{M_1^2}\cdot \int_{-1}^{1}\int_{-1}^{1}\int_{-1}^{1}\int_{-1}^{1}\left(\left[\frac{\eta-1}{3-\xi}(\xi-1)+\eta-1\right]^2+\left(\frac{1-\nu}{2}\right)\left[\frac{8}{3-\xi}(\xi-1)\right]^2\right)\times \\ & \left(\left[\frac{w-1}{3-u}(u-1)+w-1\right]^2+\left(\frac{1-\nu}{2}\right)\left[\frac{8}{3-u}(u-1)\right]^2\right)\times \\ & (0.375-0.125\xi)\cdot(0.375-0.125u)\cdot e^{-i(\kappa_1\cdot s_1+\kappa_2\cdot s_2)}\, d\xi\, d\eta\, du\, dw \end{aligned} \tag{9.91}$$

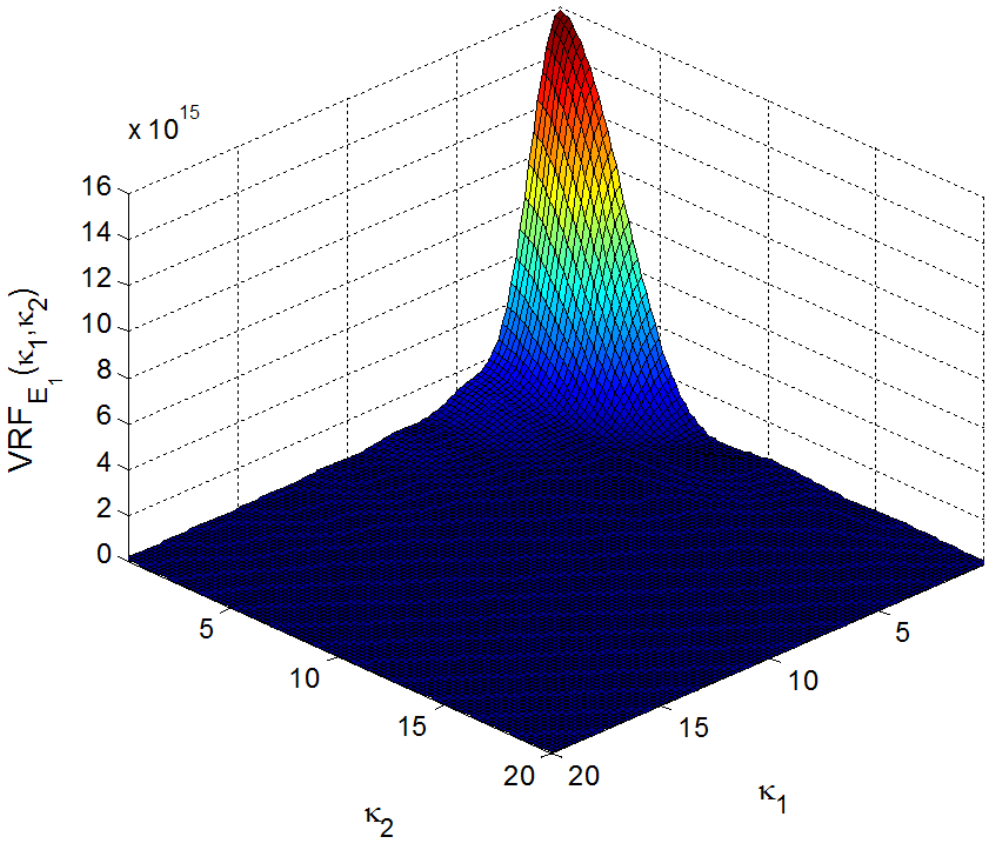

Figure 9.13: $VRF_{\bar{E}_1}(\kappa_1,\kappa_2)$ of 1^{st} degree of freedom of 4-node example trapezoid element shown in Figure 9.12.

Although the analytical integration of the above expression can be very cumbersome, it can be numerically integrated relatively easily. Figure 9.13 depicts the plot of $VRF_{\bar{E}_1}$ for the 1^{st} degree of freedom of the example trapezoid element, in one quadrant along positive values of κ_1 and κ_2, with the various parameters assigned as following: $E_0 = 125 \cdot 10^6$ and $\nu = 0.3$. The characteristics of this VRF are similar to the ones described in Figure 9.3 for the case of a square isoparametric plane stress element in natural coordinate system in Section 9.3. The curved surface peaks for $\kappa_1 = \kappa_2 = 0$ at the value of E_0^2, while displaying a decaying sequence of peaks with increasing wavenumber. In addition, the VRF is not isotropic in the κ space, since the decay rate is faster along the $\kappa_1 = \kappa_2$ diagonal than along the κ_1 and κ_2 axes. The decay rate is also faster along κ_1 axis, while it is slower along κ_2 axis. The VRF also naturally reaches the asymptotic values of $\lim_{\kappa_1,\kappa_2\to\infty} VRF_{\bar{E}}(\kappa_1, \kappa_2) = 0$.

Similarly, the rest of the VRFs are derived for the remaining 7 degrees of freedom, by imposing unit displacements in the respective d.o.f. according to Figure 9.11 and performing the same calculations. The expressions for the rest of the VRFs are as following:

$$\begin{aligned} VRF_{\bar{E}_2}(\kappa_1,\kappa_2) \;=\; & \frac{E_0^2}{M_2^2} \cdot \int_{-1}^{1}\int_{-1}^{1}\int_{-1}^{1}\int_{-1}^{1} \left(\left[\frac{8}{3-\xi}(\xi-1)\right]^2 + \left(\frac{1-\nu}{2}\right)\left[\frac{\eta-1}{3-\xi}(\xi-1)+\eta-1\right]^2 \right) \times \\ & \left(\left[\frac{8}{3-u}(u-1)\right]^2 + \left(\frac{1-\nu}{2}\right)\left[\frac{w-1}{3-u}(u-1)+w-1\right]^2 \right) \times \\ & (0.375-0.125\xi)\cdot(0.375-0.125u)\cdot e^{-i(\kappa_1\cdot s_1+\kappa_2\cdot s_2)}\, d\xi\, d\eta\, du\, dw \end{aligned} \tag{9.92}$$

$$\begin{aligned} VRF_{\bar{E}_3}(\kappa_1,\kappa_2) \;=\; & \frac{E_0^2}{M_3^2} \cdot \int_{-1}^{1}\int_{-1}^{1}\int_{-1}^{1}\int_{-1}^{1} \left(\left[\frac{\eta-1}{3-\xi}(-\xi-1)+1-\eta\right]^2 + \left(\frac{1-\nu}{2}\right)\left[\frac{8}{3-\xi}(-\xi-1)\right]^2 \right) \times \\ & \left(\left[\frac{w-1}{3-u}(-u-1)+1-w\right]^2 + \left(\frac{1-\nu}{2}\right)\left[\frac{8}{3-u}(-u-1)\right]^2 \right) \times \\ & (0.375-0.125\xi)\cdot(0.375-0.125u)\cdot e^{-i(\kappa_1\cdot s_1+\kappa_2\cdot s_2)}\, d\xi\, d\eta\, du\, dw \end{aligned} \tag{9.93}$$

$$
\begin{aligned}
VRF_{\bar{E}_4}(\kappa_1,\kappa_2) \;=\; & \frac{E_0^2}{M_4^2}\cdot\int_{-1}^{1}\int_{-1}^{1}\int_{-1}^{1}\int_{-1}^{1}\left(\left[\frac{8}{3-\xi}(-\xi-1)\right]^2+\left(\frac{1-\nu}{2}\right)\left[\frac{\eta-1}{3-\xi}(-\xi-1)+1-\eta\right]^2\right)\times \\
& \left(\left[\frac{8}{3-u}(-u-1)\right]^2+\left(\frac{1-\nu}{2}\right)\left[\frac{w-1}{3-u}(-u-1)+1-w\right]^2\right)\times \\
& (0.375-0.125\xi)\cdot(0.375-0.125u)\cdot e^{-i(\kappa_1\cdot s_1+\kappa_2\cdot s_2)}\,d\xi\,d\eta\,du\,dw
\end{aligned}
\tag{9.94}
$$

$$
\begin{aligned}
VRF_{\bar{E}_5}(\kappa_1,\kappa_2) \;=\; & \frac{E_0^2}{M_5^2}\cdot\int_{-1}^{1}\int_{-1}^{1}\int_{-1}^{1}\int_{-1}^{1}\left(\left[\frac{\eta-1}{3-\xi}(\xi+1)+\eta+1\right]^2+\left(\frac{1-\nu}{2}\right)\left[\frac{8}{3-\xi}(\xi+1)\right]^2\right)\times \\
& \left(\left[\frac{w-1}{3-u}(u+1)+w+1\right]^2+\left(\frac{1-\nu}{2}\right)\left[\frac{8}{3-u}(u+1)\right]^2\right)\times \\
& (0.375-0.125\xi)\cdot(0.375-0.125u)\cdot e^{-i(\kappa_1\cdot s_1+\kappa_2\cdot s_2)}\,d\xi\,d\eta\,du\,dw
\end{aligned}
\tag{9.95}
$$

$$
\begin{aligned}
VRF_{\bar{E}_6}(\kappa_1,\kappa_2) \;=\; & \frac{E_0^2}{M_6^2}\cdot\int_{-1}^{1}\int_{-1}^{1}\int_{-1}^{1}\int_{-1}^{1}\left(\left[\frac{8}{3-\xi}(\xi+1)\right]^2+\left(\frac{1-\nu}{2}\right)\left[\frac{\eta-1}{3-\xi}(\xi+1)+\eta+1\right]^2\right)\times \\
& \left(\left[\frac{8}{3-u}(u+1)\right]^2+\left(\frac{1-\nu}{2}\right)\left[\frac{w-1}{3-u}(u+1)+w+1\right]^2\right)\times \\
& (0.375-0.125\xi)\cdot(0.375-0.125u)\cdot e^{-i(\kappa_1\cdot s_1+\kappa_2\cdot s_2)}\,d\xi\,d\eta\,du\,dw
\end{aligned}
\tag{9.96}
$$

$$
\begin{aligned}
VRF_{\bar{E}_7}(\kappa_1,\kappa_2) \;=\; & \frac{E_0^2}{M_7^2}\cdot\int_{-1}^{1}\int_{-1}^{1}\int_{-1}^{1}\int_{-1}^{1}\left(\left[\frac{\eta-1}{3-\xi}(1-\xi)-\eta-1\right]^2+\left(\frac{1-\nu}{2}\right)\left[\frac{8}{3-\xi}(1-\xi)\right]^2\right)\times \\
& \left(\left[\frac{w-1}{3-u}(1-u)-w-1\right]^2+\left(\frac{1-\nu}{2}\right)\left[\frac{8}{w-3}(w-1)\right]^2\right)\times \\
& (0.375-0.125\xi)\cdot(0.375-0.125u)\cdot e^{-i(\kappa_1\cdot s_1+\kappa_2\cdot s_2)}\,d\xi\,d\eta\,du\,dw
\end{aligned}
\tag{9.97}
$$

$$
\begin{aligned}
VRF_{\bar{E}_8}(\kappa_1,\kappa_2) \;=\; & \frac{E_0^2}{M_8^2}\cdot\int_{-1}^{1}\int_{-1}^{1}\int_{-1}^{1}\int_{-1}^{1}\left(\left[\frac{8}{3-\xi}(1-\xi)\right]^2+\left(\frac{1-\nu}{2}\right)\left[\frac{\eta-1}{3-\xi}(1-\xi)-\eta-1\right]^2\right)\times \\
& \left(\left[\frac{8}{3-u}(1-u)\right]^2+\left(\frac{1-\nu}{2}\right)\left[\frac{w-1}{3-u}(1-u)-w-1\right]^2\right)\times \\
& (0.375-0.125\xi)\cdot(0.375-0.125u)\cdot e^{-i(\kappa_1\cdot s_1+\kappa_2\cdot s_2)}\,d\xi\,d\eta\,du\,dw
\end{aligned}
\tag{9.98}
$$

where the deterministic quantities of $M_2 - M_8$ are defined as

$$
M_2=\int_{-1}^{1}\int_{-1}^{1}\left(\left[\frac{8}{3-\xi}(\xi-1)\right]^2+\left(\frac{1-\nu}{2}\right)\left[\frac{\eta-1}{3-\xi}(\xi-1)+\eta-1\right]^2\right)(0.375-0.125\xi)\,d\xi\,d\eta \tag{9.99}
$$

$$
M_3=\int_{-1}^{1}\int_{-1}^{1}\left(\left[\frac{\eta-1}{3-\xi}(-\xi-1)+1-\eta\right]^2+\left(\frac{1-\nu}{2}\right)\left[\frac{8}{3-\xi}(-\xi-1)\right]^2\right)(0.375-0.125\xi)\,d\xi\,d\eta \tag{9.100}
$$

$$
M_4=\int_{-1}^{1}\int_{-1}^{1}\left(\left[\frac{8}{3-\xi}(-\xi-1)\right]^2+\left(\frac{1-\nu}{2}\right)\left[\frac{\eta-1}{3-\xi}(-\xi-1)+1-\eta\right]^2\right)(0.375-0.125\xi)\,d\xi\,d\eta \tag{9.101}
$$

$$
M_5=\int_{-1}^{1}\int_{-1}^{1}\left(\left[\frac{\eta-1}{3-\xi}(\xi+1)+\eta+1\right]^2+\left(\frac{1-\nu}{2}\right)\left[\frac{8}{3-\xi}(\xi+1)\right]^2\right)(0.375-0.125\xi)\,d\xi\,d\eta \tag{9.102}
$$

$$
M_6=\int_{-1}^{1}\int_{-1}^{1}\left(\left[\frac{8}{3-\xi}(\xi+1)\right]^2+\left(\frac{1-\nu}{2}\right)\left[\frac{\eta-1}{3-\xi}(\xi+1)+\eta+1\right]^2\right)(0.375-0.125\xi)\,d\xi\,d\eta \tag{9.103}
$$

$$M_7 = \int_{-1}^{1}\int_{-1}^{1}\left(\left[\frac{\eta-1}{3-\xi}(1-\xi)-\eta-1\right]^2+\left(\frac{1-\nu}{2}\right)\left[\frac{8}{3-\xi}(1-\xi)\right]^2\right)(0.375-0.125\xi)\,d\xi\,d\eta \quad (9.104)$$

$$M_8 = \int_{-1}^{1}\int_{-1}^{1}\left(\left[\frac{8}{3-\xi}(1-\xi)\right]^2+\left(\frac{1-\nu}{2}\right)\left[\frac{\eta-1}{3-\xi}(1-\xi)-\eta-1\right]^2\right)(0.375-0.125\xi)\,d\xi\,d\eta \quad (9.105)$$

Figure 9.14 depicts the VRFs of degrees of freedom $\bar{E}_1 - \bar{E}_8$ in diagonal sections with $\kappa_1 = \kappa_2$ and in edge sections obtained by setting $\kappa_2 = 0$. All VRFs display their maximum value of E_0^2 for zero wavenumber. It should be noted at this point that unlike the cases for the isoparametric 2×2 square and the rectangular element, there are no identical VRF pairs and thus all VRFs for all degrees of freedom are displayed in the graph.

Let us again consider the non-symmetric spectral density function of equation (9.40). The analytically calculated variances of apparent properties for the 8 degrees of freedom through the respective variability response functions $VRF_{\bar{E}_1} - VRF_{\bar{E}_8}$ and equation (9.90) are:

$$\begin{aligned} Var\left[\bar{E}_1\right] &= Var\left[\bar{E}_7\right] = 2.229 \cdot 10^{13} \\ Var\left[\bar{E}_2\right] &= Var\left[\bar{E}_8\right] = 2.442 \cdot 10^{13} \\ Var\left[\bar{E}_3\right] &= Var\left[\bar{E}_5\right] = 3.051 \cdot 10^{13} \\ Var\left[\bar{E}_4\right] &= Var\left[\bar{E}_6\right] = 3.762 \cdot 10^{13} \end{aligned} \quad (9.106)$$

If the spectrum utilized were to be symmetric as is the case with the spectral density function of equation (9.42), the analytically calculated variances of apparent properties for

the 8 degrees of freedom are:

$$\begin{aligned} Var\left[\bar{E}_1\right] &= Var\left[\bar{E}_7\right] = 2.167 \cdot 10^{13} \\ Var\left[\bar{E}_2\right] &= Var\left[\bar{E}_8\right] = 2.411 \cdot 10^{13} \\ Var\left[\bar{E}_3\right] &= Var\left[\bar{E}_5\right] = 2.964 \cdot 10^{13} \\ Var\left[\bar{E}_4\right] &= Var\left[\bar{E}_6\right] = 3.672 \cdot 10^{13} \end{aligned} \tag{9.107}$$

In contrast to the isoparametric 2×2 square and the rectangular element, there are 4 different values for the predicted variances which lead to the conclusion that for an arbitrary quadrilateral element, there are 4 independent expressions for the VRFs of different degrees of freedom. The VRF pairs that produce the same variances are $\bar{E}_1$ & $\bar{E}_7$, $\bar{E}_2$ & $\bar{E}_8$, $\bar{E}_3$ & $\bar{E}_5$ and $\bar{E}_4$ & $\bar{E}_6$. Furthermore, the calculated variances deviate much more from each other, compared to the minor differences of the variances for the square and rectangular element. It is therefore obvious that the usage of square or rectangular elements render the computation of apparent material properties of a finite element model more straightforward; there are only one (for square elements) or two (for rectangular elements) independent VRF expressions and most importantly the analytically calculated variances for all degrees of freedom are almost identical or very similar. However, when utilizing arbitrary shaped elements, there are four independent expressions for the VRFs and also the apparent property variability varies more significantly for different degrees of freedom. This conclusion will be further confirmed by the following example of an arbitrary irregular 4-node element with no symmetry whatsoever.

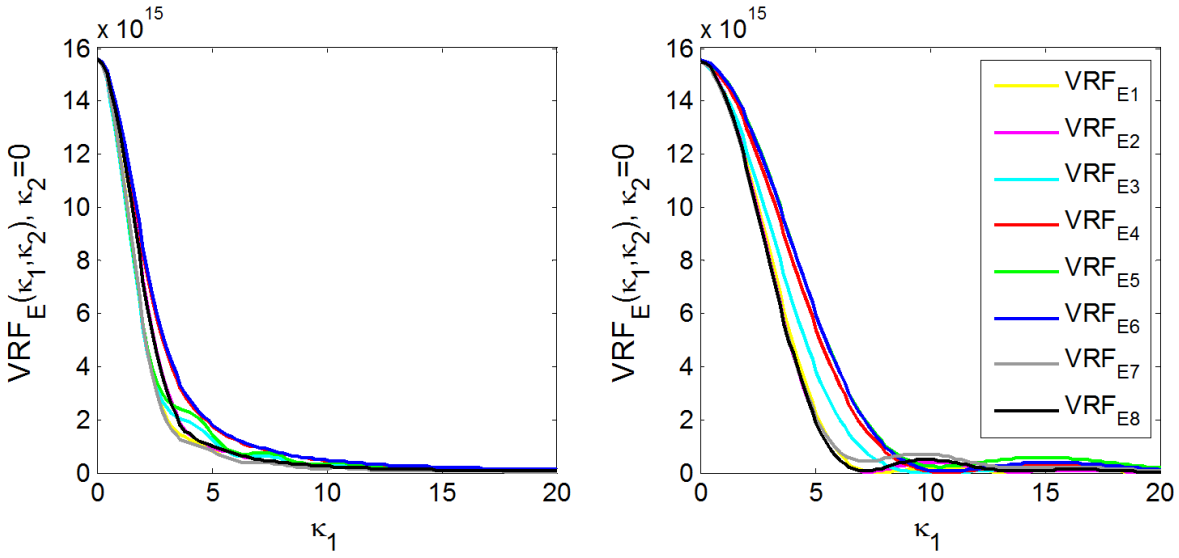

(a) Edge sections with $\kappa_1 = 0$ and $\kappa_2 = 0$.

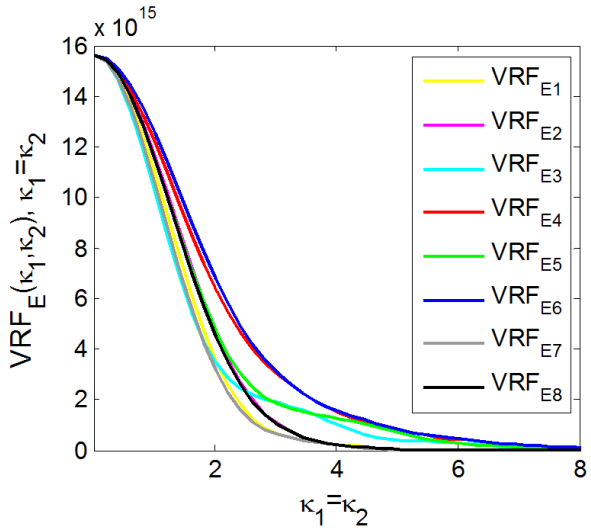

(b) Diagonal sections with $\kappa_1 = \kappa_2$.

Figure 9.14: VRFs of degrees of freedom $\bar{E}_1 - \bar{E}_8$ of 4-node example trapezoid element.

9.5.1 Example: Arbitrary Shaped Element

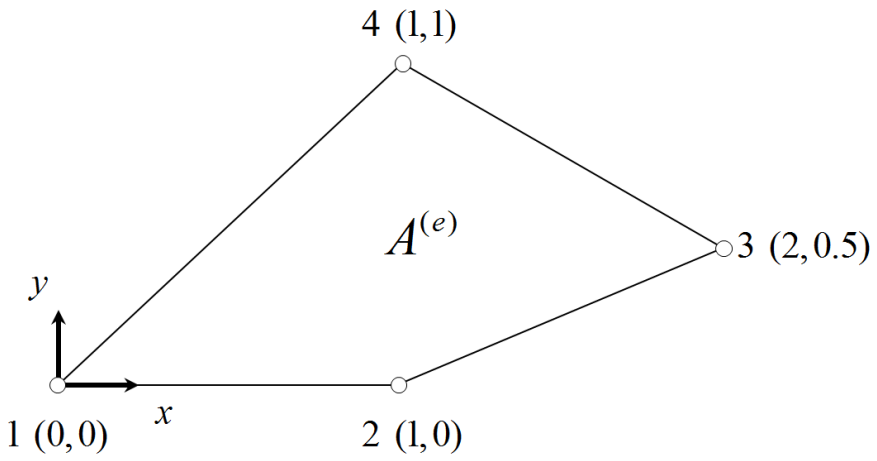

Figure 9.15: Arbitrary shaped example element with nodal coordinates.

Let us now consider an even more irregularly shaped arbitrary 4-node element as the one shown in Figure 9.15, with the following nodal coordinates

$$[x^{(e)}\ y^{(e)}] = \begin{bmatrix} 0 & 0 \\ 1 & 0 \\ 2 & 0.5 \\ 1 & 1 \end{bmatrix} \tag{9.108}$$

After formulating the VRFs for the 8 degrees of freedom in the same way as the example trapezoid shown in Figure 9.12, we obtain the following expressions for the VRFs

$$\begin{aligned} VRF_{\bar{E}_1}(\kappa_1,\kappa_2) \;=\; & \frac{E_0^2}{M_1^2}\cdot\int_{-1}^{1}\int_{-1}^{1}\int_{-1}^{1}\int_{-1}^{1}\left(\left[\frac{-2\xi+6}{\eta-\xi+4}(\eta-1)+\frac{2\eta+2}{\eta-\xi+4}(\xi-1)\right]^2+\left(\frac{1-\nu}{2}\right)\left[\frac{-8}{\eta-\xi+4}(\eta-1)+\frac{8}{\eta-\xi+4}(\xi-1)\right]^2\right)\times \\ & \left(\left[\frac{-2u+6}{w-u+4}(w-1)+\frac{2w+2}{w-u+4}(u-1)\right]^2+\left(\frac{1-\nu}{2}\right)\left[\frac{-8}{w-u+4}(w-1)+\frac{8}{w-u+4}(u-1)\right]^2\right)\times \\ & [0.0625(\eta-\xi)+0.25]\cdot[0.0625(w-u)+0.25]\cdot e^{-i(\kappa_1\cdot s_1+\kappa_2\cdot s_2)}\,d\xi\,d\eta\,du\,dw \end{aligned} \tag{9.109}$$

$$VRF_{\bar{E}_2}(\kappa_1,\kappa_2) = \frac{E_0^2}{M_2^2}\cdot\int_{-1}^{1}\int_{-1}^{1}\int_{-1}^{1}\int_{-1}^{1}\left(\left[\frac{-8}{\eta-\xi+4}(\eta-1)+\frac{8}{\eta-\xi+4}(\xi-1)\right]^2+\left(\frac{1-\nu}{2}\right)\left[\frac{-2\xi+6}{\eta-\xi+4}(\eta-1)+\frac{2\eta+2}{\eta-\xi+4}(\xi-1)\right]^2\right)\times$$
$$\left(\left[\frac{-8}{w-u+4}(w-1)+\frac{8}{w-u+4}(u-1)\right]^2+\left(\frac{1-\nu}{2}\right)\left[\frac{-2u+6}{w-u+4}(w-1)+\frac{2w+2}{w-u+4}(u-1)\right]^2\right)\times$$
$$[0.0625(\eta-\xi)+0.25]\cdot[0.0625(w-u)+0.25]\cdot e^{-i(\kappa_1\cdot s_1+\kappa_2\cdot s_2)}\,d\xi\,d\eta\,du\,dw \tag{9.110}$$

$$VRF_{\bar{E}_3}(\kappa_1,\kappa_2) = \frac{E_0^2}{M_3^2}\cdot\int_{-1}^{1}\int_{-1}^{1}\int_{-1}^{1}\int_{-1}^{1}\left(\left[\frac{-2\xi+6}{\eta-\xi+4}(1-\eta)+\frac{2\eta+2}{\eta-\xi+4}(-\xi-1)\right]^2+\left(\frac{1-\nu}{2}\right)\left[\frac{-8}{\eta-\xi+4}(1-\eta)+\frac{8}{\eta-\xi+4}(-\xi-1)\right]^2\right)\times$$
$$\left(\left[\frac{-2u+6}{w-u+4}(1-w)+\frac{2w+2}{w-u+4}(-u-1)\right]^2+\left(\frac{1-\nu}{2}\right)\left[\frac{-8}{w-u+4}(1-w)+\frac{8}{w-u+4}(-u-1)\right]^2\right)\times$$
$$[0.0625(\eta-\xi)+0.25]\cdot[0.0625(w-u)+0.25]\cdot e^{-i(\kappa_1\cdot s_1+\kappa_2\cdot s_2)}\,d\xi\,d\eta\,du\,dw \tag{9.111}$$

$$VRF_{\bar{E}_4}(\kappa_1,\kappa_2) = \frac{E_0^2}{M_4^2}\cdot\int_{-1}^{1}\int_{-1}^{1}\int_{-1}^{1}\int_{-1}^{1}\left(\left[\frac{-8}{\eta-\xi+4}(1-\eta)+\frac{8}{\eta-\xi+4}(-\xi-1)\right]^2+\left(\frac{1-\nu}{2}\right)\left[\frac{-2\xi+6}{\eta-\xi+4}(1-\eta)+\frac{2\eta+2}{\eta-\xi+4}(-\xi-1)\right]^2\right)\times$$
$$\left(\left[\frac{-8}{w-u+4}(1-w)+\frac{8}{w-u+4}(-u-1)\right]^2+\left(\frac{1-\nu}{2}\right)\left[\frac{-2u+6}{w-u+4}(1-w)+\frac{2w+2}{w-u+4}(-u-1)\right]^2\right)\times$$
$$[0.0625(\eta-\xi)+0.25]\cdot[0.0625(w-u)+0.25]\cdot e^{-i(\kappa_1\cdot s_1+\kappa_2\cdot s_2)}\,d\xi\,d\eta\,du\,dw \tag{9.112}$$

$$VRF_{\bar{E}_5}(\kappa_1,\kappa_2) = \frac{E_0^2}{M_5^2}\cdot\int_{-1}^{1}\int_{-1}^{1}\int_{-1}^{1}\int_{-1}^{1}\left(\left[\frac{-2\xi+6}{\eta-\xi+4}(1+\eta)+\frac{2\eta+2}{\eta-\xi+4}(\xi+1)\right]^2+\left(\frac{1-\nu}{2}\right)\left[\frac{-8}{\eta-\xi+4}(1+\eta)+\frac{8}{\eta-\xi+4}(\xi+1)\right]^2\right)\times$$
$$\left(\left[\frac{-2u+6}{w-u+4}(1+w)+\frac{2w+2}{w-u+4}(u+1)\right]^2+\left(\frac{1-\nu}{2}\right)\left[\frac{-8}{w-u+4}(1+w)+\frac{8}{w-u+4}(u+1)\right]^2\right)\times$$
$$[0.0625(\eta-\xi)+0.25]\cdot[0.0625(w-u)+0.25]\cdot e^{-i(\kappa_1\cdot s_1+\kappa_2\cdot s_2)}\,d\xi\,d\eta\,du\,dw \tag{9.113}$$

$$VRF_{\bar{E}_6}(\kappa_1,\kappa_2) = \frac{E_0^2}{M_6^2}\cdot\int_{-1}^{1}\int_{-1}^{1}\int_{-1}^{1}\int_{-1}^{1}\left(\left[\frac{-8}{\eta-\xi+4}(1+\eta)+\frac{8}{\eta-\xi+4}(\xi+1)\right]^2+\left(\frac{1-\nu}{2}\right)\left[\frac{-2\xi+6}{\eta-\xi+4}(1+\eta)+\frac{2\eta+2}{\eta-\xi+4}(\xi+1)\right]^2\right)\times$$
$$\left(\left[\frac{-8}{w-u+4}(1+w)+\frac{8}{w-u+4}(u+1)\right]^2+\left(\frac{1-\nu}{2}\right)\left[\frac{-2u+6}{w-u+4}(1+w)+\frac{2w+2}{w-u+4}(u+1)\right]^2\right)\times$$
$$[0.0625(\eta-\xi)+0.25]\cdot[0.0625(w-u)+0.25]\cdot e^{-i(\kappa_1\cdot s_1+\kappa_2\cdot s_2)}\,d\xi\,d\eta\,du\,dw \tag{9.114}$$

$$VRF_{\bar{E}_7}(\kappa_1,\kappa_2) = \frac{E_0^2}{M_7^2}\cdot\int_{-1}^{1}\int_{-1}^{1}\int_{-1}^{1}\int_{-1}^{1}\left(\left[\frac{-2\xi+6}{\eta-\xi+4}(-1-\eta)+\frac{2\eta+2}{\eta-\xi+4}(1-\xi)\right]^2+\left(\frac{1-\nu}{2}\right)\left[\frac{-8}{\eta-\xi+4}(-1-\eta)+\frac{8}{\eta-\xi+4}(1-\xi)\right]^2\right)\times$$
$$\left(\left[\frac{-2u+6}{w-u+4}(-1-w)+\frac{2w+2}{w-u+4}(1-u)\right]^2+\left(\frac{1-\nu}{2}\right)\left[\frac{-8}{w-u+4}(-1-w)+\frac{8}{w-u+4}(1-u)\right]^2\right)\times$$
$$[0.0625(\eta-\xi)+0.25]\cdot[0.0625(w-u)+0.25]\cdot e^{-i(\kappa_1\cdot s_1+\kappa_2\cdot s_2)}\,d\xi\,d\eta\,du\,dw \tag{9.115}$$

$$VRF_{\bar{E}_8}(\kappa_1,\kappa_2) = \frac{E_0^2}{M_8^2}\cdot\int_{-1}^{1}\int_{-1}^{1}\int_{-1}^{1}\int_{-1}^{1}\left(\left[\frac{-8}{\eta-\xi+4}(-1-\eta)+\frac{8}{\eta-\xi+4}(1-\xi)\right]^2+\left(\frac{1-\nu}{2}\right)\left[\frac{-2\xi+6}{\eta-\xi+4}(-1-\eta)+\frac{2\eta+2}{\eta-\xi+4}(1-\xi)\right]^2\right)\times$$
$$\left(\left[\frac{-8}{w-u+4}(-1-w)+\frac{8}{w-u+4}(1-u)\right]^2+\left(\frac{1-\nu}{2}\right)\left[\frac{-2u+6}{w-u+4}(-1-w)+\frac{2w+2}{w-u+4}(1-u)\right]^2\right)\times$$
$$[0.0625(\eta-\xi)+0.25]\cdot[0.0625(w-u)+0.25]\cdot e^{-i(\kappa_1\cdot s_1+\kappa_2\cdot s_2)}\,d\xi\,d\eta\,du\,dw \tag{9.116}$$

where the deterministic quantities of $M_1 - M_8$ are defined as

$$M_1=\int_{-1}^{1}\int_{-1}^{1}\int_{-1}^{1}\int_{-1}^{1}\left(\left[\frac{-2\xi+6}{\eta-\xi+4}(\eta-1)+\frac{2\eta+2}{\eta-\xi+4}(\xi-1)\right]^2+\left(\frac{1-\nu}{2}\right)\left[\frac{-8}{\eta-\xi+4}(\eta-1)+\frac{8}{\eta-\xi+4}(\xi-1)\right]^2\right)\times$$
$$[0.0625(\eta-\xi)+0.25]\,d\xi\,d\eta \tag{9.117}$$

$$M_2=\int_{-1}^{1}\int_{-1}^{1}\int_{-1}^{1}\int_{-1}^{1}\left(\left[\frac{-8}{\eta-\xi+4}(\eta-1)+\frac{8}{\eta-\xi+4}(\xi-1)\right]^2+\left(\frac{1-\nu}{2}\right)\left[\frac{-2\xi+6}{\eta-\xi+4}(\eta-1)+\frac{2\eta+2}{\eta-\xi+4}(\xi-1)\right]^2\right)\times$$
$$[0.0625(\eta-\xi)+0.25]\,d\xi\,d\eta \tag{9.118}$$

$$M_3=\int_{-1}^{1}\int_{-1}^{1}\int_{-1}^{1}\int_{-1}^{1}\left(\left[\frac{-2\xi+6}{\eta-\xi+4}(1-\eta)+\frac{2\eta+2}{\eta-\xi+4}(-\xi-1)\right]^2+\left(\frac{1-\nu}{2}\right)\left[\frac{-8}{\eta-\xi+4}(1-\eta)+\frac{8}{\eta-\xi+4}(-\xi-1)\right]^2\right)\times$$
$$[0.0625(\eta-\xi)+0.25]\,d\xi\,d\eta \tag{9.119}$$

$$M_4=\int_{-1}^{1}\int_{-1}^{1}\int_{-1}^{1}\int_{-1}^{1}\left(\left[\frac{-8}{\eta-\xi+4}(1-\eta)+\frac{8}{\eta-\xi+4}(-\xi-1)\right]^2+\left(\frac{1-\nu}{2}\right)\left[\frac{-2\xi+6}{\eta-\xi+4}(1-\eta)+\frac{2\eta+2}{\eta-\xi+4}(-\xi-1)\right]^2\right)\times$$
$$[0.0625(\eta-\xi)+0.25]\,d\xi\,d\eta \tag{9.120}$$

$$M_5 = \int_{-1}^{1}\int_{-1}^{1}\int_{-1}^{1}\int_{-1}^{1}\left(\left[\frac{-2\xi+6}{\eta-\xi+4}(1+\eta)+\frac{2\eta+2}{\eta-\xi+4}(\xi+1)\right]^2+\left(\frac{1-\nu}{2}\right)\left[\frac{-8}{\eta-\xi+4}(1+\eta)+\frac{8}{\eta-\xi+4}(\xi+1)\right]^2\right)\times [0.0625(\eta-\xi)+0.25]\,d\xi\,d\eta \tag{9.121}$$

$$M_6 = \int_{-1}^{1}\int_{-1}^{1}\int_{-1}^{1}\int_{-1}^{1}\left(\left[\frac{-8}{\eta-\xi+4}(1+\eta)+\frac{8}{\eta-\xi+4}(\xi+1)\right]^2+\left(\frac{1-\nu}{2}\right)\left[\frac{-2\xi+6}{\eta-\xi+4}(1+\eta)+\frac{2\eta+2}{\eta-\xi+4}(\xi+1)\right]^2\right)\times [0.0625(\eta-\xi)+0.25]\,d\xi\,d\eta \tag{9.122}$$

$$M_7 = \int_{-1}^{1}\int_{-1}^{1}\int_{-1}^{1}\int_{-1}^{1}\left(\left[\frac{-2\xi+6}{\eta-\xi+4}(-1-\eta)+\frac{2\eta+2}{\eta-\xi+4}(1-\xi)\right]^2+\left(\frac{1-\nu}{2}\right)\left[\frac{-8}{\eta-\xi+4}(-1-\eta)+\frac{8}{\eta-\xi+4}(1-\xi)\right]^2\right)\times [0.0625(\eta-\xi)+0.25]\,d\xi\,d\eta \tag{9.123}$$

$$M_8 = \int_{-1}^{1}\int_{-1}^{1}\int_{-1}^{1}\int_{-1}^{1}\left(\left[\frac{-8}{\eta-\xi+4}(-1-\eta)+\frac{8}{\eta-\xi+4}(1-\xi)\right]^2+\left(\frac{1-\nu}{2}\right)\left[\frac{-2\xi+6}{\eta-\xi+4}(-1-\eta)+\frac{2\eta+2}{\eta-\xi+4}(1-\xi)\right]^2\right)\times [0.0625(\eta-\xi)+0.25]\,d\xi\,d\eta \tag{9.124}$$

and $s_1, s_2 \in \mathbb{R}$ are vectors of separation distances with

$$\begin{aligned} s_1 &= 0.5(\xi+\eta-u-w) \\ s_2 &= -0.125(\xi-u)+0.375(\eta-w)-0.125(\xi\cdot\eta-u\cdot w) \end{aligned} \tag{9.125}$$

Figure 9.16 depicts the plot of $VRF_{\bar{E}_1}$ for the 1^{st} degree of freedom of the example arbitrary shaped element, in one quadrant along positive values of κ_1 and κ_2, with the various parameters assigned as following: $E_0 = 125\cdot 10^6$ and $\nu = 0.3$. The VRF plot exhibits all the usual characteristics as described previously, while the main attribute of this plot is the very slow decay of the VRF along κ_2 axis. Figure 9.17 depicts the VRFs of degrees of freedom $\bar{E}_1 - \bar{E}_8$ in diagonal sections with $\kappa_1 = \kappa_2$ and in edge sections obtained by setting $\kappa_2 = 0$. All VRFs display their maximum value of E_0^2 for zero wavenumber.

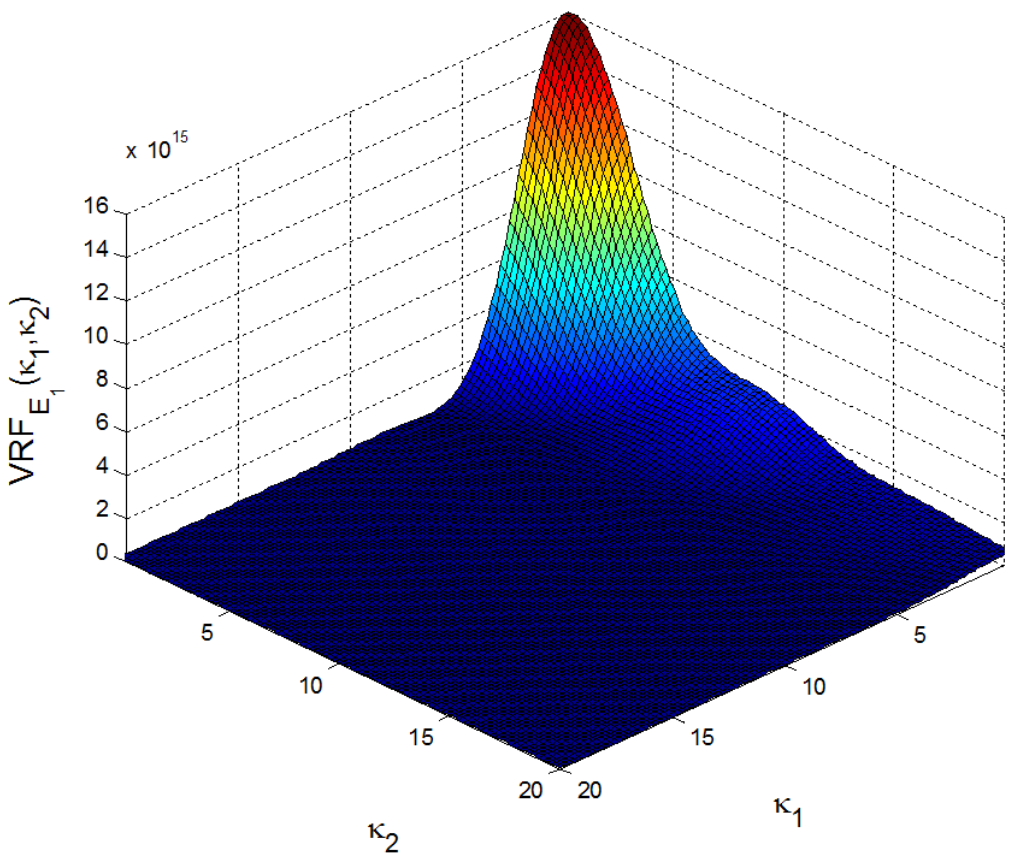

Figure 9.16: $VRF_{\bar{E}_1}(\kappa_1, \kappa_2)$ of 1^{st} degree of freedom of arbitrary shaped example element shown in Figure 9.15.

Let us again consider the non-symmetric spectral density function of equation (9.40). The analytically calculated variances of apparent properties for the 8 degrees of freedom through the respective variability response functions $VRF_{\bar{E}_1} - VRF_{\bar{E}_8}$ and equation (9.90) are:

$$\begin{aligned} Var\left[\bar{E}_1\right] &= Var\left[\bar{E}_2\right] = 3.391 \cdot 10^{13} \\ Var\left[\bar{E}_3\right] &= Var\left[\bar{E}_4\right] = 4.096 \cdot 10^{13} \\ Var\left[\bar{E}_5\right] &= Var\left[\bar{E}_6\right] = 3.111 \cdot 10^{13} \\ Var\left[\bar{E}_7\right] &= Var\left[\bar{E}_8\right] = 2.915 \cdot 10^{13} \end{aligned} \tag{9.126}$$

If the spectrum utilized were to be symmetric as is the case with the spectral density function of equation (9.42), the analytically calculated variances of apparent properties for

the 8 degrees of freedom are:

$$\begin{aligned} Var\left[\bar{E}_1\right] &= Var\left[\bar{E}_2\right] = 3.230 \cdot 10^{13} \\ Var\left[\bar{E}_3\right] &= Var\left[\bar{E}_4\right] = 3.820 \cdot 10^{13} \\ Var\left[\bar{E}_5\right] &= Var\left[\bar{E}_6\right] = 3.018 \cdot 10^{13} \\ Var\left[\bar{E}_7\right] &= Var\left[\bar{E}_8\right] = 2.829 \cdot 10^{13} \end{aligned} \tag{9.127}$$

It is thus obvious that for this irregular arbitrary quadrilateral there are again 4 different values for the predicted variances which refer to 4 independent VRF expressions. This constitutes a major conclusion, since the number of independent VRF expressions continues to be 4 even when there is no symmetry whatsoever for the element examined. The VRF pairs that produce the same variances are $\bar{E}_1$ & $\bar{E}_2$, $\bar{E}_3$ & $\bar{E}_4$, $\bar{E}_5$ & $\bar{E}_6$ and $\bar{E}_7$ & $\bar{E}_8$. It should be noted that for this particular element the VRF pairs that produce the same variances have changed, when compared to the VRF pairs of the example trapezoid element of the previous section or the VRF pairs of the square and rectangle elements. The calculated variances continue to deviate significantly from each other, which strengthens the argument that estimation of apparent property variability via the usage of square or rectangle elements is more straightforward.

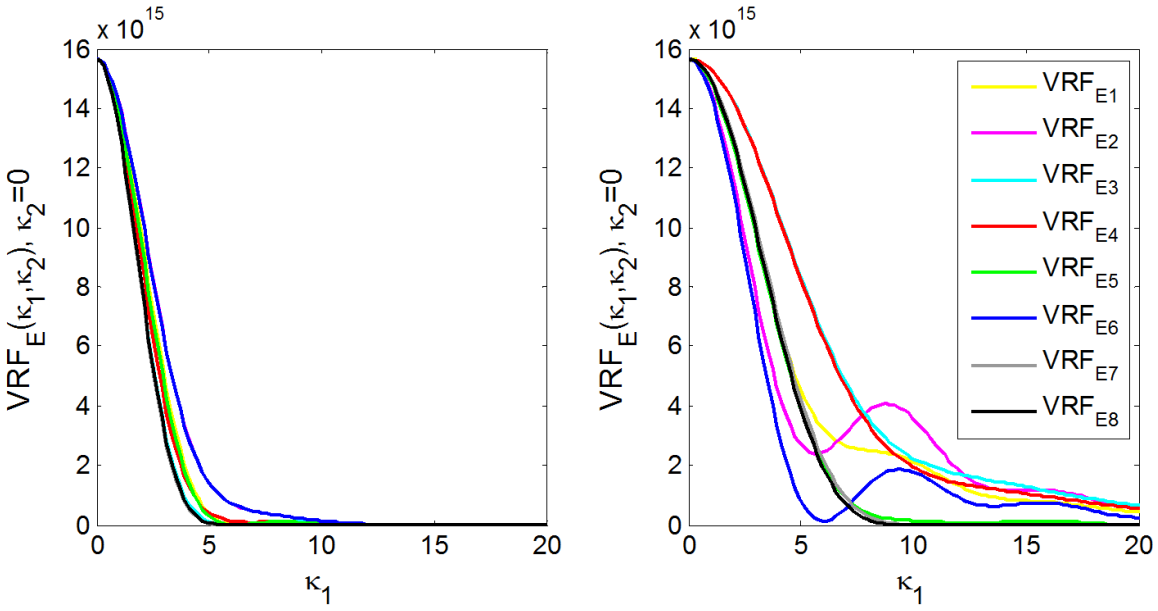

(a) Edge sections with $\kappa_1 = 0$ and $\kappa_2 = 0$.

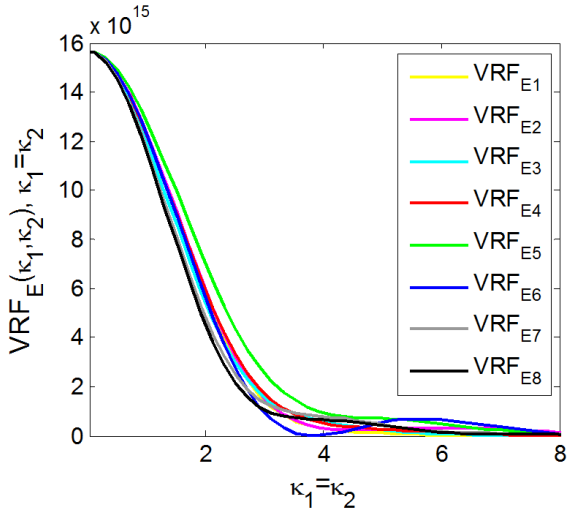

(b) Diagonal sections with $\kappa_1 = \kappa_2$.

Figure 9.17: VRFs of degrees of freedom $\bar{E}_1 - \bar{E}_8$ of 4-node example arbitrary shaped element.

9.5.2 Analytical Verification

9.5.2.1 Example 1

The methodology presented in Section 9.5 for the VRF formulation of arbitrary quadrilateral isoparametric plane stress elements in natural coordinate system will be verified by comparing the resulting VRFs of an example rectangle element with the equivalent VRFs obtained by the methodology for VRF formulation of rectangular plane stress elements in physical Cartesian coordinate system of Section 9.4. The example rectangle element chosen to demonstrate the comparison of the two methodologies has the following dimensions; $L_x^{(e)} = 1$ and $L_y^{(e)} = 2$.

On the one hand, equation (9.53) provides a straightforward way of computing $VRF_{\bar{E}_1}$ by simply substituting $L_x^{(e)} = 1$, $L_y^{(e)} = 2$, $E_0 = 125 \cdot 10^6$ and $\nu = 0.3$. On the other hand, if the methodology of Section 9.5 is to be followed, the nodal coordinates and the Jacobian matrix of the element are

$$[x^{(e)}\ y^{(e)}] = \begin{bmatrix} x_1^{(e)} & y_1^{(e)} \\ x_2^{(e)} & y_2^{(e)} \\ x_3^{(e)} & y_3^{(e)} \\ x_4^{(e)} & y_4^{(e)} \end{bmatrix} = \begin{bmatrix} 0 & 0 \\ 1 & 0 \\ 1 & 2 \\ 0 & 2 \end{bmatrix} \tag{9.128}$$

$$J^{(e)} = \begin{bmatrix} 0.5 & 0 \\ 0 & 1 \end{bmatrix} \tag{9.129}$$

with $|J^{(e)}| = 0.5$. The resulting VRF for the first degree of freedom is

$$VRF_{\bar{E}_1}(\kappa_1,\kappa_2) = \frac{E_0^2}{M_1^2}\cdot\int_{-1}^{1}\int_{-1}^{1}\int_{-1}^{1}\int_{-1}^{1}\left[4\left(\eta-1\right)^2+\left(\frac{1-\nu}{2}\right)\left(\xi-1\right)^2\right]\times \left[4\left(w-1\right)^2+\left(\frac{1-\nu}{2}\right)\left(u-1\right)^2\right]\cdot e^{-i(\kappa_1 s_1+\kappa_2 s_2)}\cdot 0.5\cdot 0.5\, d\xi\, d\eta\, du\, dw \tag{9.130}$$

where

$$M_1 = \int_{-1}^{1}\int_{-1}^{1}\left[4\left(\eta-1\right)^2+\left(\frac{1-\nu}{2}\right)\left(\xi-1\right)^2\right]\cdot 0.5\, d\xi\, d\eta \tag{9.131}$$

and

$$s_1 = 0.5(\xi-u) \qquad \& \qquad s_2 = \eta - w \tag{9.132}$$

Figure 9.18 demonstrates that the two VRFs obtained by the two methodologies are identical and thus verifies the validity of both VRF formulations.

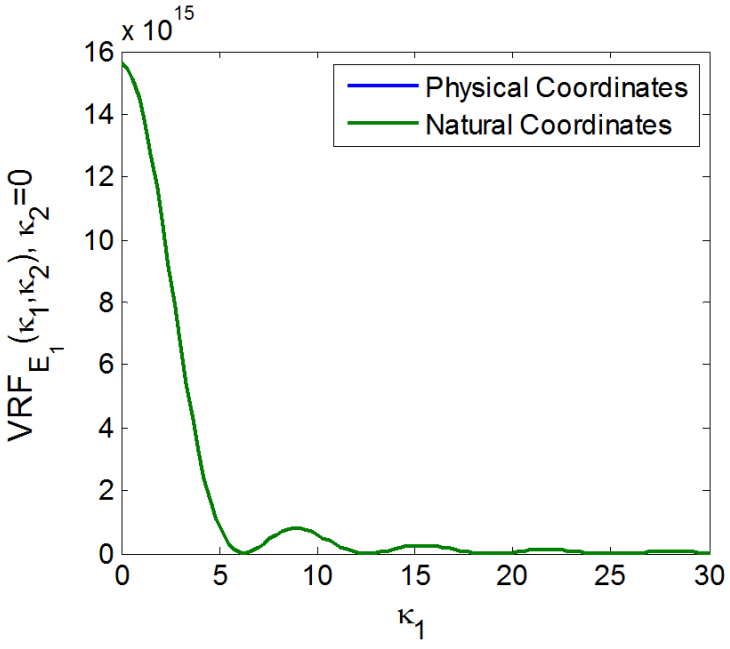

Figure 9.18: Comparison of $VRF_{\bar{E}_1}$ curves of rectangle element with $L_x^{(e)} = 1$ and $L_y^{(e)} = 2$ for the two methodologies of VRF formulation presented in Sections 9.4 for physical coordinates and Section 9.5 for natural coordinates.

9.5.2.2 Example 2

Let us now consider the trivial example of a rectangle element with $L_x^{(e)} = 2$ and $L_y^{(e)} = 2$. In Section 9.4.1, it was shown that the equation (9.25) of $VRF_{\bar{E}_1}$ for the square isoparametric plane stress element in natural coordinate system provides an identical VRF curve as equation (9.53) of the rectangular plane stress element in physical Cartesian coordinate system with $L_x^{(e)} = 2$ and $L_y^{(e)} = 2$ (Figure 9.9). Therefore, the methodologies of Sections 9.3 and 9.4 reduce to the same VRF curves for this trivial example. The next analytical verification is to compare the VRFs derived from Section 9.5 for the same trivial example but obtained through the formulation of mapping from the natural to the physical coordinates by using the Jacobian matrix. The nodal coordinates and the Jacobian matrix of the element are

$$[x^{(e)}\ y^{(e)}] = \begin{bmatrix} x_1^{(e)} & y_1^{(e)} \\ x_2^{(e)} & y_2^{(e)} \\ x_3^{(e)} & y_3^{(e)} \\ x_4^{(e)} & y_4^{(e)} \end{bmatrix} = \begin{bmatrix} 0 & 0 \\ 2 & 0 \\ 2 & 2 \\ 0 & 2 \end{bmatrix} \tag{9.133}$$

$$J^{(e)} = \begin{bmatrix} 1 & 0 \\ 0 & 1 \end{bmatrix} \tag{9.134}$$

which is the essentially the identity matrix $\mathbf{I}$. Therefore, the VRF expression reduces to the equation (9.25) of $VRF_{\bar{E}_1}$ for the square isoparametric element (which is already proven to be identical to equation (9.53) of the rectangular element with $L_x^{(e)} = 2$ and $L_y^{(e)} = 2$). The methodology of Section 9.5 is thus successfully verified.

9.6 Concluding Remarks

After finalizing the apparent property VRF formulation procedure for the isoparametric 2×2 square in natural coordinates, for rectangles in physical coordinates as well as for any 4-node arbitrary quadrilateral element through mapping in the natural coordinate system, it is obvious that the variance assessment of apparent material properties can be performed for any shape of finite element and thus any system geometry. For well-constructed meshes where the system geometry can be divided into the simplest square elements in the natural coordinate system, the VRF is provided analytically through equation (9.25). For more complicated meshes where the geometry allows for simulation of rectangular elements with different values of $L_x^{(e)}$ and $L_y^{(e)}$, the VRF is also analytically estimated through equation (9.53). Finally, if the system geometry is complicated enough so that it cannot be simulated by rectangles but rather by arbitrary 4-node quadrilateral elements (or a combination of rectangles and quadrilaterals), it is encouraged to follow the procedure presented in this section in order to analytically derive the desired VRF in integral form for each quadrilateral separately, and consequently integrate the result numerically.

The VRF formulation procedure presented in this chapter reveals a set of VRFs corresponding to a 4-node plane stress element, i.e. one VRF for each of the 8 degrees of freedom. It is shown that the inherent symmetries embedded in the isoparametric 2×2 square in natural coordinates render the 8 VRF expressions to be reduced to only one truly independent VRF expression that yields either one or two very similar values for the variance of apparent material properties, for a given symmetric or a non-symmetric SDF, respectively. Similar conclusions are drawn for the rectangular element, where the VRF formulation in physical Cartesian coordinates yields only two independent VRF expressions that also predict two similar values for the variance of apparent material properties (for either a symmetric or non-symmetric SDF). However, the VRF formulation for arbitrary shaped elements yields four independent VRF expressions with predicted variances that may deviate significantly from

each other. It is therefore obvious that the usage of square or rectangle elements render the computation of apparent material properties of a finite element model more straightforward. These results are quite encouraging as regards to the application of the VRF methodology to a broad set of finite element models that comprise mainly rectangular elements.

Towards the direction of surmounting the challenge of the VRFs not being uniquely defined for a single element, future research work should be dedicated on establishing a unified VRF which corresponds to a single apparent material property and thus a single value for its variance. One way of achieving the above is to introduce a weighted sum of the VRFs (Arwade et al. 2015 [100]) in a way that the selected weights minimize the error between the homogeneous and the heterogeneous versions of the problem.

Chapter 10

Effect of Element Geometry on VRF Form

After formulating the variability response functions of apparent material properties of rectangular elements and 4-node arbitrary quadrilateral elements, the calculation of a series of VRFs for rectangles with different values of $L_x^{(e)}$ and $L_y^{(e)}$, as well as for arbitrary quadrilateral elements with different nodal coordinates, will be presented in this chapter. The following examples display observations based on those VRFs, regarding the effect of the element geometry on the form of the VRFs. More specifically, the dependencies of the VRFs on scale, shape and aspect ratio of the example rectangular elements will be illustrated and discussed. For reference, the VRF only for the 1^{st} degree of freedom of each element will be presented, without loss of generality for the rest of degrees of freedom, especially due to the minor differences observed between VRFs of different d.o.f's when considering square and rectangle elements.

10.1 Scale Effect

Firstly, the scale effect on the form of the VRFs is addressed. Consider the following rectangular elements with constant aspect ratio $\frac{L_y^{(e)}}{L_x^{(e)}} = 2$

1. R_1: $L_x^{(e)} = 1 \quad ; \; L_y^{(e)} = 2$
2. R_2: $L_x^{(e)} = 2 \quad ; \; L_y^{(e)} = 4$
3. R_3: $L_x^{(e)} = 4 \quad ; \; L_y^{(e)} = 8$
4. R_4: $L_x^{(e)} = 6 \quad ; \; L_y^{(e)} = 12$

For all the example rectangles, $VRF_{\bar{E}_1}$ is analytically computed according to equation (9.53) for the 1^{st} degree of freedom and $E_0 = 125 \cdot 10^6$ and $\nu = 0.3$. The diagonal sections with $\kappa_1 = \kappa_2$ of those VRFs, along with edge sections obtained by setting $\kappa_1 = 0$ and $\kappa_2 = 0$, are depicted in Figure 10.1. The plots exhibit the usual VRF characteristics of peak around zero wavenumbers at the value of E_0^2 and asymptotic values with increasing wavenumbers. There is also a decaying sequence of peaks at the $\kappa_2 = 0$ edge sections, when compared to a smoother decay for the $\kappa_1 = \kappa_2$ diagonal sections. The series of VRFs demonstrate a sensitivity of the VRF to the area of the rectangular element, given a uniform aspect ratio for all cases: the larger the element (R_4), the faster the decay of the VRF.

The effect of scale in the VRF form is most effectively demonstrated by calculating the associated variances of $\bar{E}_1$ through equation (9.23) when considering the non-symmetric spectrum of equation (9.40). The calculated results are as follows: $Var\left[\bar{E}_1\right]_{R_1} = 2.255 \cdot 10^{13}$, $Var\left[\bar{E}_1\right]_{R_2} = 0.670 \cdot 10^{13}$, $Var\left[\bar{E}_1\right]_{R_3} = 0.178 \cdot 10^{13}$ and $Var\left[\bar{E}_1\right]_{R_4} = 0.079 \cdot 10^{13}$. It is evident that the larger the area of the element the smaller the variance is predicted, indicating that larger elements reduce the variance and thus provide higher stability of apparent material properties.

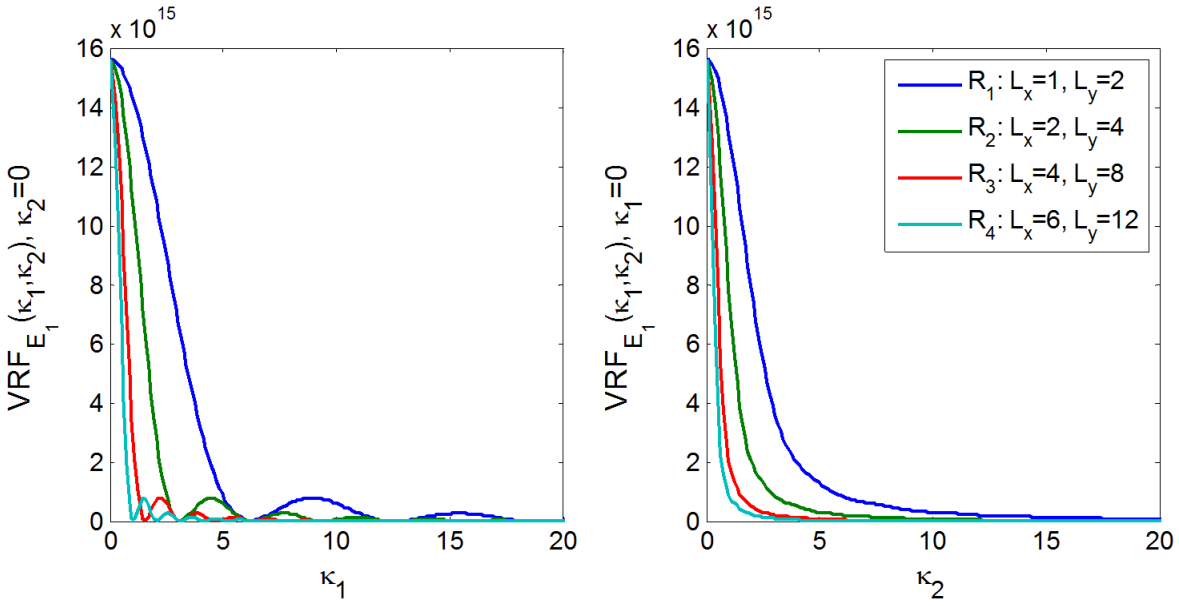

(a) Edge sections with $\kappa_1 = 0$ and $\kappa_2 = 0$.

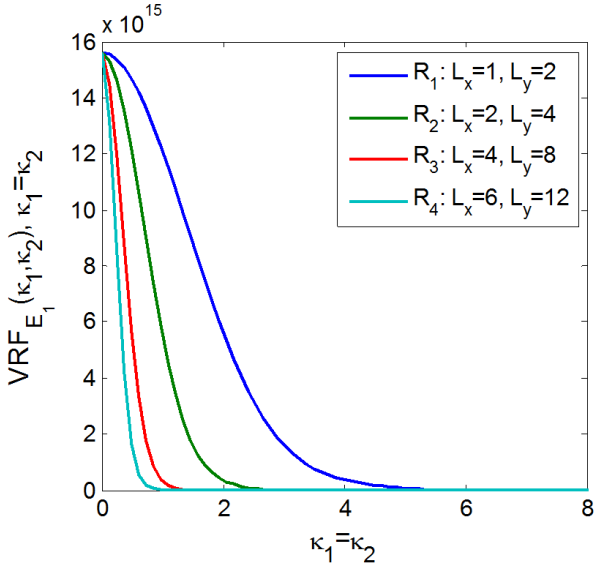

(b) Diagonal sections with $\kappa_1 = \kappa_2$.

Figure 10.1: $VRF_{\bar{E}_1}$ for rectangular 4-node elements $R1 - R4$ with dimensions $L_x^{(e)}$ and $L_y^{(e)}$. Scale effect on VRF form.

The VRFs for elements with dimensions with constant aspect ratio can be scaled to coincide when the wavenumber is also scaled by the following quantity, for example for elements R_1 and R_2

$$\hat{\kappa_1} = \kappa_1 \sqrt{\frac{A_1}{A_2}} \qquad \& \qquad \hat{\kappa_2} = \kappa_2 \sqrt{\frac{A_1}{A_2}} \tag{10.1}$$

and therefore

$$VRF_{\bar{E}}^{(R_1)}(\kappa_1, \kappa_2) = VRF_{\bar{E}}^{(R_2)}(\hat{\kappa_1}, \hat{\kappa_2}) \tag{10.2}$$

as depicted in Figure 10.2.

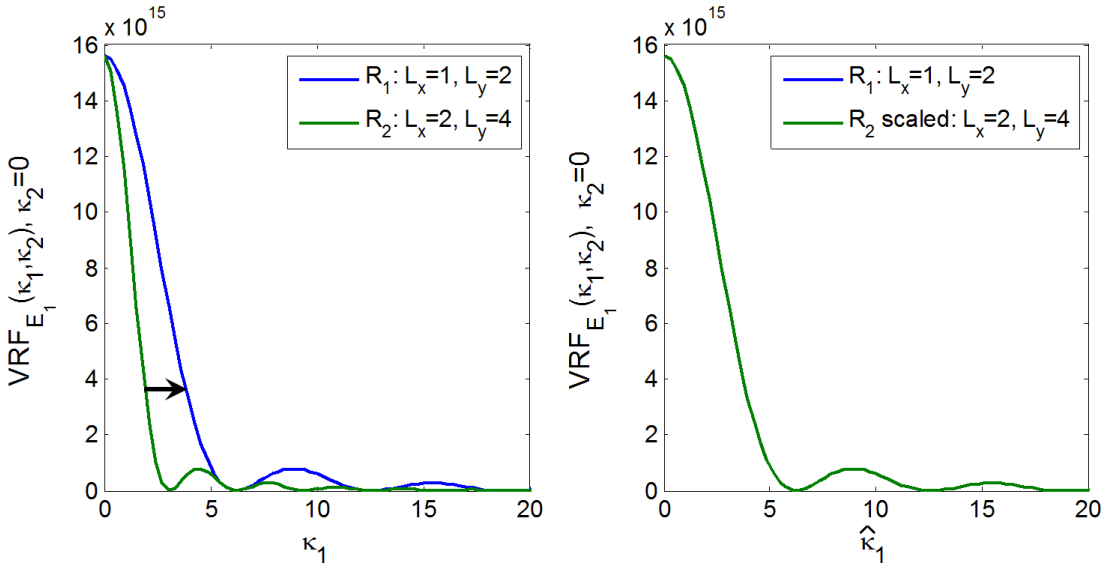

Figure 10.2: $VRF_{\bar{E}_1}(\kappa_1, \kappa_2)$ of 1^{st} degree of freedom of 4-node elements $R1$ and $R2$ with same aspect ratio, showing that VRFs coincide with appropriate scaling of the wavenumber $\hat{\kappa_1}, \hat{\kappa_2}$.

The same equality holds for the rest of example rectangles when the respective VRFs are scaled accordingly:

$$\begin{aligned} VRF_{\bar{E}}^{(R_1)}(\kappa_1, \kappa_2) &= VRF_{\bar{E}}^{(R_3)}(\hat{\kappa_1}, \hat{\kappa_2}) \quad for \quad \hat{\kappa_1} = \kappa_1\sqrt{\frac{A_1}{A_3}} \quad \& \quad \hat{\kappa_2} = \kappa_2\sqrt{\frac{A_1}{A_3}} \\ VRF_{\bar{E}}^{(R_1)}(\kappa_1, \kappa_2) &= VRF_{\bar{E}}^{(R_4)}(\hat{\kappa_1}, \hat{\kappa_2}) \quad for \quad \hat{\kappa_1} = \kappa_1\sqrt{\frac{A_1}{A_4}} \quad \& \quad \hat{\kappa_2} = \kappa_2\sqrt{\frac{A_1}{A_4}} \end{aligned} \tag{10.3}$$

10.2 Aspect Ratio Effect

Next, the following paragraphs will discuss the influence of aspect ratio on the VRF form. Consider the below example rectangular elements with common $L_x^{(e)} = 1$

1. A_1: $L_x^{(e)} = 1$; $L_y^{(e)} = 1$
2. A_2: $L_x^{(e)} = 1$; $L_y^{(e)} = 2$
3. A_3: $L_x^{(e)} = 1$; $L_y^{(e)} = 3$
4. A_4: $L_x^{(e)} = 1$; $L_y^{(e)} = 5$

the VRFs of which are illustrated in Figure 10.3, both as edge sections with $\kappa_1 = 0$ and $\kappa_2 = 0$ and diagonal sections with $\kappa_1 = \kappa_2$. As expected, the VRFs decay more rapidly with increasing wavenumber as the height of the element increases. Naturally, this leads to an equivalent decrease in the associated variances with increasing element height, when the variances of $\bar{E}_1$ are calculated through equation (9.23) and the non-symmetric spectrum of equation (9.40); $Var\left[\bar{E}_1\right]_{A_1} = 3.462 \cdot 10^{13}$, $Var\left[\bar{E}_1\right]_{A_2} = 2.255 \cdot 10^{13}$, $Var\left[\bar{E}_1\right]_{A_3} = 1.643 \cdot 10^{13}$ and $Var\left[\bar{E}_1\right]_{A_4} = 1.046 \cdot 10^{13}$ (those values become $Var\left[\bar{E}_1\right]_{A_1} = 3.380 \cdot 10^{13}$, $Var\left[\bar{E}_1\right]_{A_2} = 2.238 \cdot 10^{13}$, $Var\left[\bar{E}_1\right]_{A_3} = 1.644 \cdot 10^{13}$ and $Var\left[\bar{E}_1\right]_{A_4} = 1.054 \cdot 10^{13}$ if the symmetric spectrum of equation (9.42) is utilized).

This effect can be largely attributed to the increasing area of the elements with larger side lengths. In order to highlight the effect of aspect ratio only, while neglecting the effect of scale associated with larger areas of those example elements, the same plots are illustrated in Figure 10.4 with respect to the scaled wavenumbers $\hat{\kappa_1}$ and $\hat{\kappa_2}$ as defined in Section 10.1. For $\kappa_2 = 0$, the VRFs decay more rapidly with decreasing of the maximum element side length (until $L_x^{(e)} = 1$; $L_y^{(e)} = 1$) but the exact opposite holds for $\kappa_1 = 0$, where the VRFs decay more rapidly with increasing of the maximum element side length (until $L_x^{(e)} = 1$; $L_y^{(e)} = 5$). The new associated variances, when considering the spectrum of

equation (9.40), are: $Var\left[\bar{E}_1\right]_{A_1} = 3.462 \cdot 10^{13}$, $Var\left[\bar{E}_1\right]_{A_2} = 3.854 \cdot 10^{13}$, $Var\left[\bar{E}_1\right]_{A_3} = 3.881 \cdot 10^{13}$ and $Var\left[\bar{E}_1\right]_{A_4} = 3.779 \cdot 10^{13}$ (those values become $Var\left[\bar{E}_1\right]_{A_1} = 3.380 \cdot 10^{13}$, $Var\left[\bar{E}_1\right]_{A_2} = 3.821 \cdot 10^{13}$, $Var\left[\bar{E}_1\right]_{A_3} = 3.875 \cdot 10^{13}$ and $Var\left[\bar{E}_1\right]_{A_4} = 3.808 \cdot 10^{13}$ if the symmetric spectrum of equation (9.42) is utilized). It therefore follows that while the curves are significantly shifted due to scaling of the wavenumber, the final computed variances are very similar, meaning that the aspect ratio does not impose any significant effect on the VRF form. The initial variance discrepancies are attributed to the different areas of the example elements rather than their different aspect ratios (strengthening the effect of scale of Section 10.1). However, it should be noted here that the element that produces the minimum variance of apparent properties is the square element, meaning that it demonstrates slightly higher stability compared to the rest of the rectangular elements.

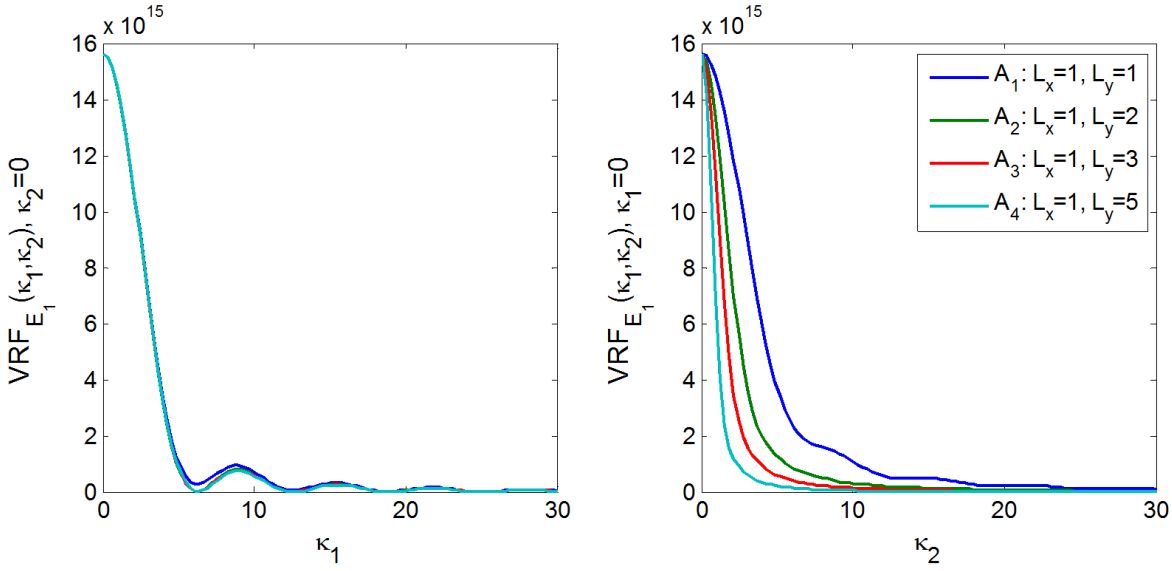

(a) Edge sections with $\kappa_1 = 0$ and $\kappa_2 = 0$.

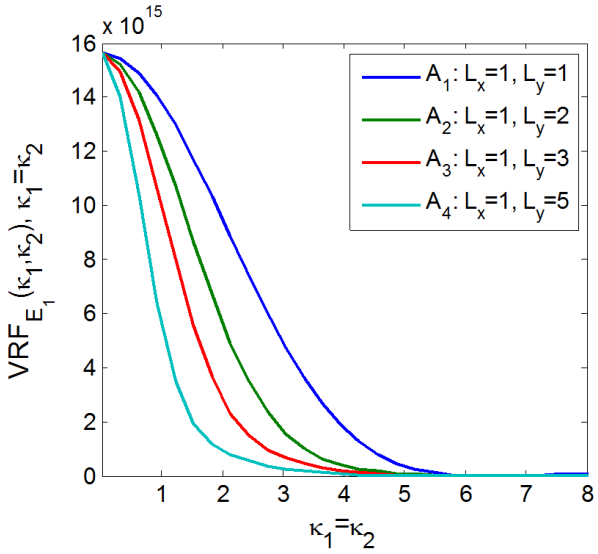

(b) Diagonal sections with $\kappa_1 = \kappa_2$.

Figure 10.3: $VRF_{\bar{E}_1}$ for rectangular 4-node elements $A1 - A4$ with dimensions $L_x^{(e)}$ and $L_y^{(e)}$. Aspect ratio effect on VRF form.

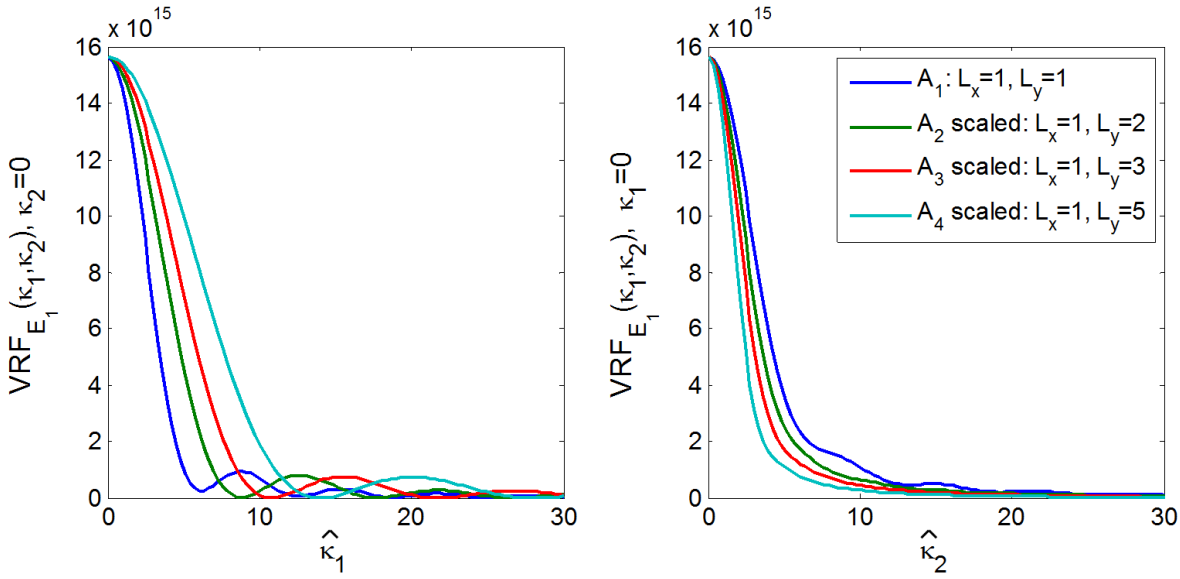

(a) Edge sections with $\hat{\kappa_1} = 0$ and $\hat{\kappa_2} = 0$.

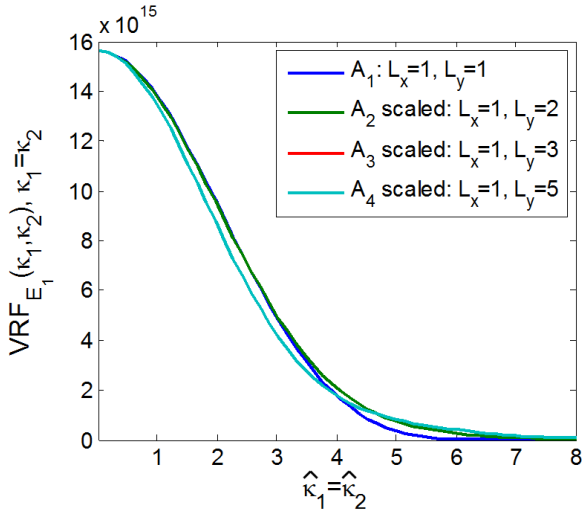

(b) Diagonal sections with $\hat{\kappa_1} = \hat{\kappa_2}$.

Figure 10.4: $VRF_{\bar{E}_1}$ for rectangular 4-node elements $A1-A4$ plotted against scaled wavenumbers $\hat{\kappa_1}, \hat{\kappa_2}$.

10.3 Shape Effect

Lastly, in order to address the effect of shape in the form of VRFs, consider the following rectangular and trapezoid elements with same area (equal to 9) but different shape

1. S_1: $L_x^{(e)} = 3$; $L_y^{(e)} = 3$
2. S_2: $L_x^{(e)} = 2$; $L_y^{(e)} = 4.5$
3. S_3: $L_x^{(e)} = 1$; $L_y^{(e)} = 9$
4. T_1 with nodal coordinates $(x_1, y_1) = (0, 0)$, $(x_2, y_2) = (2, 5)$, (x_3, y_3)=(2,7) and $(x_4, y_4) = (0, 7)$

The variability response functions $VRF_{\bar{E}_1}$ for the rectangular elements will be calculated according to equation (9.53) for the specific values of $L_x^{(e)}$ and $L_y^{(e)}$ for each case, while for the trapezoid element T_1 the calculation of the VRF follows the procedure presented in Section 9.5. For all cases, $E_0 = 125 \cdot 10^6$ and $\nu = 0.3$. The resulting $VRF_{\bar{E}_1}$ of the trapezoid can be expressed as

$$\begin{aligned} VRF_{\bar{E}_1}(\kappa_1, \kappa_2) \;=\; & \frac{E_0^2}{M_1^2} \cdot \int_{-1}^{1}\int_{-1}^{1}\int_{-1}^{1}\int_{-1}^{1} \left(\left[\frac{5\eta - 5}{12 - 5\xi}(\xi - 1) + \eta - 1 \right]^2 + \left(\frac{1-\nu}{2} \right) \left[\frac{4}{12 - 5\xi}(\xi - 1) \right]^2 \right) \times \\ & \left(\left[\frac{5w - 5}{12 - 5u}(u - 1) + w - 1 \right]^2 + \left(\frac{1-\nu}{2} \right) \left[\frac{4}{12 - 5u}(u - 1) \right]^2 \right) \times \\ & (3 - 1.25\xi)(3 - 1.25u) e^{-i(\kappa_1 \cdot s_1 + \kappa_2 \cdot s_2)} \, d\xi \, d\eta \, du \, dw \end{aligned} \tag{10.4}$$

where

$$M_1 = \int_{-1}^{1}\int_{-1}^{1} \left(\left[\frac{5\eta - 5}{12 - 5\xi}(\xi - 1) + \eta - 1 \right]^2 + \left(\frac{1-\nu}{2} \right) \left[\frac{4}{12 - 5\xi}(\xi - 1) \right]^2 \right) (3 - 1.25\xi) \, d\xi \, d\eta \tag{10.5}$$

and

$$s_1 = \xi - u \qquad \& \qquad s_2 = 1.25(\xi - u) + 2.25(\eta - w) - 1.25(\xi \cdot \eta - u \cdot w) \tag{10.6}$$

For reference and demonstration purposes, only the VRF for the 1^{st} degree of freedom will be presented, although in Chapter 9 it was proven that there can be a significant deviation between the VRFs of different degrees of freedom for arbitrary quadrilaterals. Therefore, the following comparisons are considered by the author as preliminary, until future research on the topic of defining a unified VRF which corresponds to a single apparent material property is conducted.

The VRFs of the aforementioned elements are depicted in Figure 10.5, both as edge sections with $\kappa_1 = 0$ and $\kappa_2 = 0$ and diagonal sections with $\kappa_1 = \kappa_2$. The same trend as in the Section 10.2 is observed herein; for $\kappa_2 = 0$, the VRFs decay more rapidly with decreasing of the maximum element side length (until $L_x^{(e)} = 3$; $L_y^{(e)} = 3$) but the exact opposite holds for $\kappa_1 = 0$, where the VRFs decay more rapidly with increasing of the maximum element side length (almost until $L_x^{(e)} = 1$; $L_y^{(e)} = 9$). The associated variances, when considering the non-symmetric spectrum of equation (9.40), are: $Var\left[\bar{E}_1\right]_{S_1} = 0.530 \cdot 10^{13}$, $Var\left[\bar{E}_1\right]_{S_2} = 0.608 \cdot 10^{13}$, $Var\left[\bar{E}_1\right]_{S_3} = 0.596 \cdot 10^{13}$ and $Var\left[\bar{E}_1\right]_{T_1} = 0.624 \cdot 10^{13}$ (those values become $Var\left[\bar{E}_1\right]_{S_1} = 0.526 \cdot 10^{13}$, $Var\left[\bar{E}_1\right]_{S_2} = 0.606 \cdot 10^{13}$, $Var\left[\bar{E}_1\right]_{S_3} = 0.604 \cdot 10^{13}$ and $Var\left[\bar{E}_1\right]_{T_1} = 0.632 \cdot 10^{13}$ if the symmetric spectrum of equation (9.42) is utilized). Consequently, the predicted variances are very similar, meaning that the shape effect does not impose any significant effect on the VRF form. Nevertheless, the square element continues to provide the minimum variance, as was the case at Section 10.2, and thus enhances the stability of apparent material properties.

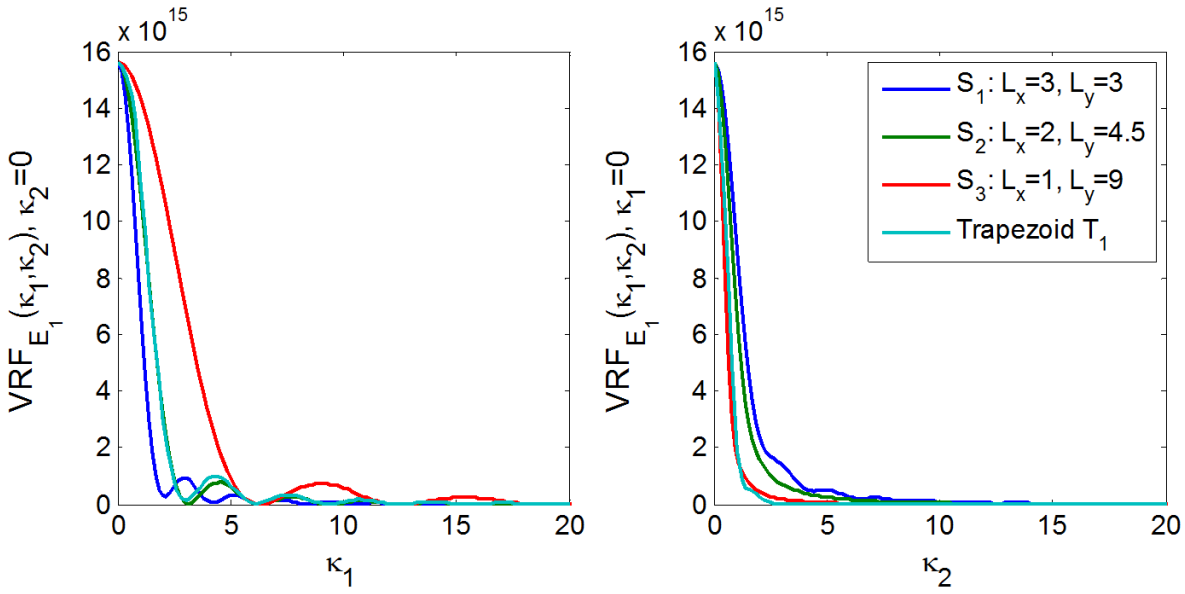

(a) Edge sections with $\kappa_1 = 0$ and $\kappa_2 = 0$.

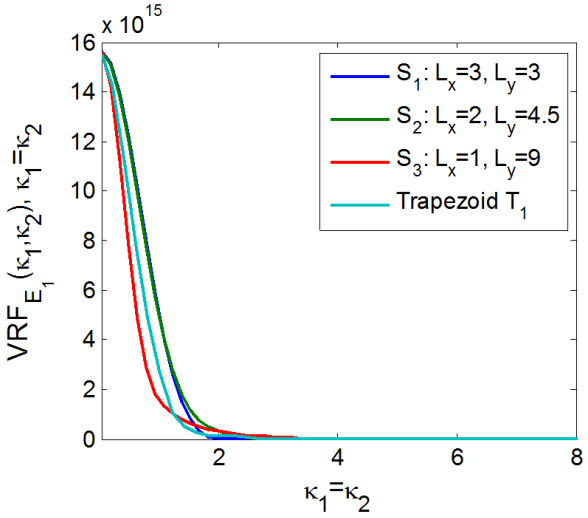

(b) Diagonal sections with $\kappa_1 = \kappa_2$.

Figure 10.5: $VRF_{\bar{E}_1}$ for rectangular 4-node elements $S1 - S3$ with dimensions $L_x^{(e)}$ and $L_y^{(e)}$ and trapezoid element T_1. Shape effect on VRF form.

10.4 Concluding Remarks

All the above examples underline the significant effect of the element geometry on the form of variability response functions. The most significant influence on the VRF form is proven to be the element scale, since different elements of increasing scale clearly produce very distinct VRFs in the sense that they decay more rapidly. Moreover, the influence of element aspect ratio on the VRF form is shown to be eliminated through appropriate scaling of the wavenumber. Finally, no significant effect of the element shape (for elements with constant area) was detected in this study, since the associated variances computed for each different shaped element were similar.

The influence of the element geometry on the form of variability response functions demonstrates that the estimation of apparent property variability through the VRF concept in a finite element domain can be challenging, since a different VRF has to be computed for each element in a mesh. The computational effort to calculate different VRFs for square and rectangle elements in a finite element mesh is relatively small since analytical expressions are provided in this dissertation for either cases, i.e. for a simple 2×2 square and for rectangles of any geometry with L_x and L_y. The associated variances of apparent material properties can be calculated by using the analytical VRF expressions and performing Gauss quadrature to integrate the product of the VRFs and the given SDF (equation 8.7). Nevertheless, there is an additional computational cost when calculating the VRFs for arbitrary quadrilateral elements, since this dissertation provides only the analytical expression of their integral definition. Although it is very cumbersome to calculate this integral definition analytically, the integration can be instead numerical (Gauss quadrature is again applicable) but will of course increase the computational intensity of the approach.

The aforementioned computational cost for the estimation of apparent property variability through the VRF concept in a finite element domain is to be compared with the classical FEA approach of calculating the local stiffness matrices for every element in a mesh and

then assembling into a global stiffness matrix. Let us consider a very unstructured mesh where a different VRF has to be computed for each element.....

Moreover, this VRF dependence on the element geometry constitutes a further justification for the use of well-constructed meshes with elements of consistent size and shape, in order not only to achieve small condition numbers of the characteristic FE matrices (e.g. stiffness matrix) but also an approximate uniformity in the VRF form across the FE model. Finally, in the case where it is practically impossible to simulate a system with finite elements of uniform size and shape, an alternative of computing a separate VRF for each element would be to compute a single VRF for an average-sized element geometry that would essentially represent an average VRF. Although this would lead to a less accurate estimation of the apparent property variability, the error introduced would be relatively small provided that the elements size and shape do not vary significantly throughout the finite element model.

Chapter 11

Conclusions: Part II

11.1 Research Contributions

This dissertation presents the formulation of variability response functions for apparent properties in 2D plane stress problems discretized in a finite element domain. The VRFs introduced here provide an efficient means for evaluating the variance of apparent material properties averaged over finite material volumes. The VRFs are also independent of the spectrum and marginal distribution of the underlying material property homogeneous random field $f(x, y)$. Thus, the VRFs need to be calculated analytically only once and then they can be used to compute the variance of apparent material properties for any underlying random field, provided that the spectral characteristics are available. In other words, the VRFs are useful for conducting a full sensitivity analysis of the apparent property variability to the spectral contents of the underlying material property stochastic field, without recourse to any additional Monte Carlo simulation and with the minimal computational effort of a simple analytical integration.

The analytical formulation of the apparent property VRFs is performed through strain energy equivalence between a randomly varying (heterogeneous) material property, i.e. modulus of elasticity, and an equivalent homogeneous spatially constant material property. The

VRF formulation for 4-node quadrilateral elements is performed for the following cases, which summarize all possibilities for simulating any geometry of finite element models, from simple square domains to more complicated or arbitrary shapes:

1. Square isoparametric finite element in natural coordinate system
2. Generic rectangular element in physical Cartesian coordinate system
3. Arbitrary quadrilateral element that is mapped from physical to natural coordinate system

The estimation of apparent property variability is conducted for every degree of freedom of 4-node elements by imposing unit displacements in the respective d.o.f. For square elements, it is shown that there is only one truly independent VRF for all the degrees of freedom of a single element. For rectangular elements, it is shown that there is not a unique VRF expression for all the degrees of freedom but rather two independent expressions. However, for both square and rectangular elements, it is demonstrated through relevant examples that the analytically computed variances of apparent material properties (associated with either a single independent VRF or two independent VRFs) are quantitatively very similar. For arbitrary quadrilateral elements, it is proven that there are four independent VRF expressions with predicted variances that may deviate significantly from each other, depending on the specific element geometry. It is therefore obvious that the usage of square or rectangle elements render the computation of apparent material properties of a finite element model more straightforward. These results are quite encouraging as regards to the application of the VRF methodology to a broad set of finite element models that comprise mainly rectangular elements.

For demonstration purposes, a series of example VRFs have been calculated and compared, in order to highlight the efficacy of the VRF approach for predicting the variance of apparent material properties and underline the effect of the element scale, shape and aspect

ratio in the resulting VRF form. No significant effect of aspect ratio or shape of the element was detected, provided that the scale effect is eliminated by appropriate scaling of the wavenumber. However, it is proven that there is a strong dependence of the VRF form on the scale of the element; the larger the size of an element, the faster decay is exhibited in the VRF curve and thus the smaller associated apparent property variance is computed.

11.2 Future Research Opportunities

An important assumption made in this work is that the Poisson's ratio ν is a deterministic constant, while the only varying quantity is the heterogeneous elastic modulus $E(x, y)$. This assumption also leads to the statement that the shear modulus $G(x, y) = \dfrac{E(x, y)}{2(1 + \nu)}$ must also be heterogeneous and perfectly correlated to the elastic modulus in order to preserve isotropy. An interesting research direction is to investigate the validity of this assumption by exploring the stochasticity of Poisson's ratio and its effect on the analytical calculation of variability response functions for apparent material properties. In order to treat Poisson's ratio as another randomly varying quantity, it is also necessary that appropriate correlation functions between Poisson's ratio and the already varying modulus of elasticity are established.

The methodology presented in this dissertation reveals that the VRFs of apparent material properties of 4-node plane stress elements are not uniquely defined, since there is a minimum of one truly independent VRF expression (for the case of square elements), and intermediate case of two independent VRF expressions (for rectangular elements) and a maximum of four independent VRF expressions (for the case of arbitrary shaped elements). In further work on this topic, it is anticipated that a unified VRF is defined which corresponds to a single apparent material property and thus a single value for its variance. One way of achieving the above is to introduce a weighted sum of the VRFs (Arwade et al. 2015 [100]) in a way that the selected weights minimize the error between the homogeneous and the heterogeneous versions of the problem.

In this dissertation, the analytical procedure to calculate VRFs for apparent material properties has been developed over a single finite element rather than a global finite element model of an entire body. The methodology presented herein may constitute an important accomplishment towards a multiscale analysis of stochastic material properties. Let us consider a body that is discretized into finite elements with randomly fluctuating elastic modulus. By utilizing the VRF formulations described in the Chapter 9 for any 4-node element geometry, it is possible that the elastic modulus can be modeled as a random variable with mean value E_0 and variance computed by equation 8.7, for every element. The marginal distribution of those random variables ought also to be assumed or approximated, for example as a Gaussian distribution. The next step towards a real stochastic material upscaling is to determine whether those random variables are element-to-element independent or not. If the elements are large enough then the random variables representing the elastic modulus of each element can be considered independent, however there is a threshold where the size of the elements could approach the RVE and thus the variances of the random variables may become very small or negligible. Therefore, a more realistic approach is to consider the random variables as dependent by establishing appropriate covariance matrices. Once the covariance matrices are determined, along with the marginal distribution, mean value and variance of those random variables, generation of sets of sample realizations over the entire finite element model could be possible.

Bibliography

[1] Unified Facilities Criteria (UFC). Design of buildings to resist progressive collapse. US Department of Defense, 2009.

[2] US General Services Administration. Progressive collapse analysis and design guidelines for new federal buildings and major modernization projects. GSA. 2003.

[3] Frangopol D.M., Curley J.P. Effects of damage and redundancy on structural reliability. Journal of Structural Engineering 1987; 113: 1533-1549.

[4] Ettouney M., Smilowitz R., Tang M., Hapij A. Global System Considerations for Progressive Collapse with Extensions to Other Natural and Man-Made Hazards. Journal of Performance of Constructed Facilities ASCE 2006; 20: 403-417.

[5] Starossek U. Progressive collapse of structures. Hamburg: Thomas Telford; 2009.

[6] Ellingwood B.R., Smilowitz R., Dusenberry D.O., Dutinh D., Lew H.S., Carino N. Best practices for reducing the potential for progressive collapse in buildings. U.S.A. USA: Department of Commerce; 2007.

[7] Marjanishvili S., Agnew E. Comparison of various procedures for progressive collapse analysis. Journal of performance of constructed facilities 2011; 20: 365-374.

[8] Gerasimidis S., Deodatis G., Kontoroupi T., Ettouney M. Loss-of-stability induced progressive collapse modes in 3D steel moment frames. Structure and Infrastructure Engineering 2014; 11: 1-25.

[9] Kim J, Kim T. Assessment of progressive collapse-resisting capacity of steel moment frames. Journal of Constructional Steel Research 2009; 65: 169-179.

[10] Khandelwal L., El-Tawil S. Pushdown resistance as a measure of robustness in progressive collapse analysis. Engineering Structures 2011; 33: 2653-2661.

[11] Gerasimidis S., Sideri J. A new partial distributed damage method for progressive collapse analysis of buildings. Journal of Constructional Steel Research 2016; 119: 233–245.

[12] Kwasniewski L. Nonlinear dynamic simulations of progressive collapse for a multistory building. Engineering Structures 2010; 5: 1223–35.

[13] Baker J.W., Schubert M., Faber M. On the assessment of robustness. Structural Safety 2008; 30: 253-267.

[14] Izuddin B.A., Vlassis A.G., Elghazouli A.Y., Nethercot D.A. Progressive collapse of multi-storey buildings to sudden column loss—part I: simplified assessment framework. Engineering Structures 2008; 30: 1308-1318.

[15] Foley C.M., Martin K., Schneeman C. Robustness in structural steel framing systems. Final report submitted to American Institute of Steel construction. Chicago: Marquette University; 2007.

[16] Galal K., El-Sawy T. Effect of retrofit strategies on mitigating progressive collapse of steel frame structures. Journal of Constructional Steel Research 2010; 66: 520–31.

[17] Fu F. Progressive collapse analysis of high-rise building with 3-D finite element modeling method. Journal of Constructional Steel Research 2009; 65: 1269–78.

[18] Fu F. Response of a multi-storey steel composite building with concentric bracing under consecutive column removal scenarios. Journal of Constructional Steel Research 2012; 70: 115–126.

[19] Tsai M.H., Lin B.H. Investigation of progressive collapse resistance and inelastic response for an earthquake-resistant RC building subjected to column failure. Engineering Structures 2008; 30: 3619–28.

[20] Szyniszewski S., Krauthammer T. Energy flow in progressive collapse of steel framed buildings. Engineering Structures 2012; 42: 142–153.

[21] Alashker Y., Li H., El-Tawil S. Approximations in progressive collapse modeling. Journal of Structural Engineering 2011; 137: 914–924.

[22] Ettouney M., DiMaggio P. Integrated study of progressive collapse of buildings. In Proceedings of structural engineering world congress 1998. San Francisco.

[23] Kim T., Kim J., Park J. Investigation of progressive collapse-resisting capability of steel moment frames using push-down analysis. Journal of Performance of Constructed Facilities 2009; 23: 327–335.

[24] Gerasimidis S. Analytical assessment of steel frames progressive collapse vulnerability to corner column loss. Journal of Constructional Steel Research 2014; 95: 1-9.

[25] Spyridaki, A., Gerasimidis, S., Deodatis, G., Ettouney, M. Safety, reliability, risk and life-cycle performance of structures and infrastructures. Proceedings of the 11th international conference on structural safety and reliability. ICOSSAR 2013, pp. 5053–5058.

[26] Sideri J., Gerasimidis S., Deodatis G., Ettouney M. Ductile progressive collapse mechanisms of steel moment frames. ICOSSAR 2013, New York, USA.

[27] Yan Y., Gerasimidis S., Deodatis G., Ettouney M. A study on the global loss of stability progressive collapse mechanisms of steel moment frames. ICOSSAR 2013, New York, USA.

[28] Ellingwood B.R. Load and resistance factor criteria for progressive collapse design. Available from http://www.nibs.org; 2002.

[29] Sasani M., Kazemi A., Sagiroglu S., Forest S. Progressive collapse resistance of an actual 11-story structure subjected to severe initial damage. Journal of Structural Engineering 2011; 137(9): 893–902.

[30] Shi Y., Li Z-X., Hao H. A new method for progressive collapse analysis of RC frames under blast loading. Engineering Structures 2010; 32: 1691-1703.

[31] McConnell J.R., Brown H. Evaluation of progressive collapse alternate load path Analyses in designing for blast resistance of steel columns. Engineering Structures 2011; 33: 2899-2909.

[32] Jayasooriya R., Thambiratnam D., Perera N., Kosse V. Blast and residual capacity analysis of reinforced concrete framed buildings. Engineering Structures 2011; 33: 3483-3495.

[33] Mlakar P.F., Corley W.G., Sozen M.A., Thornton C.H. The Oklahoma City bombing: analysis of blast damage to the Murrah Building. Journal of Performance of Constructed Facilities 12.3 (1998): 113-119.

[34] Abboud, N., Levy, M., Tennant, D., Mould, J., Levine, H., King, S., Ekwueme, C., Jain, A., Hart, G. Anatomy of a disaster: A structural investigation of the World Trade Center collapses. ASCE 3^{rd} Forensic Congress, San Diego, California. 2003.

[35] Gerasimidis S, Bisbos CD, Baniotopoulos CC. A computational model for full or partial damage of single or multiple adjacent columns in disproportionate collapse analysis via linear programming. Structure and Infrastructure Engineering 2014; 10: 670-683.

[36] Kachanov L. Introduction to continuum damage mechanics. Brookline, MA: Springer; 1986.

[37] Lemaitre J. A Continuous Damage Mechanics Model for Ductile Fracture. Journal of Engineering Materials and Technology 1985; 107: 83-89.

[38] CEN (Comité Européen de Normalisation). Eurocode 8: Design provisions for earthquake resistance of structures (ENV 1998-1-Parts 1, 2, 3). 1994, 1995.

[39] CEN Eurocode 3: Design of steel structures. (EN 1993-1: 1993). Brussels: May; 1993.

[40] Gerasimidis S, Bisbos CD, Baniotopoulos CC. Vertical geometric irregularity assessment of steel frames on robustness and disproportionate collapse. Journal of Constructional Steel Research 2012; 74: 76-89.

[41] Simulia. ABAQUS Theory Manual. Version 6.12 Dassault Systemes.

[42] Risk management series, Reference Manual to mitigate potential terrorist attacks against buildings. FEMA, 426; December 2003.

[43] Marchand A.K., Alfawakhiri F. Facts for steel buildings: blast and progressive collapse. Chicago (IL): American Institute of Steel Construction; 2005.

[44] Le Blanc G., Adoum M., Lapoujade V. External blast load on structures—Empirical approach. 5th European LS-DYNA Users conference, 2005.

[45] Hamburger R., Whittaker A. Design of steel structures for blast-related progressive collapse resistance. Modern Steel Construction 2004.

[46] Krauthammer T. AISC research on structural steel to resist blast and progressive collapse. Chicago (IL): American Institute of Steel Construction; 2005.

[47] Luccioni B.M., Ambrosini R.D., Danesi R.F. Analysis of building collapse under blast loads. Engineering Structures 2004; 26: 63-71.

[48] Krauthammer T., Otani R.K. Mesh, gravity and load effects on finite element simulations of blast loaded reinforced concrete structures. Computers & Structures 1997; 63: 1113–1120.

[49] Yi Z., Agrawal A. K., Ettouney M., Alampalli S. Blast Load Effects on Highway Bridges. I: Modeling and Blast Load Effects. Journal of Bridge Engineering 2013; 19(4): 04013023.

[50] Shi Y., Hao H., Li Z.X. Numerical derivation of pressure-impulse diagrams for prediction of RC column damage to blast loads. International Journal of Impact Engineering 2008; 35: 1213–27.

[51] Fu F. Dynamic response and robustness of tall buildings under blast loading. Journal of Constructional Steel Research 2013; 80: 299-307.

[52] Li J., Hao H. Numerical study of structural progressive collapse using substructure technique. Engineering Structures 2013; 52: 101-113.

[53] Elsanadedy H.M., Almusallam T.H. , Alharbi Y.R., Al-Salloum Y.A., Abbas H. Progressive collapse potential of a typical steel building due to blast attacks. Journal of Constructional Steel Research 2014; 101: 143-157.

[54] Tadepalli T., Mullen C.L. Vulnerability of Low Rise Buildings to External Blast Events: Damage Mapping. EM08, Inaugural International Conference of the Engineering Mechanics Institute, Minneapolis, MN, 2008.

[55] SAC-FEMA-355C. State of the art report on systems performance of steel moment frames subject to earthquake ground shaking. Federal Emergency Management Agency 2000.

[56] Agarwal A., Varma A. H. Fire induced progressive collapse of steel building structures: The role of interior gravity columns. Engineering Structures 2014; 58: 129–140.

[57] Applied Research Associates. Vulnerability Assessment and Protection Option (VAPO); 2005.

[58] Kingery, C.N., Bulmash, G. Airblast Parameters from TNT Spherical Air Burst and Hemispherical Surface Burst. ARBRL-TR-02555, Ballistic Research Laboratory; 1984.

[59] Kinney, G.F., Graham, K.J. Explosive Shocks in Air, 2nd Ed. Springer-Verlag New York Inc., 1985.

[60] Unified Facilities Criteria (UFC 3-340-02). Structures to resist the effects of accidental explosions. US Department of Defense; 2008.

[61] TM5-1300. Structures to resist the effects of accidental explosions. US Departments of the Army Technical manual, the Navy and the Air force; 1990.

[62] Conventional weapons effects (ConWep). Computer software produced by U.S. army Waterways Experimental station. Mississippi, USA; 1990.

[63] Applied Research Associates. A.T.-BLAST. Version 2.1; 2000.

[64] Baker, W.E. Explosions in Air. University of Texas Press, Austin, 1973.

[65] Timoshenko S.P., Gere J.M. Theory of Elastic Stability McGraw-Hill, 1961 (Dover reprint of 2nd edition, 2009).

[66] Chen W.F., Liu E.M. Structural Stability: Theory and Implementation. Prentice Hall, 1987.

[67] AISC 360-10. Specification for Structural Steel Buildings. American Institute for Steel Construction, 2010.

[68] Biggs J.M. Introduction to Structural Dynamics. McGraw-Hill, 1964.

[69] Wolfram Mathematica. Version 9.0 Wolfram Research, Inc.

[70] Matlab. Version 2014a. The Mathworks, Inc.

[71] Karnovsky I.A., Lebed O.I. Formulas for Structural Dynamics: Tables, Graphs, and Solutions. McGraw-Hill, 2001.

[72] Bokaian, A. Natural frequencies of beams under compressive axial loads. Journal of Sound and Vibration 1988; 126(1): 49-65.

[73] Bažant Z.P., Cedolin L. Stability of Structures: Elastic, Inelastic, Fracture, and Damage Theories. Oxford University Press, 1991 (Dover reprint, 2003).

[74] Chopra A.K. Dynamics of Structures: Theory and Applications to Earthquake Engineering. 4th Ed. Prentice-Hall, 2011.

[75] Lubliner J., Oliver J., Oller S., Oňate E. A plastic-damage model for concrete. International Journal of Solids and Structures 1989; 25: 299-329.

[76] Lee J., Fenves G.L. Plastic-damage model for cyclic loading of concrete structures. Journal of Engineering Mechanics 1998; 124(8): 892-900.

[77] Kmiecik P., Kaminski M. Modelling of reinforced concrete structures and composite structures with concrete strength degradation taken into consideration. Archives of Civil and Mechanical Engineering 2011; 11(3): 623-636.

[78] Sideri J., Gerasimidis S., Deodatis G., Ettouney M. The effect of partial distributed damage on the progressive collapse mechanisms and collapse loads of high-rise steel buildings. Engineering Mechanics Institute Conference 2015, Stanford, CA, USA.

[79] Sideri J., Mullen C., Gerasimidis S., Deodatis G. Progressive collapse vulnerability of 3D high rise steel buildings under external blast loading. Engineering Mechanics Institute Conference 2015, Stanford, CA, USA.

[80] Mullen C., Sideri J., Gerasimidis S., Deodatis G. Influence of beam-column parameter interdependency on SDOF based damage mapping in blast impact region of a high-rise steel building. Engineering Mechanics Institute Conference 2015, Stanford, CA, USA.

[81] Sideri J., Mullen C., Gerasimidis S., Deodatis G. The role of interior gravity columns on blast-induced progressive collapse potential of tall buildings. Engineering Mechanics Institute Conference 2016, Vanderbilt, TN, USA.

[82] Sab K. On the homogenization and the simulation of random materials. European journal of mechanics. A. Solids 1992; 11(5): 585-607.

[83] Shinozuka M. Structural response variability. Journal of engineering mechanics 1987; 113(6): 825-842.

[84] Deodatis G., Shinozuka M. Bounds on response variability of stochastic systems. Journal of Engineering Mechanics 1989; 115(11): 2543-63.

[85] Deodatis G. Bounds on response variability of stochastic finite element systems. Journal of Engineering Mechanics 1990; 116(3): 565-85.

[86] Shinozuka M., Deodatis G. Response variability of stochastic finite element systems. Journal of Engineering Mechanics 1988; 114(3): 499-519.

[87] Deodatis G. Weighted integral method. I: stochastic stiffness matrix. Journal of Engineering Mechanics 1991; 117(8): 1851-64.

[88] Deodatis G., Shinozuka M. Weighted integral method. II: response variability and reliability. Journal of Engineering Mechanics 1991; 117(8): 1865-77.

[89] Wall F.J., Deodatis G. Variability response functions of stochastic plane stress/strain problems. Journal of engineering mechanics 1994; 120(9): 1963-1982.

[90] Graham-Brady L., Deodatis G. Variability response functions for stochastic plate bending problems. Structural safety 1998; 20(2): 167-188.

[91] Deodatis G., Graham-Brady L., Micaletti R. A hierarchy of upper bounds on the response of stochastic systems with large variation of their properties: random variable case. Probabilistic Engineering Mechanics 2003; 18(4): 349-63.

[92] Deodatis G., Graham-Brady L., Micaletti R. A hierarchy of upper bounds on the response of stochastic systems with large variation of their properties: random field case. Probabilistic engineering mechanics 2003; 18(4): 365-75.

[93] Graham-Brady L., Deodatis G. Response and eigenvalue analysis of stochastic finite element systems with multiple correlated material and geometric properties. Probabilistic Engineering Mechanics 2001; 16(1): 11-29.

[94] Papadopoulos V., Deodatis G., Papadrakakis M. Flexibility-based upper bounds on the response variability of simple beams. Computer Methods in Applied Mechanics and Engineering 2005; 194(12): 1385-1404.

[95] Miranda M, Deodatis G. Generalized variability response functions for beam structures with stochastic parameters. Journal of Engineering Mechanics 2012; 138(9): 1165-1185.

[96] Teferra K., Deodatis G. Variability response functions for beams with nonlinear constitutive laws. Probabilistic Engineering Mechanics 2012; 29: 139-148.

[97] Arwade S.R., Deodatis G. Variability response functions for effective material properties. Probabilistic Engineering Mechanics 2011; 26(2): 174-181.

[98] Teferra K., Arwade, S.R., Deodatis G. Stochastic variability of effective properties via the generalized variability response function. Computers & Structures 2012; 110: 107-115.

[99] Teferra K., Arwade, S.R., Deodatis G. Generalized variability response functions for two-dimensional elasticity problems. Computer Methods in Applied Mechanics and Engineering 2014; 272: 121-137.

[100] Arwade S.R., Deodatis G., Teferra K. Variability response functions for apparent material properties. Probabilistic Engineering Mechanics, In Press 2015.

[101] Miranda M. On the Response Variability of Beam Structures with Stochastic Variations of Parameters. PhD thesis, Columbia University, 2009.

[102] Teferra K. Developments in the Theory and Applications of the Variability Response Function Concept. PhD thesis, Columbia University, 2012.

[103] Shinozuka M., Jan C. M. Digital simulation of random processes and its applications. Journal of sound and vibration 1972; 25(1): 111-128.

[104] Karhunen K. Über lineare Methoden in der Wahrscheinlichkeitsrechnung. Vol. 37. Universitat Helsinki, 1947.

[105] Kac M., Siegert A.J.F. An explicit representation of a stationary Gaussian process. The Annals of Mathematical Statistics 1947; 18(3): 438-442.

[106] Loève P. Fonctions aléatoires du second ordre, A note in P. Lévy, Processus stochastiques et mouvement Brownien, Paris, Gauthier-Villars, 1948.

[107] Ghanem R.G., Spanos P.D. Stochastic finite elements: a spectral approach. Courier Corporation, 2003.

[108] Wiener N. Generalized harmonic analysis. Acta Mathematica 1930; 55: 117-258.

[109] Khintchine A. Korrelationstheorie der stationären stochastischen Prozesse. Mathematische Annalen 1934; 109(1): 604-615.

[110] Priestley M. Spectral Analysis and Times Series Volume 1: Univariate Series. Academic Press, 1981.

[111] Papoulis A. Probability, Random Variables, and Stochastic Processes. WCB/McGraw-Hill, 3rd edition, 1991.

[112] Shinozuka M., Deodatis G. Simulation of stochastic processes by spectral representation. Applied Mechanics Reviews 1991; 44(4): 191-204.

[113] Brigham E.O. Fast Fourier Transform and its Applications. Prentice-Hall Inc. 1988.

[114] Shinozuka M., Deodatis G. Simulation of multi-dimensional Gaussian stochastic fields by spectral representation. Applied Mechanics Reviews 1996; 49(1): 29-53.

[115] Sideri J., Spyridaki A., Deodatis G. Variability response functions for apparent material properties in two-dimensional elasticity problems. Probabilistic Mechanics & Reliability Conference 2016, Vanderbilt, TN, USA.

[116] Hughes T.J.R. The Finite Element Method: Linear Static and Dynamic Finite Element Analysis Prentice-Hall Inc. 1987.

[117] Segerlind L.J. Applied finite element analysis. John Wiley, New York, NY 1984.